On the Generation and Fate of Free Carriers in Non-Fullerene Acceptor Organic Solar Cells

---

Kumulative Dissertation

zur Erlangung des akademischen Grades
"doctor rerum naturalium"
(Dr. rer. nat.)
in der Wissenschaftsdisziplin Experimentalphysik

eingereicht an der
Mathematisch-Naturwissenschaftlichen Fakultät
der Universität Potsdam

von

Lorena Perdigón Toro

Ort und Tag der Disputation: Potsdam, 11. Juli 2022

Supervisor: Prof. Dr. Dieter Neher

First reviewer: Prof. Dr. Dieter Neher
Second reviewer: Prof. Dr. Safa Shoaee
Third reviewer: Prof. Dr. Heinz Bässler

Published online on the
Publication Server of the University of Potsdam:
https://doi.org/10.25932/publishup-55807
https://nbn-resolving.org/urn:nbn:de:kobv:517-opus4-558072

Our feelings are our most genuine paths to knowledge

— Audre Lorde

Dedicated to all the women in my life

Abstract

Organic solar cells offer an efficient and low-cost alternative for solar energy harvesting. In this type of photovoltaic devices, two organic semiconductors molecules are typically blended to create the so-called bulk heterojunction (BHJ) morphology: an electron donating polymer and a small molecule acceptor. Traditionally, fullerenes were used as acceptors, while recently, the appearance and development of new small molecules referred to as non-fullerene acceptors (NFAs) has injected new life into the organic electronics' community. Rapid progress over the past 4 years has enabled record efficiencies of 19%, bringing the technology close to commercial viability. Nowadays, NFA-based devices approach their inorganic competitors in terms of photocurrent generation, owing to their strong and complementary absorption, but lag behind with regard to the open-circuit voltage (V_{OC}) and in part the fill factor (FF). However, compared to fullerene blends, NFAs generally exhibit lower voltage losses, as a result of moderate energy offsets at the donor-acceptor heterojunction. There are other important features that set NFAs apart from fullerenes. In contrast to fullerenes, the lowest excited state of an NFA is a singlet exciton, and NFA layers with reasonable high photoluminescence quantum efficiencies have been reported. In addition, NFAs usually have a planar conjugated backbone, which promotes morphological order and ensures the fabrication of highly crystalline active layers that go along with low energetic disorder.

My thesis focuses on understanding the interplay between the unique attributes of NFAs and the physical processes occurring in solar cells. By combining different techniques with drift-diffusion simulation, this work examines free charge generation, recombination and transport in state-of-the-art non-fullerene acceptor BHJs. For this purpose, the blend of the donor polymer PM6 and the NFA Y6 is thoroughly investigated. PM6:Y6 has become the most notorious NFA-based solar cell because of its high efficiency (> 15%), reproducible now in many laboratories around the world. The efficiency of free charge generation in PM6:Y6 is shown to be independent of the electric field regardless of whether the donor, the acceptor, or states in the tail of the blend absorption are excited. Temperature-dependent measurements reveal a very small activation energy for photocurrent generation of only 6 meV, indicating barrierless charge separation. Detailed theoretical modelling suggests that Y6 dimers bear large quadrupole moments, which create an electrostatic interfacial field and band bending across the donor-acceptor interface. This compensates the Coulomb dissociation barrier and thus assists free charge generation. With photocurrent generation being barrierless, poor free charge extraction in competition with nongeminate recombination is identified as a major factor limiting the performance of PM6:Y6. This conclusion is experimentally validated utilizing two charge extraction methods: time-delayed collection field (TDCF) and bias-assisted charge extraction (BACE). Detailed drift-diffusion simulations of these two techniques are implemented to support the reliability of our experimental results and confirm that nongeminate losses in thin PM6:Y6 solar cells are dominated by processes in the bulk and that surface recombination is negligible. Additional simulations of the steady-state charge carrier densities and photocurrent in organic solar cells demonstrate the detrimental role of electrode-induced charges close to the metal contacts, as bimolecular recombination of these charges with photogenerated charges can dominate the fill factor losses. As such, this type of recombination must be carefully examined in recombination data obtained from charge extraction methods. A second focus of this work is the study of the spectral properties of photocurrent generation and recombination in PM6:Y6 solar cells, thereby disentangling the contributions from the Y6 singlet excitons and charge transfer (CT) states. Photon emission under open-circuit conditions is almost entirely due to the re-formation of Y6 excitons due to free charge recombination. Despite this, less than 1% of the total recombination

proceeds through the singlet state. As such, the V_{OC} of the PM6:Y6 blend is determined by the energetics and kinetics of the CT state, which is, however, barely visible in the spectra due to the small oscillator strength of the CT transitions. Hence, a large gain in the V_{OC} can only be expected when the density and/or recombination rate of the interfacial CT is substantially reduced. From photoluminescence and temperature-dependent electroluminescence measurements, the singlet energy is estimated to lie 120 meV above the effective transport gap, which explains efficient free charge formation and the low yield of exciton reformation. Finally, the role of energetic disorder in NFA solar cells is thoroughly investigated, by comparing Y6 to a close derivative, namely, N4. Morphology measurements show distinct differences of the molecular orientation and order for the two acceptors blended with PM6, while temperature-dependent charge transport studies reveal a significantly smaller energetic disorder in case of PM6:Y6. In both PM6:Y6 and PM6:N4, disorder influences the V_{OC} value at room temperature, but also its progression with temperature. In this regard, PM6:Y6 benefits substantially from narrower Gaussian-type density of state distributions and as such, has a considerably higher V_{OC}. In the analysis of the V_{OC} dependence on temperature, an important finding is that the free charge carrier density increases with decreasing temperature, pointing to a down-hill energetic driving force for free charge formation assisted by energetic disorder, as it provides lower-lying states.

Overall, important processes have been identified which determine the photovoltaic parameters of high-efficiency NFA solar cells, and most importantly the losses due to the non-radiative recombination of the CT state and the energetic disorder in such blends. Therefore, the findings of this thesis offer optimization guidelines to realize NFA-based devices with even smaller V_{OC} losses, upon a further reduction of both nongeminate recombination and energetic disorder, towards a new generation of organic solar cells with over 20% efficiency.

Contents

Publications and Contribution Statement

Here, the publications that are part of this thesis are listed, including the authors contribution statement.

1. L. Perdigón-Toro, H. Zhang, A. Markina, J. Yuan, S. M. Hosseini, C. M. Wolff, G. Zuo, M. Stolterfoht, Y. Zou, F. Gao, D. Andrienko, S. Shoaee, and D. Neher. Barrierless Free Charge Generation in the High-Performance PM6:Y6 Bulk Heterojunction Non-Fullerene Solar Cell. *Adv. Mater.* **2020**, 32, 1906763.

I planned the project together with D.N. and H.Z., drafted the manuscript and reviewer's response, fabricated all cells together with H.Z., and performed optoelectronic measurements and analysis, including T-dependent TDCF, BACE, and *J-V*. H.Z. performed T-dependent $\mathrm{EQE_{PV}}$ measurements. A.M. and D.A. conducted the theoretical modeling of Y6 quadrupole moments. J.Y. and Y.Z synthesized the acceptor molecule Y6. S.M.H. and M.S. contributed to device optimization. C.M.W performed transfer-matrix simulations. G.Z. provided photoluminescence data. D.A., F.G., S.S. and D.N. supervised the study, analyzed, and interpreted the measurements, and contributed to manuscript drafting. All co-authors contributed to proof reading of the manuscript and addressing reviewer comments.

2. J. Kniepert, A. Paulke, L. Perdigón-Toro, J. Kurpiers, H. Zhang, F. Gao, J. Yuan, Y. Zou, V. M. Le Corre, L. J. A. Koster, and D. Neher. Reliability of charge carrier recombination data determined with charge extraction methods. *J. Appl. Phys.* **2019**, 126, 205501.

L.J.A. and D.N. initiated the project. J.N. and A.P. performed drift-diffusion simulations. I fabricated the cells, with help from H.Z., and measured and analyzed the experimental data obtained from TDCF and BACE. J.Y. and Y.Z synthesized the acceptor molecule Y6. J.K. provided important conceptual ideas regarding the TDCF and BACE setups and corresponding data analysis. V.M.L-C. and L.J.A.K. provided the codes, assisted with the simulations, and contributed to project planning. J.K. drafted the manuscript together with D.N. and myself. All co-authors contributed to data interpretation and proof reading of the manuscript.

3. U. Würfel, L. Perdigón-Toro, J. Kurpiers, C. M. Wolff, P. Caprioglio, J. J. Rech, J. Zhu, X. Zhan, W. You, S. Shoaee, D. Neher, and M. Stolterfoht. Recombination between Photogenerated and Electrode-Induced Charges Dominates the Fill Factor Losses in Optimized Organic Solar Cells. *J. Phys. Chem. Lett.* **2019**, 10, 3473–3480.

U.W. D.N. and M.S. planned the project. M.S. drafted the manuscript. I fabricated the cells and performed TDCF. I performed IPC measurements together with M.S, and the corresponding data analysis and interpretation. U.W. and M.S. conducted drift-diffusion simulations. J.K. helped with cell fabrication and provided conceptual ideas regarding the TDCF setup. C.M.W. and P.C. contributed to the data analysis and in the project planning. J.J.R. synthesized the donor polymer under the supervision of W.Y. J.Z. synthesized the acceptor material under the supervision of X.Z. S.S. and D.N. contributed to project planning and manuscript drafting. All co-authors contributed to proof reading of the manuscript.

4. L. Perdigón-Toro, L. Quang Phuong, S. Zeiske, K. Vandewal, A. Armin, S. Shoaee, and D. Neher. Excitons Dominate the Emission from PM6:Y6 Solar Cells, but This Does Not Help the Open-Circuit Voltage of the Device. *ACS Energy Lett.* **2021**, 6, 557–564.

D.N. and I planned the project and drafted the manuscript. I fabricated all the films and solar cells under investigation, and performed optical characterization, including T-dependent PL and EL. L.Q.P. conducted PIA and EMIA spectroscopy studies, and the corresponding data analysis. S.Z. performed sensitive $\mathrm{EQE_{PV}}$ measurements. K.W., A.A. and S.S. provided important conceptual ideas regarding the interpretation of PL and EL spectra. S.S. and D.N. supervised the project. D.N. and I carried out all the calculations reported in the manuscript. All co-authors contributed to data interpretation and proof reading of the manuscript.

5. L. Perdigón-Toro, L. Quang Phuong, F. Eller, G. Freychet, E. Saglamkaya, J. I. Khan, Q. Wei, S. Zeiske, D. Kroh, S. Wedler, A. Köhler, A. Armin, F. Laquai, E. M. Herzig, Y. Zou, S. Shoaee, and D. Neher. Understanding the Role of Order in Y-Series Non-Fullerene Solar Cells to Realize High Open-Circuit Voltages. *Adv. Energy Mater.* **2022**, 2103422.

I planned the project together with D.N. and drafted the manuscript and reviewer's response. I fabricated all samples and solar cells under investigation. I performed optoelectronic measurements and analysis, including T-dependent BACE and *J-V*, and TDCF. L.Q.P. conducted T-dependent PIA spectroscopy studies, and the corresponding data analysis. G.F. measured GIWAXS and F.E. performed the data analysis under the supervision of E.M.H. E.S. helped with the preparation of only-devices, performed all SCLC measurements, and contributed to the data analysis. J.I.K. contributed with TRPL measurements and analyzed data under the supervision of F.L. Q.W. synthesized the N4 molecule under the supervision of Y.Z. S.Z. performed sensitive $\mathrm{EQE_{PV}}$ measurements under the supervision of A.A. D.K. S.W. and A.K. provided important conceptual ideas regarding the interpretation of the optical and morphology data. S.S. and D.N. supervised the project. I carried out the analysis and calculations necessary for the reproduction of the V_{OC} vs.T data with help from D.N. All co-authors contributed to data interpretation and proof reading of the manuscript.

Chapter 1. Introduction

1.1. The inevitable shift toward renewable energies

In November 2021, the most important UN Convention on Climate Change (COP 26), since the Paris Agreement in 2015, took place in Glasgow. At the closure of the summit, over 190 countries agreed on climate plans to reduce their emissions by 2030, with the goal of limiting global warming to 1.5°C.[1] As such, we find ourselves in a critical decade to tackle the climate crisis – a great challenge of our times. The long-term goal is to achieve net-zero greenhouse gas (GHG) emissions by mid-century.[2] Achieving this goal will be demanding, as it will require a profound transformation of the energy systems that sustain global economies and the further development of clean energy technologies that may not even be in the market yet.

The "Global Energy Transformation" report from the International Renewable Energy Agency (IRENA),[3] published in 2019, identifies electrification in combination with renewable energy as the key solution to the energy transition. The report presents a Renewable Energy Roadmap (Remap) to 2050, focused on long-term decarbonization. Figure 1.1 depicts the predicted use of renewable energy in 2050 compared to 2016. Panel a in Figure 1.1 envisions an electrified future, in which the share of electricity in final energy would increase from just 20% today to almost 50% by 2050. Consequently, the share of fossil fuels (i.e., oil, coal, natural gas) would go down from 66% to 26% and electricity becomes the main energy source. To realize this, the scaling up of electrification must come from renewables, with an increase from 24% of renewable electricity generation in 2016 to 86% in 2050. Of this 86% renewable share, three-fifths would come from solar and wind. Thus, as shown in Figure 1.1b, solar photovoltaic (PV) and wind technologies dominate by 2050 in terms of installed power capacity, with over 8500 GW and 6000 GW, respectively.

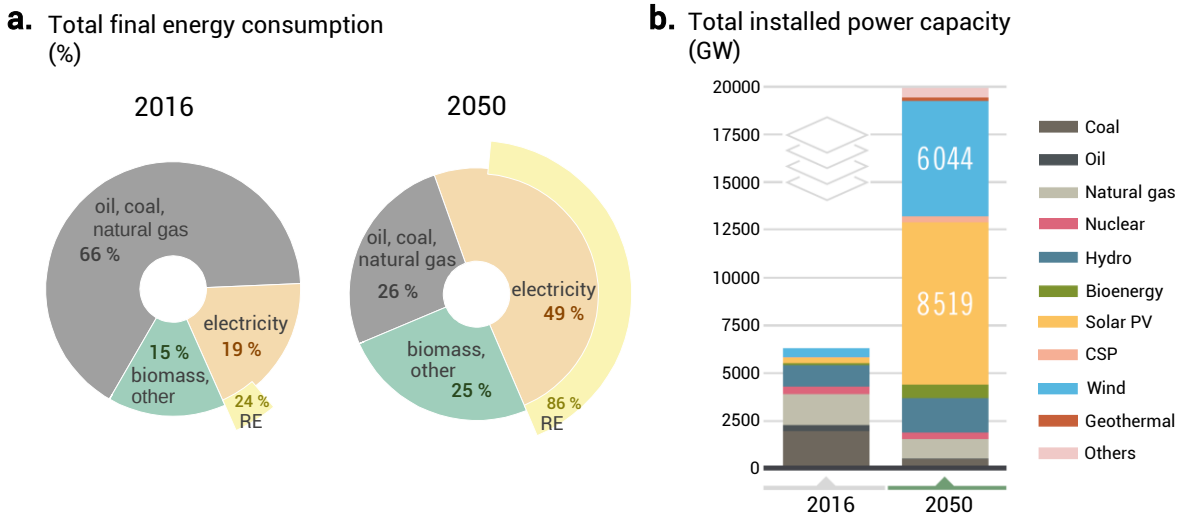

Figure 1.1: Predicted use of renewable energy in 2050 compared to 2016. a Total energy consumption by energy source in 2016 compared to the Renewable Energy Roadmap Case 2050. RE refers to renewable energy. **b** Power generation installed capacity by fuel in 2016 compared to the Renewable Energy Roadmap Case 2050. CSP refers to concentrated solar power. Adapted from the IRENA Global Energy Transformation – A Road Map to 2050 Report, 2019 Edition [3].

The energy of the sunlight reaching the surface of the earth is a prime renewable energy source for our planet. While the annual global primary energy consumption was at ~600 EJ in 2019,[4] the total solar energy reaching the surface of Earth is 340×10^4 EJ each year.[5] Thereupon, solar energy can be used as a heat source and/or converted into electricity. With regard to solar thermal generation, the sun's heat is concentrated and used to drive a heat engine. Differently, a photovoltaic cell, also called a solar cell, converts sunlight directly into electrical power. In a solar cell, the photoactive layer is a semiconductor. Established photovoltaic (PV) technologies include silicon (Si) and gallium arsenide, being Si the most commercialized type of solar modules. Silicon continues to dominate the market as module prices continue to decrease, despite its numerous drawbacks such as complex and energy-intensive production steps and the need for thick absorber layers (100-500 µm) due to the low absorption efficiency of Si because of its indirect bandgap.[6] Therefore, research focuses on alternative semiconductors for emerging photovoltaic (e-PV) technologies of thin-film solar cells.[7] The list of available materials includes organic semiconductors, organic dyes, halide perovskites and chalcogenides.

1.2. Organic Solar Cells: Non-Fullerene Acceptors take the lead

Organic solar cells (OSCs), also referred to as organic photovoltaics (OPV), are a type of sunlight harvesting technology based on organic semiconductors, that is, conjugated small molecules and polymers. The advantages of OSCs go well beyond the fact of it being a carbon-based green technology. The active layer of OSCs consists of thin films (below the micrometer range) that can be processed from solution or by low temperature vacuum deposition.[8] Solution processability allows for low-cost production techniques such as roll-to-roll printing, inkjet printing, or blade-coating enabling lightweight and flexible devices.[9–11] The large library of materials available also allows to fabricate semitransparent devices of different colors that can be integrated into novel applications such as net-zero energy greenhouses,[12, 13] and semitransparent or electrochromic windows,[14–16] for energy efficient buildings envisioned for our cities of the future. In addition, OSCs can be combined with perovskites, another emerging PV technology, to make tandem solar cells and push the efficiency of both technologies further up.[17, 18]

In contrast to silicon, light absorption in organic semiconductor thin films does not lead to efficient generation of free carriers but strongly bound excitons, and thus simply sandwiching an organic semiconductor between electrodes gave initial efficiencies below 1%.[19] A major breakthrough in OSCs research was the invention of the so-called “bulk-heterojunction” (BHJ) configuration in the 90s.[20] From then on, devices based on BHJs have delivered the highest efficiencies in the field. Typically, in a BHJ, an electron donating polymer (analogous to a p-type semiconductor), and a small molecule electron acceptor (analogous to n-type semiconductor), are blended to form an interpenetrating, phase-separated network with a nanoscale morphology.[21–23] While the list of available polymer donors is large and has continuously grown, research on acceptor materials was traditionally focused and dominated by C_{60} and its soluble derivatives, known as fullerenes.[24] This is illustrated in Figure 1.2a, which shows that cell efficiencies for fullerene based OSCs increased from 2% in the early 2000s to above 10% by 2012 but became then limited to values around 12%. Unfortunately, these values remain too low to compete with silicon. From 2015, the OSC technology owes its resurgence to the appearance and development of new small molecule electron acceptors referred to as non-fullerene acceptors (NFAs).[25] In 2017, Zhao et al. reported the first NFA OSC with efficiencies higher than those of state-of-the-art fullerene blends.[26] They achieved a certified efficiency of 13.1% by fluorinating ITIC (Figure 1.2b), which had become the most notorious NFA molecule by that point.

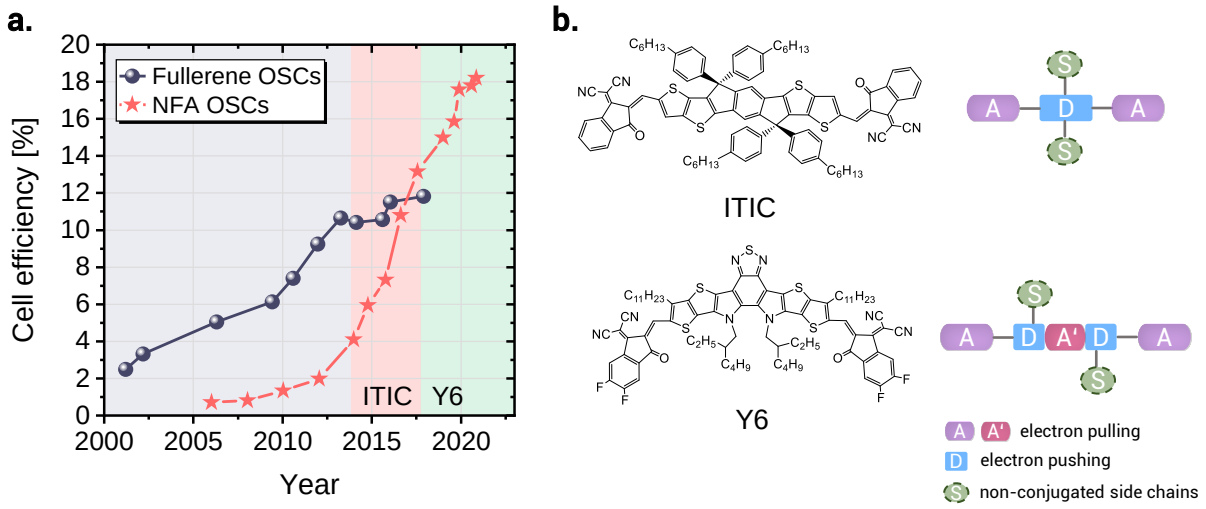

Figure 1.2: Non-fullerene acceptors take the lead. a Progress of solution-processed organic solar cells based on fullerene and non-fullerene acceptor (NFA) blends, over the last 20 years. **b** Chemical structures of the representative small molecule NFAs ITIC and Y6, and schematic representation of A-D-A and A-DA'-A type acceptors. Adapted from Refs.[24, 27]

The ITIC molecule is an example of fused-ring electron acceptor (FREA), in which strongly electron-pulling (also called electron withdrawing) end units are attached to an electron-pushing (electron donating) fused-ring conjugated core bearing out-of-plane non-conjugated substituents.[27, 28] This results in acceptor-donor-acceptor (A-D-A) type molecules (Figure 1.2b), where the "A" end groups form $\pi - \pi$ interactions with the polymer donors and/or adjacent acceptor molecules in the blend film, which promotes electron transfer and transport. In 2019, the group of Yingping Zou strengthened the intramolecular electron push-pull effect by designing Y6, [29] a novel A-DA'D-A type acceptor (Figure 1.2b).

Y6 perfectly exemplifies one of the main advantages of organic semiconductors, which is the ability to control the absorption properties of the material via chemical design. As such, Y6 is a narrow bandgap material with absorption in the near-infrared (NIR) region, extending to 900 nm (Figure 1.3). Zou's group initially reported a record short-circuit current (J_{SC}) of 25.3 mAcm^{-2} and a record efficiency of 15.7% for a 100 nm layer of the blend of the polymer PM6 (also known as PBDB-T-2F) and Y6, owing to their strong and complementary light absorption. This is in fact a superior trait of polymer:NFA devices in comparison to polymer:fullerene solar cells. In the past, the blend of the polymer P3HT with the fullerene PCBM was the most studied model system in OSC research. However, as shown in Figure 1.3, PCBM absorbs strongly only below 400 nm, range in which the solar irradiance drops. Due to this, the J_{SC} of P3HT:PCBM solar cells reaches values around 10 mAcm^{-2} for 200 nm active layers.[30] On the other hand, PM6:Y6 solar cells cover a much broader range of the solar spectrum, allowing such devices to approach their inorganic competitors in terms of photocurrent generation with very thin (100 nm) layers. This blend has presently taken the lead as the model NFA system, given that the materials are commercially available and the high efficiencies of PM6:Y6 devices (> 15%) are now reproducible in many laboratories around the world.

Further advantages of the PM6:Y6 blend, and NFA-based OSCs in general, compared to fullerenes include firstly lower energy losses which result in an improved open-circuit voltage (V_{OC}). This is related to the moderate energy offsets at the donor-acceptor heterojunction.[31] Figure 1.3b takes P3HT:PCBM and PM6:Y6 as examples to compare the energy levels in fullerene versus NFA OSCs, and shows how the acceptor becomes the low bandgap component in NFA blends and the energy

offset between the highest occupied molecular orbitals (HOMO-HOMO) is largely reduced. However, maintaining a certain offset is generally considered to be needed to split excitons into free charges. In this regard, the high efficiency of charge generation in PM6:Y6 solar cells has been linked to improved morphological order, due to the planar conjugated backbone of Y6. As such, charge separation is assisted by the presence of crystalline Y6 domains where charges are effectively delocalized.[32, 33] In addition, high crystallinity of the active layer results in a low energetic disorder and low charge trapping in PM6:Y6,[34] which potentially reduces the voltage loss and improves charge transport. Despite this, PM6:Y6 devices exhibit moderate hole and electron mobilities, in the range 10^{-4}-10^{-3} $cm^2V^{-1}s^{-1}$.[35–37] Therefore, numerous studies have focused on the optimization of device fabrication to further improve the blend film morphology. To this end, the effect of different processing conditions was investigated, including the processing solvent and thermal annealing conditions,[38] the use of additives,[35] and the ternary and quaternary blend approach.[39, 40] Upon the introduction of Y6, a series of Y-derivatives were developed by modifying the electron-deficient core, alkyl chains, and end groups to tune the solubility and aggregation of the NFAs.[41–44] Novel polymers have also been designed to pair with Y6.[45, 46] This has allowed OSCs to reach PCEs of 19%.[43, 44]

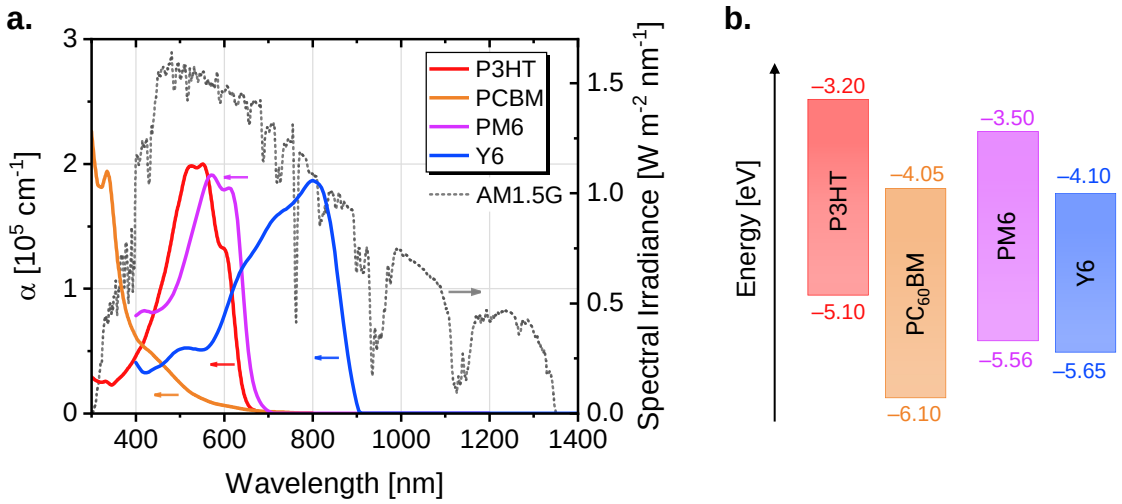

Figure 1.3: Absorption coefficient and energy levels of exemplary polymer donors and acceptors. a Absorption coefficient α (left axis) of the conjugated polymers P3HT and PM6, the fullerene PCBM and the NFA Y6 as a function of wavelength together with the AM1.5G solar spectrum (right axis). **b** Energy levels of P3HT, PCBM, PM6 and Y6, taken from literature, from cyclic voltammetry data.[29, 47] It should be noted that the absolute energy levels are dependent upon measurement methodology. In addition, the values for PM6 and Y6 were taken from the original paper of the Zou group, but several subsequent studies have reported a higher lying HOMO for PM6, at ca. - 5.20 to - 5.40 eV.[33, 34, 48]; HOMO refers to the highest occupied molecular orbital.

On the path to commercialization, NFA blends have come along with great advances and an efficiency of 20% is now within reach. However, OSCs are still not as competitive as other PV technologies mostly due to losses in efficiency upon scaling up the device area of high performing NFA systems, and because their long-term light and thermal stability must be further improved.[49] Finally, pushing efficiencies further up still requires a deeper and more comprehensive understanding of the underlying physical mechanisms that decide the fate of free carriers and thus govern photon energy conversion in NFA OSCs.

1.3. Scope of the work

With the advent of non-fullerene acceptors to organic solar cells research, the field soon started questioning what sets NFAs apart from fullerenes. To address this intriguing question, this thesis aims to advance the understanding of the particularities of free charge generation, recombination, and charge transport in NFA OSCs, with a particular focus on the omnipresent PM6:Y6 blend. To reach this goal, the experimental and theoretical work done for this thesis is structured as shown in the scheme in Figure 1.4. To address each subject in the chart, we must first go over the fundamentals of organic solar cells in Chapter 2, which details the theoretical background which forms the basis of the current work. Chapter 3 summarizes the methods used in the following chapters, including device fabrication, characterization techniques and simulation tools. Thereafter, the main results are included from Chapter 4 to Chapter 8.

Chapter 4 examines the efficiency of free charge generation in PM6:Y6, in terms of its dependence on the electric field, temperature and excitation energy. The work was inspired by on-going debates on fullerene blends, for example, on whether free charge formation involves “hot” charge transfer (CT) states or thermalized “cold” CT states. The pathways of generation are even more interesting in PM6:Y6 given the small driving force for hole transfer. The studied physical parameters (specified in Figure 1.4) demonstrate that the activation energy for photocurrent generation is very small and theoretical modelling of Y6 dimers reveals large quadrupole moments, which create an electrostatic interfacial field to compensate for the Coulomb dissociation barrier. In the following, the simulation work done in Chapter 5 and Chapter 6 complements the experimental results. The conclusions of this thesis regarding generation and recombination of free charges are largely based on charge extraction techniques, i.e. time-delayed collection field (TDCF) and bias-assisted charge extraction (BACE). Therefore, Chapter 5 presents detailed drift-diffusion simulations on both methods to analyze the benefits and limitations of each, and their applicability under different experimental conditions. The robustness of the methods is further validated by a comparison with a wide range of experimental data sets on PM6:Y6. In addition to charge generation, the recombination and transport of free carriers determines the overall performance of OSCs. Importantly, the order of recombination differentiates between bimolecular recombination and first order channels such as geminate (CT state) or trap-assisted recombination, or the recombination of minority carriers at the electrodes (surface recombination). The numerical simulations in Chapter 6 show that recombination scaling with the first order of the light intensity is a direct consequence of bimolecular recombination between photogenerated and excess dark charge near the metal contacts. Further experiments highlight that FF losses in optimized OSCs are dominated by this “pseudo”-first order recombination process. Jointly, these simulation chapters show that recombination happens mostly through processes in the bulk and that dark-injected charges need to be accounted for when evaluating charge extraction transients. Chapter 7 takes yet another close look at free charge recombination and open-circuit voltage losses by examining the spectral properties of recombination in PM6:Y6. Photoluminescence and electroluminescence spectra reveal a high yield of Y6 singlet exciton emission in the blend but less than 1% of the total recombination proceeds through this state, meaning that interfacial CT recombination still dominates in this high-performance blend. Finally, Chapter 8 focuses on the role of (energetic) order and the shape of the density of states on nongeminate recombination and consequently, on the open-circuit voltage, V_{OC}. The latter is comprehensively described by analytical models with experimental data as input parameters. The comparison of the blends of PM6 with Y6 and its close derivative N4 further confirm that energetic disorder influences the value of the V_{OC} at room temperature, as well as its progression with temperature.

Finally, this work is concluded through evaluation of the main experimental findings, which ultimately provide analysis tools and decisive guidelines towards NFA OSCs with much smaller recombination and voltage losses and overall improved efficiency.

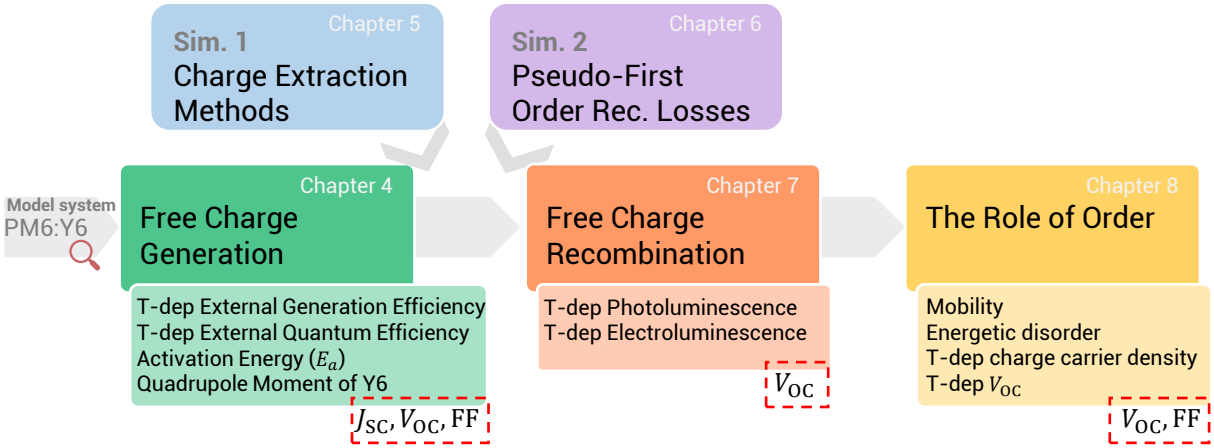

Figure 1.4: Scope of the experimental and theoretical work in the thesis. This scheme details the main topic under investigation in each chapter of the thesis and specifies the studied physical parameters, which are fundamentally related to the marked photovoltaic parameters, J_{SC}, V_{OC} and/or FF (red dashed boxes), in the model system PM6:Y6. Chapter 4 deals with free charge generation, while Chapter 5 and Chapter 6 complement the experimental results by including drift-diffusion simulations on the reliability of charge extraction methods and the origin of pseudo-first order recombination losses in organic solar cells. Chapter 7 examines free charge recombination and finally, Chapter 8 focuses on the role of order.

Chapter 2. Fundamentals

This chapter presents the physical concepts relevant to the results obtained in this thesis. First, the origin of the semiconducting properties of organic conjugated molecules is described. The basic physics of organic semiconductors are linked to the working mechanism of the bulk heterojunction, and the power conversion efficiency of solar cells is defined. Next, free charge generation in organic solar cells is discussed based on the energetics and kinetics of the relevant three species – excitons, charge transfer states, and charge-separated states. Then, the driving forces for efficient charge formation are reviewed. The fundamentals of charge extraction and nongeminate recombination are detailed as well, based on theoretical models from the literature. Finally, the parameters that define the open-circuit voltage of organic solar cells are elaborated, aiming to present the most relevant analytical descriptions.

2.1. Organic Semiconductors

Organic materials are hydrocarbon-based compounds. In organic small molecule and polymers, semiconducting properties are based on the nature of the chemical carbon bonds. The electronic configuration of a single carbon atom in the ground state is $1s^2 2s^2 2p^2$. In conjugated organic compounds, mixing of the 2s and 2p orbitals leads to the formation of hybrid orbitals, for example the 2s and two 2p orbitals (p_x and p_y) form three sp^2 hybrid orbitals which arrange in a plane, while the unhybridized p_z orbital sits orthogonal to this plane (see Figure 2.1a). Each orbital is occupied with one electron. In the case of ethylene ($H_2C = CH_2$), the electrons in the sp^2 orbitals of two neighboring carbon atoms form strongly localized covalent σ-bonds along the axis of the nuclei. The overlap of the perpendicular p_z orbitals creates a more delocalized π-bond, leading to a double bond between the carbon atoms.[50] In an extended chain of carbon atoms with alternating single and double bounds, the hybridized sp^2 orbitals result in bonding σ and anti-bonding σ^* molecular orbitals lying far apart from each other in terms of energy. On the other hand, the interaction of p_z orbitals occurs at a finite distance from the nuclei and therefore bonding π and anti-bonding π^* molecular orbitals are much closer in energy (Figure 2.1b). In addition, because of the coupling of p_z orbitals, the electrons in the π orbitals are delocalized across the entire molecule. As such, carbon atoms form molecules with extended, delocalized π-electron systems. The linear combination of atomic orbitals (LCAO) is used to approximate the energy of the molecular orbitals, since the electron wave functions of the atomic orbitals interfere constructively or destructively. The π orbitals are filled with the valence electrons and the π^* orbitals remain empty, introducing the terms of highest occupied molecular orbital (HOMO) and lowest unoccupied molecular orbital (LUMO).

The HOMO and LUMO are also known as frontier orbitals, given that filled orbitals end at the HOMO and empty orbitals start at the LUMO. Therefore, the difference in energy between HOMO and LUMO is the equivalent to the bandgap of inorganic semiconductors, which determines the semiconducting properties of the molecule. The bandgap decreases with increasing the conjugation length. For a one-dimensional chain, it would approach 0 for an infinite number of carbon atoms. However, according to Peierls' theorem,[51] such a one-dimensional equally spaced chain with one electron per atom is unstable. Therefore, the conjugated chain dimerizes, with a periodic variation of the bond length, leading to a distortion of the symmetry. This results in the formation of a fully occupied π "band", analogous to the valance band in inorganic semiconductors, and a completely empty π^* "band", analogous to the conduction band, separated by a finite bandgap.

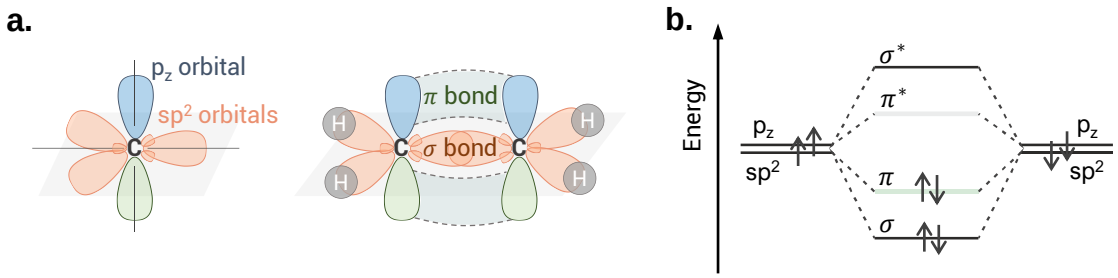

Figure 2.1: Molecular orbitals in conjugated organic compounds. a Scheme of the sp^2-hybrized carbon atom which features three sp^2 atomic orbitals in a common plane and one perpendicular p$_z$ orbital (left). In ethylene, $H_2C = CH_2$, two sp^2 orbitals form the σ-bond and two p$_z$ orbitals from the π-bond (right). The remaining sp^2 orbitals form four σ-bonds with hydrogens. **b** Simple energy level scheme of the formation of σ- and π- molecular orbitals ('*' denotes the antibonding character of the orbitals). The 1s orbitals are omitted. Adapted from [50].

For polymers, conjugation is disrupted due to coiling of the chains, and the presence of kinks and twists. Chemical defects and impurities, originating from synthesis or sample preparation, also interrupt the delocalization of π electrons of conjugated systems. Consequently, a polymer chain separates into many conjugated segments or "sites", also known as chromophores. This introduces many different energy sites, also affected by intra- and intermolecular interactions. As a consequence, the HOMO and LUMO become a broad distribution of energy states, without well-defined onsets. The broadening of the density of states (DOS) is statistically distributed and thus is commonly described by a Gaussian or exponential function. The characteristic broadening of the DOS defines the energetic disorder in the organic semiconductor. Note that this disorder is not intrinsic to the molecular structure, but it is a property of the material's solid film and as such depends on film preparation.[52] Disorder is an important parameter that will be treated at length in section 2.4. in terms of its impact on charge transport and nongeminate recombination.

2.2. Working Mechanism of Organic Solar Cells

A fundamental aspect that establishes the working mechanism of an organic solar cell (OSC) is the nature of the excited states of organic materials. In their inorganic counterparts, photoexcitation leads to the formation of loosely bound and delocalized excitons because of their relatively high dielectric constant ($\varepsilon > 10$), which enables effective polarization of the surrounding material and screening of the Coulomb attraction between electron and hole. This type of exciton, called Wannier-Mott exciton, has a small binding energy that can be overcome by thermal energy at room temperature. In organic semiconductors, however, their low dielectric constant ($\varepsilon \approx 2-4$)[53] causes, upon photoexcitation, the formation of tightly bound Frenkel excitons that are localized on a single molecule or the same conjugated segment.[54] Therefore, one distinguishes between electrical gap and optical gap in organic semiconductors. The electrical gap is the energy difference between the ionization energy and the electron affinity of a molecule in the condensed phase, while the optical gap is the energy of the first singlet excited state E_{S_1}, thus the minimum energy to generate an exciton. The difference between the electrical and optical gap is the exciton binding energy. In order to generate free charges from excitons in OSCs, binding energies of several hundred meV must be overcome.[55, 56]

To ensure exciton dissociation, the active layer of OSCs consists of two materials: a donor (D) and an acceptor (A) with energy level offsets of their frontier molecular orbitals, HOMO and LUMO. Photogenerated singlet excitons (S_1) in organic semiconductors have typical exciton diffusion lengths of 5-15 nm,[57] though NFA films are currently reported to have higher diffusion lengths

up to ~45 nm.[58] Nevertheless, such values are still well below film thicknesses required for efficient light absorption. This leads to the wide-spread usage of the bulk-heterojunction (BHJ). In a device optimized BHJ morphology, donor and acceptor form a nanostructured blend with bicontinuous interpenetrating donor and acceptor networks that provide hole and electron pathways, respectively, as depicted in Figure 2.2a. Here, excitons are generated within their diffusion length to the donor-acceptor (DA) interface, which allows for thicker active layers. In the structure shown in Figure 2.2a, the so-called transport layers (or interfacial layers) act as blocking layers for the minority carriers and transport layers for the majority carrier. In this given example, electrons are extracted at the bottom electrode, the cathode, and holes are transported to the top electrode, the anode, illustrating the inverted architecture of BHJ organic solar cells.

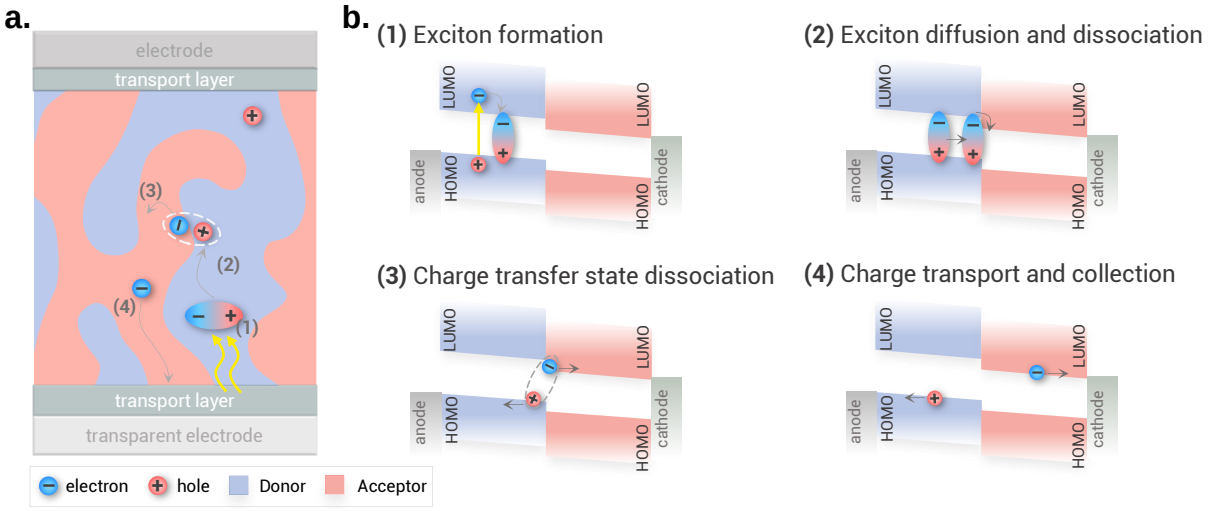

Figure 2.2: The structure and working mechanism of a bulk-heterojunction organic solar cell. **a** The structure of a bulk-heterojunction (BHJ) solar cell. In the ideal BHJ morphology, donor and acceptor undergo nanoscale phase separation and form bicontinuous interpenetrating networks with large donor-acceptor interfacial areas. Transport layers act as charge-blocking and transporting layers. In this structure, electrons are extracted at the bottom transparent electrode, the cathode, and holes are transported to the top electrode, the anode, exemplifying the inverted architecture of BHJ organic solar cells. **b** Overview of the fundamental processes for photocurrent generation in a BHJ solar cell, marked from 1 to 4 (as in panel a), for the case of donor excitation. (1) photoexcitation of the donor creates a Coulombically bound electron-hole pair, known as exciton. (2) the exciton diffuses to the donor-acceptor interface, where the electron is transferred to the acceptor LUMO, which splits the exciton. (3) the transferred electron and the remaining hole in the donor HOMO form the charge transfer (CT) state, which is still Coulombically bound. The CT state then dissociates into free charges. (4) free charges are finally transported and collected at the respective electrodes. These processes are competing with potential recombination of electron and hole. The process for acceptor excitation is similar and of comparable importance for photocurrent generation in non-fullerene acceptor solar cells. HOMO, highest occupied molecular orbital; LUMO, lowest occupied molecular orbital. Adapted from [59].

The processes displayed in panel a of Figure 2.2 are the key steps of photocurrent generation in BHJ OSCs and are further detailed in the simplified energy diagrams of a DA interface in panel b, for the case of donor excitation.[59, 60] First, upon absorption of a photon with energy larger than the optical gap of the D or A, an electron is excited from the ground state to the vibronic levels of an excited state, depending on the excitation energy. The excited electron thermalizes, creating an exciton formally defined as a Coulombically bound electron-hole pair pseudo-particle (1). The exciton then diffuses to the DA interface, where the electron lowers its energy by transfer to the acceptor LUMO and the exciton is dissociated (2). The transferred electron and the remaining hole

in the donor HOMO form a geminate pair, the so-called charge transfer (CT) state, which is still Coulombically bound. The mirror process of hole transfer from the acceptor HOMO to the donor HOMO happens upon acceptor excitation and is of comparable importance for photocurrent generation in non-fullerene acceptor (NFA) solar cells. The photoinduced electron transfer is also referred to as *Channel I*, while the photoinduced hole transfer is through *Channel II*. In the framework of classical Marcus theory, the efficiency of CT formation via interfacial charge transfer is related to the so-called driving force for charge generation, commonly considered to be the difference in the energies of the initial and final states of the system.[61] This means that the driving force is the difference in energy of the S_1 excited state on the donor or acceptor and the CT state, expressed as ΔE_{S_1-CT}. Next, the CT dissociates into free carriers (3). In the last step, free charges are transported via drift within the internal built-in electric field and collected at the respective electrodes to generate photocurrent (4). All these processes compete with potential loss pathways that involve the recombination of the electron and the hole. Charge carrier recombination can be broadly divided into two types: geminate and nongeminate recombination. Geminate recombination is defined as the recombination of charges that stem from the same exciton (i.e., initially formed CT state), while nongeminate recombination occurs between free charges that stem from different excitons (see section 2.4.2). Finally, the efficiency comprising the processes 1 to 4 in Figure 2.2 introduces an important parameter for solar cell characterization, the photovoltaic external quantum efficiency, $\mathrm{EQE_{PV}}$. The $\mathrm{EQE_{PV}}$ is defined as the number of collected charge carriers per incident photon of energy E and can be split in the following efficiency factors:

$$\mathrm{EQE_{PV}}(E) = \eta_{\mathrm{abs}}(E)\eta_{\mathrm{ex}}\eta_{\mathrm{CT}}\eta_{\mathrm{CE}} = \eta_{\mathrm{abs}}\mathrm{IQE}, \qquad (2.1)$$

where η_{abs} is the efficiency of absorption in the active layer. η_{ex} is the efficiency of exciton diffusion to the heterojunction and their subsequent dissociation, while η_{CT} and η_{CE} are the efficiencies of separation of the CT state into free charges and free charge extraction, respectively. These last three factors represent the internal quantum efficiency, IQE, which gives the number of collected charge carriers per absorbed photon.

2.2.1. Power Conversion Efficiency

The performance of a solar cell is defined by the power conversion efficiency (PCE). The PCE is the ratio of the electrical output power density from the solar cell (P_{el}) to the sun spectrum power density (P_{in}) incident on the device. Thereby, the characterization of a solar cell is based on the measurement of the current density (J) as a function of applied bias (V) under illumination to obtain the *J-V* characteristics, or *J-V* curve, as shown exemplarily in Figure 2.3. The main photovoltaic parameters in the figure are the short-circuit current (J_{SC}), the open-circuit voltage (V_{OC}) and the fill factor (FF), which determine the output power density, such that

$$\mathrm{PCE} = \frac{P_{\mathrm{el}}}{P_{\mathrm{in}}} = \frac{J_{\mathrm{SC}}V_{\mathrm{OC}}FF}{P_{\mathrm{in}}}. \qquad (2.2)$$

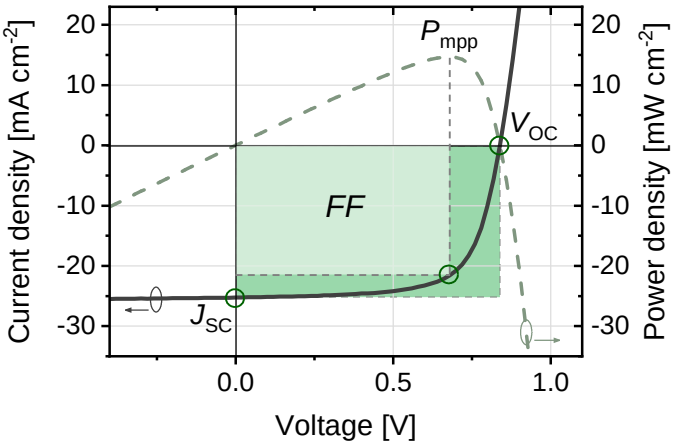

Figure 2.3: Typical current density versus voltage characteristics of a solar cell under illumination. Current density-voltage (*J-V*) curve (left axis) and calculated power output (right axis). Marked photovoltaic parameters are the short-circuit current (J_{SC}), open-circuit voltage (V_{OC}), maximum power point (P_{mpp}) and fill factor (FF).

At J_{SC}, the external voltage applied to the device is 0 V, which means that J_{SC} is the current caused mainly by the incident photons and the internal field. At V_{OC}, the external current is zero, meaning that V_{OC} is the voltage at which charge recombination exactly balances charge generation (limitations on the V_{OC} of OSCs will be part of section 2.5.). The FF evaluates how efficiently charges are extracted and is calculated as the ratio between the real maximum power point (MPP), i.e. the maximum product of current and voltage along the *J-V* curve, and the theoretical maximum power achievable which is the product of J_{SC} and V_{OC}:

$$\mathrm{FF} = \frac{J_{MPP}V_{MPP}}{J_{SC}V_{OC}}. \qquad (2.3)$$

Having reviewed the above-described operating principles of a BHJ, it becomes evident that understanding the PCE of an OSC entails proper characterization of the charge generation, recombination and extraction processes taking place following photoexcitation of the DA blend. Accordingly, the next sections examine the variables that govern these key processes.

2.3. Energetic Landscape and Free Charge Generation

The process of charge photogeneration is of vital importance for the operation of OSCs. However, the underlying mechanisms by which the bound CT state is separated into free charges at the donor-acceptor interface are still under debate. The general consensus is that free charge generation involves three relevant energetic states; excitons (S), the interfacial charge transfer (CT) states, and the charge-separated (CS) states, which are characterized by the separation distance of the electron and the hole as illustrated in the state diagram in Figure 2.4. In the case of blends based on NFAs, the system is regarded as a low-offset (mainly of the HOMO-HOMO levels) OSC, as introduced in the previous chapter. In this scenario, the (lowest singlet) exciton energy of the donor is much higher than both the (lowest singlet) exciton energy E_{S_1} of the acceptor and the CT state energy E_{CT} .[62] Figure 2.4 deals with excitons only in the acceptor and shows the relevant rates between the different species. Here, triplet states are omitted for simplification. Initially, excitons are photogenerated in the acceptor, which can undergo hole transfer to the donor and form CT states with the rate constant k_{ht} or recombine with the rate constant k_S. Apart from being populated via excitons from the acceptor (and the donor), CT states

can be directly formed through sub-bandgap photoexcitation,[63–65] and repopulated via bimolecular free charge encounter described by the rate coefficient β_{enc}. The CT state is radiatively coupled to the ground state and thus electron and hole are still in close vicinity. Once populated, CT states either decay directly to the ground state with the rate constant k_{f} (geminate recombination) or undergo back-transfer into excitons described by k_{bt}, or dissociate into free charge carriers with the rate constant k_{d}. Finally, spatially-separated electrons and holes with negligible Coulomb interaction are found in the CS states, and free charges are generated in the active layer. Free electrons and holes can be then extracted at the contacts, provided they do not form again CT states. Inversely, free electrons and holes can be injected at the electrodes, which form CT states that can either recombine radiatively or non-radiatively or reform the excitons. The net injection-extraction rate of free charge carriers is given by $|J - J_{\mathrm{surf}}|/qd$ (see Ref.[62]), with J being the total current density and J_{surf} the surface recombination current which is defined by the sum of the minority carrier currents, that is the electron current at the anode and the hole current at the cathode (see section 2.4.2 for more details on surface recombination); q is the elementary charge, d is thickness. The effect of the relative energetics of excitons, CT states and free charge carriers on the open-circuit voltage of NFA OSCs will be further examined in section 2.5.2.

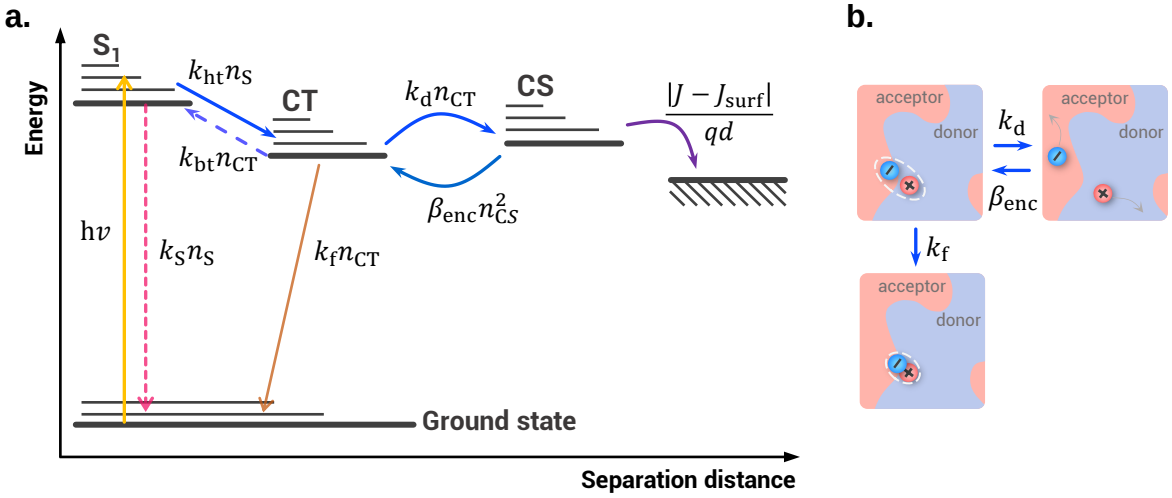

Figure 2.4: Schematic representation of a kinetic model for charge photogeneration and recombination at a donor-acceptor interface. a Schematic energy-level diagram showing the relevant kinetic processes occurring between excitons (S) in the acceptor, charge transfer (CT) states, and free charge carriers in the charge-separated states (CS). Here, n_{S_1}, n_{CT} and n_{CS} are the densities of excitons in the acceptor, of CT states and of free carriers. CT states can decay to the ground state with the rate constant k_{f}, or dissociate into free carriers with the rate constant k_{d}, while they also undergo back-transfer into excitons with the rate constant k_{bt}. CT states are repopulated through bimolecular recombination of free carriers, with the coefficient for bimolecular free charge encounter β_{enc}. For an active layer of thickness d, free charges are finally collected at the electrodes at rate $|J - J_{\mathrm{surf}}|/qd$. Note that CT states can also be formed via photoexcited excitons in the donor (not represented in this scheme). **b** Schematic overview of CT state dissociation that relates to the rate constants in panel a. Adapted from Refs.[59, 62]

The energies of the states involved in free charge generation are difficult to determine precisely for DA blends. The energy of the frontier orbitals of donor and acceptor measured in neat layers can differ from those at the DA interface, especially due to morphological changes upon mixing. This makes it hard to obtain $E_{\mathrm{CS}} = \mathrm{EA_A} - \mathrm{IE_D}$, where $\mathrm{EA_A}$ is the electron affinity of the acceptor and $\mathrm{IE_D}$ is the ionization energy of the donor (with respect to vacuum level). $\mathrm{IE_D}$ and $\mathrm{EA_A}$ represent the onsets (or edges) of the occupied and unoccupied molecular electronic states,

respectively.[66] These energy levels are often more relevant than HOMO or LUMO, because the onsets are determined by the energy at which the states start to become discernible in typically employed experimental techniques such as photoemission spectroscopy or cyclic voltammetry.[52] Moreover, resolving CT signals to obtain E_{CT} is especially challenging in low-offset systems where E_{CT} approaches E_{S_1}, since absorption and emission in such blends are dominated by the exciton while any CT contribution remains hidden.[28, 67, 68] Nonetheless, the relative energetic positions of these states determine the efficiency of free charge generation as they account for the driving force. This point is elaborated in the next section.

2.3.1. Dissociation of Charge Transfer States

In general, when considering free charge generation from CT states, one of the most interesting and widely spread debate has been on the dominant pathway of free charge formation. It has been stated that charge transfer occurs into electronically or vibronically excited ("hot") CT states. Those higher lying CT levels have been proposed to be more loosely bound due to a higher degree of charge delocalization.[69, 70] Therefore, the compelling question was whether excess energy (e.g., from above bandgap optical excitation) effectively assists to the formation of charges, or if the excess energy is lost in a thermalization process prior to dissociation. Regarding fullerene-based research, the terms of "hot" vs "cold" CT dissociation were introduced. Early transient absorption spectroscopy (TAS) studies demonstrated that higher energy excitations generate free charges faster,[71] indeed suggesting that charge separation benefited from excess energy (for excitons or CT states). Vandewal et al.[63] addressed the issue by measuring the photocurrent response of the solar cell as a function of excitation energy, comprising the spectral range that excites exclusively low-lying CT states. Interestingly, measurements on fullerene-based blends showed that the internal quantum efficiency (IQE) does not decrease if the primary excitation is a CT state instead of an exciton, thus evidencing a "cold" dissociation pathway involving an equilibrated CT state manifold. Albrecht et al.[64] and Kurpiers et al.[65] investigated free charge generation by means of time-delayed collection field (TDCF) as a function of electric field and excitation energy for different BHJ blends. In these studies, the excess energy had no appreciable effect on the field-dependence of charge generation, supporting the "cold" model as well. These findings suggest a "cold" generation pathway and indicate that thermalization from higher energy CT states happens faster than separation. Consequently, the free carrier yield will be exclusively determined by the competition between dissociation (k_{d}) and geminate recombination (k_{f}) of the thermally relaxed CT manifold (see Figure 2.4).

Discussions on charge generation continued as NFAs spread in the OSC research field. At the center of the debate the prevailing question is how CT states are able to split into free charge carriers, contributing to photocurrent. This is particularly remarkable in systems with internal quantum efficiencies close to 100%, given that the binding energy of CT states is in the range of 100 to 500 meV,[72–75] thus significantly larger than the thermal energy at room temperature ($k_{\mathrm{B}}T \approx 25$ meV; with k_{B} the Boltzmann constant and T the temperature). In section 2.2. , the driving force for charge generation, $\Delta E_{\mathrm{S}_1-\mathrm{CT}}$, was introduced as the energy difference between the S_1 (of the low gap component) and the CT state. While the value of $\Delta E_{\mathrm{S}_1-\mathrm{CT}}$ primarily influences the efficiency of charge transfer, it may also affect the dissociation of the formed CT state. In this regard, very small LUMO and/or HOMO offsets at the DA heterojunction suggest a small (or even negligible) $\Delta E_{\mathrm{S}_1-\mathrm{CT}}$, but also a small energetic driving force for charge separation, $\Delta E_{\mathrm{CS}} = E_{\mathrm{S}_1} - E_{\mathrm{CS}}$. For various fullerene-based blends, the CT dissociation yield was shown to strongly correlate with the ΔE_{CS}.[76–78] In NFA solar cells, several studies reported higher charge generation efficiency and external quantum efficiencies to be related to larger driving forces, favoring the

"hot" dissociation model.[79–82] In addition, small level offsets have been shown to limit the performance because of inefficient charge transfer and/or enhanced geminate recombination due to a lower yield of dissociated CT states.[80, 83, 84] It has been reported that the HOMO level offset should be 100 meV or more to avoid inefficient hole transfer to the acceptor and to reduce geminate losses.[85]

In addition to the above defined driving forces, other processes have been reported to assist CT separation. The relevant distances for free charge formation are of the order of nanometers.[86] Some processes that may contribute to initial long-range charge separation include entropy,[87] due to the rapid rise in the number of available states as carriers diffuse away from the interface; and high local mobilities associated to carrier delocalization and fast intermolecular hopping, or rapid charge transport along conjugated chains.[88, 89] Similarly, delocalization of charges in ordered aggregated phases of the donor and/or acceptor was proposed to facilitate charge separation as well,[32, 90–92] and pointed to the importance of having crystalline domains that induce strong intermolecular coupling.

As the search for even more factors that can contribute to CT dissociation continues, energetic disorder in organic semiconductors has been thus far neglected. Disorder is generally expected to lower the charge carrier mobility (see section 2.4.1), potentially hindering charge generation.[86, 93] Nevertheless, several experimental and theoretical studies highlight the role of energetic disorder in providing low energy sites for the dissociation of CT states in DA blends, through broadening of the DOS distribution of electrons and/or holes. In effect, disorder encourages spatial separation of the slower carrier away from the DA interface through energetically favorable down-hill jumps until the carrier is most likely trapped in a position where recombination cannot take place, while the faster carrier diffuses away from the interface.[94] Furthermore, energetic disorder increases the number of available dissociation pathways. Based on this, Hood and Kassal,[95] employed basic thermodynamic calculations to report that the energy barrier for separation decreases through an entropic contribution $S = k_{\mathrm{B}} T\, ln(\Omega(\mathrm{r}))$, where $\Omega(\mathrm{r})$ is the number of charge carrier configurations. Importantly, the authors found that a Gaussian disorder σ of 100 meV is sufficient to reduce the free-energy barrier to ca. 25 meV, entailing CT dissociation by thermal energy at room temperature. The study also showed that entropy and energetic disorder play a role even if the charges are localized and thermally relaxed, thus concluding that there is not an extra requirement of sufficient initial separation and/or excess energy. However, a study of the role of disorder in PM6:Y6 and PM6 blended with a different Y-series NFA, which composes Chapter 8 of this thesis and includes measurements of steady-state free carrier densities as a function of temperature, suggests that in these blends charge separation is neither temperature-assisted nor entropy-driven. The reasons for this will be discussed in Chapter 8.

Disorder is in turn related to morphology. Besides the distinct morphology of donor and acceptor domains, the morphology at the BHJ interfaces might be different, leading to a third (intermixed) phase. This different morphology may introduce an energy cascade for electrons or holes when moving from the CT state into the domains of the neat materials.[33, 88]

For state-of-the-art NFA-based OSCs, the energetics at the donor-NFA interface has been shown to be crucial for efficient free charge generation due to the acceptor-donor-acceptor (A-D-A) molecular architecture of the acceptor leading to a large quadrupole moment of a molecule.[96–98] Most NFAs have zero dipole moments or dimerize in a unit cell such that the dipoles of neighbors compensate each other. Therefore, the electrostatics representation of an NFA molecule gets reduced to a nonpolarizable linear quadrupole, with a distinctive negative

component of the quadrupole moment tensor along the long molecular axis.[66, 99, 100] The theoretical modeling work by Markina et al.[74] places an electron, modeled as a negative point charge, on the acceptor molecule at different distances from the heterojunction and evaluates its electrostatic interaction energy with the surrounding quadrupoles. The charge-quadrupole interactions and the concentration gradient at the acceptor-vacuum interface results in the introduction of an interfacial bias potential, B_e^{A}, and energy level bending at the interface. B_e^{A} depends on the molecular packing and orientation, and interface width w. Modeling shows that parallel and perpendicular molecular orientations at the interface are the most favorable. Also, a certain degree of intermixing of the donor and acceptor, which increases w, is required to observe band bending. Thereupon, the energy level bending can be incorporated into the conventional energy level diagram of an organic solar cell (Figure 2.5). This diagram shows a relative alignment of ionization energies and electron affinities of the donor and acceptor. The direction of the energy level bending is the result of calculations for a A-D-A structure of the acceptor and corresponds to the (negative) sign of the quadrupole moment when the long molecular axis is oriented parallel to the donor-acceptor interface. Because of energy level bending, the energy of the CT state is increased by the positive bias potential, $B = B_e^{\mathrm{A}} + B_h^{\mathrm{D}}$, where the subscript e and h represent electrons and holes, respectively. Note that both donor and acceptor contribute to the level bending, thus causing electron destabilization in the acceptor, and hole destabilization in the donor (that corresponds to what a D-A-D architecture of NFA would induce) at the heterojunction. Then, E_{CT} can be expressed as

$$E_{\mathrm{CT}} = \mathrm{EA}_{\mathrm{A,interface}} - \mathrm{IE}_{\mathrm{D,interface}} - E_{\mathrm{b,CT}} = \mathrm{EA}_{\mathrm{A,bulk}} - \mathrm{IE}_{\mathrm{D,bulk}} - E_{\mathrm{b,CT}} + B, \qquad (2.4)$$

where $E_{\mathrm{b,CT}}$ is the Coulomb binding energy of the CT state in the solid state. On the other hand, the CS state is not affected by the energy level bending since both electron and hole are apart from the interface and EA and IE are bent in the same direction ($E_{\mathrm{CS}} = \mathrm{EA}_{\mathrm{A,bulk}} - \mathrm{IE}_{\mathrm{D,bulk}}$, as defined previously).

Evidently, energy level bending has an impact on the formation and dissociation of the CT state. For the acceptor exciton, $E_{\mathrm{S}_1} = \mathrm{EA}_{\mathrm{A}} - \mathrm{IE}_{\mathrm{A}} - E_{\mathrm{b,S}_1}$, where $E_{\mathrm{b,S}_1}$ is the hole-electron binding energy of a Frenkel-type exciton. Therefore, for hole transfer from the acceptor, the main driving force is the offset of the ionization energies at the interface, or $\Delta\mathrm{IE}$ in the bulk reduced by the bias potential:

$$\Delta E_{\mathrm{S}_1-\mathrm{CT}} = E_{\mathrm{S}_1} - E_{\mathrm{CT}} = \Delta\mathrm{IE} - B - (E_{\mathrm{b,S}_1} - E_{\mathrm{b,CT}}). \qquad (2.5)$$

Next, the CT state dissociation energy is the energy difference between the CT and CS states, and corresponds to $E_{\mathrm{b,CT}}$ minus the bias potential, such that

$$\Delta E_{\mathrm{CT-CS}} = E_{\mathrm{CS}} - E_{\mathrm{CT}} = E_{\mathrm{b,CT}} - B. \qquad (2.6)$$

According to this expression, the optimal condition is achieved for $B = E_{\mathrm{b,CT}} \approx$ 0.4-0.5 eV, which corresponds to the Coulomb energy of an electron and hole at an ideally flat DA interface.[74] Such values of the bias potential have been reported for well-optimized NFA-based blends. For PM6:Y6, the band bending phenomenon explains the observation of barrierless charge separation of CT states, as will be revealed in Chapter 4 of this thesis. However, band bending imposes an intrinsic limit for the minimum bulk ionization energy offset required to avoid the creation of a barrier for hole transfer. As shown in Figure 2.5b, a barrier appears if the excess energy provided by $\Delta\mathrm{IE}$ is lower than the bias potential B. For a large material series, the work by Karuthedath et al. concludes that IE offsets of ~0.5 eV are needed to ensure near-unity charge generation efficiency.

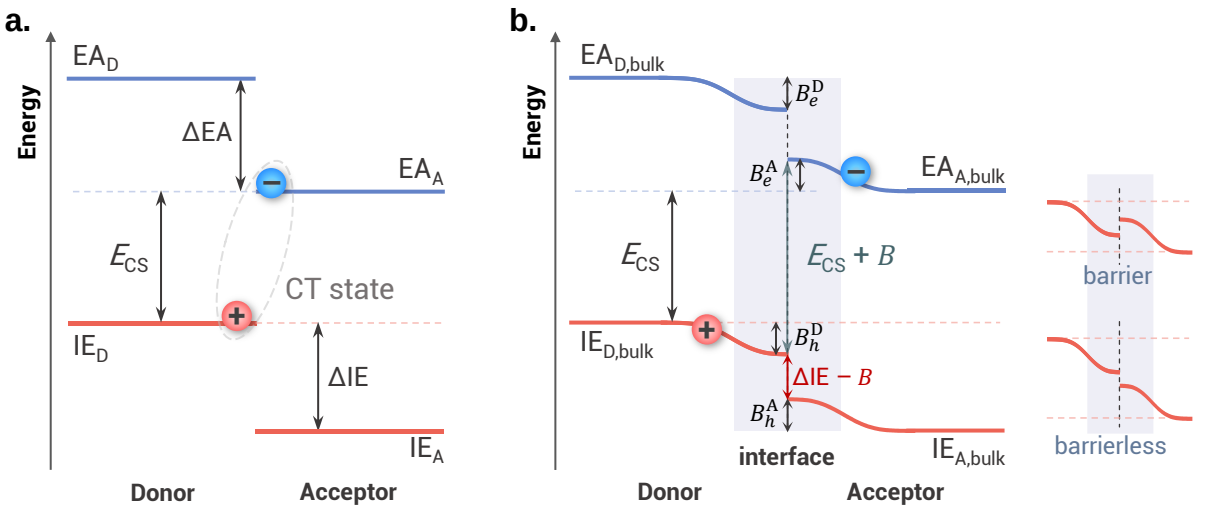

Figure 2.5: Schematic of the energy level diagram at a donor-acceptor interface illustrating energy level bending and the concept of interfacial bias potential. a Energy levels of donor (D) and acceptor (A) materials in an organic solar cell without interfacial energy level bending. EA is the electron affinity and IE the ionization energy with respect to vacuum level. The charge transfer (CT) state is shown by the ellipse (dashed lines). **b** Energy levels of donor and acceptor with interfacial energy level bending due to the electrostatic interaction of charges with quadrupole moments of surrounding molecules. The electron is more stable in the phase with lower EA and the hole is more stable in the phase with higher IE. The direction of the energy level bending is calculated for a A-D-A structure of the acceptor and long molecular axis parallel to the DA interface. A positive interfacial bias potential B destabilizes the CT state, driving the dissociation of CT states into free charges in the charge-separated states (CS). The inset in the right exemplifies energy diagrams for hole dissociation with an energetic barrier if $\Delta IE < B$, and without in case of barrierless free charge generation. Note that in this scheme, the donor is assumed to also provide band bending. Adapted from Refs.[66, 74, 101]

Finally, following efficient free charge generation, separated electrons and holes are transported to their respective electrodes, yet charge collection competes with nongeminate recombination. Of the above-mentioned factors that may assist in free charge generation, charge carrier mobility and energetic disorder also play key roles in charge extraction and free charge recombination. The interplay between these processes and the principles of nongeminate recombination are discussed in the next sections.

2.4. Charge Extraction and Nongeminate Recombination

Charge transport and carrier mobilities in OSCs can be understood once energetic disorder is properly described. Both mobility and disorder present a limiting factor to efficient charge extraction, and as such can be closely related to nongeminate recombination as the competing process. Once the nongeminate recombination processes are properly discussed and categorized according to their reaction order, recombination models that depend on the spectral width and shape of the density of states distributions can be established.

2.4.1. Mobility and Energetic Disorder

Following photogeneration or injection of free charge carriers in a semiconductor, the charges will be free to move. In general, current flow is driven by a gradient in the electrostatic potential Φ (i.e., by an electric field), as well as by a gradient of the charge concentration n, such that the total current density is defined as

$$J = qn\mu\nabla\Phi - qD\nabla n, \qquad (2.7)$$

where q is the elementary charge and μ is the charge carrier mobility. D is the diffusion constant. Note that this equation is simplified and does not account separately for the contribution of free electrons and holes to current. The first term in Equation 2.7 results in a drift current, while the second contribution results in diffusion current. In inorganic semiconductors, the charge concentration, and its gradient, is large whereas potential gradients are rather small, for example because of efficient dielectric screening (high dielectric constants). Therefore, the current is often dominated by diffusion. Conversely, drift current typically dominates in organic semiconductors.[50] The charge carrier mobility μ is a key parameter to describe the motion of charges and is defined as the ratio of the drift velocity v and electric field F:

$$\mu = \frac{v}{F}. \qquad (2.8)$$

As introduced in section 2.2. , organic semiconductors are disordered in nature. Systems without long range order are also called amorphous. Due to the absence of a three-dimensional periodical lattice structure, transport cannot be described by classical (inorganic and crystalline) semiconductor models, such as charge transport in bands. Interestingly, infinite long polymer chains with perfect conjugation would suggest band-like transport along the chains. However, the disruption of the conjugation, and thus the delocalization of π electrons, lead to the formation of localized states. Charge transport is then mainly determined by the spatial and energetic distribution of these localized states. A charge carrier moving through the material "hops" between these localized states, following non-coherent transfer events, which led to the term hopping transport.[102] Hopping transport entails lower carrier mobilities than those attainable with band transport and as such mobilities in disordered organic semiconductors are typically several orders of magnitude lower than in inorganic semiconductors. Mobilities range from 10^{-6} to 10 $cm^2V^{-1}s^{-1}$ but depend on the material and the device structure under study.[103]

In the presence of spatial and energetic disorder, the distance and energy difference between hopping (or "jump") sites must be considered. If the forward jump is downhill in energy, the backward jump is evidently uphill, and vice versa. This requires an asymmetric jump rate. In this picture, one may consider that excess energy is dissipated in the downhill process, while the uphill jump requires an activation energy in the form of a Boltzmann factor. This energy dependence has to be multiplied with the transfer rate due to the electronic coupling between the two sites, which can be defined as $\exp(-2\gamma r_{ij})$. This information enters the expression of the hopping rate w_{ij} in the Miller and Abrahams model,[104]

$$w_{ij} = \nu_0 \exp(-2\gamma r_{ij}) \begin{cases} \exp\left(-\frac{E_j - E_i}{k_B T}\right), & E_j < E_i \\ 1, & E_j \geq E_i \end{cases} \qquad (2.9)$$

where ν_0 is the attempt-to-hop frequency, and γ is the inverse localization radius of the electron wavefunction that describes how well charges can tunnel from site i to j; r_{ij} is the distance between the sites with energies E_i and E_j; k_B is the Boltzmann constant and T the temperature.

From Equation 2.9 above, it becomes evident that hopping transport is temperature assisted. Because the energy of the hopping sites also enters the equation, the shape of the density of states (DOS), which represents the distribution of transport states in energy, controls the properties of charge transport. A Gaussian distribution is commonly used to describe the DOS of disordered systems,[52, 105–108] as depicted in Figure 2.6. In this case, the standard deviation of the DOS σ, becomes the parameter that quantifies the energetic disorder. In this disordered environment, it becomes useful to introduce the concept of effective transport energy.[107] In organic semiconductors, charge carriers reside in the tail states of the DOS distribution and in order for carriers to move, thermal activation is required. However, if thermal excitation promotes a carrier to a nearby site from which further hopping is energetically unfavorable, the carrier is likely to relax back to its original site. On the contrary, excitations to states closer to the center of the DOS provide a high probability for charges to subsequently jump away from the initial site. The energy that enables such continuous motion of charges is called effective transport energy, E_{tr}. For a Gaussian-type HOMO and LUMO, $E_{\mathrm{tr}} = E_{\mathrm{LUMO}} - \sigma_{\mathrm{DOS}}^2/2k_{\mathrm{B}}T$ for electrons and $E_{\mathrm{tr}} = E_{\mathrm{HOMO}} + \sigma_{\mathrm{DOS}}^2/2k_{\mathrm{B}}T$ for holes. Hence, the transport energy for electrons is below the center of the Gaussian DOS, E_{LUMO}, and for holes is above the center of the DOS, E_{HOMO}.[109] Once carriers sink deeper into the DOS, their motion requires thermal excitation back to E_{tr}. The carrier below the transport energy may be considered as trapped even if no trap states, such as chemical defects, are present in the organic semiconductor (see the following sections). Consequently, the carrier mobility decreases with time. In Figure 2.6, the charge carrier (an electron in this case) hops from one to site to the next, while inevitably relaxing toward the tails of the distribution. Initially, downhill hops dominate, and the mean energy of the carriers continuously decreases until eventually, a balanced equilibrium is established between downhill and thermally activated uphill jumps. The mean energy of the carriers is then known as the equilibrium energy, E_{∞}, which for electrons (holes) is $\sigma_{\mathrm{DOS}}^2/k_{\mathrm{B}}T$ below (above) the center of the respective DOS,[102] as marked in the figure. When equilibrium has been established, the mobility is time-independent and approaches steady-state values.

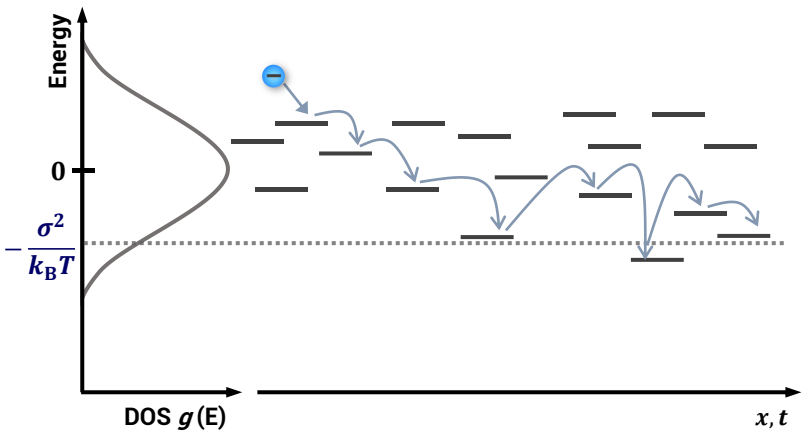

Figure 2.6: Hopping transport in a Gaussian density of states distribution. Illustration of a charge carrier (an electron in this example), generated at an arbitrary energy, that hops within a Gaussian density of states (DOS). The dotted horizontal line marks the energy of the equilibrated carriers, E_{∞}, which for electrons (holes) is $\sigma_{\mathrm{DOS}}^2/k_{\mathrm{B}}T$ below (above) the center of the respective DOS. Adapted from [59].

The effect of energetic disorder in organic semiconductors is often also described through an exponential model of the DOS.[110–113] In an exponential DOS, the standard deviation of the distribution is expressed as $E_0 = k_B T_0$, with T_0 being the characteristic distribution temperature of the DOS. Importantly, in an exponential DOS, there is no equilibrium energy and as such, carrier motion slows down continuously with time up to the point where state filling occurs. The significance of each DOS model on free charge recombination is further discussed in section 2.4.3. As for the charge transport efficiency, μ depends on several parameters such as electric field, temperature, and charge carrier densities. Various models exist to relate mobility to such parameters, depending on whether the DOS is described by a Gaussian or an exponential distribution. For the former, Heinz Bässler first developed in 1993 the Gaussian disorder model (GDM).[102] The GDM assumes highly localized sites and charge transport occurring via hopping between these states, thus the hopping rate follows the Miller and Abrahams expression (Equation 2.9). The model includes the energetic and spatial disorder parameters, σ and Σ, to account for the site energies and hopping distances, respectively. From Monte Carlo simulations, an empirical expression that predicts a temperature and field-dependence for mobility was obtained:

$$\mu(F,T) = \mu_0 \exp\left(-\left(\frac{2}{3}\frac{\sigma}{k_B T}\right)^2 + C\left[\left(\frac{\sigma}{k_B T}\right)^2 - \Sigma^2\right]\sqrt{F}\right), \Sigma \geq 1.5 \qquad (2.10)$$

where μ_0 is the zero-field and infinite temperature mobility and C is an empirical constant. By means of Equation 2.10, the GDM is able to explain the $1/T^2$ temperature dependence of mobility, and a Poole-Frenkel field dependence ($\mu(F) \sim \exp(\gamma\sqrt{F})$), both observed experimentally. The GDM can be extended to successfully describe electron or hole transport in the space charge limited current (SCLC) regime (as done in Chapter 4 and Chapter 8 of this thesis). Noticeably, Equation 2.10 does not account for a charge carrier density dependence of the mobility. In a system with energetic disorder, the mobility μ increases with charge carrier density because the lowest energy states are filled up, thus more carriers occupy states closer to the center of the DOS. This dependence has been calculated using various methods that extend the GDM, including notably the work by Pasveer et al.[114]

Separately, the multiple trapping and release model, also called mobility edge model, assumes that localized states act as traps and thus, there is no charge transport (hopping) between them. The mobility edge separates transport states from trap states, thus representing E_{tr}.[115] As such, transport occurs in a dense band of delocalized states near the center of the DOS with mobility μ_0. Meanwhile, trapped charges require thermal activation back to the transport band to contribute to transport. Here, an exponential distribution is used to characterize the tail of trap states that extends from the band into the bandgap (see Ref.[113]). The effective mobility, controlled by trapping and detrapping processes, is given by:[116]

$$\mu = \mu_0 \frac{n_f}{n_f + n_t} \qquad (2.11)$$

where n_f is the density of free carriers in the delocalized band, and n_t is the density of carriers in trap states.

Ultimately, disorder in OSCs can be linked to morphology. In BHJ solar cells, positional or structural disorder describes the placement of molecules and quantifies the loss of order over longer length scales, for example in a stacking direction. Energetic and positional disorder in a BHJ arise from molecular and interfacial interactions and the multiple possible morphologies upon mixing of donor and acceptor. Given that mobility is influenced by disorder and electronic

coupling between hopping sites, a straightforward approach to improve transport in OSCs involves increasing the structural order. Accordingly, the formation of interconnected aggregates in polymers and small molecules is crucial to charge transport.[117, 118] The molecular packing within these domains is divided into lamellar stacking, i.e., conjugated backbone ordering, and π-π stacking between conjugated groups.[119] The preferential stacking direction is specified with respect to the substrate, meaning in-plane or out-of-plane. In general, π-π stacking parallel to the substrate is known as *edge-on* orientation while perpendicular π-π stacking is referred to as *face-on* orientation.[120] The *edge-on* and *face-on* terms originate from the fact that the conjugated backbone of small molecules and polymers used in OSCs typically contain fused hydrocarbon rings, and the terms refer to their orientation relative to the substrate. Given that charge transport in OSCs occurs in the vertical direction, preferential *face-on* orientation allows for a higher charge mobility via intermolecular hopping through π-π stacking. Lamellar and π-π stackings are observed in the nm range; therefore, X-ray scattering techniques are required to probe the ordered regions of a BHJ blend.

NFA molecules are known for their superior molecular ordering and high crystallinity. Among NFAs, Y6 and its derivatives certainly stand out. Y6 and Y-series molecules are bent in shape, unlike many other NFAs, leading to an "unconventional" packing behavior. Analysis of Y6 crystal structures revealed a distinctive structure combining π-π interaction between end-groups (J aggregation) and face-to-face π-core interaction between central groups (H aggregation).[32] This creates a three-dimensional interpenetrating network in a Y6 single crystal, which improves charge transport by increasing the number of available pathways. Such a special packing is different than in most ITIC-type acceptors, which can explain why Y-type acceptors generally demonstrate higher mobilities.[121] It is important though to examine the molecular packing in Y6 layers as well. It has been extensively reported that pristine films of Y6 have more preferential *face-on* orientation with in-plane lamellar peaks that show long range ordering.[36, 38, 121] In turn, extended ordered domains lead to a narrow DOS distribution for electrons, that is, a lower energetic disorder and higher electron mobilities. Moreover, large electronic couplings promote large exciton diffusion lengths of above 30 nm in Y6,[58] which makes the BHJ more robust against domain size variation.

2.4.2. Monomolecular and Bimolecular Recombination

Nongeminate recombination, NGR, occurs between free (statistically independent) electrons and holes. For photogenerated charges, nongeminate recombination denotes that the electron and hole originated from different CT dissociation processes before recombining (as introduced in section 2.2.). Free electrons and holes can be injected at the electrodes as well.

The recombination rate R is defined as the decay of charge carriers n with time:

$$R = -\frac{dn}{dt} = \gamma n^{\delta}, \qquad (2.12)$$

where δ is the recombination order and γ is the recombination coefficient. The recombination process can be the divided into monomolecular or bimolecular recombination depending on the number of particles involved, that is, the recombination order.[122]

Monomolecular recombination involves one particle, as the name suggests, which can be a quasi-particle like an exciton or a geminate pair. A geminate pair is in this case a CT state which has not dissociated yet, meaning that geminate recombination is monomolecular in nature. Monomolecular recombination kinetics are also observed in nongeminate recombination

processes if free carriers recombine via one recombination center. Recombination centers can be impurities or chemical defects. The nature of the impurities can be categorized as an acceptor-type trap state if negatively charged when occupied by an electron, or a donor-type trap state if positively charged when unoccupied. Then, for example, free electrons can recombine by being trapped by a donor-type state, followed by capture of a hole. This process is referred to as trap-assisted recombination, as first described for inorganic semiconductors by Shockley, Read and Hall (SRH) in 1952.[123] The recombination rate follows from a kinetic argument, e.g., whenever an electron that moves in the conduction band at its thermal velocity ν_e comes within the capture cross section σ_e of a trap occupied by a hole, it will be captured. For midgap traps, the recombination rate for electrons of density n is defined as $R_{\mathrm{SRH}} = \sigma_e \nu_e n p_t$, where p_t is the density of traps occupied by holes.[124] Importantly, if the energy of the trap states lies between the quasi-Fermi levels of electrons and holes, the occupation of traps is not defined by either of the Fermi distributions (i.e., the occupation does not follow Fermi-Dirac statistics, see next section) but is rather determined by the kinetics of trapping (and detrapping). Given that monomolecular recombination is a first-order recombination process with respect to the density of species involved, the recombination rate R is also generally written as $R = k_1 n$, with k_1 being the monomolecular recombination coefficient.

In OSCs, though, bimolecular recombination is found to be the dominant loss mechanism. Two free charge carriers are involved in bimolecular recombination, and in the case of photogeneration, the electron density, n, and the hole density, p, can be assumed to be equal ($n = p$). The recombination rate depends then quadratically on n as

$$R = k_2 n^2, \tag{2.13}$$

with k_2 being the bimolecular recombination coefficient. In principle, k_2 can be described by the Langevin recombination theory. A limiting step when considering recombination in low mobility systems (< 1 cm^{2}V^{-1}s^{-1}), such as organic semiconductors, is the probability of two oppositely charged carriers to encounter each other. This process was first described by Langevin on the recombination of ions in gases,[125] but is commonly applied to organics when electrons and holes are considered. The theory establishes that recombination inevitably occurs when the distance between the electron and the hole decreases below the Coulomb capture radius. Then, recombination is considered as the drift of the two charges in their mutual Coulomb field and the Langevin recombination coefficient k_L depends linearly on the sum of electron and hole mobilities, μ_e and μ_h:

$$k_L = (\mu_e + \mu_h)\frac{q}{\varepsilon_r \varepsilon_0}, \tag{2.14}$$

where ε_0 and ε_r are the vacuum and relative dielectric constants, respectively. Equation 2.14 represents the simplest case of encounter-dominated recombination in a homogeneous medium. In efficient BHJ OSCs, k_2 values are generally much smaller than k_L, corresponding at times to more than 100 times suppression of recombination compared to the Langevin limit.[126–128] In 2015, Burke et al.[129] postulated that suppressed recombination is a result of efficient resplitting of CT states into free charges. This means that free charge recombination proceeds via reformation of interfacial CT states, which either decay back to the ground state or re-dissociate into free carriers. Nonetheless, determining k_L allows to compare different DA blends, in terms as well of their reduction factors. In effect, k_2 can be written in terms of the three following factors:

$$k_2 = \gamma_{\mathrm{CT}} \gamma_{\mathrm{enc}} k_L = \gamma k_L, \tag{2.15}$$

where $\gamma_{\mathrm{enc}} = k_{\mathrm{enc}}/k_L$ describes the reduction of encounter rate compared with the Langevin theory because of phase separation in BHJs, and $\gamma_{\mathrm{CT}} = 1 - P$ is the CT recombination reduction factor, with P being the probability of (re-)dissociation of the (re-)formed CT states.[130]

Importantly, bimolecular recombination refers to the recombination between free charge carriers, regardless of whether they are photogenerated, injected or originate from doping. Electrode-induced charges, or dark-injected charges, are a result of charge carrier diffusion from the metal electrodes into the (intrinsic) active layer, which induces Fermi-level alignment and a built-in field across the active layer. As a result, there is a high density of majority carriers near the electrodes in the bulk of the active layer which are also present in the dark.[131–133] This causes a light intensity-independent cloud of dark charges close to the contacts. With increasing forward bias, this excess charge is pushed deeper into the bulk of the active layer, leading to an increased volume where bimolecular recombination between photogenerated and dark-injected charges can take place. This type of recombination is a first order process with respect to the light intensity but bimolecular in nature. Losses due to recombination of photogenerated charges with dark charges govern at lower light intensities (low generation rates) as the carrier density profiles are dominated by the injected charge in the regions close to the contacts. As the active layer thickness increases, the first order losses remain similar but the recombination between photogenerated charges only, which follows a second order with respect to light intensity, increases. This is because the volume in which the pseudo-first order recombination occurs decreases relative to the volume of the bulk. However, optimized layer thicknesses that ensure efficient charge extraction in NFA OSCs are typically close to 100 nm. In such optimized cells, there is a large contribution of recombination losses of photogenerated charges recombining with dark-injected charges, which often dominates the FF loss. This will be discussed in Chapter 6.

The recombination mechanism just described (between photogenerated and dark charges) is not to be confused with minority carrier surface recombination at the contacts. Surface recombination is a loss mechanism that takes place when photogenerated carriers travel to the wrong electrode (electrons to the anode or holes to the cathode). In this case, recombination occurs at the interface of the active layer and the electrode.[134] As a result, the carrier densities at the electrodes are reduced and an extra surface recombination current appears at the respective contact that is linearly dependent on the minority carrier density and the surface recombination velocity, S_{n} for electrons and S_{p} for holes.[135] Surface recombination is mainly due to poor contact selectivity and increases with the injection barrier offset (i.e., the difference between the anode and cathode work functions and the donor HOMO and acceptor LUMO energies).[136] In addition, interfacial recombination can occur between two different semiconductors in the cells, e.g., between the active layer and a charge transport layer.

To study and evaluate the impact of the above processes in high-efficiency blends, the order and coefficient of recombination can be studied by determining the charge carrier density in the device as a function of illumination intensity, for example by employing charge extraction techniques. The presence of the above-mentioned dark-injected charges and surface recombination losses can appear very distinctly in the obtained recombination data but still affect the reliability of charge extraction methods. Therefore, such effects are inspected carefully in Chapter 5 of this thesis.

2.4.3. Density of States and Recombination Models

The energetic disorder and shape of the DOS do not only affect the transport of free charges in organic semiconductors, as previously seen in section 2.4.1, but also influence the nongeminate recombination characteristics in OSCs. As such, it makes a difference whether the DOS is described by a Gaussian or an exponential distribution.

Charge carrier recombination in OSCs is affected by thermalization of charge carriers in the DOS. Therefore, it is important to distinguish between dispersive and steady-state recombination.[112] In a system under steady excitation, the recombination (and, if applicable, extraction) current balances the generation current at each point in the device, and a steady-state carrier density is established. Thus, thermalization stops as deep states are filled by these steady-state carriers. In the following, the presented models apply to steady-state recombination, with a thermal occupation of the respective density of states distribution following the Fermi-Dirac or its Boltzmann-approximation.

Previously, it was shown that the recombination rate R dependence on charge carrier density is defined by the recombination order δ (Equation 2.12). To determine δ in a solar cell, the carrier density can be measured at open-circuit conditions, at which generation equals recombination to fulfil zero net current conditions. At V_{OC}, the generation rate G can be expressed in terms of the generation current J_{G} as follows

$$J_G = J_R = qdR = qd\gamma n^{\delta}, \tag{2.16}$$

with the film thickness d, and J_R being the steady-state recombination current density. J_R in a solar cell is connected to the applied voltage via the Shockley equation,[52, 137] and at open-circuit conditions

$$J_R(V_{\mathrm{OC}}) = J_0 \exp\left(\frac{qV_{\mathrm{OC}}}{n_{\mathrm{id}}k_{\mathrm{B}}T}\right), \tag{2.17}$$

where J_0 is the recombination current density in the cell at thermal equilibrium in the dark (see section 2.5.1), and n_{id} is the so-called ideality factor, introduced to describe deviations from the *ideal* Shockley diode equation, where recombination is purely radiative and $n_{\mathrm{id}} = 1$.[112]

The charge carrier density of electrons n and holes p in a semiconductor is connected to the energetics via the DOS and the occupation probability distribution, which follows Fermi-Dirac statistics. The classical semiconductor theory considers an ideal intrinsic semiconductor with a valence and conduction band and sharp band edges. Then, applying the Boltzmann-approximation of the Fermi-Dirac distribution allows to calculate the product of electron and hole charge carrier density,[124] as

$$np = N_e N_h \exp\left(-\frac{E_{\mathrm{C}} - E_{\mathrm{V}}}{k_{\mathrm{B}}T}\right)\exp\left(-\frac{E_{\mathrm{F},e} - E_{\mathrm{F},h}}{k_{\mathrm{B}}T}\right) = n_i^2 \exp\left(-\frac{E_{\mathrm{F},e} - E_{\mathrm{F},h}}{k_{\mathrm{B}}T}\right), \tag{2.18}$$

with $N_{e/h}$ the effective density of states, n_i the intrinsic charge carrier density and E_{C} and E_{V} the conduction and valence band edge energy, respectively. $E_{\mathrm{F},e}$ is the quasi-Fermi level for electrons in the conduction band and $E_{\mathrm{F},h}$ is the quasi-Fermi level for holes in the valence band. Their difference is the quasi-Fermi level splitting ($\mathrm{QFLS} = E_{\mathrm{F},e} - E_{\mathrm{F},h}$), which describes the population of the free carriers in the semiconductor. The open-circuit voltage V_{OC} of the device is equal to the QFLS in the absence of surface recombination (more details coming in the next section 2.5. dedicated to the V_{OC}).

Following Equation 2.18 above and assuming $n = p$, the electron and hole densities depend exponentially on V_{OC}:

$$n = p \propto \exp\left(\frac{qV_{\mathrm{OC}}}{2mk_{\mathrm{B}}T}\right). \tag{2.19}$$

This equation applies to disordered semiconductors and the m-factor is introduced to describe the degree of disorder.[111, 138]

This dependence was investigated in detail by Hofacker and Neher.[112] In this publication, the authors calculated δ, n_{id} and m for different DOS combinations and recombination pathways. Specifically, expressions for each factor were derived by examining whether recombination takes place between electrons and holes in two Gaussian DOS or in two exponential DOS, or between holes in a Gaussian and electrons in an exponential in the case of mixed DOS. Moreover, recombination of free with free carriers, or recombination between free and trapped carriers, was differentiated. Note that trapped electrons (n_t) or trapped holes (p_t) are considered here to be those residing in low-energy states situated below the transport energy of their respective DOS (because thermal activation to E_{tr} is the limiting step for transport as seen in section 2.4.1). These trapped carriers are different from those involved in SRH recombination. As described in the previous section, the occupation of traps in SRH is a kinetic process that does not depend on the DOS distributions for holes and electrons. On the contrary, the occupation of traps states in the model by Hofacker and Neher is described by a Fermi-Dirac distribution (see below). Finally, one distinguishes between the free carrier density n_f (p_f) of carriers close to the transport energy and the total carrier density n (p). The main results are summarized in Table 2.1, where $\alpha = T_0/T$ being T_0 the characteristic distribution temperature of the exponential DOS, as introduced in section 2.4.1.

For the two narrow Gaussians model, the assumption is that the quasi-Fermi level for electrons (holes) in the steady state is well below (above) the equilibrium energy: $E_{\mathrm{F},e} < E_{\infty,e}$ and $E_{\mathrm{F},h} > E_{\infty,h}$ (i.e., not too high carrier densities). Then, most of the carriers have energies close to E_∞, and $n_f \propto n$ as well as $p_f \propto p$. Considering only free carriers, the recombination rate equation is $R = \gamma n_f p_f = k_2 n^2$. The total carrier density in the Gaussian DOS is approximated by the integral of the Fermi-Dirac distribution function with the DOS (see Refs.[112, 113]), which yields:

$$\begin{aligned} n &= N_0 \exp\left(-\frac{E_{\mathrm{L,A}} - E_{\mathrm{F},e}}{k_{\mathrm{B}}T}\right) \\ p &= N_0 \exp\left(-\frac{E_{\mathrm{F},h} - E_{\mathrm{H,D}}}{k_{\mathrm{B}}T}\right) \\ n = p &= N_0 \exp\left(-\frac{E_{\mathrm{g}}}{2k_{\mathrm{B}}T}\right)\exp\left(\frac{qV_{\mathrm{OC}}}{2k_{\mathrm{B}}T}\right), \end{aligned} \tag{2.20}$$

where $E_{\mathrm{L,A}}$ and $E_{\mathrm{H,D}}$ are the center of the LUMO in the acceptor and the HOMO in the donor (analogous to conduction and valence band), and the effective energy gap for the donor-acceptor blend is $E_{\mathrm{g}} = E_{\mathrm{L,A}} - E_{\mathrm{H,D}}$. The density of available states is assumed to be the same for electrons and holes, $N_0 = N_e = N_h$. According to the recombination rate and the total carrier density in Equation 2.20, $\delta = 2$, $n_{\mathrm{id}} = 1$ and $m = 1$ in case of two Gaussians for free-trapped and free-free recombination.

In the exponential model, significant state filling happens below or above the respective quasi-Fermi level (in the scheme in Table 2.1 this is illustrated with darker shading), thus the total carrier density is determined mostly by trapped charge $n_t = n$ and $p_t = p$. Free charges in an exponential are at the mobility edge and the free carrier density is a nonlinear function of the total carrier

density, $n_f \propto n^{\alpha}$ with $\alpha = T_0/T$. This explains why for two exponentials it makes a difference in Table 2.1 whether free or trapped charges are involved in recombination. The rate equations for recombination between free and trapped carriers is $R = \gamma(n_f p_t + n_t p_f) \propto \gamma n^{\alpha+1}$, while $R = \gamma n_f p_f \propto \gamma n^{2\alpha}$ for recombination between free carriers. For an exponential DOS the trapped carrier density is also defined by the Fermi-Dirac,[112, 113] which gives the following total charge carrier density for two exponentials:

$$\begin{aligned} n = n_t &= N_0 \exp\left(-\frac{E_{\mathrm{L,A}} - E_{\mathrm{F},e}}{k_{\mathrm{B}} T_0}\right) \\ p = p_t &= N_0 \exp\left(-\frac{E_{\mathrm{F},h} - E_{\mathrm{H,D}}}{k_{\mathrm{B}} T_0}\right) \\ n = p &= N_0 \exp\left(-\frac{E_{\mathrm{g}}}{2k_{\mathrm{B}} T_0}\right) \exp\left(\frac{qV_{\mathrm{OC}}}{2k_{\mathrm{B}} T_0}\right). \end{aligned} \tag{2.21}$$

In the last mixed model, the combination of a Gaussian and an exponential DOS is examined (Gaussian for holes and exponential for electrons in this example). Hence, this case deals with mostly trapped electrons in an exponential tail and free holes in a narrow Gaussian. The rate for recombination between trapped electrons and holes is $R = \gamma n_t p_f = k_2 n^2$, and for recombination between free electrons and holes $R = \gamma n_f p_f \propto \gamma n^{1+\alpha}$. In Table 2.1, recombination between trapped charges in the Gaussian and free electrons in an exponential distribution has been omitted (see Ref.[112] for this case).

Conclusively, recombination between charges in two Gaussians leads to the parameters δ, n_{id} and m being temperature independent, while once an exponential DOS is involved, at least two of those parameters depend on α and with that on temperature. It is in fact the presence of E_{∞} in the Gaussian DOS that ensures bimolecular recombination, $\delta = 2$ (this holds as long as $E_{\mathrm{F}} < E_{\infty}$, i.e., for not too high carrier densities). Noticeably, the ideality factor n_{id} is 1 for free-free recombination in all models. When trapped charges in the exponential DOS play a role, n_{id} becomes temperature dependent and greater than 1. Moreover, the recombination factor δ can have values larger than 2 and be temperature dependent. As expected, the m-factor is 1 for the narrow Gaussian-Gaussian model and $m > 1$ in the case of increased disorder due to an exponential tail-state distribution.

The parameters δ, n_{id} and m in Table 2.1 can be determined experimentally by measuring the recombination current dependence on the carrier density (δ), the V_{OC} dependence on the generation current (n_{id}) and the carrier density (m) under steady-state illumination conditions. However, since δ, n_{id} and m depend on the shape of the DOS and the predominant recombination mechanism, and consequently on the temperature, determining only one of these parameters or even different parameters at just one given temperature may not provide sufficient information. The relevance of the models here presented is examined in Chapter 8, where the recombination parameters are determined as a function of temperature for PM6:Y6 in comparison to the more disordered PM6:N4 blend.

On a final note, energetic disorder will inevitably reduce the maximum achievable open-circuit voltage of an OSC, because carriers accumulate in the tail of the DOS reducing the QFLS. Likewise, recombination of charges anywhere in the device also lowers the QFLS. This is shown in the following section with focus on the V_{OC}.

Table 2.1: The impact of the DOS distribution on the recombination models. Summary of the steady-state parameters δ, n_{id} and m in case of free-trapped ($f-t$) or free-free ($f-f$) recombination for three DOS models: Gaussian, exponential and mixed. The mixed model considers the combination of an exponential DOS for electrons and a Gaussian DOS for holes. Here $\alpha = T_0/T$, where T_0 is the characteristic distribution temperature of the exponential DOS. n and p are the total electron and hole density, respectively. n_f and p_f denote free electrons and holes, respectively, and n_t and p_t stand for trapped electrons and trapped holes, respectively.

Gaussian		$\boldsymbol{\delta}$	$\boldsymbol{n_{\mathrm{id}}}$	$\boldsymbol{m}$
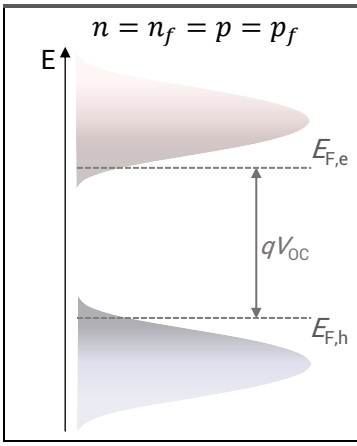	$f-t$	2	1	1
	$f-f$	2	1	1
Exponential		$\boldsymbol{\delta}$	$\boldsymbol{n_{\mathrm{id}}}$	$\boldsymbol{m}$
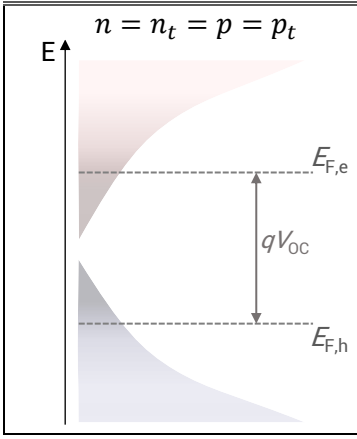	$f-t$	$1+\alpha$	$\frac{2\alpha}{1+\alpha}$	α
	$f-f$	2α	1	α
Mixed		$\boldsymbol{\delta}$	$\boldsymbol{n_{\mathrm{id}}}$	$\boldsymbol{m}$
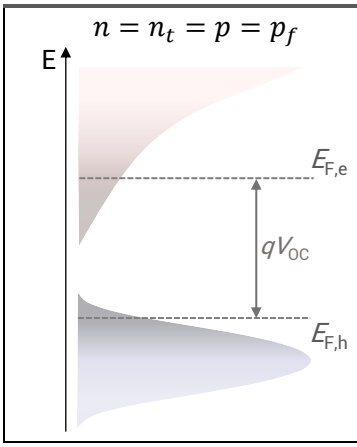	$f-t$	2	$\frac{1}{2}(1+\alpha)$	$\frac{1}{2}(1+\alpha)$
	$f-f$	$1+\alpha$	1	$\frac{1}{2}(1+\alpha)$

2.5. Open-Circuit Voltage

The open-circuit voltage, V_{OC}, is often the main target parameter in OSC research. While OSCs based on NFAs start to compete with their inorganic counterparts in terms of photocurrent generation and external quantum efficiencies, large V_{OC} losses continue to be the major drawback of OSCs compared to other technologies such as silicon and (hybrid) perovskites.[139] Understanding of the underlying physics and processes that govern the V_{OC} remain key to push the efficiency of NFA OSCs further up.[24, 140]

In a BHJ, the interfacial energy offset facilitates efficient exciton dissociation, as extensively discussed in section 2.3.1. However, the energy step decreases the energy of the resulting free charge carriers, which limits the achievable V_{OC} in favor of the short-circuit current, J_{SC}. As such, the introduction of the heterojunction reduces the V_{OC} relative to that of a single absorber of the same optical gap (Figure 2.7).[141] The interfacial gap E_i corresponds to the bandgap of the donor-acceptor blend as defined in the previous section, $E_i = E_{\mathrm{g}} = E_{\mathrm{L,A}} - E_{\mathrm{H,D}}$. This definition of the BHJ bandgap applies throughout this section.

To further understand the factors controlling the V_{OC} in OSCs, we first recall that *the open-circuit voltage of the device is defined as the difference between the quasi-Fermi levels* ($\mathrm{QFLS} = E_{\mathrm{F},e} - E_{\mathrm{F},h}$) *at the two contacts in an illuminated solar cell at zero net current flow*. As introduced in the previous section, the quasi-Fermi levels of electrons and holes will differ depending on the DOS model. For Gaussian-type HOMO and LUMO distributions, the expressions of $E_{\mathrm{F},e}$ and $E_{\mathrm{F},h}$ are extracted from Equation 2.20 in the previous section, but are adjusted to account for the energetic disorder of the charge-separated states in the LUMO of the acceptor, $\sigma_{\mathrm{L,A}}$, and in the HOMO of the donor, $\sigma_{\mathrm{H,D}}$,[138] as follows:

$$E_{\mathrm{F},e} = E_{\mathrm{L,A}} - \frac{\sigma_{\mathrm{L,A}}^2}{2k_{\mathrm{B}}T} + k_{\mathrm{B}}T\ln\frac{n}{N_0},$$
$$E_{\mathrm{F},h} = E_{\mathrm{H,D}} + \frac{\sigma_{\mathrm{H,D}}^2}{2k_{\mathrm{B}}T} - k_{\mathrm{B}}T\ln\frac{p}{N_0}. \qquad (2.22)$$

Under the assumption that the electron and holes densities are equal ($n = p$) under illumination at open-circuit conditions, the V_{OC} is finally described analytically for two Gaussian DOS as

$$qV_{\mathrm{OC}} = E_{\mathrm{F},e} - E_{\mathrm{F},h} = E_{\mathrm{g}} - \frac{\sigma_{\mathrm{L,A}}^2 + \sigma_{\mathrm{H,D}}^2}{2k_{\mathrm{B}}T} + 2k_{\mathrm{B}}T\ln\frac{n}{N_0}. \qquad (2.23)$$

This equation nicely demonstrates the role that energetic disorder plays in reducing the bandgap and unavoidably the V_{OC}. Here, it is important to remember that this expression holds in the non-degenerate limit of an equilibrated population at not too high carrier densities and high enough temperature, where the state population is described by a Boltzmann distribution (see previous section). To predict V_{OC} at low temperatures, the degenerate case is considered, as approximated in the sentinel paper by Paasch and Scheinert.[142] On the contrary, in an exponential DOS there is no distinction between non-degenerate and degenerate cases. The Paasch and Scheinert approximation and the V_{OC} expression in the exponential model will be discussed in more detail in Chapter 8.

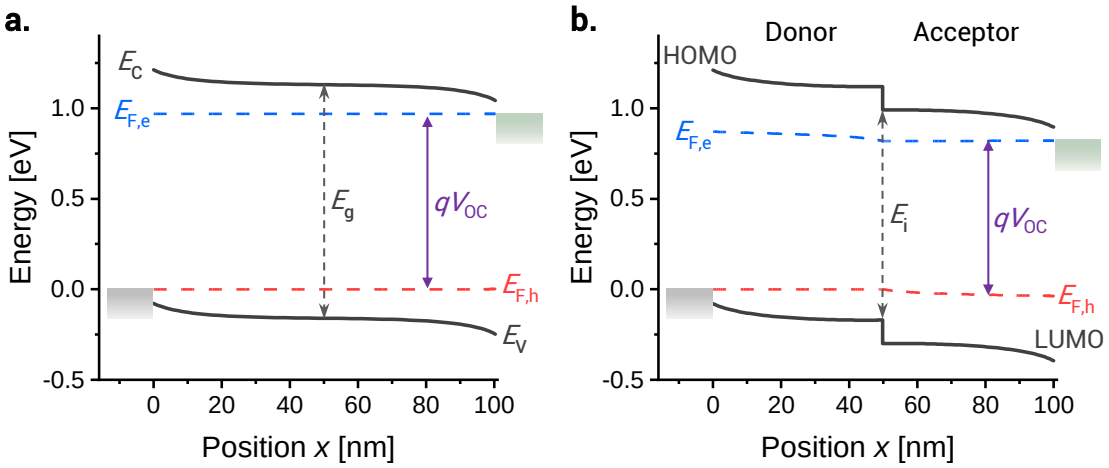

Figure 2.7: Energy levels in a solar cell at open circuit. a Band diagram of a solar cell consisting of a semiconductor with conduction band edge E_C and valence band edge E_V separated by the bandgap E_g. The difference between the quasi-Fermi levels for electrons, $E_{F,e}$ at the cathode ($x = d$), and holes, $E_{F,h}$ at the anode ($x = 0$), is the open-circuit voltage qV_{OC}. In this example, the difference of Fermi levels at the contacts is nearly identical to the Fermi level separation at any point in the device. **b** Band diagram at the donor-acceptor interface of a BHJ OSC. The interfacial energy bandgap, $E_i = E_g = E_{L,A} - E_{H,D}$ with $E_{L,A}$ and $E_{H,D}$ being the center of the LUMO in the acceptor and the HOMO in the donor, limits qV_{OC}. Adapted from [141].

The definition of the V_{OC} can also derive from its relation to the recombination processes in a solar cell. Upon free charge formation at open-circuit, the only possible process is the recombination of the electron-hole pair ($G = R$). As seen in section 2.4.2, different recombination mechanisms yield different dependence of the recombination rate on carrier density. If bimolecular recombination is considered, R depends on the product of electron and hole densities. Thus, the combination of Equation 2.12 and Equation 2.20 gives the following solution for V_{OC}:

$$qV_{OC} = E_g - k_B T \ln\left(\frac{k_2 N_0^2}{G}\right). \qquad (2.24)$$

The above expressions predict the direct dependence of the V_{OC} on the DA bandgap, which has been observed experimentally. Likewise, the V_{OC} increases at increased generation rates while a higher recombination coefficient k_2 reduces qV_{OC} relative to the bandgap.

2.5.1. Theoretical Limits of V_{OC}

In photovoltaic-based research, the analysis of voltage losses is a valuable approach to quantify the deviation from ideal performance of a solar cell. A comprehensive account of V_{OC} losses in OSCs involves the introduction of the principle of detailed balance, which sets a fundamental physical limit for solar cells. Derivations in the framework of detailed balance are based on the thermodynamics of light in the context of photovoltaic devices, and thus apply to both organic and inorganic solar cells. Firstly, Kirchhoff's law of radiation states that for a gray body emitting and absorbing thermal radiation in thermodynamic equilibrium, the emissivity is equal to the absorptivity.[143] In other words, a reciprocity relation between absorption and emission exists in thermal equilibrium. Therefore, for any body (including semiconductors), the emission of thermal radiation at a given photon energy equals the black body radiation of the surrounding with equal temperature times the absorptance of the gray body. The emission of a black body in terms of photon flux, ϕ_{BB}, is expressed as

$$\phi_{\mathrm{BB}} = \frac{1}{4\pi^2\hbar^3c^2}\frac{E^2}{\exp\left(\frac{E}{k_{\mathrm{B}}T}\right)-1}, \quad (2.25)$$

where c is the velocity of light in vacuum and $\hbar$ is the reduced Planck's constant. In accordance with reciprocity, the fraction of ϕ_{BB} absorbed by a solar cell in the dark must be reemitted since thermal equilibrium is established and no work is produced. Emission occurs via the radiative recombination of free carriers generated by the absorption of ϕ_{BB}, which implies that a radiative loss is unavoidable for light harvesting systems.

In fact, the emission flux in the dark sets the upper limit of the V_{OC} of a solar cell for a given bandgap. In the Shockley-Queisser limit,[144] the bandgap is the energy from which the external quantum efficiency goes from 0 to 1. To account for a non-ideal solar cell where the $\mathrm{EQE_{PV}}$ is not a step-function, Rau extended in 2007 the theory of detailed balance for solar cells,[145] and introduced the optoelectronic reciprocity relation between $\mathrm{EQE_{PV}}$ and electroluminescence (EL), i.e., emission after electrical injection of charge carriers via an external circuit (the solar cell is operating as a light-emitting-diode, LED). The total emitted photon flux ϕ_{em}, i.e. the EL, is linked to $\mathrm{EQE_{PV}}$ via the black body spectrum ϕ_{BB} and a non-equilibrium term accounting for the applied bias:

$$\phi_{\mathrm{em}}(V) = \int \mathrm{EQE_{PV}}(E)\,\phi_{\mathrm{BB}}(E)\mathrm{d}E\left[\exp\left(\frac{qV}{k_{\mathrm{B}}T}\right)-1\right]. \quad (2.26)$$

Rau's reciprocity therefore implies that the $\mathrm{EQE_{PV}}$ and EL spectra contain the same information. If considering only radiative recombination, the radiative current density in a solar cell can be calculated as

$$J_{0,\mathrm{rad}} = q\int \mathrm{EQE_{PV}}(E)\,\phi_{\mathrm{BB}}(E)\mathrm{d}E. \quad (2.27)$$

The significance of $J_{0,\mathrm{rad}}$ lies in the fact that this recombination current can be used to calculate the upper limit of the V_{OC} of a non-ideal solar cell, as detailed next. Under illumination, the generation current density, J_G, due to the absorption of photons in the solar cell, has to be considered. Then, the total current can be approximated by the Shockley ideal diode equation:

$$J(V) = J_0\left[\exp\left(\frac{qV}{k_{\mathrm{B}}T}\right)-1\right]-J_G, \quad (2.28)$$

where J_0 is the dark radiative current which equals $J_{0,\mathrm{rad}}$ when only radiative recombination occurs. Thereby, at open circuit when the total current of the solar cell is zero, the radiative limit of the open-circuit voltage can be calculated from Equation 2.28 with $J_0 = J_{0,\mathrm{rad}}$ (the -1 term can be neglected). This results in

$$V_{\mathrm{OC,rad}} = \frac{k_{\mathrm{B}}T}{q}\ln\left(\frac{J_{\mathrm{G}}}{J_{0,\mathrm{rad}}}\right). \quad (2.29)$$

In a real solar cell, however, not all free carriers recombine radiatively. The difference between the $V_{\mathrm{OC,rad}}$ and the measured V_{OC} results from non-radiative voltage losses, $\Delta V_{\mathrm{OC,nrad}}$, typically caused by phonon or vibration-mediated electronic transitions.[140, 146] In fact, non-radiative recombination generally dominates and thus cannot be neglected. The quantum yield of electroluminescence, ELQY (or Q_{LED}), is defined as the ratio of emitted photons to the number of injected charge pairs, and as such quantifies the external radiative efficiency. Thereby, the ELQY

can be related to the total dark recombination current as $J_0 = J_{0,\mathrm{rad}}(\mathrm{ELQY})^{-1}$. This gives an (additional) representation of the V_{OC}:

$$V_{\mathrm{OC}} = \frac{k_{\mathrm{B}}T}{q}\ln\left(\frac{J_{\mathrm{G}}}{J_0}\right) = \frac{k_{\mathrm{B}}T}{q}\ln\left(\mathrm{ELQY}\frac{J_{\mathrm{G}}}{J_{0,\mathrm{rad}}}\right). \quad (2.30)$$

From this expression, the non-radiative losses are directly connected to the ELQY as follows

$$\Delta V_{\mathrm{OC,nrad}} = V_{\mathrm{OC,rad}} - V_{\mathrm{OC}} = -\frac{k_{\mathrm{B}}T}{q}\ln(\mathrm{ELQY}). \quad (2.31)$$

Experimentally, the determination of voltage losses relies on the precise measurements of $\mathrm{EQE_{PV}}$ and/or EL spectra, and ELQY. It should be noted that the ELQY depends on the voltage or QFLS itself. Thus, to predict the V_{OC} under 1 sun conditions, the ELQY should be measured under the same conditions, i.e., same recombination current. Next, the generation current can be approximated as the J_{SC} of the device if total charge extraction at short circuit is assumed. The J_{SC} is given by:

$$J_{\mathrm{SC}} = q\int \mathrm{EQE_{PV}}(E)\,\phi_{\mathrm{sun}}(E)\mathrm{d}E. \quad (2.32)$$

with ϕ_{sun} the solar emission photon flux. The V_{OC} is finally calculated as

$$V_{\mathrm{OC}} = \frac{k_{\mathrm{B}}T}{q}\ln\left(\frac{\int \mathrm{EQE_{PV}}\,\phi_{\mathrm{sun}}\mathrm{d}E}{\int \mathrm{EQE_{PV}}\,\phi_{\mathrm{BB}}\mathrm{d}E}\right) + \frac{k_{\mathrm{B}}T}{q}\ln(\mathrm{ELQY}). \quad (2.33)$$

Ultimately, the voltage losses describe the difference between a reference energy, typically the optical gap $E_{\mathrm{g}}^{\mathrm{opt}}$, and the open-circuit voltage: $\Delta V_{\mathrm{loss}} = E_{\mathrm{g}}^{\mathrm{opt}} - V_{\mathrm{OC}}$. The optical gap, or absorption edge, may be regarded as the threshold for photon absorption. As mentioned earlier, the absorption edge is in reality not a step function and there is not a single defined value for $E_{\mathrm{g}}^{\mathrm{opt}}$. In OSCs, there are several methods to determine $E_{\mathrm{g}}^{\mathrm{opt}}$ of the system.[147] The optical gap can be extracted from the $\mathrm{EQE_{PV}}$ spectrum, with the advantage of using a full device structure for the measurement, thus accounting for internal properties of the absorbing blend materials as well as external properties like interference effects. The EQE is interpreted as a superposition of multiple step-functions with different bandgap energies. The probability distribution of gaps is obtained by taking the derivative of the EQE with respect to energy $\mathrm{d}EQE/\mathrm{d}E$, being $E_{\mathrm{g}}^{\mathrm{opt}}$ the maximum of the distribution, which is also referred to as 'photovoltaic gap' since it is a device property rather than a material property. From the losses reviewed above, the total loss is divided into three parts with respect to the optical gap:

$$\Delta V_{\mathrm{loss}} = E_{\mathrm{g}}^{\mathrm{opt}}/q - V_{\mathrm{OC}} = (E_{\mathrm{g}}^{\mathrm{opt}}/q - V_{\mathrm{OC}}^{\mathrm{SQ}}) + (V_{\mathrm{OC}}^{\mathrm{SQ}} - V_{\mathrm{OC,rad}}) + (V_{\mathrm{OC,rad}} - V_{\mathrm{OC}}). \quad (2.34)$$

The first loss term includes $V_{\mathrm{OC}}^{\mathrm{SQ}}$, which is the maximum voltage according to the Shockley-Queisser limit. As argued before, the V_{OC} is always smaller than the semiconductor bandgap due to unavoidable radiative recombination. The second term is due to additional radiative recombination from absorption below the bandgap (Equation 2.27 and 2.29). The radiative loss increases for a slowly decaying absorption, or rather $\mathrm{EQE_{PV}}$, tail. Therefore, the absorption from CT states in fullerene-based OSCs is the main contributor to this term, whereas in NFAs this loss can be quite small.[28] The last term is the non-radiative voltage loss (Equation 2.31), with values in OSCs between 200 and 500 mV.[24]

This method to divide voltage losses has turn out to be especially useful in solar cells with newly developed NFAs, since absorption and emission from CT states are hidden behind the strongly absorbing and more emissive singlet excitons in such blends. Provided that the CT state energy E_{CT} can be accessed, voltage losses can be related to the energetic states present in OSCs (see section 2.3.). In this picture, the lowest lying singlet energy E_{S_1} is the reference energy, and E_{CT} is included in the loss analysis to highlight its crucial role in sub-gap absorption.[140]

2.5.2. The V_{OC} in Non-fullerene Acceptor Organic Solar Cells

The energetic landscape in NFA OSCs, as seen in Figure 2.4 of section 2.3. , has the potential to influence the open-circuit voltage. In the context of reduced Langevin recombination, the encounter between free electrons and holes is expected to form CT states, which may subsequently split back into free charge carriers or recombine (refer to section 2.4.2). Burke et al.[129] proposed that, if free charges form CT states and dissociate much faster than they recombine, an equilibrium can be reached between the population of free carriers and the population of interfacial CT states. It is generally assumed that such an equilibrium is induced in fullerene- and NFA-based BHJs where free carrier recombination is reduced relative to the Langevin limit.[62, 148] Equilibrium in this case further implies that the V_{OC} is entirely defined by the energetics and the (radiative and non-radiative) recombination kinetics of CT states. Nonetheless, the situation becomes more interesting and complex for low offset systems, such as NFA OSCs, where reformation of the singlet exciton from CT states becomes feasible. For NFA blends with sufficiently small $\mathrm{S}_1 - \mathrm{CT}$ offsets, it has been suggested that the acceptor S_1 is in dynamic equilibrium with the CT state, meaning that the repopulation of the exciton from the CT state is faster than its decay to the ground state.[149, 150] In this case, an equilibrium would be established among excitons, CT states and free charge carriers.

For equilibrium between chemical or electronic species to be established, the fundamental requirement is that the change in the free energy on converting one species into the other is zero (so that the reaction is not spontaneous). In chemistry, the free energy of a species is often referred to as chemical potential μ, and in solid-state physics, the free energy of an electron is its quasi-Femi level $E_{\mathrm{F},e}$.[129] In essence, equilibrium between different electronic species entails that their free energy is equal (instead of their concentrations for example). Therefore, in an equilibrium between excitons, CT states and free carriers, the chemical potential of the reformed singlet state, μ_{S_1}, is the same as the chemical potential of the CT state, μ_{CT}, this being equal to the QFLS of the free charges in the bulk. By definition, equilibrium also entails that forward and backward reaction occur at the same rate, e.g., the charge carrier encounter rate is exactly balanced by the dissociation rate of CT states, $k_{\mathrm{d}} n_{\mathrm{CT}} = \beta_{\mathrm{enc}} n_{\mathrm{CS}}^2$, in CT-CS equilibrium.[62] Given that the QFLS is constant across the device and equal to qV_{OC} (Equation 2.23), the relationship between chemical potentials, quasi-Fermi levels and V_{OC} in equilibrium is

$$\begin{gathered} qV_{\mathrm{OC}} = \mu_{\mathrm{S}_1} = \mu_{\mathrm{CT}} = \mathrm{QFLS}, \\ qV_{\mathrm{OC}} = E_{\mathrm{S}_1} + k_{\mathrm{B}} T \ln \frac{n_{\mathrm{S}_1}}{N_{\mathrm{S}_1}} = E_{\mathrm{CT}} + k_{\mathrm{B}} T \ln \frac{n_{\mathrm{CT}}}{N_{\mathrm{CT}}} = E_{\mathrm{g}} + 2k_{\mathrm{B}} T \ln \frac{n}{N_0}, \end{gathered} \tag{2.35}$$

where N_{S_1} and N_{CT} are the density of available states for excitons and CT states, respectively. Note that the energetic disorders of each species have been omitted for simplicity.

As for the implications on the V_{OC}, equilibrium between excitons in the acceptor and CT states has been linked to low non-radiative losses in NFA-based devices due to the repopulation of excitons, which have a much higher radiative efficiency than CT states (i.e., the radiative rate constant for

CT states is orders of magnitude lower than the radiative decay constant of the singlet states). As such, it has been suggested that the luminescence properties of the pristine low bandgap material in OSCs define the limit of $\Delta V_{\mathrm{OC,nrad}}$.[151] On a side note, the S_1-CT states interplay can also lead to a hybridization effect related to the electronic coupling between the two states that benefits slightly the radiative efficiency of CT states through oscillator strength borrowing from S_1.[152–154] The impact of re-occupation of singlet excitons becomes evident in the EL spectra of low energy offset blends, where the intensity of the S_1 emission increases, or even dominates masking any contribution from CT states.[31] In such blends, the radiative recombination of free charges may be determined by the S_1 emission properties.[155] However, it is still under debate at which conditions the emission efficiency of the singlet benefits the V_{OC} of the device. Even if the S_1 state dominates the radiative emission, this does not necessarily indicate that free charge recombination occurs predominantly through this state. For instance, the population of singlet excitons from free carrier recombination is a thermal process which can be hindered by a significant barrier depending on the respective energy levels. In this regard, the results in Chapter 7 demonstrate for the model PM6:Y6 solar cell that more than 90% of the radiative decay proceeds through the Y6 S_1 state, but that ~99% of the total recombination is via the CT state, which inevitably has a much lower radiative efficiency. Consequently, the emissive decay of the much less populated singlet state does not help the V_{OC} of this blend.

Chapter 3. Methods

This chapter describes the main experimental setups and methods employed in this thesis. Firstly, the materials used and the procedure to fabricate samples are outlined. A broad range of techniques have been applied to layers of organic semiconductors and organic solar cells as part of this work. Here, we will reveal in detail the main techniques based on setups available at the University of Potsdam. In addition, the Appendix contains the technical details of other setups.

3.1. Materials and Device Preparation

As discussed in the previous chapter, organic solar cells (OSCs) consist of a blend of donor and acceptor materials. In this thesis, p-type polymers were used as the donor molecule and n-type small molecules as the acceptor, which can be a fullerene or non-fullerene acceptors (NFAs). Figure 3.1 displays the organic semiconductors employed in the active layer of our solar cells. The polymers PM6, also known as PBDB-T-2F, and PTB7 ($\overline{M}_w$ = 97.5 kDa, Đ = 2.1) were purchased from 1-Material Inc. FTAZ, M_n~60 kDa, Đ~1.9, was synthesized in the group of Prof. Wei You in the University of North Carolina according to literature.[156] As fullerene acceptor, we employed $PC_{70}BM$ from Solenne. The main NFA molecule studied in this work is Y6, which was synthesized by Prof. Yingping Zou,[29] and purchased from 1-Material Inc. The N4 molecule is a Y-derivative, as the core of the molecule is based on Y6. N4 was synthesized in the group of Prof. Yingping Zou according to literature.[42] Finally, we employed IDIC as a fused-ring electron acceptor, synthesized by the group of Prof. Zhan in the Peking University.[157] See the List of Abbreviations and Symbols for the full name of the materials.

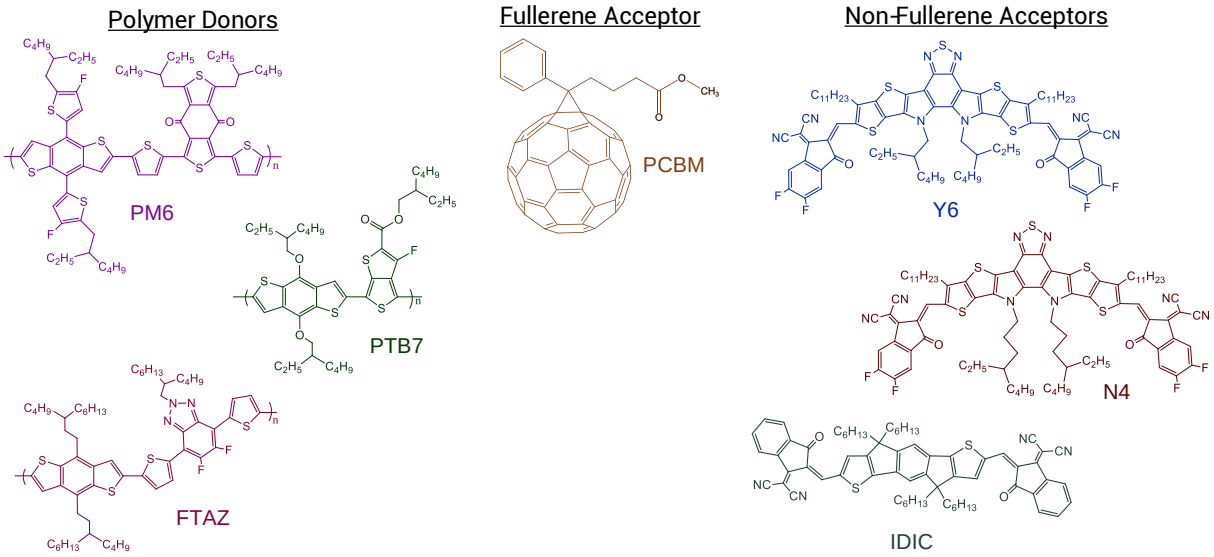

Figure 3.1: Chemical structures of the donor polymers and acceptor small molecules used in this thesis.

The typical structure of organic solar cells prepared in lab research consists of the active layer sandwiched between two selective transport layers and two metal electrodes. The transport layers can also be organic materials. Often, the devices can be prepared in a regular or inverted architecture depending on the stack. In the regular structure, the holes are extracted to the bottom electrode (anode), while in the inverted structure electrons are extracted to the bottom electrode (cathode). In both architectures, the cell is illuminated from the bottom. Figure 3.2 presents the

materials employed in the regular and inverted devices used in this thesis. We used indium tin oxide (ITO) as the transparent conducting bottom electrode and thermally evaporated silver (Ag) as the top contact. In the regular structure (Figure 3.2a), the highly doped polymer PEDOT:PSS (poly(3,4-ethylenedioxythiophene):poly(styrenesulfonate)) is spin coated on ITO to obtain a 40 nm hole transport layer (HTL). For the electron transport layer (ETL), an alcohol soluble organic material was used, namely PDINO, which can be spin coated directly on top of the active layer to obtain a very thin layer (5 to 10 nm). In the inverted structure (Figure 3.2b), zinc oxide (ZnO) nanoparticles were spin coated onto ITO to a thickness of 40 nm to obtain the ETL and 8 to 10 nm of molybdenum oxide (MoO_3) were thermally evaporated as the HTL. The active layer is the blend of polymers and small molecules in Figure 3.1. The blends studied were PM6:Y6, PTB7:PCBM, FTAZ:IDIC and PM6:N4. The optimized blend weight ratios and processing conditions were chosen according to the literature. For the PM6:Y6 blends, the materials were dissolved in chloroform ($CHCl_3$) to a total concentration of 16 $mgmL^{-1}$ with a 1 to 1.2 weight ratio, and chloronaphthalene was added as additive to chosen samples to better control the morphology properties of the blend (0.5 %v/v, CN/ $CHCl_3$). Further details for the preparation of all blend devices can be found in the Appendix.

Finally, the active area of the devices was defined by the overlap of patterned ITO with the metal electrodes evaporated through a shadow mask (see Figure 3.2c). The substrates were purchased from Lumtec to obtain six pixels with different areas. Lumtec sputters ITO through high-precision laser cut shadow masks on glass with a sheet resistance of 15 Ω/sq. Pixels with a small area of 1.1 mm^2 are used for transient experiments, such as charge extractions methods, because a low RC-time is required, as was discussed in detail in the PhD thesis of Juliane Kniepert.[158]

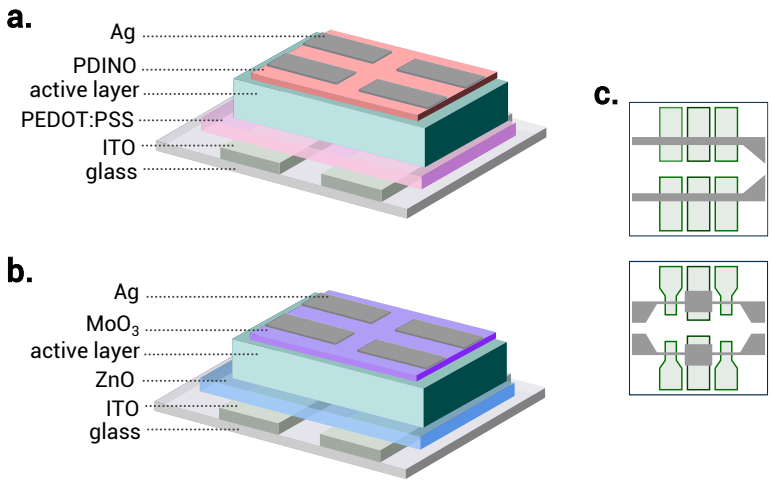

Figure 3.2: Scheme of the layer stack in organic solar cells. a Device architecture of a regular organic solar cell with the materials used in this thesis. The device is illuminated from the bottom electrode, the anode. **b** Device architecture of an inverted organic solar cell with the materials used in this thesis. The device is illuminated from the bottom electrode, the cathode. **c** Structured ITO (light green) with different pixel areas defined by the overlap with the electrodes evaporated through a shadow mask (grey), giving 6 pixels in total. Top: optimized pixel area of 6 mm^2 for device characterization. Bottom: small pixel area of 1.1 mm^2 for charge extraction (transient) measurements. The pixels in the center have a larger area of 16 mm^2.

3.2. Optical Characterization

The characterization of optical properties of the organic materials used in this work comprises absorbance and photoluminescence. Absorbance was measured in solution and solid films and photoluminescence was measured in solid films and solar cell devices. The absorbance was measured with a Varian Cary 5000 spectrophotometer in transmission and reflection mode using an integrating sphere. The optical density (OD) of the sample was then calculated as $\mathrm{OD} = \log\left(\frac{100-\%R}{\%T}\right)$, where $\%R$ and $\%T$ are the reflectance and transmittance spectra of the film in percentage, respectively.

The photoluminescence (PL) emission spectra were recorded with an Andor Solis SR393i-B spectrograph with a silicon DU420A-BR-DD detector and an Indium Gallium Arsenide DU491A-1.7 detector. A calibrated Oriel 63355 lamp was used to correct the spectral response. PL spectra were recorded with different gratings with center wavelengths of 800, 1100, and 1400 nm, and merged afterwards. The samples were excited with steady-state illumination using a 520 nm continuous wave (CW) laser (Insaneware). Illumination from the laser was perpendicular to the sample, which was tilted 20° in reference to the lenses that focus the emission onto the spectrograph. When measuring the PL spectra of solar cells, the measured pixel was masked to ensure that the exciting light only illuminated the active layer of our devices. Lastly, to perform bias dependent photoluminescence measurements, the device was hold at a constant voltage, using a Keithley 2400, for 1s. At short circuit, the voltage applied was 0 V and this measurement was the reference for the illumination condition equivalent to 1 sun. At open circuit, 0 A were applied, and the voltage was recorded.

The photoluminescence quantum yield (PLQY) of thin films can be calculated if the absolute PL emission is recorded. To achieve this, the same laser as above was used but the excitation was through an optical fiber into an integrating sphere. The intensity of the laser was adjusted to a 1 sun equivalent by illuminating a PM6:Y6 solar cell under short-circuit and matching the current density to the J_{SC} in the sun simulator. A second optical fiber was used from the output of the integrating sphere to the Andor Solis SR393i-B spectrograph. The spectral photon density was obtained from the corrected detector signal (spectral irradiance) by division through the photon energy ($h\nu$), and the photon numbers of the excitation and emission were calculated from the numerical integration, using a Matlab code. More details on the setup and the analysis of data can be found in the PhD thesis of Pietro Caprioglio.[159] Absolute PL measurements were performed on blends and also neat layers of the acceptor. The neat acceptor was also blended with the inert polymer polystyrene (PS) to obtain the PLQY of the neat material in a polymer matrix (of 0.7%). This was done because film formation is similar as in the blend with a donor polymer (solution viscosity, drying kinetics). Related to this, the formation of large NFA crystallites may be inhibited in presence of the inert polymer matrix (similar as in the blend with the donor polymer). Also, the optical density and with this reabsorption effects are similar. Finally, we took great care to avoid that the measured PLQY values with the integrating sphere were influenced by waveguided light that is outcoupled through the sides of the substrate, thus accordingly we taped the four sides of our glass substrates with black tape.

3.3. Device Characterization

3.3.1. Current Voltage Characteristics

The performance of a solar cell can be characterized by measuring the current density versus applied voltage (*J-V* characteristics), which allows to calculate the power conversion efficiency (see section 2.2.1). *J-V* curves were measured using a Keithley 2400 system in a 2-wire source configuration. Simulated AM1.5G irradiation at 100 mWcm^{-2} was provided by a filtered Oriel Class AAA Xenon lamp and the intensity was monitored simultaneously with a Si photodiode. The sun simulator is calibrated with a KG5 filtered silicon solar cell (certified by Fraunhofer ISE).

3.3.2. Photovoltaic External Quantum Efficiency

The photovoltaic external quantum efficiency ($\mathrm{EQE_{PV}}$) of a solar cell gives information on the number of extracted carriers per incident photon (Equation 2.1, section 2.2.), which is why this technique is also known as incident-photon-to-current-efficiency (IPCE). To measure the $\mathrm{EQE_{PV}}$ in our setup at the University of Potsdam, light from a broadband source (a Phillips 300 W Halogen lamp) was chopped (ThorLabs MC2000), guided through a cornerstone Monochromator and coupled into an optical quartz fiber, calibrated with Newport Photodiodes (818-UV and 818-IR), which illuminates the device. The modulated signal is lock-in amplified in a SR 830 Lock-In Amplifier which also measures the response of the solar cell.

For selected solar cells, sensitive $\mathrm{EQE_{PV}}$ was measured at the group of Ardalan Armin in the University of Swansea. The setup allows to measure $\mathrm{EQE_{PV}}$ over 8 orders of magnitude. A detailed description of the EQE apparatus is provided elsewhere.[160]

3.3.3. Electroluminescence Quantum Yield

The measurement of $\mathrm{EQE_{PV}}$ combined with the electroluminescence quantum yield (ELQY) allows to analyze the voltage losses in a solar cell (see section 2.5.1). To calculate the ELQY, the electroluminescence (EL) spectrum must be measured first. For EL measurements, the device was hold at a constant voltage, using a Keithley 2400, for 1 s. The emission spectra were recorded with an Andor Solis SR393i-B spectrograph with a silicon DU420A-BR-DD detector and an Indium Gallium Arsenide DU491A-1.7 detector (same setup as for PL spectra, see above).

For absolute EL measurements, a calibrated Si photodetector (Newport) connected to a Keithley 485 picoampere meter were used. The detector, with an active area of ~2 cm^2, was placed in front of the measured pixel with a distance <0.5 cm (as close as possible). The total photon flux was evaluated by convoluting the normalized emission spectrum of the device and the external quantum efficiency of the detector, which gives a scaling factor f. The injected current was monitored with a Keithley 2400. Thereby, the ELQY was calculated as $\mathrm{ELQY} = f\frac{J_{\mathrm{photo}}}{J_{\mathrm{inj}}}$.

3.3.4. Intensity Dependent Photocurrent

Steady-state intensity dependent photocurrent (IPC) measurements were obtained with a 445 nm continuous wave laser (Insaneware). Two continuously variable neutral density filterwheels (ThorLabs) were used to attenuate the laser power. The photocurrent was recorded with a Keithley 2400 source measure unit. In an IPC experiment, the sample is kept at a constant (forward) bias and the steady-state photocurrent $J_{\mathrm{ph}} = J_{\mathrm{L}} - J_{\mathrm{D}}$, i.e., the current under illumination (J_{L}) corrected for the stabilized dark current (J_{D}), is recorded for increasing illumination intensity. Steady-state

conditions were assured by recording the temporal evolution of the photocurrent. To quantify the recombination losses under conditions close 1 sun illumination, we defined the 1 sun equivalent laser power where the solar cell current output matches the J_{SC} under AM1.5G irradiation. To better analyze the recombination losses, we obtain the EQE from the ratio of the photocurrent and the illumination intensity and plot it versus equivalent suns. While first order losses cause an overall intensity independent decrease of the EQE with increasing bias, higher order (≥ 2) recombination results in a downward bend of the EQE with increasing intensity.

3.4. Charge Extraction Methods

Charge extraction methods are applied to determine the charge carrier density in thin film solar cells. In this thesis, the two charge extraction methods employed are time-delayed collection field (TDCF) and bias-assisted charge extraction (BACE). On the one hand, TDCF measurements give information on the efficiency of free charge generation as a function of electric field and on the nongeminate recombination dynamics. On the other hand, BACE is commonly employed to draw conclusions about the order and coefficient of nongeminate charge recombination at steady-state conditions.

TDCF-generation utilizes a short laser pulse (~5 ns) excitation while the device is held at a given prebias V_{pre}, which is commonly swept from high reverse to V_{OC}. After a delay time (t_{del}) of 6 ns (i.e. only 1 ns after the laser pulse), charges are collected by applying a high reverse bias (V_{coll}). The nanosecond time scale corresponds to the generation of free electrons and holes and the geminate recombination regime (see Ref.[65]). To ensure that nongeminate losses are insignificant during extraction, we applied a large V_{coll} of -2.5V and we chose a low laser intensity where the extracted charge is proportional to the laser fluence (in the linear regime). In this case, the total extracted charge is a direct measure of the efficiency of free charge generation under the chosen conditions, e.g., electric field and excitation energy.

For recombination studies, the basics of TDCF and BACE are briefly introduced since Chapter 5 will discuss in detail how the data obtained from these methods is analyzed. Therefore, we focus on this section on the measurement scheme and setup (Figure 3.3). In TDCF, charge carriers are once again generated with a short (nanosecond) laser pulse and subsequently extracted with V_{coll}. In this case, though, the device is held at a given V_{pre} close to the maximum power point and t_{del} is varied. During the delay between the laser pulse and extraction, recombination takes place. The extracted charge is divided into photogenerated carriers extracted during the delay (Q_{del}) and the carriers remaining in the device which are collected after t_{del} (Q_{coll}). The total charge $Q_{tot} = Q_{pre} + Q_{coll}$ corresponds to free charges that survived nongeminate recombination. Therefore, the analysis of Q_{tot} over time describes the recombination of charges (see Chapter 5). In our TDCF setup, the short ns-laser pulse comes from a diode pumped, Q-switched Nd:YAG laser (NT242, EKSPLA) with ~5 ns pulse duration at a typical repetition rate of 500 Hz, which provides stable excitation with wavelengths in the range of 410 nm to 690 nm and 800 nm to 2000 nm. To compensate for the internal latency of the pulse generator, the laser pulse was delayed and homogeneously scattered in an 85 m long silica fiber (LEONI), see Figure 3.3c. V_{pre} and V_{coll} were set by an Agilent 81150A pulse generator through a home-built amplifier attached to the sample holder (the PhD thesis of Jona Kurpiers[161] contains more information on these components). The function generation was triggered by a fast photodiode (EOT, ET-2030TTL). The current flowing through the device was measured via a 10 Ω resistor in series with the sample and recorded with an oscilloscope (Agilent DSO9104H). Great care was taken to avoid free carrier recombination prior to extraction. Therefore, a fast ramp-up (~2.5 ns) of the bias was applied.

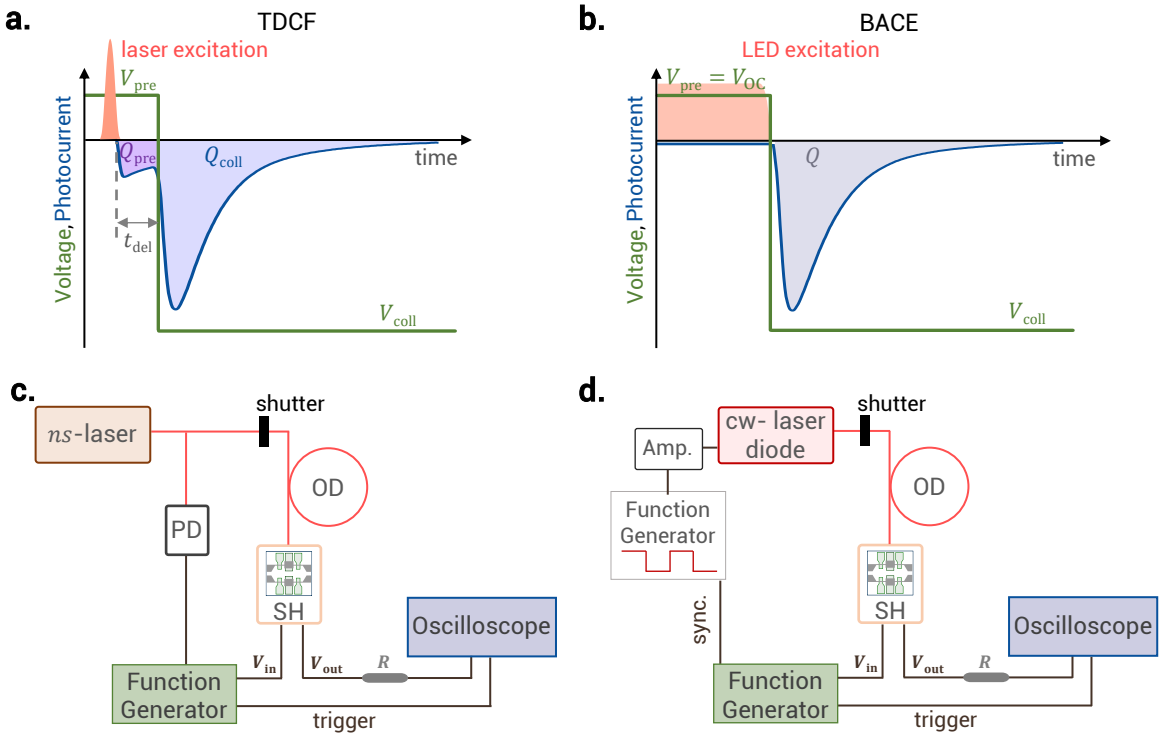

Figure 3.3: Measurement scheme and setup of the charge extraction methods TDCF and BACE. a Scheme of the TDCF measurement as a function of time. At $t = 0$, the sample is excited by a short laser pulse while the solar cell is held at a constant prebias V_{pre}. At $t = t_{del}$, a rectangular voltage pulse, V_{coll}, is applied to collect the photogenerated charge carriers. The recorded photocurrent transient is marked by the blue line. **b** Scheme of the BACE measurement as a function of time. The solar cell is at constant illumination with a laser diode and held at a prebias $V_{pre} = V_{OC}$ to establish steady-state conditions. When switching off the laser, V_{coll} is applied to collect the charge carriers present in the device under illumination. The recorded photocurrent transient is marked by the blue line. **c** Instrumental setup for TDCF. The ns-laser pulse is split into two beams. The main beam is homogenized and delayed in an optical fiber (OD) and directed to the sample holder (SH). The second beam excites a fast photodiode which triggers the function generator responsible for applying V_{pre} and V_{coll}. The current flowing through the solar cell is recorded with an oscilloscope. **d** Instrumental setup for BACE. A continuous wave laser diode is used to establish steady-state conditions. The diode is operated by a function generator which is synchronized with the function generator responsible for applying V_{pre} and V_{coll}. The laser excitation is also homogenized and delayed in an optical fiber (OD) and directed to the sample holder (SH). The current transient is recorded with an oscilloscope.

The experimental setup of BACE is similar to that of TDCF, except for the illumination conditions. BACE measures the steady-state charge carrier density in a solar cell at open-circuit conditions. Thereby, the prebias corresponds to the V_{OC} at each given intensity. When switching off the laser, V_{coll} is applied to collect the charge carriers present in the device. The carrier density at different illumination intensities is related to the generation rate, which at V_{OC} equals the recombination rate, revealing the dominant recombination order and coefficient (see Chapter 5). To establish steady-state conditions, we used a high power 1 W, 445 nm or 638 nm laser diode (Insaneware) with a switch-off time of ~10 ns. The laser diode was operated at 500 Hz with a duty cycle of 50%, such that illumination lasted 1 ms and the diode was switched off for also 1 ms. Right after switching-off the laser, V_{coll} was applied to the sample by the same fast pulse generator (Agilent 81150A) as in TDCF measurements, allowing a fast extraction time of 10-20 ns. The current transients were measured via a 10 Ω resistor in series with the sample and recorded with an oscilloscope (Agilent DSO9104H).

3.5. Photoinduced Absorption Spectroscopy

Quasi-steady-state photoinduced absorption (PIA) spectroscopy is used to probe recombination processes of charge carriers in organic solar cells and thin films. PIA is a very useful technique as it allows to monitor the yield of and dynamics of free carriers without the requirement of charge extraction.[134, 162] The measurement setup and software for automatic control were developed in the University of Potsdam by Dr. Le Quang Phuong from the group of Prof. Safa Shoaee.

PIA relies on the measurement of the differential transmission of thin films, or solar cells at open-circuit and short-circuit conditions. Therefore, semi-transparent devices were required. As shown in Figure 3.4, the pump beam emitting from a 405 nm CW laser diode was modulated a by an optical chopper (Thorlabs MC2000B) at a frequency tunable in a range from 200 Hz to 10 kHz, and then focused on the pixel of the solar cell. The excitation fluence was adjusted by a programmable attenuator. The white light emitted from a tungsten halogen lamp is optically directed into a monochromator (Spectral Products DK240), and the exiting monochromatic light is used as the probe beam. Thereby, the probe beam is focused onto the studied device, which is held at open circuit, to overlap with the photoexcitation light. The change in the transmitted probe light ΔT induced by the photoexcitation is recorded by a Si or InGaAs photodiode and a lock-in amplifier (SR830) referenced at the modulation frequency of the pump beam (step 2 in Figure 3.4). The PIA signal was corrected by subtracting the photoluminescence background (step 3). The transmitted probe light T through the unexcited sample is measured using another optical chopper (Thorlabs MC2000B) to modulate the probe light (step 1). The photocurrent was simultaneously measured with the PIA signal at short circuit. Moreover, electromodulation injection absorption (EMIA) was measured with the same setup upon modulated dark injection. In this case, a square voltage with a frequency fixed at 370 Hz and a tunable amplitude, which is provided by a function generator (Keysight 33210A), was applied to the device.

The outcome of PIA measurements is initially $-\Delta T/T$ as a function of probe energy (see Figure 3.5a). Phuong et al. identified the broad PIA bands in blends of the polymer PM6 with different acceptors.[134] As a result, the authors could assign the PIA band at ~1.25 eV to the absorption of free holes in PM6. This PIA signal yields the charge carrier density in the device at open-circuit conditions, p_{OC}, by applying the expression: $\frac{\Delta T}{T} = p_{\mathrm{OC}}\sigma d$, where σ is the absorption cross section of the free carriers and can be determined by combining PIA with another method such as BACE or capacitance-voltage measurements, and d is the active layer thickness. In addition, the in-phase and out-of-phase components of the PIA signal (e.g. at 1.25 eV) can be measured as a function of the modulation frequency to quantify the lifetime of charge carriers (Figure 3.5b). The Cole-Cole model,[162] is then used to perform global fits for each frequency-dependent PIA data set according to

$$n(\omega) = \frac{g\tau}{1 + (\mathrm{i}\omega\tau)^{\alpha}}, \qquad (3.1)$$

where n is the charge carrier density, g is the photogeneration rate, τ is the average lifetime of the charge carriers, and α is a parameter ranging from 0 to 1 which reflects the dispersive nature of the recombination process. Finally, the lifetime τ is plotted as a function of charge carrier density. If the lifetime follows the power law dependence on the carrier density $\tau \propto 1/n$, it can be concluded that the recombination process in the blend is bimolecular in nature and the bimolecular recombination can be calculated as $k_2 = \frac{1}{\tau n}$.

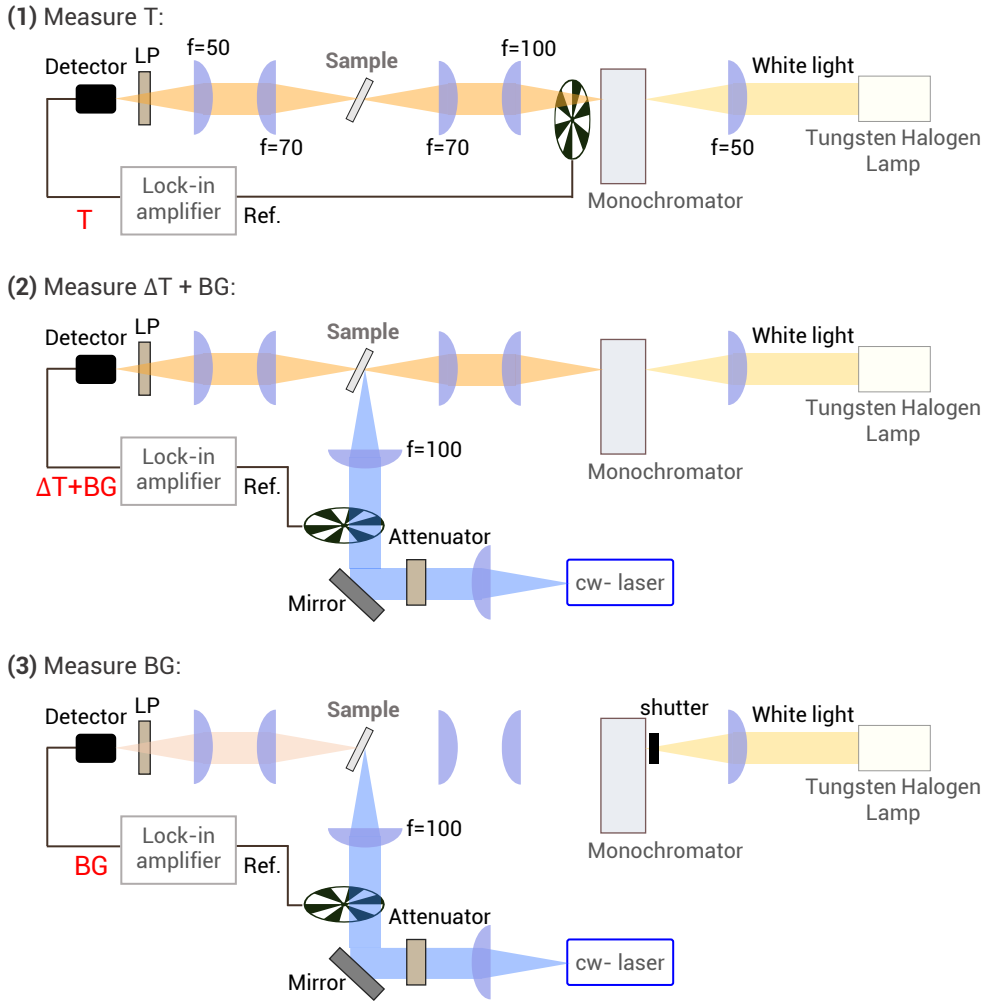

Figure 3.4: Measurement setup of photoinduced absorption spectroscopy. To obtain the PIA signal of a semi-transparent solar cell three steps are followed in the measurement. (1) The white light emitted from a tungsten halogen lamp is optically directed into a monochromator and the monochromatic light exiting is used as the probe beam and focused on the sample. After modulation of the probe light, the transmitted light $\mathbf{T}$ through the unexcited sample is recorded with a Si photodiode and lock-in amplifier. (2) The pump beam emitting from a continuous wave (cw) laser diode was modulated by an optical chopper and focused on the sample. The excitation fluence is adjusted by an attenuator. The monochromatic light is used as the probe beam, and focused on the sample as well, which is held at open circuit, to overlap with the photoexcitation light. The change in the transmitted probe light $\Delta\mathbf{T}$ induced by the photoexcitation is recorded by a Si photodiode and a lock-in amplifier. (3) The PIA signal is corrected by subtracting the photoluminescence background. Finally, the PIA signal is obtained as $\frac{\Delta T}{T} = \frac{(\Delta T + PL_{BG}) - PL_{BG}}{T}$. The variables are defined in the main text.

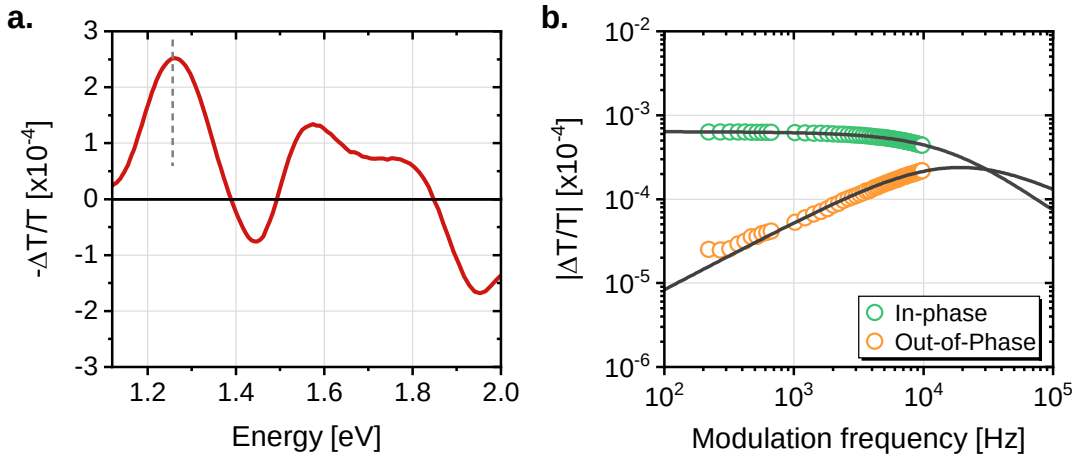

Figure 3.5: Measurement data obtainable via photoinduced absorption spectroscopy. a PIA spectrum as a function of probe energy measured at open circuit. This is the example of a semi-transparent PM6:Y6 device with the PIA band at 1.25 eV corresponding to free holes in PM6. **b** The in-phase and out-of-phase components of the PIA band under illumination equivalent to 1 sun at open-circuit conditions as a function of modulation frequency. The solid curves show the global fitting using Equation 3.1, which yields the average lifetime of the charge carriers in the device.

3.6. Drift-diffusion Simulations

In this thesis, numerical simulations have been used to complement and support the experimental results. Therefore, two types of drift-diffusion simulations were performed: steady-state device simulations and transient simulations. Simulations of the carrier densities under steady-state illumination and in the dark were performed with a code developed by Prof. Jan Anton Koster (described in Ref.[163]). Steady-state simulations were also implemented with the open-source software SCAPS. The program has been developed by the Department of Electronics and Information Systems (ELIS) of the University of Gent and is available upon request to the developers Burgelman et al.[164] This device simulation tool was also utilized to simulate the *J-V* characteristics with experimentally determined parameters. On the other hand, transient drift-diffusion simulations were applied to obtain kinetic TDCF simulations. The tool for this simulation is found in Refs.[131, 165], and the scheme to simulate TDCF is described in detail in Chapter 5.

In the following, this section briefly introduces the basic equations to be solved in 1D drift-diffusion simulations. That is, the Poisson equation:

$$\frac{\partial^2}{\partial x^2}\Phi(x) = \frac{q}{\varepsilon\varepsilon_0}[n(x) - p(x)], \qquad (3.2)$$

which relates the electrostatic potential $\Phi(x)$ to the electron and hole densities $n(x)$ and $p(x)$, respectively, and the continuity equations:

$$\frac{\partial n}{\partial t} = U(x) + \frac{1}{q}\frac{\partial J_n}{\partial x}, \qquad \frac{\partial p}{\partial t} = U(x) - \frac{1}{q}\frac{\partial J_p}{\partial x} \qquad (3.3)$$

where $J_{n(p)}$ is the electron (hole) current density and $U(x)$ is the net generation rate i.e., the difference between generation and recombination of free charge carriers. Only one spatial dimension is considered. The scheme used to solve these equations is based on the work by Gummel.[166] First, a guess is made for the potential and the carrier densities from which a

correction $\delta\psi$ is calculated (Equation 3.2). The new potential is then used to calculate the carrier density with the continuity equations (Equation 3.3). This process is iterated until convergence is reached.

In the simulations, two loss processes are considered: bimolecular recombination and surface recombination. To account for surface recombination, an estimate of the (finite) surface recombination velocity can be used, or it can be assumed that the minority carrier densities at the contacts are equal to their equilibrium values which is equivalent to infinite surface recombination (see Ref.[135]).

Chapter 4. Barrierless Free Charge Generation in the High-Performance PM6:Y6 Bulk Heterojunction Non-Fullerene Solar Cell

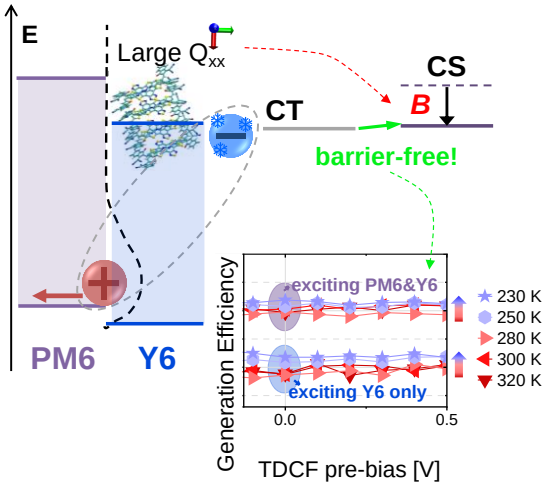

This chapter presents our initial investigations of the generation and recombination of free carriers to understand the superior efficiency of photocurrent generation in the non-fullerene PM6:Y6 blend. By applying a combination of field- and temperature-dependent optoelectronic measurements, we found that free charge generation is barrierless, despite a small driving force. Theoretical modelling suggests the existence of a large electrostatic interfacial field, which repels charges from the donor-acceptor interface. This leaves free charge recombination as the main loss process in these devices.

This chapter is an adapted preprint of:

L. Perdigón-Toro, H. Zhang, A. Markina, J. Yuan, S. M. Hosseini, C. M. Wolff, G. Zuo, M. Stolterfoht, Y. Zou, F. Gao, D. Andrienko, S. Shoaee, and D. Neher. Barrierless Free Charge Generation in the High-Performance PM6:Y6 Bulk Heterojunction Non-Fullerene Solar Cell. *Adv. Mater.* **2020**, 32, 1906763.

4.1. Abstract

Organic solar cells (OSCs) are currently experiencing a second golden age thanks to the development of novel non-fullerene acceptors (NFAs). Surprisingly, some of these blends exhibit high efficiencies despite a low energy offset at the heterojunction. Herein, we thoroughly investigate free charge generation in the high-performance blend of the donor polymer PM6 with the NFA Y6 as a function of field, temperature and excitation energy. Results show that generation is essentially barrierless with near-unity efficiency, regardless of excitation energy. Efficient generation is maintained over a wide temperature range, down to 100 K, despite the small driving force for charge generation. Studies on a blend with a low concentration of the NFA, measurements of the energetic disorder, and theoretical modelling suggest that charge generation is assisted by the electrostatic interfacial field which for Y6 is large enough to compensate the Coulomb dissociation barrier.

4.2. Introduction

Organic solar cells (OSCs) have gained renewed interest with the emergence of non-fullerene acceptors (NFAs). NFA-based blends benefit from a strong and red-shifted absorption of the acceptor (A), complementary to the donor (D) absorption range, and small ionization energy offsets at the DA heterojunction. As a direct consequence, short-circuit currents (J_{SC}) over 25 mAcm^{-2} and open circuit voltages (V_{OC}) above 0.8 V have been reported for different NFA blends.[29, 41, 167, 168] Notably, high J_{SC} values have been shown for NFA-based blends with moderate driving forces at the donor-acceptor heterojunction.[29, 167, 169] Low driving forces go along with reduced voltage losses, slightly above 0.5 V.[31, 141, 170, 171] These new attributes and the remarkable efficiencies ask for a detailed analysis of the pathways of free charge generation.

As introduced in Chapter 2 (section 2.2.), photoexcitation creates strongly bound excitons in organic semiconductors because of their low dielectric constant. Therefore, photocurrent generation in OSCs comprises two steps. The first is charge generation, where a photogenerated exciton diffuses to the DA interface to form an interfacial charge transfer (CT) state. This is followed by the second step, the dissociation of the CT into free carriers.[172] In the framework of Marcus theory, the efficiency of the first step, CT formation via interfacial charge transfer, is related to the so-called driving force for charge generation, $\Delta E_{\mathrm{S_1-CT}}$, which is the difference in energy of the intramolecular singlet ($\mathrm{S_1}$) excited state on the donor or acceptor and the CT state.[61, 173] Various recent publications deal with the efficiency and dynamics of charge generation in NFA blends, revealing efficient interfacial charge transfer also for small $\Delta E_{\mathrm{S_1-CT}}$.[31, 84, 174] Efficient charge generation has been rationalized by for example favorable microelectrostatics.[175] In contrast, information on the dominant pathway and efficiency of the dissociation of the CT state to the fully charge-separated (CS) state is rare for NFA-based blends. For homogeneous media, theory predicts a CT binding energy of around 400 meV,[176] in clear contrast to the high external quantum efficiency (EQE) for photocurrent generation of many NFA-containing devices. Several studies showed high EQE to be related to a larger driving force.[79–81, 84] This situation reminds of the “hot” dissociation model, where exciton dissociation creates a more loosely bound electronically/vibronically excited CT state.[177, 178] A popular method to address this issue is to measure the photocurrent response as function of excitation energy, comprising the spectral range which only excites low lying CT states. Interestingly, measurements on fullerene-based blends gave evidence for a cold dissociation pathway, which involves an equilibrated CT state manifold.[63, 179] An elegant approach to study the binding of the involved

CT state is to measure the temperature dependence of CT dissociation. Notably, the activation energy for CT dissociation is unaffected by entropic effects.[72] Temperature studies on fullerene-based blends revealed activation energies for CT dissociation ranging mostly between few tens to ca. 100 meV,[65, 72, 180–182] with some important exemptions as discussed below. We are aware of only one publication reporting temperature dependent measurements on the CT binding in a NFA blend.[183] Here, pump-push photocurrent spectroscopy (PPPc) was applied to a blend of the donor PffT4T with the NFA EH-IDTBR, suggesting a CT binding energy of 100 meV. This blend exhibits very small LUMO and HOMO offsets at the DA heterojunction of only 0.21 and 0.24 eV, respectively, suggesting a small (or even negligible) ΔE_{S_1-CT}. As detailed in Chapter 2 (section 2.3.1) the value of ΔE_{S_1-CT} primarily dictates the efficiency of charge generation but is also expected to affect the dissociation of the formed CT state. For example, increasing the CT state energy will go along with the suppression of vibronic coupling to the ground state, thereby reducing the non-radiative CT decay rate as the competing process to CT dissociation.[146, 153] In agreement to this, recent work on low donor content blends revealed a power-law dependence of the CT dissociation efficiency on the energy of the lowest CT state.[184] We, therefore, expect that in NFA-based blends, the benefit of a smaller energy driving force and higher lying CT state manifold is not only an increased V_{OC} but also a more efficient CT dissociation, due to slower geminate recombination. However, when the CT approaches the S_1, electronic coupling may result in the formation of hybridized states with mixed exciton-CT character.[173, 185] Following this rational, recent work predicted a stronger binding and faster geminate recombination of such mixed states to the ground state, thereby reducing the efficiency of CT dissociation.[153, 186, 187]

In this chapter, we perform a comprehensive study of free charge generation and of non-geminate losses in a state-of-the-art NFA blend with a low driving force, using a combination of temperature dependent time-delayed collection field (TDCF), EQE and V_{OC} measurements. Our system of choice is the wide band gap polymer PM6 and the small molecule Y6 (see List of Abbreviations and Symbols for the complete names). The chemical structures are shown in Figure 4.1a. PM6:Y6 devices have been reported to exhibit a power conversion efficiency (PCE) of up to 15.7% despite a relatively low ionization energy offset for hole transfer (see Figure 4.1a).[29] Given the broad absorption spectrum and the large difference of the S_1 energies of the donor and acceptor, the PM6:Y6 blend is a relevant system for the study of free charge generation in relation to excess energy and driving force. Our experiments show that the efficiency of free charge generation is independent of the electric field regardless of whether the donor, the acceptor, or states in the tail of the blend absorption are excited. Temperature dependent optoelectronic studies reveal nearly barrierless free charge formation. Our experimental findings are consistent with theoretical modeling which reveals an electrostatic interfacial field which for Y6 is large enough to compensate the Coulomb dissociation barrier.

4.3. Photovoltaic Characterization and Field Dependence of Charge Generation

All our studies were performed on optimized PM6:Y6 (1:1.2, w/w) blends in an inverted solar cell geometry (see Note A1.1, Appendix A1, for the preparation details), given the superior stability of this device architecture under prolonged pulsed laser illumination. Table A1.1 (Appendix A1) contains the averaged photovoltaic parameters of devices prepared in this work. Our devices exhibit a PCE of 13.7%, which is ca. 10% smaller than the PCE of 15.3% as reported by Yuan et al. for the as-cast blend in conventional architecture.[29] Inspection of the photovoltaic (PV) parameters shows that the difference originates mainly from a lower J_{SC} (22.4 mAcm^{-2} in our as-cast 100 nm inverted devices versus 24.3 mAcm^{-2} in 150 nm regular devices), while differences in the fill factor (FF) and V_{OC} are minor. This suggests that our cells suffer mainly from a less

efficient photon absorption and/or exciton harvesting, while all other processes are virtually the same as in the blend reported by Yuan et al. Remarkably, we were able to upscale the devices to an active area of 1 cm2 with only ~2% losses in FF (see Figure A1.1 for the PV parameters and Figure A1.2, Appendix A1, for the current density-voltage (*J-V*) characteristics of a 1.0229 cm^2 area certified cell). This cell delivered a PCE of 13.45% - the highest certified value reported at the time of publication for a >1 cm^2 single junction OSC device.

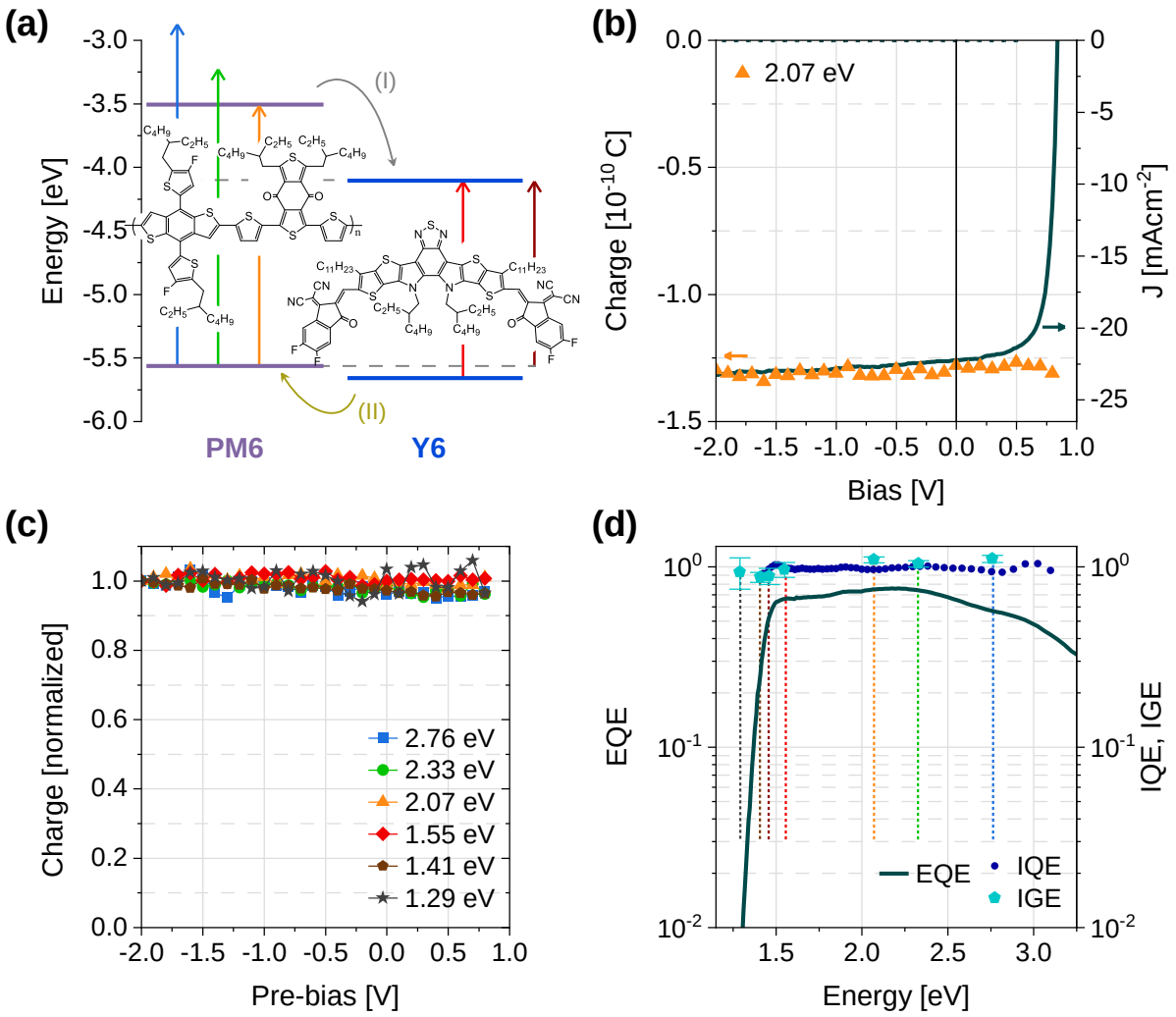

Figure 4.1: Photovoltaic characterization and field-dependence of charge generation in PM6:Y6 solar cells. a Chemical structure of PM6 and Y6 and energy levels measured by cyclic voltammetry, taken from ref.[29] The curved arrows indicate the pathways for charge generation via electron transfer (channel I) or hole transfer (channel II), respectively. **b** Bias-dependent free charge generation (symbols, left axis) for an inverted PM6:Y6 device measured by TDCF for an excitation of 2.07 eV with a low fluence of 0.05 μJcm^{-2} and V_{coll} =2.5 V. For comparison, the current density-voltage characteristics of the device under simulated AM1.5G light are also shown (solid lines, right axis). **c** Total charge Q as a function of prebias (V_{pre}) normalized to the value at −2V for energies corresponding primarily to PM6 excitation (2.76 eV, 2.33 eV and 2.07 eV), Y6 excitation (1.55 eV and 1.41 eV) and CT state excitation (1.29 eV). **d** EQE (left axis) experimentally measured for a PM6:Y6 device and IQE and IGE as optically modelled from EQE and TDCF results, respectively.

Figure 4.1a shows the energy diagram as derived from cyclovoltametric measurements on films of neat materials in ref.[29] (see Note A1.2 Appendix A1). As a consequence of the small IE offset of only 0.09 eV, we expect a small driving force ΔE_{S_1-CT}. Figure A1.3 (Appendix A1) shows the comparison of the sensitive external quantum efficiency ($\mathrm{EQE_{PV}}$) of the pristine NFA and the blend where we indeed observe very little difference between the spectra. However, the electroluminescence (EL) spectrum of PM6:Y6 displays low energy features which could indicate the presence of CT state emission (see Figure A1.4, Appendix A1). To determine the CT energy, we fitted the reduced $\mathrm{EQE_{PV}}$ and EL spectra following the approach by Vandewal et al.[188] The resulting E_{CT} = 1.41 eV is consistent with the value taken from the maximum of the derivative of the $\mathrm{EQE_{PV}}$ curve,[147] as also shown in Figure A1.4 (Appendix A1). Alternatively, we fitted only the low energy shoulder of the EL spectra using Marcus theory (as previously done in the work by Tang et al.[79]) which yields E_{CT} = 1.29 eV. The singlet exciton energy of PM6 and Y6 were obtained from the crossing point of the absorption and photoluminescence (PL) spectra of the pristine films. This gives an energy of the lowest excited singlet exciton S_1 of 1.90 eV for PM6 and of 1.42 eV for Y6 (Figure A1.4, Appendix A1). Conclusively, the driving force for charge generation through channel I (electron transfer) is $E_{S_1(D)-CT} \cong$ 0.60 eV, while it is much smaller through channel II (hole transfer), with an estimated $E_{S_1(A)-CT} \leq$ 0.13 eV.

In order to elucidate the role of the pathways on the free carrier generation, we performed time-delayed collection field (TDCF) experiments as a function of the electric field and temperature with excitation at different photon energies. The experimental details on TDCF are found in Chapter 3 and have also been described elsewhere.[65, 189] In short, the device is excited with a short laser pulse (~5 ns) while being held at a given prebias (V_{pre}). After a delay time of 6 ns all charges are extracted by applying a high reverse collection bias (V_{coll}). To ensure that nongeminate losses are insignificant during the measurement, we apply a sufficiently large V_{coll} of -2.5 V and the laser intensity is chosen to lie in the linear regime (the extracted charge is strictly proportional to the laser fluence). Then, the total extracted charge (Q) is a direct measure of the efficiency of free charge generation under these conditions.

Figure 4.1b shows the results of such a measurement, where V_{pre} is swept from reverse bias to V_{OC}. Here, the excitation energy was 2.07 eV which excites primarily the donor polymer at its low energy absorption maximum (see the absorption spectra of donor, acceptor, and the blend in Figure A1.5, Appendix A1). We find that the total charge Q does not depend on the applied bias V_{pre}, even when approaching V_{OC}, meaning that the photocurrent does not suffer from increased geminate recombination when decreasing the internal field. Theory predicts that an appreciable barrier for CT dissociation would cause a dependence of the dissociation efficiency on the electric field; because of electrostatic barrier lowering.[172, 190] Any gradient of the *J-V* at J_{SC} (green solid line and right axis in Figure 4.1b) must, therefore, originate from bias-dependent nongeminate recombination (NGR), which will be addressed later in this work.

Figure 4.1c assembles the result of bias-dependent TDCF generation experiments for different excitation energies, ranging from 2.76 eV to excite a high energy exciton state manifold down to 1.29 eV, which is within the low energy shoulder of the EL spectra attributed to emission from the CT state. With this, our experiments cover an exceptional wide range in photon energy, including predominate channel I and channel II excitation, hot exciton creation or the direct formation of CT states. Clearly, charge generation is field-independent for all used excitation energies, irrespective of the predominant channel of charge transfer or whether we directly excite the CT state. To complement this finding we calculated the internal quantum efficiency (IQE) spectra of PM6:Y6 from the experimental EQE spectrum by taking the reflection (R) and parasitic absorption (PA)

losses in the device stack (i.e. $\mathrm{IQE} = \mathrm{EQE}/(1 - R - PA)$)[64] into account (see Note A1.3 and Figure A1.5, Appendix A1, for further details on the procedure). Note that the main source of PA in the considered photon energy range is by the MoO_3 layer. The same procedure was applied to the TDCF data to determine the internal generation efficiency (IGE), which is the number of generated charges per absorbed photon. As shown in Figure 4.1d, both IQE and IGE are independent of excitation energy and are close to unity. This has important implications. First, free charge generation does not benefit from a larger driving force (channel I versus channel II) nor from excess photon energy. These findings substantiate the conclusions from earlier studies on fullerene-based solar cells, which were interpreted in terms of a cold generation process, involving a low energy CT state manifold as a precursor to free charges.[63–65] Second, the lack of a field-dependence of generation, independent of the excitation energy, suggests a low energetic barrier for the dissociation of such low energy precursor states. Third, with IQE and IGE being close to one, losses due to exciton harvesting, geminate recombination or charge extraction must be very small. This points to an ideal morphology, where the domains of the phase separated blend allow all photogenerated excitons to diffuse to the donor-acceptor interface, while a good interpenetration of donor- and acceptor-rich regions prevents trapping of photogenerated charges on isolated domains.[191] Indeed, recent work by Chandrabose et al.[192] reported an exceptionally high exciton diffusion coefficient in well-ordered domains of a NFA, which was assigned to the rigid nature of the molecule and low energetic disorder. We finally note that optical modeling shows the EQE (and J_{SC}) of our inverted device to be significantly affected by reflection and parasitic absorption, causing the PCE to lie below published PM6:Y6 record values.

4.4. Temperature Dependence of Charge Generation

Figure 4.2a shows the results of temperature dependent TDCF experiments at 1.55 eV, exciting exclusively the NFA at its absorption maximum and at 2.33 eV, which excites both components of the blend. We observe that cooling down the device to 230 K has essentially no effect on the efficiency of charge generation and that it remains field independent even for the lowest temperature tested. The same holds for other excitation energies (Figure A1.7, Appendix A1). Figure A1.8 (Appendix A1) plots the results from Figure 4.2a as function of temperature, normalized to the value at 320 K for two different excitation energies, where we observe a less than 10 % drop of the free charge generation efficiency when decreasing the temperature from 320 K to 230 K. This suggests a very small (if any) barrier towards CT dissociation. To substantiate this finding, our TDCF results were complemented by taking EQE spectra at different temperatures, with results shown in Figure 4.2b. Those measurements were performed at low intensity to avoid second order losses (i.e. recombination of free charge carriers), meaning any losses in the EQE should be mainly geminate.[180] We observe a gradual but only weak decrease of the EQE down to $T \cong 150$ K, followed by a steeper drop when decreasing the temperature further; possibly related to charge transport issues. Notably, changing the temperature leaves the shape of the spectrum essentially unaffected down to ~125 K (see Figure A1.9, Appendix A1). To extract an activation energy (E_a) for charge generation, we plotted the EQE versus $(k_{\mathrm{B}}T)^{-1}$ according to

$$\mathrm{EQE} = \mathrm{EQE}_0 \exp\left(-\frac{E_a}{k_{\mathrm{B}}T}\right), \qquad (4.1)$$

using EQE values at the same energies as measured by TDCF. Here EQE_0 is the EQE at infinite temperature. The result is depicted in Figure 4.2c, together with fits of Equation 4.1 (dashed line) to the high temperature region. The analysis yields a very small activation energy E_a of only 6 meV

for all excitation energies, confirming our conclusion from TDCF that charge generation at room temperature in this high-performance blend is essentially barrierless.

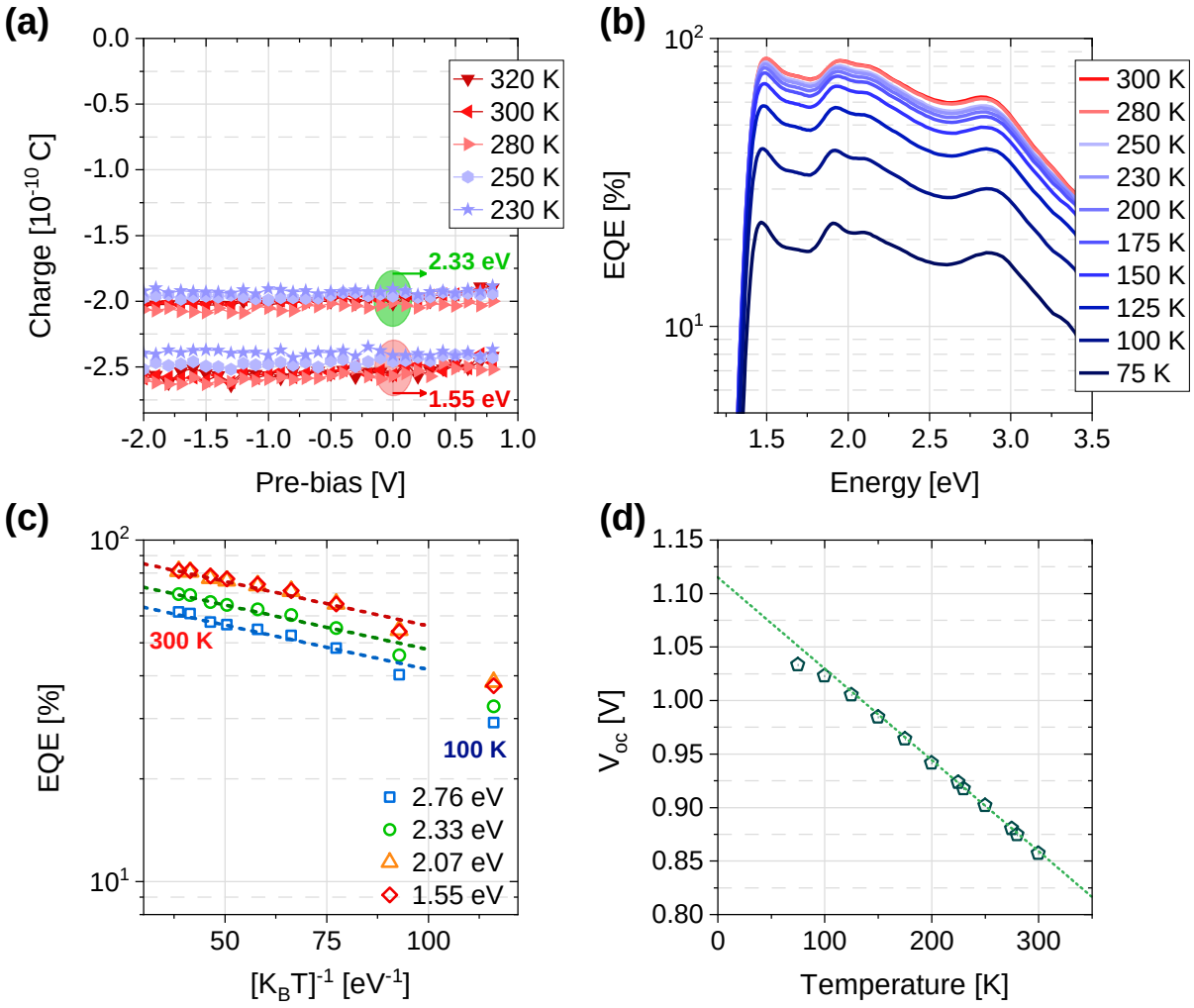

Figure 4.2: Temperature dependence of charge generation in PM6:Y6 solar cells. a Bias-dependent charge generation for a PM6:Y6 device measured at different temperatures by TDCF (with a fluence of 0.1 µJcm^{-2} and V_{coll} =2.5 V). The excitation was chosen to excite exclusively Y6 at 1.55 eV or both components at 2.33 eV. **b** External quantum efficiency (EQE) at different temperatures measured at short-circuit conditions and low intensity. **c** Temperature dependence of EQE values at different excitation energies. Open symbols correspond to the raw data and the dashed lines are fits to Equation 4.1 with a calculated E_a = 6 meV for all excitation energies. **d** Temperature dependence of V_{OC}. The linearity of the plot reveals that the free carrier density (np) in the device remains essentially constant down to a temperature of ~100 K.

As outlined earlier, there is a more pronounced effect of temperature on the EQE below ca. 150 K, which we propose to be caused by increased nongeminate recombination due to extraction issues, but whose origin may also lie in the onset of geminate recombination. To address this issue, we performed measurements of the V_{OC} over a wide temperature range, following the routine proposed by Gao et al.[180] At open-circuit conditions, generation equals recombination and extraction does not obscure the interpretation of the results (see Note A1.4 and Figure A1.10, Appendix A1). Figure 4.2d shows the resulting data for an illumination intensity equivalent to 1 sun. The V_{OC} increases in a linear fashion with temperature down to ~100 K, which rules out an appreciable effect of temperature on the free carrier density for this temperature range.

Conclusively, the above measurements reveal efficient free charge generation down to ~125 K with an activation energy below 10 meV, ruling out a significant barrier for charge separation in PM6:Y6.

4.5. Nongeminate Recombination

As pointed out above, studies with different methods and on different blend systems revealed values for the activation energies of CT dissociation between few tens of meV to ca. 100 meV.[65, 72, 180–182] A notable exemption is the annealed blend of P3HT with PCBM for which barrierless free charge generation was consistently shown.[193] This blend stands out by the strong tendency of the constituting components to phase-separate into well-crystallized domains but also by its large driving force of 0.9 eV.[194] A second example where a very low temperature dependence of CT dissociation was being proposed is the blend of TQ1 with PCBM.[195] This blend exhibits a reasonably large ΔE_{S_1-CT} (> 0.2 eV),[196] but more importantly a large energetic disorder of the donor HOMO and acceptor LUMO.[197]

This important finding raises the question about the origin of the processes compensating the unavoidable Coulomb attraction between the electron and the hole of the geminate pair in our PM6:Y6 blend. As argued in Chapter 2 (section 2.3.1) CT separation can be assisted by various processes (besides ΔE_{S_1-CT}) such as entropy,[87, 95] high local mobilities[88, 89] and delocalization of charges on aggregated phases of the donor and/or the acceptor.[72, 90–92, 198–200] In addition, several recent papers highlighted the role of energetic disorder in providing low energy sites for the dissociation of CT states in DA blends or even singlet excitons in neat organic semiconductors.[72, 95, 201, 202] For instance, Hood and Kassal[95] concluded that a Gaussian disorder σ of 100 meV is sufficient to reduce the free-energy barrier to ca. 25 meV. Accordingly, we performed a temperature dependent study of space-charge limited currents (SCLC) in electron- and hole-only devices to quantify the energetic disorder in the PM6:Y6 blend (see Figure A1.11, Appendix A1). The data was modelled with 1D drift-diffusion simulations based on the extended Gaussian disorder model (Chapter 2, section 2.4.1), according to Felekidis et al.[203] We found the energetic disorder of the HOMO to be $\sigma_{H,D} = 83$ meV and that of the LUMO, $\sigma_{L,A} = 71$ meV. That the σ is lower for electribs confirms conclusions from GIWAXS measurements by Yuan et al.,[29] that the NFA forms well-ordered domains in the blend. Such small values for σ exclude energetic disorder as the main driving force for charge separation. Note that the study on barrier lowering in ref.[95] includes the combined effect of energetic disorder and of entropy, while the activation energy for CT dissociation is unaffected by entropic effects.[72]

It has been argued that SCLC measurements are not well suited to study the density of states (DOS) that is involved in the photogeneration process.[102] This is because SCLC is by the motion of dark-injected charges, which are situated in the tail of the DOS right from the beginning, while photogenerated charges may initially occupy states near the center of the DOS. We have recently shown that studies of dispersive recombination with TDCF provide direct access to the thermalization properties of photogenerated carriers in the actual device.[112, 189, 204] For this measurement, the device is held at a given V_{pre}, typically close to the maximum power point, while the delay time (t_{del}) is now varied from few ns to µs (Chapter 3, section 3.4.). Figure A1.12 (Appendix A1) shows the total extracted charge n_{tot} as a function of t_{del} at different excitation fluences, where the differential of n_{tot} over time is the free charge recombination rate R. There is a significant acceleration of recombination with increasing fluence, meaning that recombination is a higher order process. To gain information on how the rate depends on carrier density and time, R is plotted as a function of the charge carrier density n_{coll} present in the sample at t_{del}, with

the result shown in Figure 4.3a. Except for some tailing at low fluences and early times, we observe that all $R(n_{\mathrm{coll}}, t_{\mathrm{del}})$ data fall onto one line, independent of the initial fluence, and this line has a slope equal to 2 in the log-log plot. This proves that R does not explicitly depend on t_{del} and that non-dispersive bimolecular recombination of free charges is the predominant mechanism in this blend.[112] The situation is clearly different from donor-acceptor blends with large energetic disorder, such as TQ1:PCBM, where recombination was found to be dispersive up to the microsecond time range.[189, 204] We have complemented this transient study by investigating the recombination properties under steady-state conditions, using bias assisted charge extraction (BACE), (Chapter 3, section 3.4. , contains the details on the measurement).[135, 205] The results are included as squares data points in Figure 4.3a for direct comparison to TDCF. These steady state recombination data lie exactly on the results from TDCF, meaning that recombination involves the same site distribution, from the nanosecond time scale to steady state. The dashed line corresponds to a fit to Equation 2.12 (section 2.4.2 in fundamentals) with $\delta = 2.14$. A recombination order close to 2 rules out trap-assisted recombination as discussed in Chapter 2 (section 2.4.3).[206, 207] The analysis of the recombination data according to $R = k_2 n^2$ (Equation 2.13, section 2.4.2) yields a bimolecular recombination coefficient $k_2 = 1.7 \times 10^{-17}$ m^{3}s^{-1}, depending only weakly on charge carrier density, as shown in Figure 4.3b. We also examined the dependence of the carrier density and the recombination current on V_{OC}, which gave an ideality factor n_{id} of 1.17 and an m-factor of 1.18 (see Figure A1.13, Appendix A1 for details). The models presented in Chapter 2 (section 2.4.3), according to the work by Hofacker and Neher,[112] describe how the exact values of δ, n_{id} and m, depend on the shape of the DOSs and the predominant recombination pathway. The data here on PM6:Y6 strongly support that nongeminate losses occur exclusively through recombination of carriers situated in a Gaussian DOS.

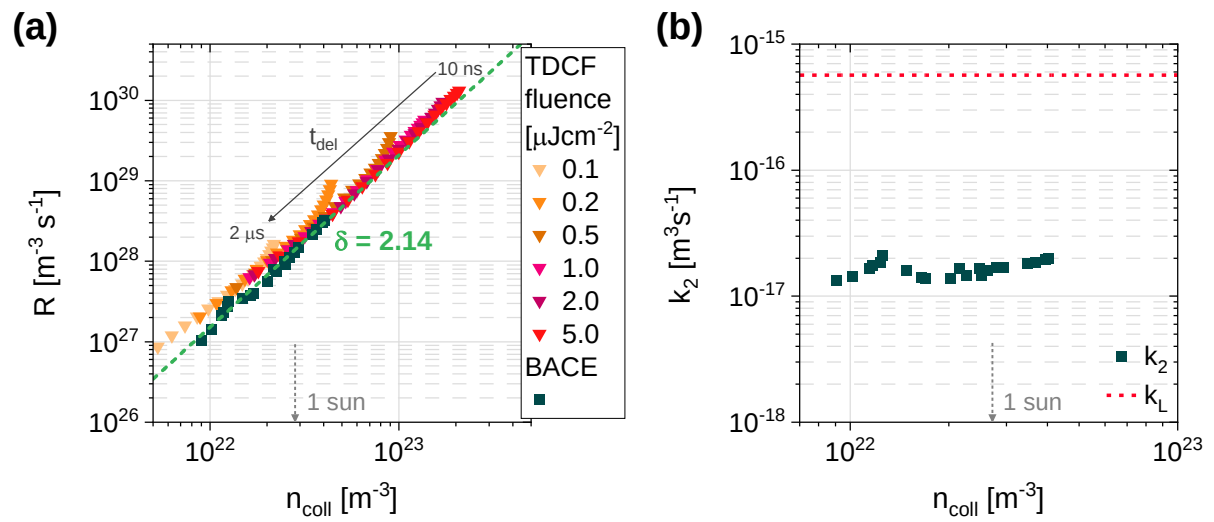

Figure 4.3: Nongeminate recombination in PM6:Y6 solar cells. a Recombination rate vs. photogenerated charge carrier density. For TDCF measurements (triangles), R is plotted as function of the remaining charge in the device (n_{coll}) after a given certain delay time (t_{del}). Squared data depict steady-state recombination from BACE experiments, and the dashed line is the result of Equation 2.12 (section 2.4.2 in fundamentals) with a recombination order δ of 2.14. **b** Bimolecular recombination coefficient as function of charge carrier density calculated from the BACE data via $R = k_2 n^2$. For comparison, the dashed red line shows the recombination coefficient k_L as predicted by Langevin recombination (Equation 2.14, section 2.4.2).

Our results question energetic disorder and charge thermalization in a broad DOS as the origin of efficient charge generation in our PM6:Y6 blend. It has been recently proposed that an aggregation-dependent electron affinity causes an energy cascade which drives electrons out from the more disordered DA heterojunction into the well-crystallized domains of the neat NFA.[208] Also, measurements of the activation energy for CT dissociation for different blends revealed a direct correlation with the nanomorphology, while there was no consistent dependency on the driving force.[65, 181] We have so far observed strong evidence of NFA aggregation, such as the strong red-shift in absorption for films, the small energy shift from $\mathrm{EQE_{PV}}$ to electroluminescence emission and the low energetic disorder in the LUMO. A recent study of the morphology of PM6 blended with Y6 revealed phase separation into well-crystallized domains with an average domain size of ca. 20 nm.[42] In order to elucidate the role of NFA aggregate formation on the efficiency of free charge generation, additional experiments were performed on "diluted" low-acceptor-content PM6:Y6 (10:1, w/w) blends. Evidence for the de-aggregation of Y6 comes from the marked blue-shift of the NFA absorption and photoluminescence in the dilute blend compared to the 1:1.2 ratio and the neat acceptor layer (see Figure A1.14, Appendix A1). TDCF experiments on such a dilute blend revealed a pronounced effect of the electric field on the photogeneration efficiency (Figure A1.15, Appendix A1), where larger geminate losses appear at lower fields. The even stronger effect of bias on the steady state photocurrent points to additional nongeminate losses, which we attribute to slow electron extraction in combination with a significant faster rate for NGR (see the results of TDCF recombination studies on the dilute blend in Figure A1.16, Appendix A1). Notably, free charge generation in this dilute acceptor blends is temperature dependent, with an activation energy of ca. 22 meV (Figure A1.17, Appendix A1).

4.6. Mechanism of Barrierless Free Charge Generation

We now discuss the potential microscopic mechanism of barrierless charge generation in the PM6:Y6 blend. As already mentioned, charge separation involves two steps: exciton dissociation into a CT state and the subsequent dissociation of that CT state into a free electron-hole pair. Since the PM6:Y6 donor-acceptor interface has a sufficiently large driving force between the excited donor/acceptor (D*/A*) and the CT state (~0.61 eV for the D* and 0.13 eV for the A*), the transition from the D*/A* states to the CT state is barrierless. On the other hand, we expect the Coulomb binding energy between the CT and charge-separated (CS) states to be of the order of 0.4 eV.[176] Our temperature dependent measurements, however, show that charge separation is barrierless in our PM6:Y6 blend.

To understand this, we first point out that because of the phase-separated structure the electrostatic potential at a DA interface can have a pronounced bend due to a molecular concentration gradient.[209] This concentration gradient modulates the solid-state crystal field around the charge.[96–98] In other words, a hole away from the interface interacts with a smaller density of acceptors dispersed in the donor phase. For the acceptor-donor-acceptor molecular architecture of Y6, the electrostatic potential, termed here as a bias potential B, has a sign which pushes electrons and holes away from the interface. Another important implication of such bias potential is that it reduces the energetic difference between the CT and CS states, thus enabling the barrierless CT state dissociation [209] as extensively presented in Chapter 2 (see Equation 2.6 in section 2.3.1). Therefore, the bend of the bias potential may compensate, at least partially, the Coulomb attraction of the CT state.

An exact evaluation of the bias potential requires the knowledge of an atomically-resolved donor-acceptor interface. Simulating such interfaces is computationally demanding, and here we

provide only an upper bound for the bias potential, by assuming that in a CT state a hole on a donor molecule is dressed by the acceptor crystal field and vice versa. The crystal fields are evaluated using the polarizable force-field tailored specifically for Y6,[210, 211] (see Note A1.5 and Figure A1.18, Appendix A1 for details). The estimated B value for Y6 is 1.1 eV. According to recent simulation work, barrierless CT dissociation requires $B > 1$. The large positive bias can be clearly traced back to the Y6 A-D'-A''-D'-A molecular architecture, which leads to a large static quadrupole moment of a molecule ($Q_{xx} = -120$, $Q_{yy} = 80$, $Q_{zz} = 40$ Debye Angstrom) and hence large crystal fields, as shown in Figure 4.4a. Note that the molecular dipole moments cancel out due to the dimerization in a unit cell, as shown in Figure A1.19 (Appendix A1). Absence of a unit cell dipole and high crystallinity of Y6 films also imply its relatively narrow density of states, which is shown in Figure 4.4b. Measured and calculated DOS widths exclude effects of non-equilibrium relaxation of charges which could assist charge splitting. Note that the electron affinity and ionization energy are both within the "trap-free" window, hinting at a trap-free ambipolar transport in pristine Y6 films.[212, 213] In addition, the calculated excited state reorganization energy of Y6 has a very small value of 0.24 eV, which promotes large exciton diffusion rates and lengths and makes it less sensitive to the morphological variation in a bulk heterojunction.

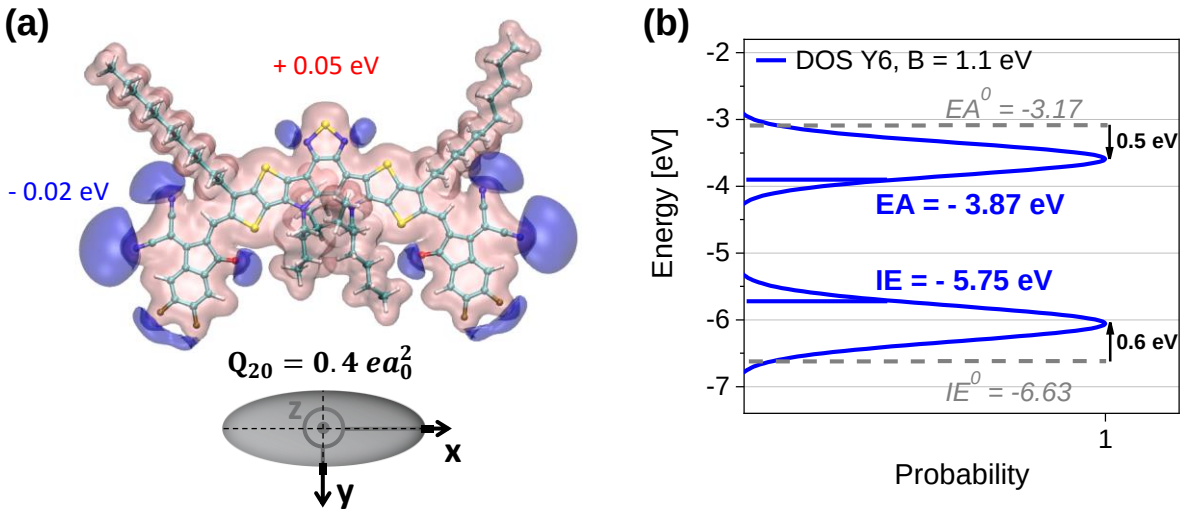

Figure 4.4: Electrostatic potential and density of states of Y6. a Isosurfaces of the electrostatic potential of Y6 leading to its large quadrupolar moment, together with the ellipsoid of the quadrupole tensor. See Figure A1.20 (Appendix A1) for the equivalent calculation of the isosurfaces of the electrostatic potential of PM6. **b** Calculated density of states (DOS) for electrons (EA) and holes (IE) in a model crystal of Y6. The onset of the DOS, evaluated as its maximum plus/minus 2σ for (electrons/holes) gives the ionization energy and electron affinity of the Y6 crystal.

4.7. Efficiency Limitations and Conclusions

With the exceptional free charge generating properties in PM6:Y6 demonstrated, the efficiency of our devices is mainly limited by insufficient photon absorption and free charge extraction. Our time-resolved and steady-state measurements showed consistently that nongeminate recombination is bimolecular in nature, with a NGR coefficient $k_2 = 1.7 \times 10^{-17}$ at one sun illumination conditions. This value needs to be compared to the charge encounter rate according to the Langevin model, giving $k_L = 5.5 \times 10^{-16}$ m^3s^{-1}, shown by a dashed line in Figure 4.3a and calculated according to Equation 2.14 (section 2.4.2 in fundamentals) with the mobility values found in Figure A1.21 (Appendix A1). The comparison shows that NGR is not largely suppressed in our blend. Recent impedance spectroscopy on PM6:Y6 gave k_2 values $3 - 5.8 \times 10^{-19}$ m^3s^{-1}.

[214] These measurements were performed on a regular device geometry, with a PEDOT:PSS bottom electrode. The lower k_2 reported in ref.[214] may result from a specific blend morphology, due to a different bottom electrode. To ensure that our measurements on inverted devices are not affected by the choice of the bottom electrode, we studied the steady state non-geminate recombination in a regular device (PEDOT substrate electrode) using BACE (see Figure A1.22, Appendix A1). This device had a PCE of 14.7%. Within the uncertainty of the experiment both device geometries exhibit the same order and coefficient of recombination. Since nongeminate recombination is highly sensitive to the blend morphology,[215] we conclude that the bulk properties are only little depending on the bottom electrode. The efficiency limitation that comes with a high k_2 value can be illustrated with numerical drift-diffusion simulations.[135, 163, 216] As demonstrated in Figure A1.2, (Appendix A1), using the well-established drift-diffusion simulation software SCAPS,[164] we could fully reproduce the *J-V* curve of our certified 1 cm^2 device using the measured parameters (i.e. k_2 and mobilities) as input parameters. Finally, we show that for PM6:Y6 with the reported initial J_{SC} close to 25 $mAcm^{-2}$, a PCE of over 18% is within reach if the recombination coefficient is substantially smaller and the carrier mobility can be increased by one order of magnitude (a summary of all simulation parameters is given Table A1.2, Appendix A1).

In summary, we studied free charge generation in inverted PM6:Y6 devices, using a combination of TDCF, EQE and V_{OC} measurements. We find that CT dissociation is field-independent regardless of whether the acceptor, the donor, or the CT state is excited, pointing to a cold free charge generation pathway with a very small dissociation barrier. Temperature dependent measurements reveal an exceptional small activation energy for CT dissociation of only 6 meV and efficient photocurrent generation down to $T \sim$100 K. We exclude that charge separation is mainly driven by disorder, given the small σ values in the HOMO and LUMO and that nongeminate recombination is a non-dispersive, purely second order process. We propose that the large quadrupolar moments of Y6 on a molecular scale, its dimerization in a unit cell, and the specific acceptor-donor-acceptor molecular architecture create an electrostatic bias potential which compensates the Coulomb binding of the charge transfer state, thus enabling barrier-free dissociation of CT states.

Chapter 5. Reliability of Charge Carrier Recombination Data determined with Charge Extraction Methods

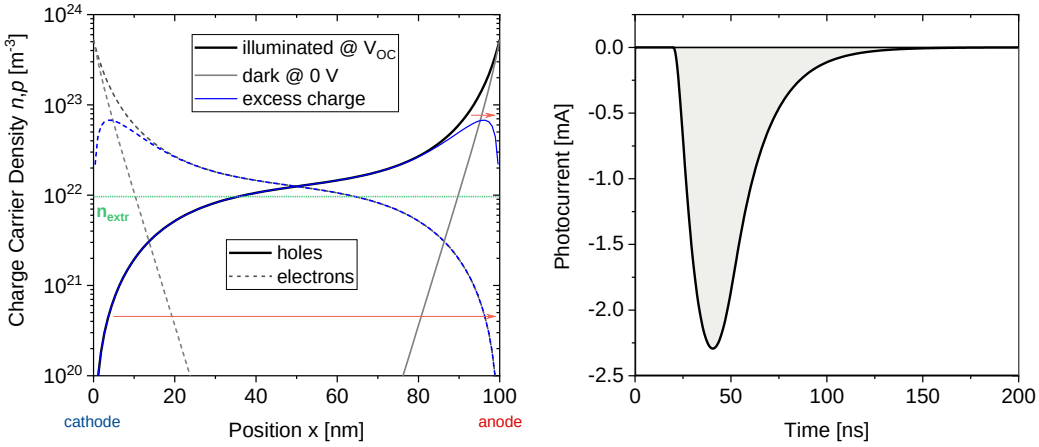

Charge extraction methods are used to draw conclusions on the mechanism of free charge recombination in organic solar cells. Two complementary experiments are transient time-delayed collection field and bias-assisted charge extraction. These methods are especially sensitive to the charge carrier density profiles in the device under investigation. Therefore, the main motivation behind this work was the analysis of the advantages and limitations of these techniques via drift-diffusion simulations. Experimental data on PM6:Y6 was compared to the simulations, which demonstrates the accuracy of the experimental approach and confirms that nongeminate losses in this blend occur mainly in the bulk.

This chapter is an adapted preprint of:

J. Kniepert, A. Paulke, L. Perdigón-Toro, J. Kurpiers, H. Zhang, F. Gao, J. Yuan, Y. Zou, V. M. Le Corre, L. J. A. Koster, and D. Neher. Reliability of charge carrier recombination data determined with charge extraction methods. *J. Appl. Phys.* **2019**, 126, 205501.

5.1. Abstract

Charge extraction (CE) methods are popular for measuring the charge carrier density in thin film organic solar cells and drawing conclusions about the order and coefficient of nongeminate charge recombination. However, results from such studies may be falsified by inhomogeneous steady state carrier profiles or surface recombination. Here, we present a detailed drift-diffusion study of two charge extraction methods, bias-assisted charge extraction (BACE) and time-delayed collection field (TDCF). Simulations are performed over a wide range of the relevant parameters. Our simulations reveal that both charge extraction methods provide reliable information about the recombination order and coefficient if the measurements are performed under appropriate conditions. However, results from BACE measurements may be easily affected by surface recombination, in particular for small active layer thicknesses and low illumination intensities. TDCF, on the other hand, is more robust against surface recombination due to its transient nature but also because it allows for a homogeneous high carrier density to be inserted into the active layer. Therefore, TDCF is capable to provide meaningful information on the order and coefficient of recombination even if the model conditions are not exactly fulfilled. We demonstrate this for an only 100 nm thick layer of a highly efficient non-fullerene acceptor (NFA) blend, comprising the donor polymer PM6 and the NFA Y6. TDCF measurements were performed as a function of delay time for different laser fluences and bias conditions. The full set of data could be consistently fitted by a strict second order recombination process, with a bias- and fluence independent bimolecular recombination coefficient $k_2 = 1.7 \times 10^{-17}$ m^3s^{-1}. BACE measurements performed on the very same layer yielded identical results, despite the very different excitation conditions. This proves that recombination in this blend is mostly through processes in the bulk and that surface recombination is of minor importance despite the small active layer thickness.

5.2. Introduction

The field of organic solar cells (OSC) has seen tremendous progress in the last 15 years and is now on the verge of commercial application with certified power conversion efficiencies (PCE) around 19 % for single junction structures.[43, 44, 46] Despite this success, current PCEs are still far below the theoretical Shockley-Queisser limit, issuing an ongoing challenge to the OSC research community. One of the key parameters limiting the performance is the nongeminate recombination (NGR) of photogenerated charge carriers in the active medium. In organic solar cells, free carrier recombination is mostly through bimolecular recombination (BMR),[217] implying that the carrier lifetime is a strong function of the carrier density. As a consequence, the fill factor is depending on generation rate, the bimolecular recombination coefficient, the layer thickness and the carrier mobilities.[218–221] As such, BMR sets a limit to the optimum layer thickness of the absorber layer.[86] In particular for blends with efficient charge generation, thin active layers are often chosen in order to extract most photogenerated charge carriers before they recombine in the bulk. Yet, thin layers mean a loss of the overall absorption of light and generation of free charges which limits the output current of the device. On the other hand, while BMR is a second order process, the presence of traps and recombination of minority carriers at the electrode (surface recombination) lead to additional first order recombination channels. To further push the efficiency of OSC it is a crucial task to identify and quantify recombination processes in operational devices under relevant conditions and at the relevant times scales – from nanoseconds to steady state.

In the past, time-resolved transient absorption spectroscopy (TAS) has been one of the most frequently employed techniques to measure charge carrier decay dynamics and rate coefficients.[222–224] However, only few studies were made on complete devices[225] and, in general, TAS requires high fluences, beyond the regime relevant to photovoltaics, to obtain reasonable signal-to-noise ratios. Likewise, this technique does not deliver steady state recombination data. The method of photogenerated charge extraction by linearly increasing voltage (photo-CELIV) is well suited to perform recombination measurements at low fluences and carrier densities,[226, 227] but it lacks the time resolution to capture early time recombination. Alternatively, small perturbation optoelectronic measurements based on transient photovoltage (TPV) are conducted on devices under relevant working conditions.[228–230] However, it was pointed out recently that lifetimes obtained by TPV on thin film devices may be influenced by capacitive contributions.[231, 232]

An indirect way to study the order and coefficient of recombination is to determine the charge carrier density in the device as a function of illumination intensity (and bias) and connect it with the recombination current under the same conditions. Popular methods are charge extraction (CE),[233] differential charging (DC),[228] or impedance spectroscopy (IS).[234] It has, however, been noted that in devices under steady-state operating conditions, charge carrier profiles can become highly inhomogeneous because of dark injection from the electrodes, as introduced in Chapter 2 (section 2.4.2).[206, 232, 235, 236] The effect is most pronounced for thin active layers and low illumination conditions (low excess carrier density). As a result, the extracted carrier density from CE, which is the drift-length weighted average of the charge carrier distribution (see below) may differ largely from the mean density, leading to e.g. an apparent higher order of mobility.[206, 236] However, even if the average charge density is determined correctly (e.g. via DC), an inhomogeneous carrier profile will cause the recombination rate to vary across the active layer, meaning that the analysis of total recombination current in combination with the spatially averaged carrier densities may not give the true (local) recombination order and coefficient.[235] The situation becomes even more complicated in presence of surface recombination. In this case, photogenerated carriers exit the device at the wrong contact (electrons at the anode or holes at the cathode), due to poor contact selectivity. As a result, the carrier density profile becomes highly inhomogeneous[136] but also, the extra surface recombination current (being linear in the minority carrier density at the respective contact) may mask the nature of the bulk recombination process.[206]

Recently, we have reported on two complementary techniques to measure the recombination order and coefficients, namely time-delayed collection field (TDCF)[30] and bias-assisted charge extraction (BACE).[135] Although both methods are based on the extraction of photogenerated charge carriers upon application of a reverse bias voltage, there are distinctive differences in the measurement conditions and the physical concepts behind the data analysis. As detailed in the previous chapter and the methods Chapter 3, in TDCF charge carriers are generated with a short (nanosecond) laser pulse and subsequently extracted with a high reverse bias (collection bias V_{coll}) after a variable delay time. During generation and delay, the device is held at a given prebias (V_{pre}) close to V_{OC} or the maximum power point. The delay between the laser pulse and the extraction pulse allows recombination to evolve for a well-defined time period. The analysis of the extracted charge (Q_{pre}) during prebias and the extracted charge (Q_{coll}) during application of the collection bias yields information on how the charges move and recombine. In contrast, in a BACE experiment, the device is illuminated with a steady-state light source of defined intensity while being held at a constant bias that corresponds exactly to the V_{OC} of that intensity. In good approximation, the net current density at each point in the bulk is zero and the rates of generation

and recombination are equal. When switching off the light source, the external bias is rapidly changed to reverse direction. Integration of the photocurrent transient then yields the amount of mobile charge that was present in the device under illumination. Analysis of the carrier density at different illumination intensities as a function of generation rate reveals information on the dominant recombination order and coefficient in the bulk.

Both techniques have been extensively used to examine time-dependent and steady-state recombination properties for a wide range of materials, revealing important information on the rate and order of recombination.[189, 205, 237–240] The accuracy of these results was confirmed by drift-diffusion simulations of the transient and steady-state photocurrents.[135, 216] However, the analysis of the TDCF and BACE photocurrent data relies on several simplified assumptions. The most critical one is that the spatial distribution of the charge carriers is assumed to be uniform across the layer before extraction. Only in this case does every charge carrier travel on average half the layer thickness and the integral over time corresponds exactly to the total carrier density in the device. To take injected dark charge into account in the analysis of the TDCF experiments, an additional background charge is included, which, for simplification, is assumed to be homogenous in the layer.[135] However, the true distribution of the background charge depends on layer thickness, external bias and injection barriers and might in fact be very inhomogeneous. This raises the question of how the background charge influences the charge carrier dynamics in the TDCF experiment and how it can be accounted for.

In this paper we use one dimensional drift-diffusion simulations to study charge extraction under realistic conditions, i.e. taking into account the injection of charges from the electrodes and resulting inhomogenous charge carrier profiles. In particular, we investigate the influence of recombination coefficients, layer thickness, illumination intensity and bias on the outcome of TDCF and BACE measurements. A particular focus is on the influence of surface recombination on the results from BACE and TDCF. It turns out that both methods work surprisingly well even if the simplified assumptions are not fulfilled. We identify the parameter range and conditions that lead to reliable results and point out conditions where special care is necessary.

5.3. Methods

1D Drift-Diffusion Simulations: Numerical drift-diffusion simulations of the carrier densities under steady-state illumination and in the dark were performed with a code developed by Koster et al. and published in Ref.[163]. The kinetic TDCF simulations were performed using a transient drift-diffusion simulation tool as described in [131, 165], following closely the experimental measurement scheme. At first the device is held for a sufficient time in equilibrium in the dark at a certain prebias, which allows establishing a steady state background charge distribution in the device. The injection barriers in all simulations were set to 0.1 eV, and the contacts are assumed to be in thermodynamic equilibrium where Boltzmann statistics are used to determine the carrier densities at the first and last grid point of the device. At $t = 0$, an additional homogeneous charge carrier density is instantaneously inserted in the layer, imitating the laser pulse in the measurement. The additional charge carriers may then either leave the device or recombine with each other or with the dark carriers. Recombination between any charge carriers is implemented as a bimolecular process with a constant BMR coefficient k_2. After the time delay a high reverse bias (V_{coll}) is applied to rapidly collect all remaining charge carriers from the device. The motion of the charge carriers results in an electrical current I_{ext} in the external circuit, through a measurement resistor R. Like in the real experiment, the same voltage jump is also performed without illumination to account for capacitive charging. The difference between those yields the

photocurrent I_{photo} of the photogenerated excess charge carriers. Notably, if dark charge is present, this voltage jump in the dark will also account for the drift-length weighted dark charge distribution. For each delay time, the photocurrent transients are integrated to yield the pre-extracted charge: $Q_{\mathrm{pre}}(t_{\mathrm{del}}) = \int_0^{t_{\mathrm{del}}} I_{\mathrm{photo}}\, dt$, the charge present in the device at t_{del}: $Q_{\mathrm{coll}}(t_{\mathrm{del}}) = \int_{t_{\mathrm{del}}}^{t_{\mathrm{max}}} I_{photo}\, dt$, and the total charge: $Q_{\mathrm{tot}}(t_{\mathrm{del}}) = \int_0^{t_{\mathrm{max}}} I_{\mathrm{photo}}\, dt$; the latter being the photogenerated charge surviving charge recombination. Dividing Q by the active sample volume yields the carrier density n. From these data, the recombination rate R is calculated via: $R(t_{\mathrm{del}}) = (n_{\mathrm{tot}}(t_{\mathrm{del}} + \Delta t) - n_{\mathrm{tot}}(t_{\mathrm{del}}))/\Delta t$, where Δt is the time increment in the simulation. To construct the differential decay plots, $R(t_{\mathrm{del}})$ is plotted versus n_{coll} , where the latter is represented by its average value $(n_{\mathrm{coll}}(t_{\mathrm{del}} + \Delta t) + n_{\mathrm{coll}}(t_{\mathrm{del}}))/2$.

The experimental details on TDCF and BACE and on device preparation of inverted PM6:Y6 devices and are found in Chapter 3, section 3.4.

5.4. Results from Drift-diffusion Simulations

It has been shown that in devices under steady-state illumination and bias conditions, the distribution of charge carriers is rather inhomogeneous.[206, 235] In particular if the injection barriers are low, the charge carrier densities near the contacts may be very high, possibly several orders of magnitude higher than in the bulk.[241] Figure 5.1a shows simulated carrier density profiles at open circuit conditions for a typical device of 100 nm with injection barriers of $\varphi_{\mathrm{B}} = 0.1$ eV and assuming infinite surface recombination velocities at both contacts. The simulated generation rate was $G = 5 \times 10^{27}$ $\mathrm{m^{-3}s^{-1}}$, the BMR coefficient was set to $k_2 = 1 \times 10^{-17}$ $\mathrm{m^3s^{-1}}$ and electron and hole mobility were $\mu_e = \mu_h = 10^{-3}$ $\mathrm{cm^2V^{-1}s^{-1}}$. The simulation used here is based on a drift-diffusion model where nongeminate recombination is implemented as a bimolecular process and the contacts are assumed to be in thermodynamic equilibrium with the adjacent organic layer.[163] At steady state, the carrier distribution in the device is then established by a combination of photogeneration, recombination, injection and extraction of charge carriers. Especially at low illumination levels and low layer thicknesses, the injected charge carriers dominate the distribution in the device.

In a charge extraction experiment the carrier density is determined from the integral of the extraction current transient over time, as shown in Figure 5.1b. Charge extraction from thin layers of intrinsic semiconductors has been treated in several publications.[232, 242] In short, let us consider a positive charge Q, situated at position x in a semiconductor layer of thickness d and permittivity $\varepsilon = \varepsilon_0\varepsilon_r$, sandwiched between a cathode at $x = 0$ and an anode at $x = d$. According to Poisson's equation, when this charge is moved to the anode, the electrostatic potential of the anode (relative to the cathode) increases by $\Delta V = \frac{Q/A}{\varepsilon}(d - x) = \frac{Q}{C_g}\frac{d-x}{d}$, where A is the area and C_g the geometric capacity of the device. If the external bias is kept constant, this causes a current in the external circuit to compensate the potential change due to charge displacement. The integral of this external current gives what we measure as the extracted charge: $Q_{\mathrm{extr}} = C_g \Delta V = Q\ \frac{d-x}{d}$. Therefore, $Q_{\mathrm{extr}} < Q$, except for the case where the charge travels through the entire layer during extraction. If now $n_h(x)$ is the hole density in the moment when the extraction starts, complete extraction of all holes to the anode causes an extracted charge of

$$Q_{h,\mathrm{extr}} = \frac{qA}{d}\int_0^d (d - x) \cdot n_h(x)\mathrm{d}x \equiv (qAd)n_{h,\mathrm{extr}}\,, \qquad (5.1)$$

where q is the elementary charge. Therefore, the extracted hole density can be written as

$$n_{h,\mathrm{extr}} = \bar{n}_h \frac{(d - \bar{x}_h)}{d}, \qquad (5.2)$$

where $\bar{n}_h = \frac{1}{d}\int_0^d n_h(x)dx$ is the spatially averaged hole density and $\bar{x}_h = \frac{\int_0^d x \cdot n_h(x)dx}{\int_0^d n_h(x)dx}$ is the mean position of the hole distribution. For electrons extracted at the cathode ($x = 0$):

$$n_{e,\mathrm{extr}} = \bar{n}_e \frac{\bar{x}_e}{d} \qquad (5.3)$$

Accordingly, the extracted carrier density is determined by the average carrier density and the average distance travelled by each carrier during extraction. In case of the carrier distribution shown in Figure 5.1a, there are many charge carriers close to the extracting electrode that travel only a small distance and only few charge carriers at the opposite electrode that travel the whole distance. Therefore, $n_{\mathrm{extr}} < \bar{n}$. Also, even if the average electron and hole density is the same, the average drift length may differ largely for the two types of carriers, leading to $n_{e,\mathrm{extr}} \neq n_{h,\mathrm{extr}}$. Only when electrons and holes are homogeneously distributed and their densities are equal,

$$n_{\mathrm{extr}} = n_{e,\mathrm{extr}} + n_{e,\mathrm{extr}} = \frac{1}{2}n_e + \frac{1}{2}n_h \cong n_e = n_h = n. \qquad (5.4)$$

Though this condition is generally not fulfilled, the analysis of data from extraction experiments relies on the assumption that the extracted carrier density is equal to the average electron resp. hole density. The same is actually true in impedance spectroscopy, where it is assumed that the extra charge $dQ = CdV$, which is injected into the device upon a small voltage increase dV, distributes homogeneously across the active volume.

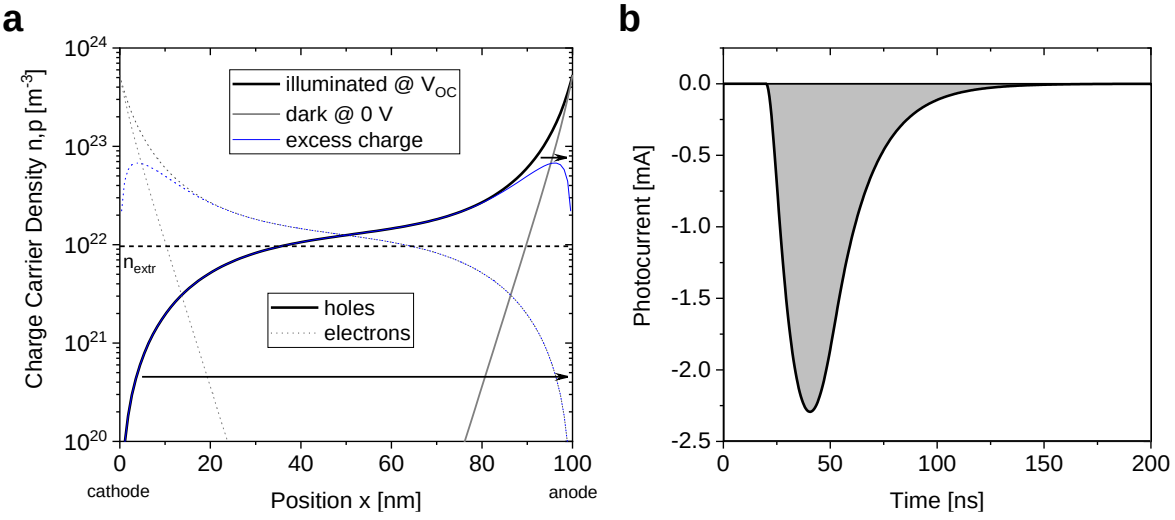

Figure 5.1: Simulated charge carrier density profiles and photocurrent transient. a Simulated charge carrier density profiles for a 100 nm device under illumination at V_{OC} = 0.705 V with injection barriers of 0.1 eV, a generation rate of $G = 5 \times 10^{27}$ m^{-3}s^{-1}, a BMR coefficient of $k_2 = 1 \times 10^{-17}$ m^{3}s^{-1} and electron and hole mobilities of $\mu_e = \mu_h = 10^{-3}$ cm^{2}V^{-1}s^{-1}. The surface recombination velocity was set to infinite at both contacts. In the absence of electrodes, the generation-recombination balance would establish a steady-state carrier density $n_e = n_h = 2.2 \times 10^{22}$ m^{-3}. Under reverse bias, electrons move to the cathode ($x = 0$) and holes to the anode ($x = d$). As indicated by the arrows, a large amount of charge travels a short distance to the electrode, while only a few charge carriers move through the whole layer thickness. Therefore, the extracted carrier density n_{extr} (see Equation 5.2 to 5.4) is smaller than predicted from the simply generation-recombination balance. **b** Simulated transient under the assumption that all holes from the device in panel a are extracted at the anode with an extraction voltage of -5 V. The large reverse bias leads to rapid extraction of charges.

In addition, BACE as well as TDCF measurements always include the correction by a dark reference pulse, starting at 0 V or V_{pre}, respectively, and using the same voltage step to negate capacitance effects. We show below that such dark carrier densities are generally inhomogeneously distributed throughout the active layer. We call the carrier density out of the BACE or TDCF measurement that is corrected by the dark reference measurement at 0 V the excess carrier density n_{exc}. This is the physical quantity accessible in the experiments.

5.4.1. Bias-assisted Charge Extraction

Having introduced the important physical quantities, we now turn to the analysis of recombination coefficient and order using the bias-assisted charge extraction (BACE) method. In a BACE measurement the device is illuminated with a steady-state light source with varying intensities while being held at a constant bias equal to the V_{OC} at that intensity. The V_{OC} and short-circuit current (J_{SC}) of the device are measured for each particular light intensity. Assuming that under short-circuit conditions, all charge carriers are extracted, the charge carrier generation rate G can be determined from the J_{SC} according to: $G = J_{\mathrm{SC}}/ed$ with e being the elementary charge and d being the device thickness. In general J_{SC} conditions are not sufficient to extract all charge carriers. In this case the current density at a higher reverse bias is used to determine the generation rate.[135]

The integrated carrier densities from the BACE current transients are then plotted against the generation rates. Under the assumption that the net current density at each point in the bulk was zero, the rates of generation and recombination R are equal and the slope of the log-log plot of G versus n corresponds to the recombination order δ according to Equation 2.12 (section 2.4.2):

$$G = R = \gamma n^{\delta}.$$

In case of bimolecular recombination, $\delta = 2$ and the recombination coefficient is k_2.

Figure 5.2a shows the results for two layer thicknesses (100 nm and 250 nm) and three different BMR coefficients ($k_2 = 10^{-16}, 10^{-17}, 10^{-18}$ m^{3}s^{-1}). Here the surface recombination was set to zero for both contacts. The dashed lines indicate the theoretical dependence of carrier density on generation rate for the three BMR coefficients. It is obvious that in absence of surface recombination, in all cases the results from our analysis correspond well to the input value of k_2, except for very low charge carrier densities. For high enough carrier densities in the bulk, the charge carrier density profiles become fairly homogeneous, and the drift length weighted carrier density approaches the bulk carrier density. Example carrier density profiles for different generation rates and layer thicknesses are shown in Figure A2.1 (Appendix A2). It becomes evident that for low generation rates the density profiles are very inhomogeneous as they are dominated by the injected charge in the space charge regions close to the contacts. In this case the extracted carrier density becomes almost independent of the generation rate and the $G(n)$ plot reveals a slope that is greater than 2. This would suggest a recombination order higher than 2, however as our simulations clearly show, this deviation is the result of an inhomogeneous carrier distribution. For the 250 nm device we find a slope of 2 also for lower carrier densities down to approximately 10^{21} m^{-3}. This is because the space charge regions become less important compared to the bulk for larger layer thicknesses and the density profiles are homogeneous also for lower generation rates.

Recombination orders higher than 2 have been frequently reported in literature.[122, 216, 229] In some cases this phenomenon has been interpreted as BMR with a $k_2(n)$ being dependent on carrier density. While the participation of more than two particles in a recombination process is

quite unlikely, it cannot be ruled out that k_2 is a function of n if for instance the mobilities are carrier density dependent.[122] Likewise, recombination among carriers which occupy a broad density of states distribution may be the reason of an apparent higher recombination order, as discussed in Chapter 2 (see Table 2.1, section 2.4.3).[112] Experimental conditions should be carefully examined and reviewed to exclude measurement artefacts. Our general advice is to work at charge carrier densities greater than 5×10^{21} m^{-3} to be on the safe side and with layer thicknesses as large as possible for a certain material combination. The exact values for illumination intensity and layer thickness also depend on the injection barriers and recombination coefficient. In general, the lower the injection barriers the more inhomogeneous will be the carrier density profile as the injected charge at the contacts largely dominates the spatial distribution. Therefore, larger layer thicknesses should be used and higher illumination intensities are necessary to achieve reliable measurement conditions. For the recombination coefficient the opposite tendency is true. The faster the recombination, the higher is the required illumination intensity to reach the same bulk carrier density. Hence, the recombination coefficient is implicitly accounted for in the correct choice of the carrier density range. We finally note that according to Figure 5.2, BACE has the tendency to overestimate the recombination coefficient for relevant carrier densities of $10^{22} - 10^{23}$ m^{-3} (the simulated data lie above the exact rate). This is in part due to the fact that under steady-state illumination, the carrier density profile is never homogeneous: due to recombination with dark charge, the photogenerated hole (electron) density is diminished at the cathode (anode).

Figure 5.2b shows the simulation results for the same parameters as in Figure 5.2a, except here the surface recombination was set to infinity for both contacts. Now, the agreement between theory and simulation is worse for all parameters. In general, the simulated carrier density in the device is lower (and therefore the apparent k_2 is higher) than expected because a significant amount of charge carriers are lost at the contacts due to surface recombination. This also lowers the carrier density in the bulk due to diffusion. The charge carrier density profiles with and without surface recombination for comparison can be found in Figure A2.1 (Appendix A2). Only for the highest bulk recombination coefficient, reasonable agreement is found since in this case bulk recombination still dominates over surface recombination, which means that losses at the contacts are less severe and the carrier density probed by BACE is mainly determined by bimolecular recombination.

Interestingly, none of the cases presented in Figure 5.2a display a recombination order of one, which would be expected especially for dominant surface recombination (low BMR coefficients = insignificant bulk recombination). Our simulations show instead that a slope of one is only observed for very high carrier densities, which cannot be achieved in realistic experiments. The reason for the higher recombination order at low to intermediate carrier densities may lie in the employed contact energetics, where we set the injection barriers in all simulations to be 0.1 eV, only. Sandberg et al. simulated the effect of surface recombination for the case of small (ohmic contacts) and large (non-ohmic contacts) injection barriers.[243] In the former case, band bending within the organic semiconductor creates an energetic barrier for carriers to reach the "wrong contact", and this barrier will be dependent on the carrier density (quasi Fermi-level splitting) in the bulk. As a consequence, the surface recombination current becomes a superlinear (in the limit of dominant surface recombination strictly quadratic) function of the bulk carrier density (see Equation 14 and 16 in Ref.[243]), exactly what we are seeing here. Therefore, if steady-state recombination measurements reveal a second order dependence of the recombination rate, this does not necessarily mean that it is dominated by free carrier encounter in the bulk.

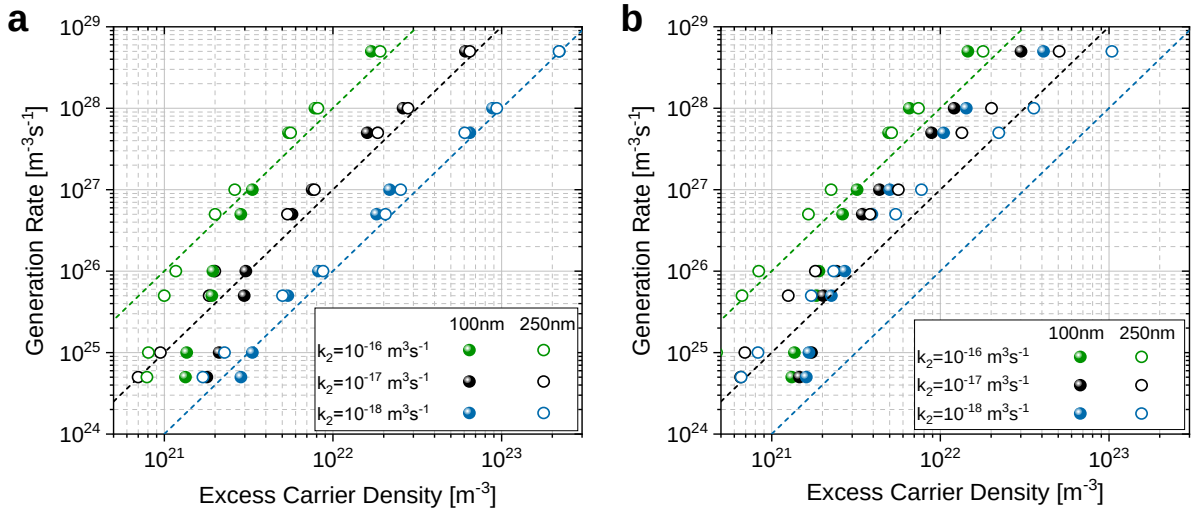

Figure 5.2: Simulation results of bias-assisted charge extraction experiments. a Simulated excess carrier density (dots), calculated according to Equation 5.2 to 5.4 and corrected for the dark charge from the reference measurement at 0 V, as a function of the generation rate for different layer thicknesses and BMR coefficients. Surface recombination at both contacts was set to 0. **b** As in panel a, except that here, the surface recombination was set to infinity at both contacts. In both graphs, the electron and hole mobility were $\mu_e = \mu_h = 10^{-3}$ cm²V⁻¹s⁻¹ and injection barrier was 0.1 eV at both contacts. The dashed lines indicate the carrier density according to $G = R = k_2 n^2$ for each respective BMR coefficient, which serves as an "electrodeless" reference for the simulated values (dots).

As expected, the extracted values of k_2 are closer to the input parameter when going to higher layer thicknesses (250 nm, empty circles), as for thicker devices losses at the contacts become less important for the carrier density in the bulk. However, for the lowest recombination coefficient, the k_2 values from the simulations are still up to one order of magnitude too high and the slope in the log-log plot is smaller than two. Only for the highest recombination coefficient, BACE reproduces the order and the input values of k_2 well.

In summary, in the case of infinite surface recombination, no reliable results regarding the recombination order and coefficient can be obtained from a BACE experiment. Only for very high BMR, carrier densities and layer thicknesses does the bulk recombination dominate over losses at the contacts and the values obtained with BACE are correct. For intermediate and low BMR the contact losses are predominant and this changes the apparent recombination coefficient and order measured with BACE. However, in a single experiment, it cannot be distinguished whether surface recombination is present or not. To exclude the case of infinite surface recombination, BACE experiments should be performed at various layer thicknesses. Only if all curves for all layer thicknesses fall onto one line, reliable results can be expected.

5.4.2. Time-delayed Collection Field

In this section, we discuss the analysis of recombination order and coefficients in time-delayed collection field (TDCF) measurements with special emphasis on the range of validity. A detailed description of the measurement scheme and experimental setup is found in Chapter 3 (section 3.4.). In TDCF, the charge carriers are generated with a short laser pulse at $t = 0$ and, after a variable delay time, extracted with a high reverse bias. As described in the above Methods section, the current transients are integrated over time to yield the density of photogenerated charge carriers exiting the device before the extraction voltage is applied, $n_{\mathrm{pre}}(t_{\mathrm{del}})$, and the photogenerated carrier density being present in the device at the delay time, $n_{\mathrm{coll}}(t_{\mathrm{del}})$. Then,

$n_{\mathrm{tot}}(t_{\mathrm{del}}) = n_{\mathrm{pre}}(t_{\mathrm{del}}) + n_{\mathrm{coll}}(t_{\mathrm{del}})$ is the total extracted charge carrier density, which is the carrier density that survived recombination for a given t_{del}. Note that, as in a real TDCF experiment, measured carrier densities are corrected for the corresponding dark values, which are obtained from TDCF measurement in the dark on the same device and under the same bias conditions.

In contrast to BACE, which relies on the steady-state carrier distribution, the initial density profile of photogenerated electrons and holes is the same, though it might vary spatially depending on the absorption of the active material and cavity effects. In the ideal case, with a homogeneous carrier distribution and no dark-injected charge, the fate of the photogenerated carrier population is given by a simple second order process with a bimolecular recombination coefficient k_2: $\frac{\mathrm{d}n_{\mathrm{tot}}}{\mathrm{d}t} = -k_2 n_{\mathrm{coll}}^2$. Importantly, during the delay the device is usually held at a forward bias close to flat band conditions in order to reduce the internal electric field. Under these conditions, a considerable density of background charge (n_{BG}) due to dark injection from the contacts is expected to be present in the device before the laser pulse, also taking part in the recombination process with the photogenerated carriers. A simplistic model describing this situation has been developed previous to this work in the group of Dieter Neher,[135, 189]

$$\frac{\mathrm{d}n_{\mathrm{tot}}}{\mathrm{d}t} = -k_2\left(n_{\mathrm{coll}}^2 + 2n_{\mathrm{coll}}n_{\mathrm{BG}}\right). \qquad (5.5)$$

According to this expression, the decay of n_{tot} with increasing t_{del} is no more a simply quadratic function of n_{coll}. In order to determine how the recombination process depends on the carrier density, the recombination rate $R(t_{\mathrm{del}}) = (n_{\mathrm{tot}}(t_{\mathrm{del}} + \Delta t) - n_{\mathrm{tot}}(t_{\mathrm{del}}))/\Delta t$ is plotted versus n_{coll} on a double logarithmic scale. Then, the apparent recombination order at a given time delay is read off from the slope δ of the curve. According to this model, for high carrier densities (i.e. high pulse fluences) recombination between photogenerated charge carriers is dominating, leading to a slope of 2, while for low carrier densities, bimolecular recombination with the background charge is dominating, leading to a slope of 1 in the log-log plot. By fitting the experimental data with Equation 5.5 and leaving k_2 and n_{BG} as free fit parameters, the model can be used to extract the recombination coefficient and the effective background charge from the TDCF data.

The derivation of Equation 5.5 is based on a number of simplifying assumptions. First of all, the background carrier density is assumed to be distributed homogeneously across the layer at the time when the photogenerated carriers are inserted. This is probably the most critical point of the model, as the dark carrier profile is governed by the injection, diffusion and recombination. Depending on the exact prebias, layer thickness and height of injection barriers, the background charge might in fact become very inhomogeneous. Second, it is assumed, that recombination is absent during collection and all remaining charge carriers after the delay can be extracted. This approximation might be true for low recombination constants. However, for fast or even dispersive recombination dynamics, losses of charge carriers during extraction cannot be excluded. Last but not least, the model assumes that surface recombination at the contacts is zero, i.e. minority carriers may not leave the device at the “wrong” electrode. It is not clear how the TDCF data is affected, if surface recombination at both contacts would be present. Accordingly, numerical simulations have been performed with different prebias and recombination constants to examine, under controlled conditions, how the dark charge distribution and recombination during extraction affects the data analysis and whether the model is able to produce correct results even if the simplified assumptions are not fulfilled. Finally, the influence of surface recombination on the TDCF data is carefully investigated for different layer thicknesses.

Figure 5.3 shows the results of the TDCF simulations for a 100 nm device with zero surface recombination at the contacts, electron and hole mobilities of $\mu_e = \mu_h = 10^{-3}$ cm^{2}V^{-1}s^{-1} and a BMR coefficient of $k_2 = 1 \times 10^{-17}$ m^{3}s^{-1}. The simulations were performed at a prebias of 0.7 V which is close to the open circuit voltage at one sun for the considered device ($V_{\mathrm{OC}} = 0.74$V at $G = 4 \times 10^{27}$ m^{-3}s^{-1} with an effective bandgap of 1.1eV and an effective DOS of 2.5×10^{25} m^{-3}). Figure 5.3a displays the temporal evolution of the total carrier density n_{tot} (as a function of the time delay) for different initial carrier densities (representing different laser pulse fluences in the measurement). Note that each data point in the graph corresponds to the integral of a simulated TDCF transient. From this graph it is obvious that the temporal decay of the carrier density is more pronounced for higher initial carrier densities. This is expected for a BMR process as it is implemented in the simulation. In Figure 5.3b n_{tot} (full circles) and n_{pre} (open circles) are shown, normalized to n_{tot} at a delay of 5 ns. The colors of the data points correspond to the initial carrier densities shown in Figure 5.3a with dark blue being the lowest and dark orange being the highest initial carrier density. Increasing the delay results in a continuous increase of n_{pre} as more and more charges leave the device prior to the application of the collection pulse. At the same time n_{tot}, being the initially photogenerated charge carrier density reduced by all recombination losses during the delay, exhibits a continuous drop. Finally, in Figure 5.3c, the differential change of the total carrier density $\mathrm{d}n_{\mathrm{tot}}/\mathrm{d}t$ is plotted versus n_{coll} on a double logarithmic scale. The data points for all delays and fluences (same color-code as in Figure 5.3a and b is used) are lying on one line. This result may be expected as the simulation was carried out with a time-independent recombination coefficient. However, as V_{pre} was selected to be smaller than V_{OC}, charge displacement is occurring during the delay, not only reducing the carrier density but also rendering the remaining charge carrier profile more and more inhomogeneous. Still, at high carrier densities, the rapid built-up of space charge prevents further extraction and leads to rather homogeneous, recombination-dominated carrier profiles.[244] Therefore, the data in this region can be described with a simple second order recombination model according to $\mathrm{d}n/\mathrm{d}t = -k_2 n^2$, where we find k_2 to be almost equal to the input value of 10^{-17} m^{3}s^{-1} (solid red line). For low carrier densities the curve is determined by recombination of photogenerated carriers with the background charge and follows a first order decay (black dashed line). We have then fitted the entire carrier density range with Equation 5.5 (solid grey line), leaving both k_2 and the background charge n_{BG} as free fit parameters. The result of the best fit is $k_2 = 0.93 \times 10^{-17}$ m^{3}s^{-1} which is very close to the input value. Note, that accurate fits can only be achieved if the measured data cover a sufficiently large fluence range, which includes both limiting cases of pure first and second order. The value of for n_{BG} in the fit in Figure 5.3c is 1.6×10^{22} m^{-3}, and the meaning of this value will be discussed in more detail below.

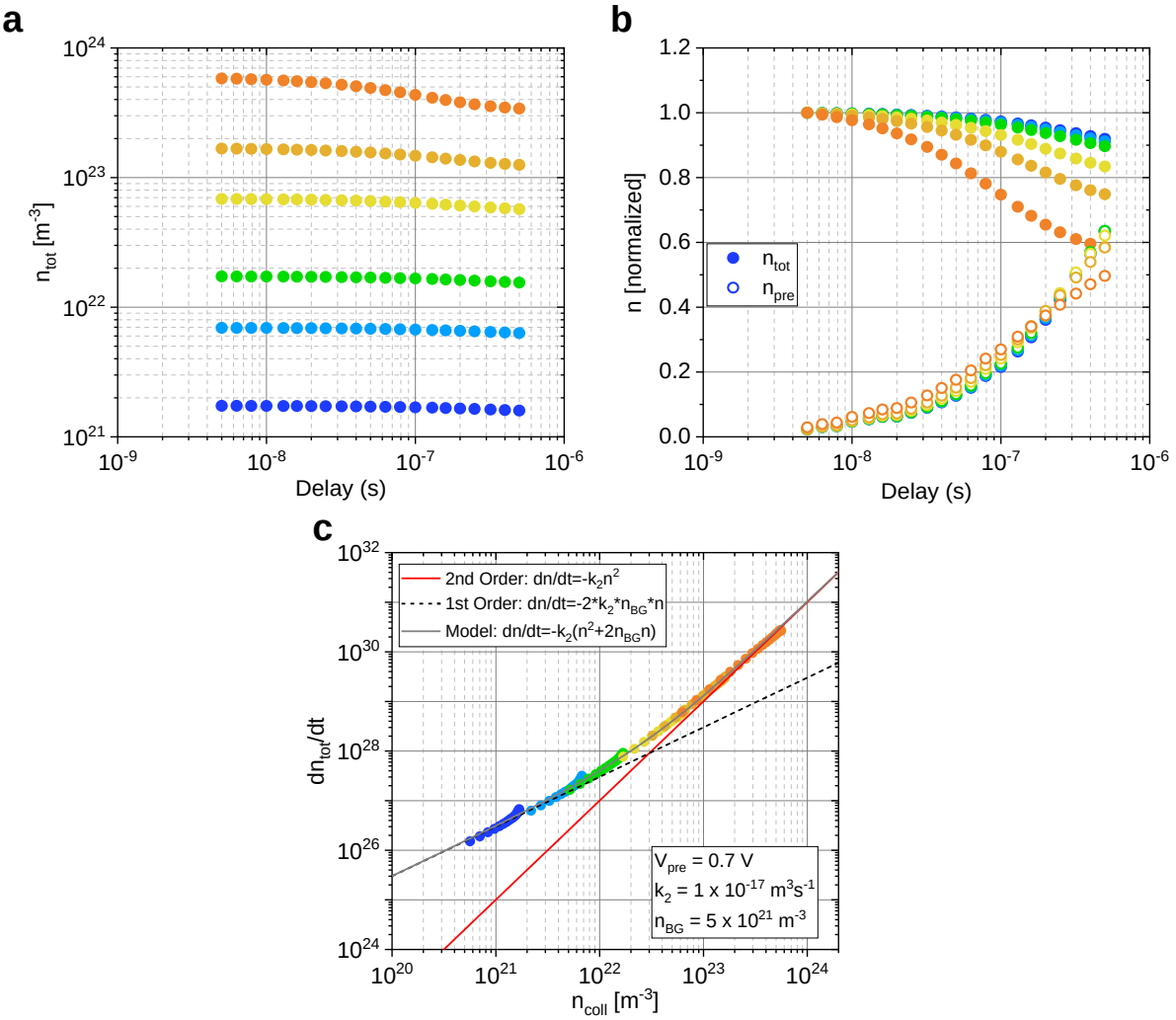

Figure 5.3: Simulation results of time-delayed collection field experiments. a n_{tot}, which is the sum of the extracted charge before and after application of the collection pulse, n_{pre} and n_{coll}, respectively, as a function of the time delay between laser pulse and extraction pulse. Simulations were performed for different initial carrier densities (corresponding to the different colors in the graph). Each data point represents the integral of a simulated TDCF transient. The parameters used in this simulation were $d = 100$ nm, $k_2 = 1 \times 10^{-17}$ m^{3}s^{-1}, $\mu_e = \mu_h = 10^{-3}$ cm^{2}V^{-1}s^{-1}, no surface recombination. V_{pre} was set to 0.7 V which is only 0.04 V below the V_{OC} at a generation rate G of 4×10^{27} m^{-3}s^{-1}. **b** n_{tot} and n_{pre} normalized to the initial n_{tot} (for a delay of 5 ns) as a function of the delay time. The colors of the data points correspond to the initial carrier densities shown in panel a. **c** Differential carrier density ($\mathrm{d}n_{\mathrm{tot}}/\mathrm{d}t$) vs. collected carrier density during collection pulse (n_{coll}). The same color code as in panel a and b is used. Also shown is a fit of the high fluence data with strict second order recombination (solid red line), of the low fluence data with first order recombination (black dashed line), and of the entire data set with a model considering bimolecular recombination in the presence of a homogeneous background charge, according to Equation 5.5 (solid grey line).

The effect of prebias and dark charge

It has been pointed out that the accuracy of TDCF to determine the order and coefficient of NGR can be falsified by the recombination of photogenerated charges with dark-injected charges.[245] A way out of this problem may be to use a prebias much smaller than the built-in potential, but this comes at the cost of accelerated extraction during the delay. Therefore, simulations have been performed at V_{pre} = 0.6 V and V_{pre} = 0.8 V, below and above the V_{OC} of the cell, with the resulting differential decay plots shown in Figure 5.4. All other parameters were the same as in

Figure 5.3. One main difference between these cases is the distribution of the dark charge due to the different prebias conditions (compare Figure 5.5a). At 0.6 V, significantly less background charge is present in the device compared to 0.7 V and 0.8 V, and the distribution is very inhomogeneous. In addition, the charge displacement during delay is more significant in this case. This is also seen in Figure A2.2 (Appendix A2), where we plot n_{tot} and n_{pre} as a function of delay time. For $V_{\mathrm{pre}} = 0.6$ V, nearly 50 % of the initially present charge is extracted after 100-200 ns, competing efficiently with NGR. Higher initial carrier densities give rise to a slower extraction, due to the formation of space charge as pointed out above. On the other hand, at 0.8 V the amount of background charge is strongly increased, and the distribution is quite homogeneous across the layer while charge extraction at V_{pre} is slow. Despite these differences, the differential decay data can be well fitted with Equation 5.5 over the entire range for either prebias, with the fit parameters $k_2 = 0.973 \times 10^{-17}$ m^{3}s^{-1} and $n_{\mathrm{BG}} = 3.7 \times 10^{21}$ m^{-3} for 0.6 V and $k_2 = 0.93 \times 10^{-17}$ m^{3}s^{-1} and $n_{\mathrm{BG}} = 5.3 \times 10^{22}$ m^{-3} for 0.8 V. Again, the extracted values for k_2 are very close to the input values of the simulation. We notice, however, that the low fluence traces in the $V_{\mathrm{pre}} = 0.6$ V differential decay plot display an apparent higher recombination rate at early times. This is mainly due to the initial recombination of photogenerated charges with dark-injected carriers, which rapidly slows down due to the small (and inhomogeneously distributed) dark change and this small prebias.

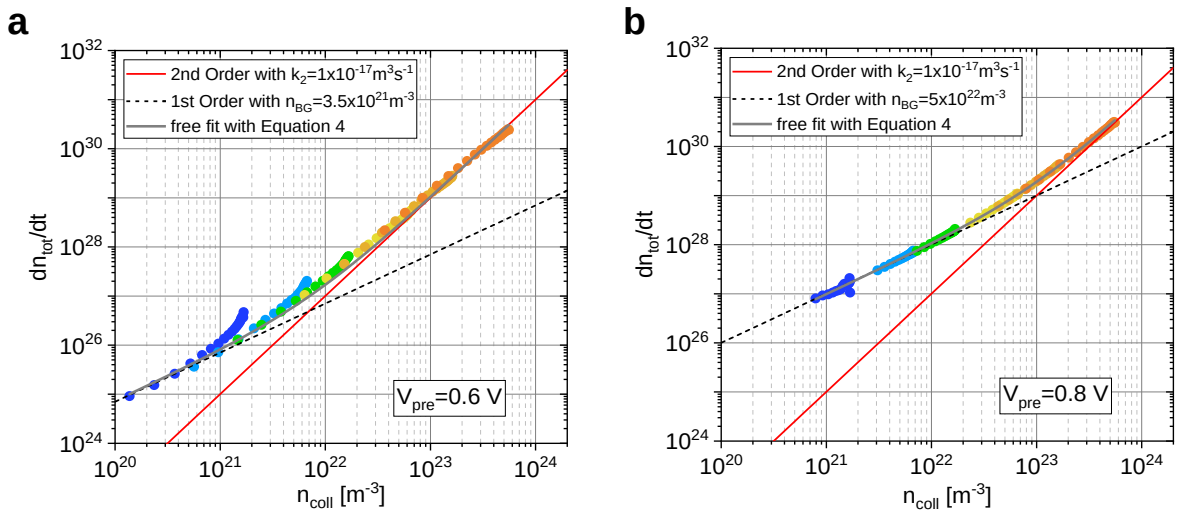

Figure 5.4: Simulation of differential decay plots at different prebias in time-delayed collection field experiments. Differential carrier density ($\mathrm{d}n_{\mathrm{tot}}/\mathrm{d}t$) vs. collected carrier density (n_{coll}) for the same device as in Figure 5.3 but at different prebias: **a** $V_{\mathrm{pre}} = 0.6$ V and **b** $V_{\mathrm{pre}} = 0.8$ V. The red lines show strict second order recombination with the input value $k_2 = 1 \times 10^{-17}$ m^{3}s^{-1}. The black dashed lines follow a first order model with $k_2 = 1 \times 10^{-17}$ m^{3}s^{-1} and $n_{\mathrm{BG}} = 3.5 \times 10^{21}$ m^{-3} in panel a, and $n_{\mathrm{BG}} = 5 \times 10^{22}$ m^{-3} in panel b. The grey lines are fits according to Equation 5.5 with k_2 and n_{BG} as free fit parameters. Best fits were obtained with $k_2 = 9.73 \times 10^{-18}$ m^{3}s^{-1} and $n_{\mathrm{BG}} = 3.7 \times 10^{21}$ m^{-3} in panel a, and $k_2 = 9.3 \times 10^{-18}$ m^{3}s^{-1}, $n_{\mathrm{BG}} = 5.3 \times 10^{22}$ m^{-3} in panel b.

We now address the question, how the extracted n_{BG} can be related to the real background charge distribution. Figure 5.5a displays the background carrier distribution for the three different prebias conditions used in Figure 5.4. As expected, the carrier density in the device increases and the distribution becomes more homogeneous for increasing prebias. Figure 5.5b plots the mean electron density in the active layer, the electron density in the center, the drift length weighted carrier density (which would be measured with dark-BACE at the particular prebias) and the value of n_{BG} gained from the fit of the TDCF recombination plots as function of prebias. Notably, the latter ones agree very well, where the slightly higher n_{BG} from the TDCF fits can be attributed to

the high carrier densities in the vicinity of the contacts that speed up recombination of the photogenerated carriers with dark charge. The best agreement is reached for the highest prebias where the distribution is the most homogenous.

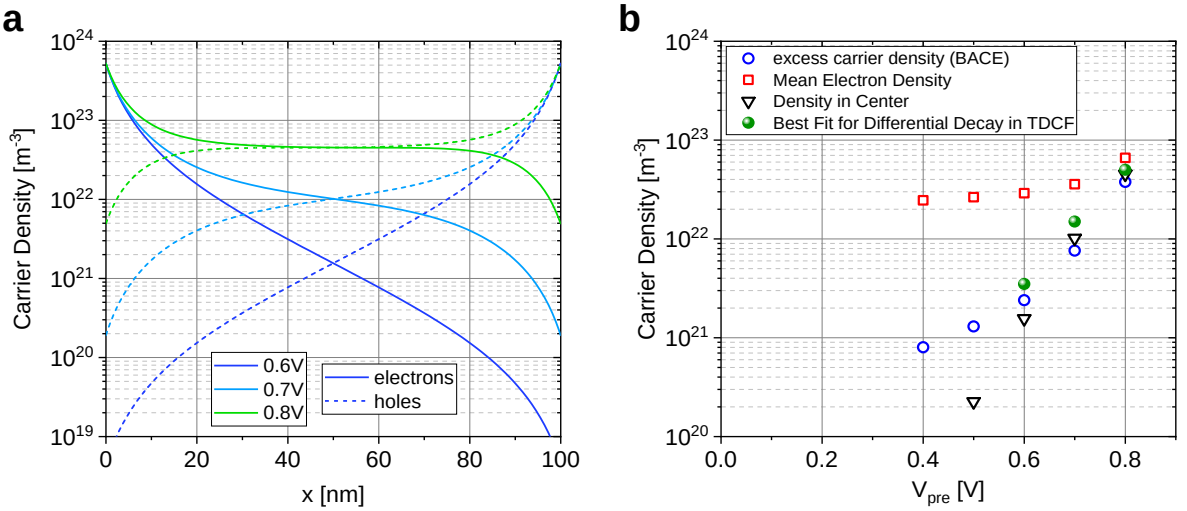

Figure 5.5: Simulated dark-charge carrier density profiles and excess carrier density. a Simulated charge carrier density profiles in the dark for the device described in Figure 5.4 at 0.6 V, 0.7 V and 0.8 V. **b** Based on the carrier density profiles in panel a, this graph displays the drift-length weighted excess carrier density as measured with dark-BACE, including a correction by a reference measurement with the same voltage jump but starting at 0 V (empty blue circles), the mean electron density (empty red squares) and the carrier density in the center of the device (empty black triangles). Also shown are the values n_{BG} used for the best fit for the differential decay in Figure 5.3c and Figure 5.4 (full green circles).

To further screen the valid parameter range of the model, simulations were then performed with higher BMR coefficients of $k_2 = 1 \times 10^{-16}$ m^{3}s^{-1} (Figure 5.6a) and $k_2 = 1 \times 10^{-15}$ m^{3}s^{-1} (Figure 5.6b), the latter corresponding to Langevin-type recombination. In a real TDCF experiment, the collection voltage is limited by the breakdown voltage of the device and, in case of very high recombination, it cannot be chosen high enough to avoid recombination during extraction. Therefore, for such high BMR coefficients, not all the charges that survived recombination during the delay can be extracted by the collection pulse and n_{coll} will be in general too small. This can be seen from the lower "initially extracted" carrier densities in Figure 5.6b compared to Figure 5.6a, despite the fact that both simulations were performed with the same input parameters (except the value of k_2). Nevertheless, in both cases the differential decay data obey Equation 5.5, yielding BMR coefficients ($k_2 = 1.2 \times 10^{-16}$ m^{3}s^{-1} in (a) and $k_2 = 1.6 \times 10^{-15}$ m^{3}s^{-1} in (b)) close to the input values in the simulation. Also, the values for n_{BG} obtained from the fits (1.9×10^{21} m^{-3} in (a) and 2.3×10^{20} m^{-3} in (b)) resemble the one order of magnitude difference in the BMR coefficient.

Here, we like to comment on the conclusions from the recent study by U. Würfel and coworkers on the reliability of recombination studies with TDCF.[245] Their drift-diffusion simulation showed (Figure 4 and 5 in that work) that the determination of the (time-dependent) recombination with TDCF becomes unreliable for initial carrier densities of 5×10^{21} m^{-3} and below. This corresponds to a fluence of ca. 20 nJcm^{-2} and smaller, depending on the exact excitation wavelength and thickness. Our TDCF recombination studies always include measurements with fluences of hundreds of nJcm^{-2} and more. This is to ensure that recombination is dominated by photogenerated charges. For a too low fluence, (and laser induced carrier density), TDCF

measurements do not provide reliable data of the charge recombination dynamics because dark-injected charge dominates the fate of the photogenerated carriers (as discussed in detail in Würfel's work). This is nicely shown in the previous Figure 5.3, where traces with initial carrier densities below 1×10^{22} m^{-3} lead to an apparent recombination order of 1. Therefore, it is of great importance to measure at sufficiently high carrier densities, where a clear second order decay is visible.

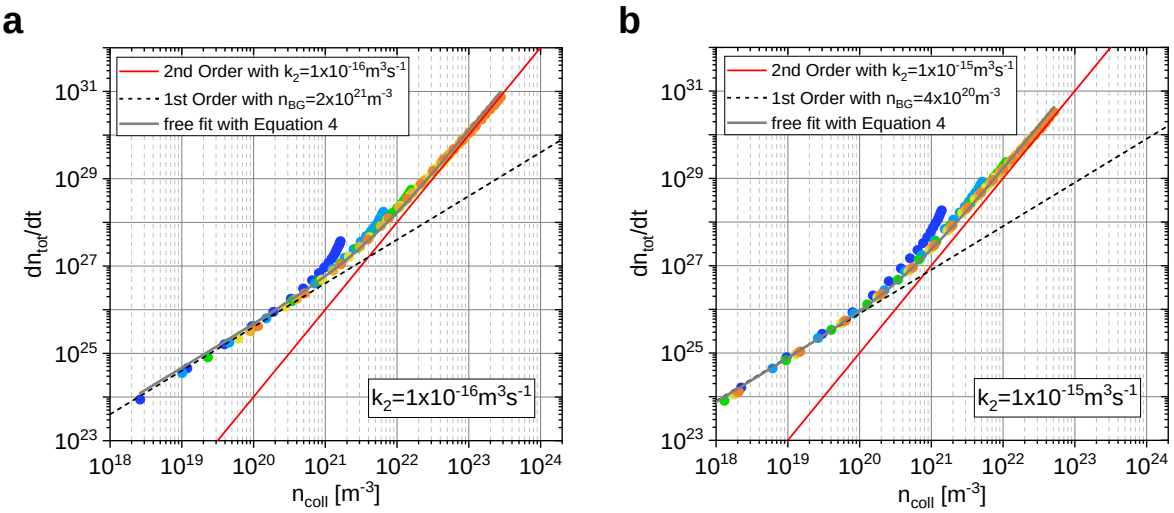

Figure 5.6: Simulation of differential decay plots with different recombination coefficient in time-delayed collection field experiments. Differential decay data for a 100 nm device with **a** $k_2 = 1 \times 10^{-16}$ m^{3}s^{-1} and **b** $k_2 = 1 \times 10^{-15}$ m^{3}s^{-1}. Mobilities were $\mu_e = \mu_h = 10^{-3}$ cm^{2}V^{-1}s^{-1} as before and surface recombination was turned off. The prebias was chosen to be 0.1 V lower than the V_{OC} at one sun which is $V_{pre} = 0.58$ V in panel a and $V_{pre} = 0.52$ V in panel b. The parameters from the free fits with Equation 5.5 (solid grey lines) were $k_2 = 1.2 \times 10^{-16}$ m^{3}s^{-1} and $n_{BG} = 1.9 \times 10^{21}$ m^{-3} for panel a and $k_2 = 1.6 \times 10^{-15}$ m^{3}s^{-1} and $n_{BG} = 2.3 \times 10^{20}$ m^{-3} for panel b.

To conclude this part, BACE and TDCF provide a consistent set of data in the absence of surface recombination. The differential decay data can be consistently explained over 3 orders of magnitude with a model utilizing bimolecular recombination in the presence of a homogenous "effective" background carrier density. Notably, k_2 values extracted from the high carrier density range in TDCF agrees exactly with the value from photo-BACE. Also, there is very little difference in the value of the background carrier density deduced from the simple fit to the low carrier density TDCF data and from dark-BACE. Clearly, the situation will change drastically in case of dispersive recombination, which has been treated extensively in different publications,[112, 189, 204] and is however not subject of this thesis.

The effect of surface recombination

If finite surface recombination at both contacts is implemented in the simulation (Figure 5.7), features of a very fast initial decay along with an apparent high recombination order appear, in particular in traces with lower initial carrier density. The reason for these features is the initial fast surface recombination of minority carriers at the "wrong" electrode, which is holes at the cathode and electrons at the anode. These "missing" charges will significantly contribute to the reduction of the extracted charge density, as according to Equation 5.2 and Equation 5.3, they have a maximum distance to the electrode through which they are collected upon application of the collection bias. As expected, the effect becomes less pronounced for increasing fluence and

thicker active layers, when bulk BMR dominates the carrier loss. The reason for the fast slow-down of the carrier loss due to surface recombination lies in the fact that this process rapidly depletes the minority carrier reservoir near the electrodes, which gradually reduces the speed at which dark-injected charge recombines with photogenerated carriers. In line with this interpretation, this decay becomes steeper for thicker layers, because losses due to surface recombination of minority carriers close to the contacts contribute now only little to the overall charge carrier dynamics.

A free fit to the long-time decay data with Equation 5.5 still gives k_2 values that are very close to the input values. For a meaningful fit it is important that the data show a clear (bulk BMR dominating) region with a slope 2. Also, the early decay data, which are clearly dominated by surface losses, have to be omitted. If these constrains are carefully considered, TDCF is a reliable method for determining BMR coefficients, even in the case of surface recombination. However, the value for n_{BG} obtained from a fit with Equation 5.5 cannot be unambiguously attributed to a background charge. This is because surface recombination causes an additional first order contribution, even for low carrier densities.

The appearance of rapid early time recombination traces in the differential decay data with surface recombination reminds of the characteristic decay pattern of dispersive recombination.[204] However, in contrast to dispersive BMR, the extra contribution from surface recombination follows a strict first order dependence on carrier density (see the dashed lines connecting the initial recombination data in Figure 5.7a,b). Equitemporal fits to the data sets with increasing initial carrier density give a recombination order close to 1 for all time delays (see Figure A2.3, Appendix A2), allowing to safely disentangle surface recombination from dispersive higher order recombination.

To summarize, surface recombination has a significant effect on the early time recombination data in TDCF, but this extra recombination loss decreases continuously with time. As a consequence, TDCF traces for different fluences merge to a common line, and the analysis of this line with Equation 5.5 yields the correct value for k_2. BACE, on the other hand, yields a significantly higher recombination rate and apparent BMR coefficient. Therefore, surface recombination should become apparent when comparing the results from these two techniques.

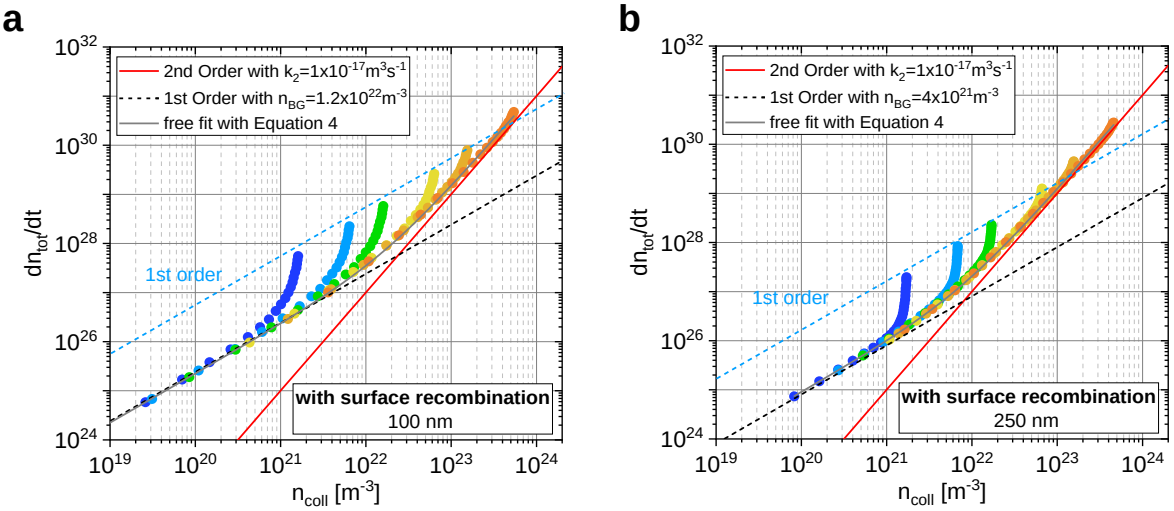

Figure 5.7: Simulation of differential decay plots with surface recombination in time-delayed collection field experiments. Differential decay data for **a** 100 nm and **b** 250 nm device with infinite surface recombination at both contacts. The input parameters were $k_2 = 1 \times 10^{-17}$ m^{3}s^{-1}, $\mu_e = \mu_h = 10^{-3}$ cm^{2}V^{-1}s^{-1}. We set $V_{\mathrm{pre}} = 0.6$ V in panel a $V_{\mathrm{pre}} =$ = 0.62 V in panel b, 0.1 V below the corresponding V_{OC} of 0.7 and 0.72 V, respectively. The solid grey lines are free fits with Equation 5.5 and yield $k_2 = 1.3 \times 10^{-17}$ m^{3}s^{-1} and $n_{\mathrm{BG}} = 0.9 \times 10^{22}$ m^{-3} in panel a and $k_2 = 1.15 \times 10^{-17}$ m^{3}s^{-1} and $n_{\mathrm{BG}} = 3.9 \times 10^{21}$ m^{-3} in panel b.

5.5. Comparison with Experimental Data

Figure 5.8 shows the results of a combined TDCF/BACE study of a device with a 100 nm thick blend of the donor polymer PM6 with the non-fullerene acceptor Y6 (see Chapter 3 for the chemical structure of the compounds). The devices were prepared in inverted structure as in the previous chapter. The PM6:Y6 material combination gives solar cells with a PCE above 15 % for rather thin devices (150 nm and below), while thicker devices suffer from a continuous drop in FF – indicative of significant nongeminate losses. TDCF was measured with different initial fluences and at three different prebias. We notice a weak early time slow-down of the recombination rate for some of the low fluence traces. While this observation may hint at an initial carrier loss due to surface recombination or recombination of photogenerated with dark-injected charge as pointed out above, there is no clear correlation with prebias. The $R(n)$ data then quickly merge to a common line, which has a slope of 2 for high carrier densities, indicating that bimolecular recombination is the dominating recombination process in this blend. To fit the data with Equation 5.5, we determined the dark background charge density n_{BG} at each prebias, using dark-BACE. As expected, increasing the V_{pre} towards V_{OC} goes along with a pronounced increase of n_{BG}. Despite the large variation of the bias condition, all data can be consistently fitted by a strict bimolecular recombination process, yielding a bias- and intensity independent BMR coefficient $k_2 = 1.7 \times 10^{-17}$ m^{3}s^{-1}, as revealed in Chapter 4 as well.

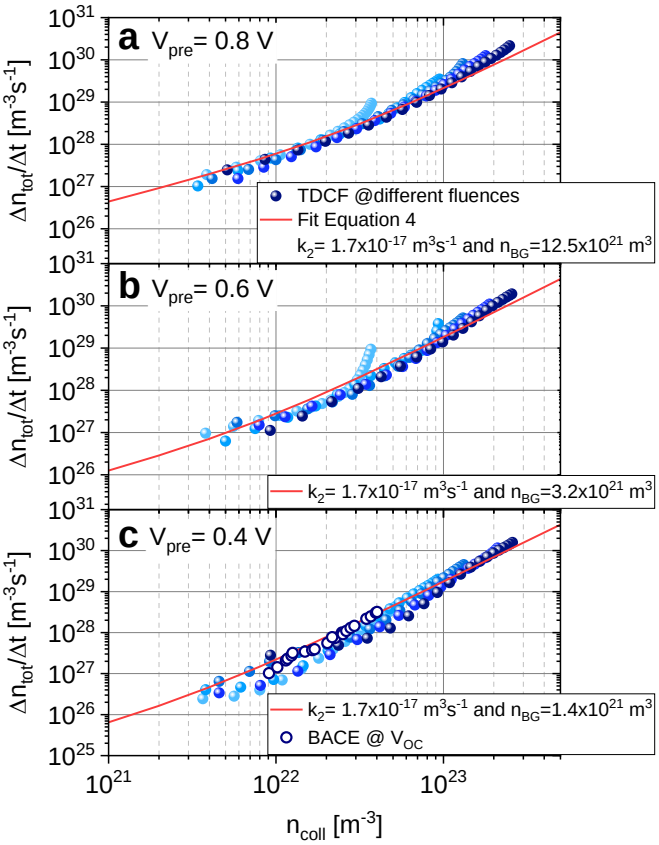

Figure 5.8: Differential decay plots from time-delayed collection field experiments in PM6:Y6 devices. TDCF differential decay data (solid circles) of a device with a 100 nm thick PM6:Y6 blend, measured at different fluences (between 0.2 and 4 µJcm^{-2}) and different prebias: **a** $V_{\mathrm{pre}} = 0.8$ V **b** $V_{\mathrm{pre}} = 0.6$ V **c** $V_{\mathrm{pre}} = 0.4$ V (compared to a V_{OC} of 0.84 V under simulated AM1.5G conditions). The solid red lines are fits to Equation 5.5 with the fit parameters k_2 and n_{BG} (measured by dark-BACE) as denoted in the graph. The empty circles in panel c correspond to BACE data measured under illumination at V_{OC}.

These findings are in perfect agreement with the prediction from the simulations above in absence of surface recombination. Also plotted in Figure 5.8c is the result of steady-state recombination measurements with BACE (open circles) on PM6:Y6. The measurement was performed with increasing steady-state illumination intensity at the respective V_{OC} where the generation rate G is equal to the recombination rate R. Therefore, the BACE data can be plotted together with the differential decay data from TDCF. It is remarkable how well the steady-state data matches the transient data, even though the conditions for both measurements are distinctly different. We conclude that nongeminate losses in this thin high-performance blend is entirely determined by a second order recombination process in the bulk and that surface recombination is of minor importance.

5.6. Discussion and Conclusions

By performing 1D drift-diffusion simulations of BACE and TDCF experiments, we examine the applicability of the two methods to determine the order of recombination and the BMR coefficient for a wide range of parameters, with and without surface recombination.

If surface recombination is excluded, BACE measurements yield accurate values for the recombination order and coefficient, provided that the illumination intensity (photogenerated carrier density) is sufficiently high. Under these conditions, the total (injected and photogenerated) carrier profiles are fairly homogeneous except in the direct vicinity of the electrodes. As expected and reported earlier, decreasing the active layer thickness causes deviations from the predicted BMR behavior, in particular at low carrier densities.

TDCF, on the other hand, reveals highly reliable values for k_2, irrespective of the layer thickness, prebias, and BMR coefficient. This has two main reasons. First, the carrier profiles of the photogenerated electrons and holes are initially the same, and are more homogeneous than the steady-state profiles. Secondly, TDCF allows higher carrier densities to be generated, thereby reducing the effect of dark injected carriers on recombination. This conclusion holds even for the case of high BMR coefficients, where photogenerated charges recombine during extraction. Interestingly, the functional dependence of the excess recombination rate R as function of excess carrier density can be exactly reproduced with a simple model which assumes a homogeneous background density (Equation 5.5), and this background density is (within a factor of 2) identical to the carrier density deduced from dark-BACE experiments. Therefore, while TDCF provides accurate values for k_2 if measurements are performed over a wide enough fluence range, BACE is a well-suited complimentary technique to confirm the results from the fitting of the TDCF data. In previous experimental work, BACE and TDCF results could be consistently explained with the very same set of parameters.[135, 216]

The situation changes drastically if surface recombination comes into play. In this case, recombination properties as deduced from BACE measurements do not, anymore, represent the bulk properties. This is because of the extra recombination loss at the electrodes and the concurrent reduction in carrier density near the contacts. It is only at high bulk recombination rates that BACE measurements provide accurate results. Importantly, if BACE measurements are performed for only one thickness, it is very difficult to distinguish between bulk and surface recombination, e.g. to decide whether an apparent high k_2 is due to fast bulk recombination or it comes from additional surface recombination.

Fortunately, TDCF is suited to differentiate between these two effects. In a transient experiment, surface recombination is strongest at early times, while bulk recombination (either between photogenerated carriers or between photogenerated and dark-injected carriers) proceeds throughout the entire time range. This is nicely reproduced by the fast-early time recombination in Figure 5.7, which remains of first order in carrier density during the entire time period but slows down rapidly, finally converting to a common $R(n)$ dependence. Notably, the final $R(n)$ dependence is again consistent with Equation 5.5, and it allows one to obtain accurate values for k_2 if experiments can be performed up to fairly high fluences.

Chapter 6. Recombination between Photogenerated and Electrode-Induced Charges Dominates the Fill Factor Losses in Optimized Organic Solar Cells

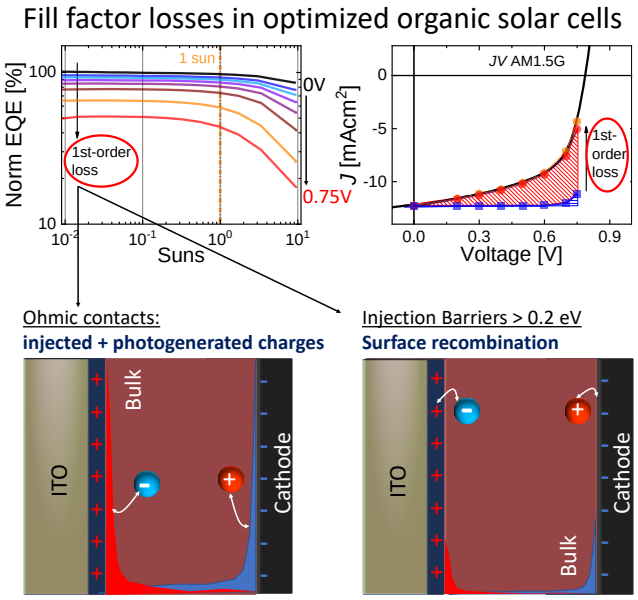

The analysis of the photocurrent dependence on illumination intensity is often used to identify the order of free charge recombination. This combined experimental/simulation work aimed to investigate the origin of the observed linear intensity dependence. It was found that this linear dependence is a result of bimolecular recombination between photogenerated and dark-injected charge near the electrodes in the bulk of the active layer. This type of recombination dominates the fill factor losses in optimized organic solar cells. This work further identifies under which conditions these losses can be mitigated, by also evaluating surface recombination.

This chapter is an adapted preprint of:

U. Würfel, L. Perdigón-Toro, J. Kurpiers, C. M. Wolff, P. Caprioglio, J. J. Rech, J. Zhu, X. Zhan, W. You, S. Shoaee, D. Neher, and M. Stolterfoht. Recombination between Photogenerated and Electrode-Induced Charges Dominates the Fill Factor Losses in Optimized Organic Solar Cells. *J. Phys. Chem. Lett.* **2019**, 10, 3473–3480.

6.1. Abstract

Charge extraction in organic solar cells (OSCs) is commonly believed to be limited by bimolecular recombination of photogenerated charges. Yet, the fill factor of OSCs is usually almost entirely governed by recombination processes that scale with the first order of the light intensity. This linear loss was often interpreted to be a consequence of geminate or trap-assisted recombination. Numerical simulations show that this linear dependence is a direct consequence of the large amount of excess dark charge near the contact. The first order losses increase with decreasing mobility of minority carriers, and we discuss the impact of several material and device parameters on this loss mechanism. This work highlights that OSCs are especially vulnerable to injected charges as a result of their poor charge transport properties. This implicates that dark charges need to be better accounted for when interpreting electro-optical measurements and charge collection based on simple figures of merit.

6.2. Introduction

Organic semiconductors are promising materials for photovoltaic energy conversion and other electronic devices.[246, 247] In particular with the emergence of non-fullerene acceptors (NFAs),[28, 248] organic solar cells (OSCs) have experienced an unprecedented rise in power conversion efficiencies (PCEs), as extensively mentioned in previous chapters.[29] However, the comparatively low fill factor (< 80%) of OSCs with absorber layer thicknesses relevant for the application of printing technologies, still represents a major challenge for commercialization. Therefore, it is essential to understand how well charges are extracted and where they are lost in the device.[249, 250] Over the years, many different models have been used to explain the fill factor losses in OSCs, such as bimolecular recombination, trap-assisted recombination and/or field-dependent CT-state dissociation.

Recently, much evidence emerged that it is bimolecular recombination of free charge carriers that leads to fill factor losses due to the comparatively slow charge transport in disordered organic semiconductors.[207] This causes an accumulation of charge carriers and hence increases recombination losses,[219, 249] or leads to field-free regions.[251] The competition of extraction (k_{e}) and second-order bimolecular recombination ($k_{\mathrm{r}} \sim k_2 np$) can be described with simple analytical expressions or figures of merit (FOM);[219, 250, 252, 253] and these FOMs have been successfully applied to a large number of OSCs from various groups.[219, 250, 252, 253] However, intensity-dependent photocurrent (IPC) and related measurements in steady-state might suggest an entirely different picture.[254–257] For example, a slope (α) close to unity, fitted to the IPC plotted in log-log, is often interpreted to be a consequence of a dominant monomolecular recombination process or negligible bimolecular recombination.[258–260] Based on this approach, several groups have proposed techniques to quantify bimolecular recombination losses from the deviation of α from unity.[218, 253, 261] Similarly, early studies by Cowan et al.[254] showed that the photocurrent (J_{ph}) losses scale mostly linearly with light intensity (I) from short-circuit conditions to voltages beyond the maximum power point. The first order recombination losses manifested thereby as a fill factor (FF) that is almost independent of light intensity. These losses were attributed to nongeminate recombination of mobile carriers with interfacial traps, while other groups have also drawn similar conclusions.[254, 256, 260, 262, 263] These results seem to be largely inconsistent with significant bimolecular recombination (being a second order process with respect to the free charge carrier density) which would lead to a strong dependence of the fill factor on the light intensity. Although, we note that a few earlier publications pointed out that a linear dependence of recombination on the light intensity does not

imply that the underlying recombination process depends linearly on the free carrier density.[264] Nevertheless, other studies have attributed these first order losses to an electric-field dependent charge-transfer state (CT) dissociation governing the current-density vs. voltage (*J-V*) characteristics.[265–267] However, this appears to be in contrast to the results of many transient studies, e.g. time-delayed-collection field (TDCF) experiments,[30, 219, 268, 269] or ultrafast spectroscopic measurements,[270, 271] where an electric field independent dissociation of CT states was often found, at least in relatively efficient bulk-heterojunction solar cells.[63, 219, 248] Considering these inconsistencies and different explanations of the FF, a conclusive understanding about the main photocurrent losses in the power generating regime remains still an important, yet challenging task.

6.3. Recombination Order along the *J-V* Curve

In order to assess the recombination order in the power generating regime of the *JV*-curve we employed IPC measurements (see methods, section 3.3.).[257, 272, 273] In the following, we will refer to the recombination order with respect to the light intensity (the terminology is further discussed in Note A3.1, Appendix A3). First, we demonstrate the IPC results on an archetypical organic solar cell blend PTB7:$PC_{70}BM$ (1:1.5 w/w),[274] as well as on a high efficiency non-fullerene system FTAZ:IDIC (1:1.5 w/w) with above 10% power conversion efficiency.[26, 157, 275] The device fabrication details are found in Note A3.2, Appendix A3. The solar cell parameters of these two blends are shown in Table 6.1. Moreover, to check the generality of our observations we investigated a large number of polymer and small-molecule solar cells as shown in Figure A3.1 (Appendix A3). The chemical structures of all materials used in this study are shown in Figure A3.2 (Appendix A3).

Table 6.1: Photovoltaic performance parameters of organic solar cells[a]

Device	J_{SC} [mAcm^{-2}]	FF [%]	V_{OC} [V]	PCE [%]
PTB7:$PC_{70}BM$ (1:1.5), d = 80 nm	13.2 ± 1.3 (15.3)	56.5 ± 2.1 (56.1)	0.777 ± 0.01 (0.767)	5.8 ± 0.4 (6.6)
FTAZ:IDIC (1:1.5), d = 100 nm	17.4 ± 0.7 (18.6)	68 ± 2.7 (67.3)	0.847 ± 0.004 (0.849)	10 ± 0.3 (10.6)

[a]Average power conversion efficiencies of the studied organic solar cells with optimized active layer thickness (d) as calculated from 18 devices for each blend including the standard errors of the short-circuit current density (J_{SC}), open-circuit voltage (V_{OC}) and fill factor (FF). Record parameters are displayed in brackets.

In the PTB7:$PC_{70}BM$ blend, under short-circuit conditions, we observe a linear increase of the photocurrent with laser power (or equivalently a constant external quantum efficiency, EQE) from 10^{-2} to approximately 5 suns (Figure 6.1a). This suggests the absence of higher-order recombination losses at short-circuit conditions and "1 sun" although in forward bias and at higher laser powers, non-linear losses become apparent from the downward bend of the EQE. Under 1 sun conditions, it can be seen that the EQE losses originate almost exclusively from first order recombination. Therefore, as shown in Figure 6.1b, the shape of the *J-V* curve in the power generating regime is, in contrast to the common belief, largely controlled by linear recombination losses (in addition to the dark current). Figure 6.1c and Figure 6.1d show analogous measurements for a FTAZ:IDIC blend with close to 10% PCE.

In order to check the influence of geminate recombination, i.e., field-dependent exciton or CT state dissociation we conducted time-delayed collection field (TDCF) experiments.[63, 219, 248] For

both cells, the external generation efficiency (EGE) is essentially flat as a function of the forward bias up to voltages close to V_{OC} as shown in Figure A3.3 (Appendix A3), which rules out a significant impact of geminate recombination on these first-order recombination losses. We also emphasize that the strong contribution of a recombination loss which is strictly linear in light intensity appears in all optimized organic solar cells that we have studied so far, with several further examples shown in Figure A3.1 (Appendix A3).

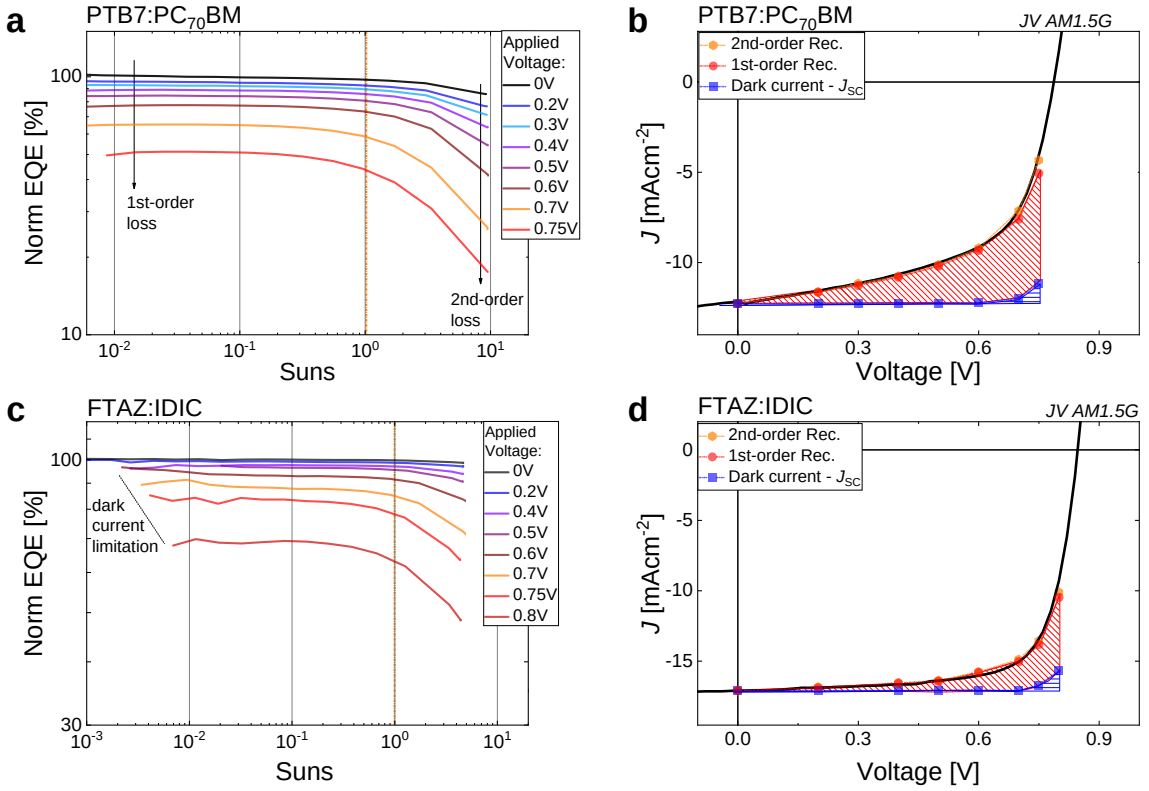

Figure 6.1: Intensity-dependent external quantum efficiency and FF losses in PTB7:PC$_{70}$BM and FTAZ:IDIC solar cells. Intensity-dependent external quantum efficiency (EQE) at different applied voltages from short-circuit close to open-circuit conditions for **a** 80 nm thick PTB7:PC$_{70}$BM (1:1.5 w/w) and c 100 nm thick FTAZ:IDIC (1:1.5 w/w) cells. The **EQE is obtained from the ratio of the photocurrent (light minus the dark current) and the illumination intensity and plotted versus equivalent suns. The 1-sun equivalent laser power (at the used excitation wavelength of 445 nm) is defined where the solar cell current output matches the J_{SC} under AM1.5G i**rradiation. The corresponding *J-V* curves of the PTB7:PC$_{70}$BM blend in panel **b** and the FTAZ:IDIC blend in panel **d** are shown right. The FF losses are decoupled into contributions from first- and second order recombination processes, as well as the dark current. It is evident that the shape of the *J-V* curve is determined by first order recombination losses resulting in intensity independent FF losses in both systems.

6.4. Numerical Simulations – Origin of First Order Recombination Losses

We first aimed to demonstrate the origin of these first order losses based on the example of the PTB7:PC$_{70}$BM blend using drift-diffusion simulations based on bimolecular and surface recombination only.[164, 276] The used parameters are given in Table A3.1 (Appendix A3). For simplicity we assumed a homogeneous generation rate ($G_{1\,\mathrm{sun}} \sim 1 \times 10^{-22}\,\mathrm{cm^{-3}s^{-1}}$), no injection barriers for electrons and holes, and balanced mobilities $\mu_e = \mu_h = 10^{-3}\,\mathrm{cm^2V^{-1}s^{-1}}$.[257, 277] Figure 6.2a shows the photocurrent normalized to the generation current J_{ph}/J_G as a function of voltage for four different illumination intensities while Figure 6.2b shows J_{ph}/J_G as a function of

illumination intensity for different applied voltages. The light intensity independent FF of the J_{ph}/J_G vs. *V* curves in Figure 6.2a indicates the presence of substantial first order recombination (shaded purple area) while second order recombination losses (shaded orange area) appear at higher intensities (> 10 suns). Equivalently, linear and non-linear losses are visible in the simulated IPC plot (Figure 6.2b). Thus, the simulations can accurately reproduce the presence of these recombination losses in the PTB7:$PC_{70}BM$ blend.

Figure 6.2c and Figure 6.2d reveal a high density of majority carriers near the electrodes in the bulk of the active layer even in the dark (shaded area) as discussed in several previous publications.[131–133, 278] These dark charges are, as introduced in Chapter 2 (section 2.4.2), simply a result of charge carrier diffusion from the metal electrodes into the (intrinsic) active layer, which leads to Fermi-level alignment and a built-in field across the active layer. This causes a light-intensity independent cloud of dark charges close to the contacts, which explains the first order recombination rate close to the contacts. Notably, at intensities below 100 suns, these are also the regions with the strongest (normalized) recombination rate in the device as shown in Figure 6.2e at 0V and in Figure 6.2f at 0.5V. The overlap of the normalized recombination profiles reveals the presence of significant first order recombination losses at all intensities < 1 sun relatively close to the electrodes (approximately 15 nm at 0 V). The recombination profiles also reveal that once a forward bias is applied, the carrier concentrations at the contacts ("+" at the anode, "-" at the cathode) are pushed deeper into the bulk of the active layer, which leads to an increased volume where the bimolecular recombination can take place (Figure 6.2f). This explains the reduction in normalized photocurrent in the panels a and b of Figure 6.2. Importantly, this recombination mechanism is different from minority carrier surface recombination of photogenerated and dark charges at the electrodes which is, in this particular simulation, relatively small. This is further discussed below in Figure 6.4.

6.5. Impact of the Carrier Mobility, Recombination Coefficient and Film Thickness

It was previously observed in several polymer:fullerene cells that the magnitude of the first order losses depends strongly on the charge carrier mobility of the slower carrier (μ_{slower}).[257] To understand the detrimental impact of μ_{slower}, we varied the hole mobility over orders of magnitude ($10^{-3} - 10^{-6}$ $cm^2V^{-1}s^{-1}$) while keeping the electron mobility constant at $\mu_e = 10^{-3}$ $cm^2V^{-1}s^{-1}$. In Figure 6.3 we plot the normalized carrier recombination profile as a function of the vertical position x in the device at 0 V. We see that the recombination at the cathode increases with decreasing μ_h, i.e., more photogenerated holes recombine with the large reservoir of injected electrons. It is also expected that the first-order losses depend on the recombination rate constant (k_2). Indeed, for a system with 100× imbalanced mobilities, a reduction of the Langevin recombination coefficient by 25 times greatly reduces the first order losses which, in turn increases the FF of the cell (Figure A3.4, Appendix A3).[129, 279] With respect to the impact of the active layer thickness, we observe that the first order losses remain similar while second order losses increase with the thickness of the active layer. This is expected considering that the volume in which first order recombination takes place decreases relative to the volume of the bulk (Figure A3.5, Appendix A3). This is also consistent with experimental IPC results on a non-optimal FTAZ:IDIC (1:1.5) blend with an active layer thickness of 250 nm (Figure A3.6, Appendix A3). For this device, we still observe large first order recombination, however, with a significant contribution of second order recombination throughout the power generating *J-V* regime. Therefore, these results suggest that first order bimolecular recombination dominate the FF in OSCs with optimized film thicknesses, while in thicker blends the contribution of additional second order recombination losses further deteriorates the FF.

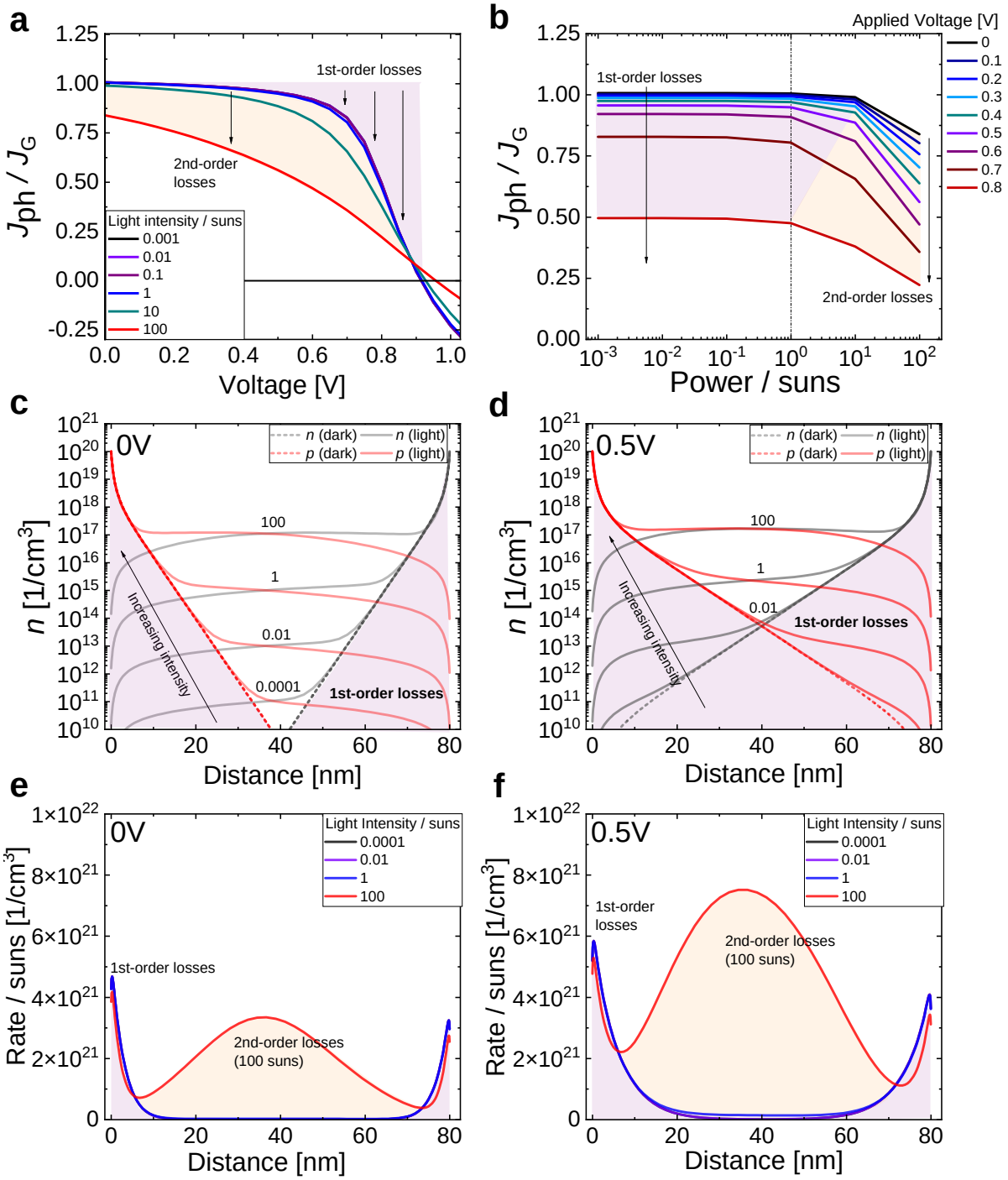

Figure 6.2: Simulation results of photocurrent, carrier density profiles and recombination profiles as a function of sun equivalents and applied voltage. a Simulated J_{ph}/J_G vs. V curves at illumination intensities ranging from 10^{-3} – 100 suns. The decrease of FF above 1 sun marks the onset of second order recombination losses, while the overlap of the J_{ph}/J_G vs. V curves at lower intensities shows the presence of first order recombination losses. **b** Equivalent plot of J_{ph}/J_G vs. light intensity at different voltages. First order recombination manifests as a decrease of the constant EQE with applied voltage independent of light intensity, while 2nd order recombination causes a downward bend of the EQE. The electron and hole densities are plotted at 0 V in panel **c** and at an applied bias of 0.5 V in panel **d**. The population of dark electrons (holes) are then given by Fermi statistics depending on the energy difference between the conduction (valence) band and the Fermi-level. The corresponding recombination profiles normalized by the generation rate along the vertical position in the active layer at 0 V in panel **e** and 0.5 V in panel **f** show first order recombination near the contacts and second order recombination emerging in the bulk at 100 suns.

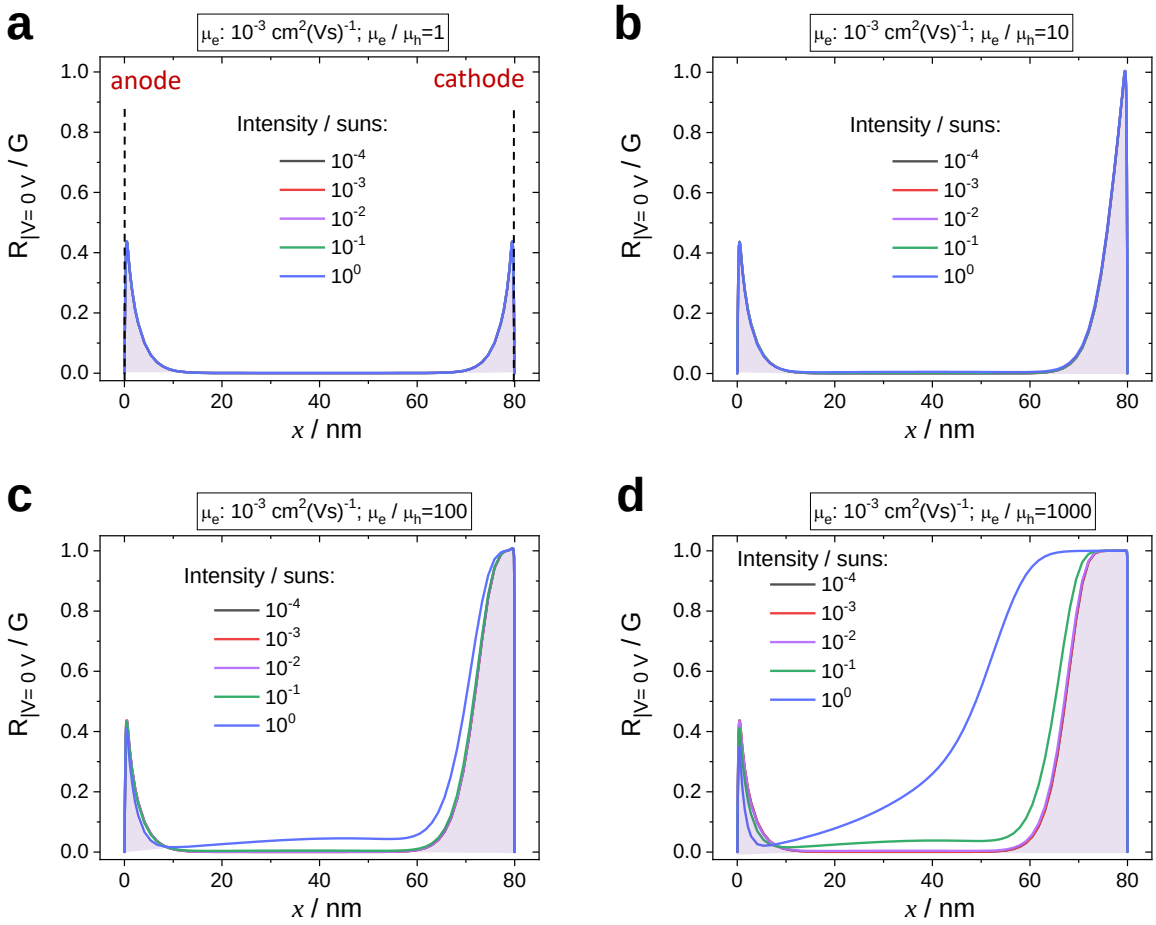

Figure 6.3: Simulation results of recombination profiles as a function of slower carrier mobility. a, b, c, d Simulated recombination profiles at 0 V normalized by the generation rate along the active layer thickness for systems with decreasing slower carrier mobility ($\mu_h = 10^{-3} - 10^{-6}$ cm^{2}V^{-1}s^{-1}) and constant electron mobility $\mu_e = 10^{-3}$ cm^{2}V^{-1}s^{-1}. Losses that increase with intensity mark the onset of significant second order recombination in panels c and d, while the overlap of the curves at lower intensities shows the presence of first order recombination losses (purple shade). The graph demonstrates that the linear and non-linear recombination losses increase with decreasing mobility of the slower charge carriers.

6.6. Impact of the Electrode Work Functions

In this section, we will discuss the impact of the contacts on the losses and potential optimization strategies by electrode engineering.[133] First, we checked the influence of the energetic offset (ΔW_f) between the metal workfunctions with respect to the highest (lowest) occupied (unoccupied) molecular orbitals (HOMO/LUMO) of the active layer material. Interestingly, although ohmic contacts ($\Delta W_f = 0$ eV) lead to more dark charge injection than injection barriers ($\Delta W_f > 0$ eV), energy level alignment between the electrodes and the active layer is actually beneficial to maximize the built-in voltage (V_{BI}) and in turn the cells' open-circuit voltage and FF. This is shown in Figure 6.4a from the J-V curves of cells where we varied ΔW_f in steps of 100 mV at both contacts. We note, a sharp drop in V_{OC} if the V_{BI} drops below the V_{OC} that can be achieved by the blend (~0.8 V) for the given device and material parameters such as k_2, G and the surface recombination velocity (S) which was set to 100 cm/s for minority carriers (see Figure A3.7, Appendix A3 for other settings). Figure 6.4b demonstrates the large differences in the carrier densities close to the contacts with (solid lines) and without (dashed lines) injection barriers at both contacts (0.2 eV). While we expected that these injection barriers will impact the interplay

between linear and non-linear recombination losses, surprisingly, also in the case with injection barriers of 0.2 eV we still obtain significant first order losses until 1 sun, which is shown in Figure 6.4c (note the similarities to the case of no injection barriers, Figure 6.2a). The reason is that surface recombination of minority carriers increases with the injection barrier offset as demonstrated in Figure 6.4d**.** We note that in the case with injection barriers (0.2 eV), the optimized cell performance (with aligned energy levels) can be regained if the surface recombination velocity S is reduced to very low values < 1 cm/s. However, we can conclude that unless in special cases where S is indeed close to 0 or where interlayers prevent surface recombination, ohmic contacts remain overall beneficial for the device performance due to the reduced surface recombination and the higher built-in field (V_{BI}) despite the strong first order recombination in the vicinity of the electrodes. The impact of interlayers is further discussed at Figure A3.8 (Appendix A3).

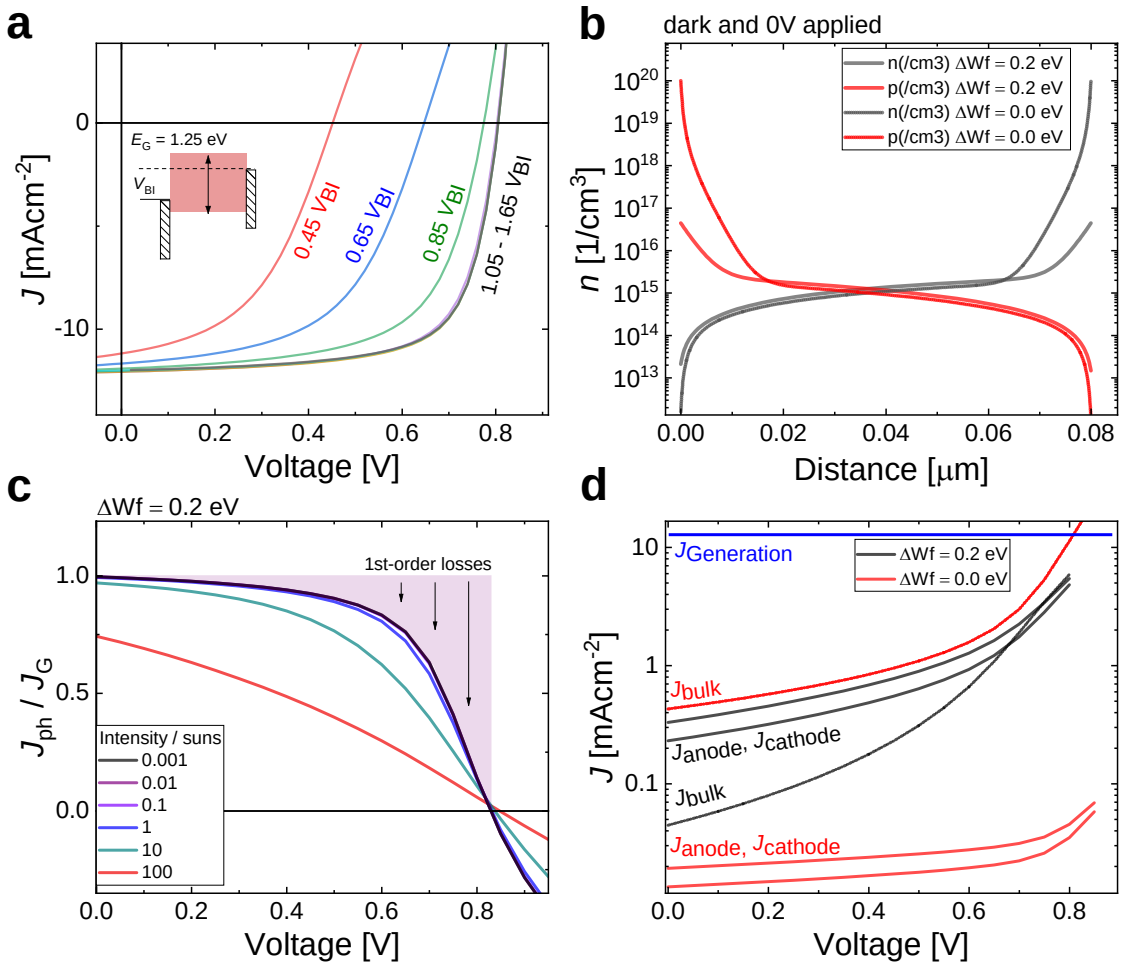

Figure 6.4: Simulation results of photocurrent and carrier density profiles in the dark as a function of energy offsets with the metal electrode. a Simulated J-V curves of organic solar cells with different energy offsets (ΔW_f) between the metal work functions and the HOMO/LUMO of the active layer. Ohmic contacts are beneficial for the V_{OC} and fill factor (FF) in case of finite (and realistic) surface recombination velocities ($S > 100$ cm/s). **b** The impact of injection barriers on the carrier distribution profile in the dark. **c** Simulated J_{ph}/J_G vs. V curves at illumination intensities ranging from 10^{-3} – 100 suns using $\Delta W_f = 0.2$ eV at both contacts. Even in the case of injection barriers, first order recombination losses dominate the J-V curve until 1 sun illumination due to enhanced surface recombination despite the reduction of first order recombination in the bulk. This is shown in panel **d** which depicts the recombination currents at the metal surfaces and the (first order recombination) in the bulk as a function of voltage for two cases with and without injection barriers.

Lastly, it is important to note that although the first order recombination in the bulk outweighs the surface recombination in the optimized case with $\Delta W_{\mathrm{f}} = 0$ eV, in general we do not know the relative contribution of these two-loss mechanism as it depends on the work function alignment and the relation between S and k_2. However, both processes are similar in the sense that photogenerated charges recombine with electrode-induced charges near or at the metal contact, and as such we do not further attempt to disentangle these two first order processes here.

6.7. Conclusions

In this chapter, we studied the light intensity dependence of photocurrent and fill factor losses in OSCs using IPC measurements and numerical drift-diffusion simulations. Experimentally, we observed in all studied OSCs that the FF is almost entirely governed by first order recombination losses, meaning that the FF of the $J_{\mathrm{ph}}(V)$-curve does not improve significantly at intensities <1 sun. Our numerical simulations show consistently that these first order losses can be very well reproduced by bimolecular recombination – without implementing trap-assisted Shockley-Read Hall or geminate recombination. This is due to the large amount of majority charge carriers close to the metal contact, which is present independent of light intensity. With increasing forward bias, this excess charge is pushed deeper into the active layer of the material, causing increased first order recombination losses which dominates the FF losses in optimized organic solar cells. We also showed that the magnitude of these linear recombination losses depends on the slower carrier mobility and the recombination coefficient, while enhancing the film thickness increases the contribution of 2$^{\mathrm{nd}}$ order recombination losses in the bulk in unoptimized blends. Lastly, we discussed the impact of the electrode work functions on this recombination mechanism which defines the relative loss due to surface recombination at the contacts and first order recombination in the bulk. In this regard we identified that ohmic contacts are beneficial for the device performance as they maximize the V_{BI} despite causing more recombination between injected and photogenerated charges. Overall, our studies highlight the importance of bimolecular recombination between photogenerated and electrode-induced charges close to the metal contacts rather than bimolecular recombination of free charges in the whole bulk. This can explain the reason for the many different explanations that have been provided to explain FF losses in OSCs. The findings have also important consequences for the interpretation of several well-established characterization techniques: (1) A linear relationship between J_{ph} and I (or the α-parameter) cannot be used to draw conclusions about the dominance of monomolecular or bimolecular recombination at 0V. (2) Consequently, the deviation from linearity does not allow to quantify the amount bimolecular recombination losses (at 0V). (3) In forward bias, the linear relationship between J_{ph} and I cannot be used to quantify the bias dependence of the charge generation yield or trap-assisted recombination. (4) FOMs that have been developed to characterize OSCs need to take into account the large impact of electrode-induced charges in the future.

Chapter 7. Excitons Dominate the Emission from PM6:Y6 Solar Cells, but This Does Not Help the Open-Circuit Voltage of the Device

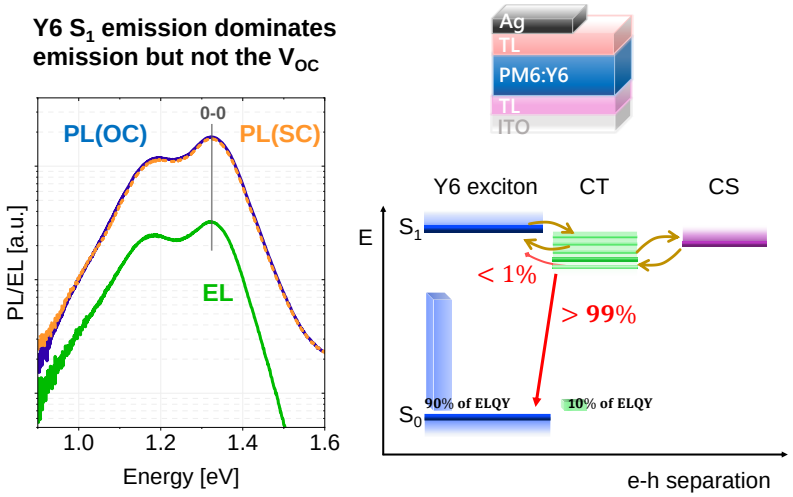

In low energy offset systems such as non-fullerene acceptor blends including PM6:Y6, the high luminescence yield of the acceptor has been proposed to lower the non-radiative voltages losses of the device. Motivated by this observation, this chapter investigates the emission spectra of the neat Y6 in comparison to PM6:Y6. Careful examination of the photoluminescence and electroluminescence reveal that most radiative recombination in the blend originates from Y6 singlet excitons but the yield of reformation to the singlet state is less than 1%. Therefore, the total recombination proceeds predominantly through the less emissive interfacial charge transfer state and the open-circuit voltage of PM6:Y6 devices does not benefit from exciton repopulation.

This chapter is an adapted preprint of:

L. Perdigón-Toro, L. Quang Phuong, S. Zeiske, K. Vandewal, A. Armin, S. Shoaee, and D. Neher. Excitons Dominate the Emission from PM6:Y6 Solar Cells, but This Does Not Help the Open-Circuit Voltage of the Device. *ACS Energy Lett.* **2021**, 6, 557–564.

7.1. Abstract

Non-fullerene acceptors (NFAs) are far more emissive than their fullerene-based counterparts. Here, we study the spectral properties of photocurrent generation and recombination of the blend of the donor polymer PM6 with the NFA Y6. We find that the radiative recombination of free charges is almost entirely due to the re-occupation and decay of Y6 singlet excitons, but that this pathway contributes less than 1% to the total recombination. As such, the open-circuit voltage of the PM6:Y6 blend is determined by the energetics and kinetics of the charge transfer (CT) state. Moreover, we find that no information on the energetics of the CT state manifold can be gained from the low energy tail of the photovoltaic external quantum efficiency spectrum, which is dominated by the excitation spectrum of the Y6 exciton. We, finally, estimate the charge-separated state to lie only 120 meV below the Y6 singlet exciton energy, meaning that this blend indeed represents a high-efficiency system with a low energetic offset.

7.2. Introduction

Organic solar cells (OSCs) based on non-fullerene acceptors (NFAs) approach nowadays their inorganic competitors in terms of photocurrent production and external quantum efficiencies (EQE), owing to their strong and complementary absorption, but lag behind with regards to their open-circuit voltage (V_{OC}).[280] However, compared to fullerene-devices, NFA-based solar cells generally exhibit lower non-radiative V_{OC} losses,[25] as a result of a higher radiative efficiency of free carrier recombination. There are indeed important features that set NFAs apart from fullerenes. First, in contrast to C_{60} and its soluble derivatives, the lowest excited state of NFAs is a singlet exciton and NFA layers with reasonably high photoluminescence quantum efficiencies, in the 0.1 to 10% range, have been reported.[31, 58] Second, NFAs usually have a planar conjugated backbone, allowing face to face π-stacking with each other and the donor molecules.[28, 32] DFT calculations indeed predict significant electronic coupling between the NFA and the donor molecules.[32] This has been proposed to result in an intensity borrowing mechanism for optical transitions from the interfacial charge transfer (CT) state, hereby increasing the radiative decay efficiency.[152, 153] More recently, it was proposed that the increased radiative decay efficiency results from the fact that the occupation of the singlet excitons is in equilibrium with the CT population, as explained in Chapter 2 (section 2.5.2).[149]

The blend of the donor polymer PM6 with the NFA acceptor Y6 has become the *fruit fly* of research on NFA-based solar cells (see Figure 7.1a for the chemical structures). This is because of the high efficiency (> 15%) of single junction PM6:Y6 solar cells, which has now been reproducibly achieved in many labs around the world. The high short-circuit current (J_{SC}) is a consequence of efficient light absorption over a wide spectral range (see Figure 7.1b) in combination with field-independent photocurrent generation.[99] On the other hand, reported V_{OC} values range from 0.82-0.85 eV, which is much smaller than the photovoltaic gap E_{g} of the blend of around 1.38 eV (see Figure A3.1, Appendix A4). Detailed understanding of the processes causing this significant voltage loss requires knowledge about the energies and decay properties of the excited states involved in the process of free charge generation and recombination. However, the deconvolution of the device absorption and emission spectra into contributions from the CT and singlet states has turned out to be difficult; where in particular the reported values for the CT energy, E_{CT}, vary significantly in the literature.[38, 66, 214] Similarly to other high performance NFA-based blends, this is in part due to the much higher oscillator strength of the NFA singlet (S_1) excited state compared to the CT state, combined with a (desired) small S_1-CT energy offset. Moreover, microcavity effects play a role in altering the spectral shape of the emission spectrum of a

complete device.[281–283] Given that those microcavity effects depend strongly on the optical properties of the film which itself depends on the layer composition, the often used approach to distinguish the spectral signatures of singlet and CT states by comparing the electroluminescence spectra of the neat NFA and of the donor:NFA blend may not be appropriate.

Here, we present the results of a careful analysis of the photoluminescence (PL) and electroluminescence (EL) spectra of PM6:Y6 blends in different sample geometries. We show that the external EL of the device is almost entirely determined by the re-occupation of the Y6 singlet. Despite this, less than 1 % of the recombination proceeds through the S_1 state and free charges recombine almost entirely through a state manifold which has a maximum radiative efficiency of 4x10^{-6}, and which we tentatively assign to the CT state manifold. We also show that absorption from S_1 completely dominates the photovoltaic external quantum efficiency, $\mathrm{EQE_{PV}}$, and that no information on the energetics of the CT state manifold can be gained from the low energy $\mathrm{EQE_{PV}}$ tails. By comparing temperature dependent PL of Y6 and temperature dependent EL of PM6:Y6, we finally estimate the charge-separated (CS) state to lie only 120 meV below the singlet energy, E_{S_1}, meaning that this blend indeed represents a high efficiency system with a low energetic offset.

7.3. Photovoltaic Characterization and Emission Properties of Films

Figure 7.1a shows the current density-voltage (*J-V*) curve of a regular PM6:Y6 bulk heterojunction (BHJ) device with an active layer thickness of 100 nm. Table A4.1 and Figure A4.2, Appendix A4, contain the *J-V* parameters and characteristics of the blend in other device configurations, prepared following the methods in Note A4.1, Appendix A4. The device in Figure 7.1a has a V_{OC} of 0.84 V, which means that the quasi-Fermi level splitting is significantly smaller than the energy of the absorption onset. Convoluting $\mathrm{EQE_{PV}}$ with the black body photon flux allows calculation of a radiative upper limit (according to Equation 2.27 and Equation 2.29 in Chapter 2, section 2.5.1), $V_{\mathrm{OC,rad}}$ of 1.08 V, ca. 0.30 eV below the photovoltaic bandgap of 1.38 eV yet, 0.24 V larger than the measured V_{OC} (see Table A4.2, Appendix A4). The latter additional voltage loss, $\Delta V_{\mathrm{OC,nrad}}$, originates from non-radiative recombination and is related to the external quantum efficiency of electroluminescence, ELQY, via $q\Delta V_{\mathrm{OC,nrad}} = k_{\mathrm{B}}T\ln(\mathrm{ELQY})$, with q being the elementary charge, k_B the Boltzmann constant and T the absolute temperature of the device. For our regular device, we measure $\mathrm{ELQY} = 2.7 \times 10^{-5}$, yielding $\Delta V_{\mathrm{OC,nrad}} = 0.27$ eV, in good agreement with the difference between $V_{\mathrm{OC,rad}}$ and the measured V_{OC} of 0.24 eV. Importantly, this $\Delta V_{\mathrm{OC,nrad}}$ is about 0.1 V lower as compared to most fullerene-based devices.[284, 285] As discussed earlier, this has been attributed to the high oscillator strength of the local exciton (LE) on the NFA, which increases the ELQY via e.g., LE-CT hybridization or by repopulation of the Y6 singlet exciton from the CT state. In the following, we will argue that exciton reformation indeed dominates the radiative recombination of free charges in this blend, but that this process has no beneficial effect on the V_{OC} of the device.

Figure 7.1c and Figure 7.1d compare the PL spectra of thin films of neat Y6, a 1:1.2 (wt.%) PM6:Y6 BHJ blend and a 1:1.2 (wt.%) blend of Y6 with the inert polymer polystyrene (PS) on glass substrates. We measure external photoluminescence quantum efficiencies (PLQY) of 7x10^{-3} in both the neat Y6 and the PS:Y6 blend, while the PM6:Y6 has a significantly smaller PLQY of 3.1x10^{-4} indicating efficient exciton dissociation with subsequent non-radiative decay. These measurements were done in such a way that they determine the external PL efficiency, i.e. the PL efficiency for photons coupled out of the thin film (see experimental details in the methods Chapter 3, section 3.2.). The shape of the PL spectrum is similar for all three films, with a

maximum at around 1.3 eV and a shoulder at ca. 1.2 eV, which we assign to the 0-0 transition and 0-1 transitions in the vibronic progression of Y6.[286] There are, however, differences in the emission energies and relative strengths already between the neat Y6 film and the PS:Y6 blend, and more prominently when compared to PM6:Y6. Besides being due to donor-acceptor interactions, these changes might be due a slightly different packing and orientation of Y6 in the different samples. Such spectral changes are expected to become even more prominent in the EL spectra of the corresponding devices due to microcavity effects.[282, 283]

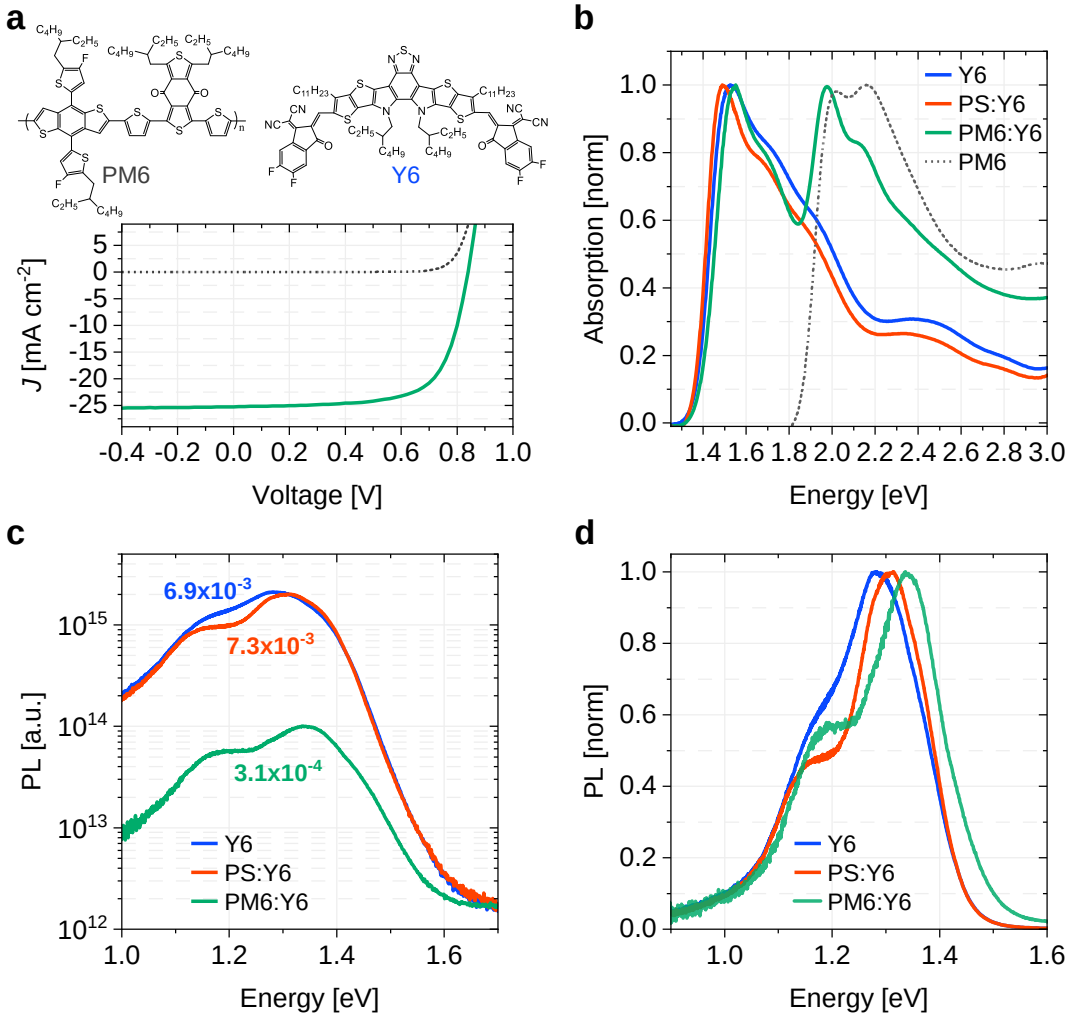

Figure 7.1: Absorption and emission properties of films of PM6, Y6 and PM6:Y6. a Chemical structure of PM6 and Y6 and the current density-voltage (*J-V*) characteristics of a regular device with a 100nm PM6:Y6 active layer measured under simulated AM1.5G light (solid line) and in the dark (dotted line). **b** Normalized absorption spectra of thin films of neat Y6 and blends of PS:Y6 and PM6:Y6 on glass (solid lines) and of neat PM6 on glass (dotted line). **c** Steady-state photoluminescence (PL) spectra of thin films of neat Y6 and blends of PS:Y6 and PM6:Y6 on glass. The values given for each data set correspond to the calculated PLQY value of the samples. **d** Normalized PL spectra of thin films of neat Y6 and blends of PS:Y6 and PM6:Y6 on glass showing the red-shift of emission peak for neat Y6 and the blend PS:Y6 with respect to the PM6:Y6 film.

7.4. Emission Properties of Devices

As the small spectral changes in the neat film and the blends might be due to orientational and morphological differences and microcavity effects, unambiguous assignment of CT emission and singlet emission is impossible. A way out of this problem is to identify conditions which provide us with the emission from Y6 singlet excitons in the actual multicomponent and multilayer device. We will argue in the following that the later can be gained from PL measurements on complete devices. To this end, we studied the emission and absorption properties of PM6:Y6 single junction devices with different active layer thickness and electrodes (see Table A4.1, Appendix A4, and Figure A4.2, Appendix A4). Figure 7.2a displays the PL spectrum of a device with a semi-transparent back electrode at V_{OC} and under short-circuit (SC) conditions, together with its EL spectrum. We also ensured that the excitation source only illuminates the active area by masking the measured pixel. The excitation intensity in PL is adjusted to generate the same photocurrent density as under simulated AM1.5G excitation, and the same current density was used to drive the device in the EL measurements. We find that the intensity and shape of the PL is virtually the same under V_{OC} and SC conditions. We expect that at SC, all photogenerated free charges are efficiently extracted while open-circuit conditions enforce the recombination of all photogenerated charges. However, the driving conditions have no appreciable effect on the shape of the PL spectrum for a wider bias range and reduce the PL intensity only slightly (see Figure A4.2, Appendix A4). A similar observation has been reported recently for another polymer:NFA blend with low energy offset.[150] We conclude that the PL of the PM6:Y6 blend in the device is dominated by the radiative decay of strongly-bound Y6 S_1 excitons and that any radiative emission from states which are reformed upon free charge recombination is hidden under the strong Y6 PL from the initially formed excitons. We also find that the intensity of the PL is ca. 10 times larger than in the EL experiment even though we inject an equivalent number of charges than what was produced during the PL experiment. This indicates that the PL of the blend device comes from incomplete dissociation of Y6 excitons generated far enough from the DA heterojunction, and that the contribution of free carrier recombination to the PL is small to negligible.

Having the Y6 exciton emission spectrum for the BHJ in the device structure at hand, we now turn to the more detailed analysis of the EL spectrum. We find that the EL emission peaks at the same energy and has a similar spectral shape as the PL. There is no indication for the presence of additional strongly-emitting low energy states. Instead, the EL overwhelmingly originates from Y6 singlet excitons formed by free charge recombination either directly or via the CT state manifold. For our semi-transparent device, subtracting the normalized PL from the normalized EL reveals a broad spectrum with a maximum at 1.15 eV, as depicted in Figure 7.2b. In contrast, the PL and EL of a neat Y6 device agree perfectly with one another (Figure A4.4, Appendix A4). This implies that the extra emission contribution in the blend EL stems from the radiative decay of an additional lower lying state, populated in the nongeminate recombination process, probably the CT state. While one may be tempted to analyze this extra emission quantitatively in terms of the energy and spectral width of the CT state manifold, we acknowledge that the spectral shape and strength depends largely on the active layer thickness and device geometry (see Figure A4.5, Appendix A4). The stronger the 0-1 (and 0-2) emission peak intensities in the PL, the more pronounced and red-shifted is this extra emission in EL. This points to severe microcavity effects. Optical modelling combined with drift-diffusion simulations would be necessary to analyze these spectra in terms of the intrinsic emission spectrum, which is beyond the scope of this manuscript. Irrespective of these details, the extra low energy contribution accounts to, at maximum, 10% to the total EL emission intensity, meaning that its ELQY is below $3\text{x}10^{-6}$.

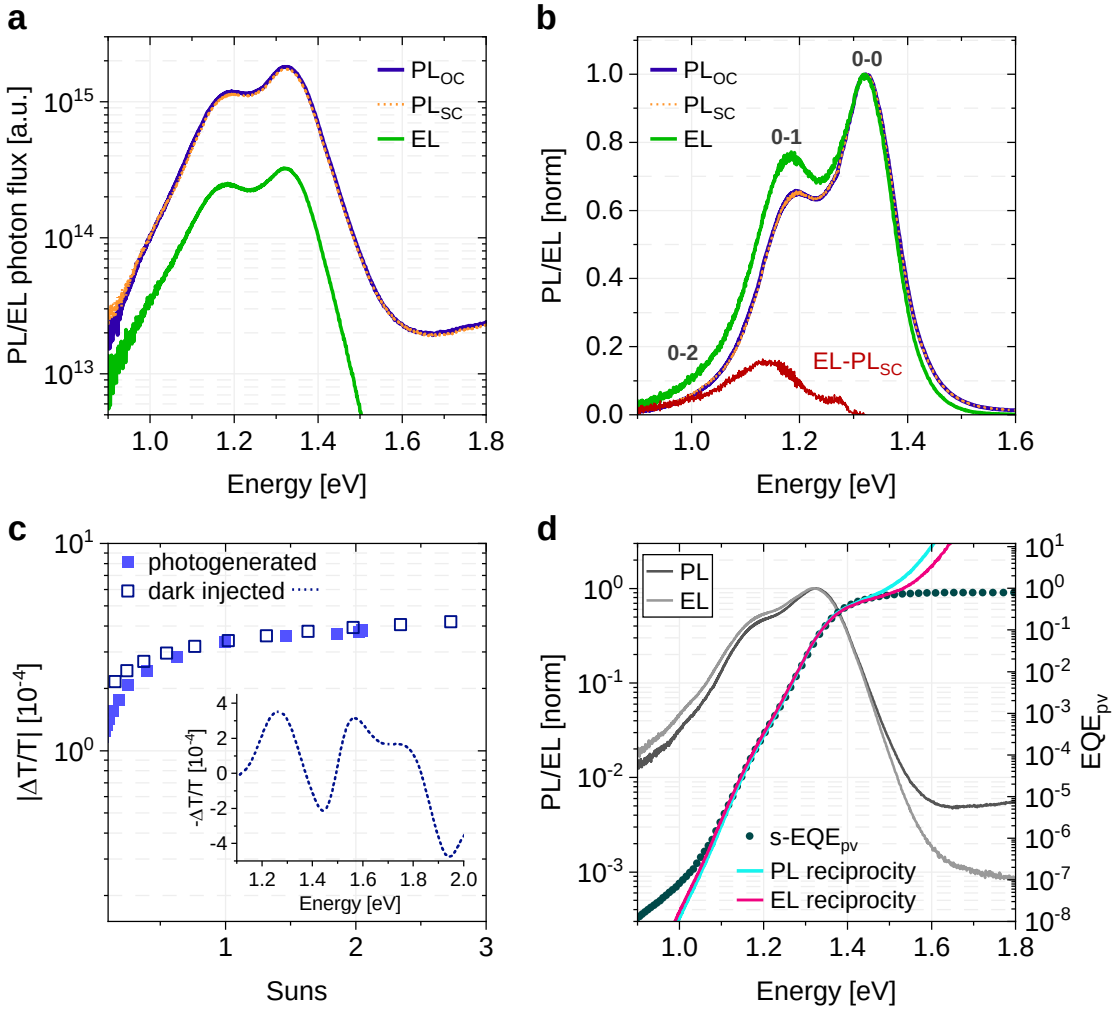

Figure 7.2: Emission properties of PM6:Y6 devices. a Steady-state photoluminescence (PL) and electroluminescence (EL) spectra of a ca. 135 nm thick regular PM6:Y6 device with semi-transparent cathode. PL was recorded at open-circuit (OC) and short-circuit (SC) conditions under a 1 sun equivalent illumination. In EL, the injected current matched the 1 sun photocurrent density at an applied voltage of 0.90 V. **b** Normalized PL and EL spectra from panel a. The subtraction EL-PL_{SC} reveals a broad emission with a maximum at 1.15 eV (dark red line). **c** Excitation intensity dependent photo-induced absorption spectroscopy (PIA) signals (photogenerated charges, full squares) and electromodulation injection absorption (EMIA) signals (dark injected charges, open squares) measured for a PM6:Y6 regular device with semi-transparent cathode, both at a photon energy of 1.25 eV. The inset figure shows the EMIA spectrum as a function of photon energy at 1 sun equivalent dark injection current. **d** Normalized PL and EL spectra of a ca. 145 nm thick regular PM6:Y6 with fully reflecting electrode (gray lines, left axis). Sensitive photovoltaic external quantum efficiency (s-EQE_{PV}) of the same PM6:Y6 device (dots, right axis). The absorption spectra calculated via the reciprocity relation from the depicted PL and EL are given in blue and pink, respectively.

Given the small differences between the EL and PL spectral shapes, but the rather large difference in intensity, the question arises whether conclusions from the analysis of the EL spectra are representative of the state population in the active layer under photoexcitation at V_{OC} conditions. For example, the EL efficiency can be easily affected by injection barriers,[287] while the bulk and surface density of photogenerated carriers may be reduced by non-selective contacts.[136] To ensure that both driving conditions create the same free carrier population, we compared the results from steady-state photoinduced absorption (PIA) and electromodulation injection absorption (EMIA) spectroscopy on the very same device. PIA measures the differential

absorption upon modulation of the intensity of quasi-steady state illumination while keeping the device at V_{OC} (see Chapter 3, section 3.5.).[162] The method has been recently applied to the PM6:Y6 blend where it was shown that carrier losses due to surface recombination are negligible in regular devices.[134] For our semi-transparent regular device, in Figure 7.2c, the dark squares show the differential absorption at a photon energy of 1.25 eV (assigned to the absorption by the PM6 polaron) as a function of illumination intensity. This is compared to the differential absorption upon modulated dark injection of the same recombination current (the inset figure shows the EMIA spectrum as a function of photon energy at 1 sun equivalent). Above 0.5 equivalent suns, both data sets agree perfectly, meaning that both kinds of excitation create the same carrier densities. Conclusions drawn from EL about the pathways of free carrier recombination are, therefore, representative for the situation under steady-state photoexcitation at V_{OC}.

Figure 7.2d shows the sensitive s-EQE_{PV} spectra of a regular device with a fully reflecting electrode, covering 8 orders of magnitude. This is compared to the S_0-S_1 absorption spectrum as calculated from the PL of the same device (dark grey line) via the optical reciprocity relation: $A(E) = \phi_{PL}(E) \times \phi_{BB}^{-1}(E)$ (see solid blue line in Figure 7.2d). The calculated absorption spectrum reproduces all characteristics of the s-EQE_{PV} spectrum, namely the steep incline below 1.4 eV and the weak shoulder at 1.18 eV. Given the proven fact that the PL stems almost exclusively from Y6 exciton emission, we conclude that exciton absorption dominates the entire low energy tail of the s-EQE_{PV}. At very low photon energies (E <1.05 eV) the absorption by trap states becomes apparent.[288] Our data show no evidence for CT-S_1 hybridization at the DA interface, which was predicted to cause an overall red-shift and broadening of the low energy tail of the s-EQE_{PV}.[185] We are further able to assign the low energy shoulder in the s-EQE_{PV} spectrum to thermally excited vibronic states of S_0 to the vibronic ground state of S_1, with little to no absorption from CT states or traps. In order to support this conclusion, we measured EQE_{PV} at a lower temperature (see Figure A4.6, Appendix A4) and observed that the low energy shoulder is indeed suppressed.

To conclude this part of the manuscript, we find that the low energy tail of the EQE_{PV} as well as the EL emission spectrum, originating from free charge recombination, are almost entirely determined by the absorption and emission properties of the Y6 singlet exciton. Therefore, these spectra are not suited to draw solid conclusions about the energy and spectral properties of additional low energy states, such as the CT state energy and width. Notwithstanding, our comparison between the EL and PL spectra and intensity suggest that such states exist and emit at very low quantum efficiency, below 4×10^{-6}. In addition, the data from the above experiments allow us to provide further insight into the role of the Y6 exciton formation and recombination with respect to free charge recombination in the PM6:Y6 blend.

7.5. Equilibrium and Energy Scheme

It has been suggested that for a sufficiently low S_1-CT offset, the S_1 is in dynamic equilibrium with the CT state, meaning that the repopulation of the exciton from the CT is faster than its decay to the ground state.[149, 150] Also, given that free-carrier recombination in PM6:Y6 is reduced relative to the Langevin-limit,[99, 214] it is safe to assume that the CT state occupation is in equilibrium with the free carrier reservoir, as observed for many fullerene and non-fullerene devices. In this case, the chemical potential of the reformed singlet state, μ_{S_1}, is the same as the chemical potential of the CT state, μ_{CT}, this being equal to the quasi-Fermi level splitting, QFLS, of the free charges in the bulk (see Equation 2.35 in section 2.5.2). We determined μ_{S_1} by relating the external photon flux under EL conditions to the excitonic photon emission in the dark: $\phi_{S_1} =$

$\phi_{S_1}^0 \exp\left(\frac{\mu_{S_1}}{k_B T}\right)$ (see Note A4.2, Appendix A4). Here, we remind the reader that we have shown above that dark injection (EL) generates the same carrier density as photoexcitation under the same injection conditions. We determine ϕ_{S_1} by assuming that at least 90 % of the total EL photon flux stems from Y6 exciton recombination. For our 145 nm thick regular device, this yields $\phi_{S_1}(\mathrm{EL}) = 6.2 \times 10^{12}$ cm^{-2}s^{-1} (see Note A4.2 for the calculation and Table A4.3, Appendix A4). To obtain $\phi_{S_1}^0$, we integrated the optical reciprocity of the device PL (aligned to the tail of the EQE_{PV} spectrum, as shown by the light blue line in Figure 7.2d), yielding $\phi_{S_1}^0 = 0.11$ cm^{-2}s^{-1}. This results in $\mu_{S_1} = 0.821$ eV, which is reasonably close to the measured $V_{OC} = 0.834$ V of the same device and compares well to the QFLS determined for a regular PM6:Y6 device of the same composition via PIA spectroscopy.[134] Thus, we conclude that the population of singlet excitons which are reformed through free charge recombination in this device is indeed in equilibrium with the free carrier reservoir. The analysis of the other devices, with different thicknesses and contacts (see Table A4.3, Appendix A4), leads to the same conclusion, though with a bit larger difference between μ_{S_1} and qV_{OC} (30 meV at maximum). While this may indicate that this dynamic equilibrium between singlet excitons and CT states is not always fully established, we also note that the value of μ_{S_1} is determined from the combined results of three different measurements, each with small systematic and statistical errors.

With the knowledge of μ_{S_1}, we can provide an estimate of the population of excited Y6 molecules, n_{S_1}, formed upon free charge carrier encounter. From Equation 2.35 (section 2.5.2):

$$n_{S_1} = N_{S_1} \exp\left(-\frac{E_{S_1}}{k_B T}\right) \exp\left(\frac{\mu_{S_1}}{k_B T}\right), \qquad (7.1)$$

(note that this equation describes an equilibrated exciton population with $n_{S_1} < N_{S_1}$ for which Boltzmann statistics holds, see Note A4.2, Appendix A4). We determined $E_{S_1} = 1.43$ eV from the intersection between the absorption and PL of the blend, as in Figure A4.1 (Appendix A4). N_{S_1} was set equal to the number density of Y6 molecules in the blend ($N_{Y6} = 2.4 \times 10^{20}$ cm^{-3}, see Note A4.3, Appendix A4). With $\mu_{S_1} \cong 0.82$ V, Equation 7.1 yields $n_{S_1} \cong 1.5 \times 10^{10}$ cm^{-3}, only. This value is low as compared to the free carrier density and thus hints at a significant barrier for exciton formation from free carrier recombination. To quantify this barrier, we estimated the energy for free electron-hole pairs, E_{CS}, in the limit of an equilibrated non-degenerate carrier population, via[124]

$$n_{CS}^2 = N_{CS}^2 \exp\left(-\frac{E_{CS}}{k_B T}\right) \exp\left(\frac{\mathrm{QFLS}}{k_B T}\right). \qquad (7.2)$$

The free carrier density in PM6:Y6 at 1 sun illumination conditions was reported to be $n_{CS} \approx 2.5 \pm 0.5 \times 10^{16}$ cm^{-3}.[99, 134] It has also been shown that the QLFS is equal to qV_{OC} for regular devices.[134] Then, with $N_{CS} = N_{Y6}$ and $qV_{OC} \cong 0.83$ V for our 145 nm thick regular device, we obtain $E_{CS} = 1.31 \pm 0.01$ eV (see Table A4.3, Appendix A4, for the other devices). This results in an $E_{CS} - E_{S_1}$ barrier of 120 meV. To confirm our estimate of this energy offset, we measured the activation energy for exciton formation upon free charge recombination by recording the temperature dependence of the EL intensity for a fixed injection current, keeping the recombination rate constant. As shown in Figure 7.3, decreasing the temperature causes a similar red-shift of the PL and EL spectra (see Figure A4.7, Appendix A4, for the normalized spectra and the effect of driving conditions), but it only decreases the EL intensity. Interestingly, the temperature does not affect the low energy tail of the EL, supporting our conclusion that it has a different origin than the main emission which is from exciton reformation and decay. Taking the

EL peak intensity as a measure for the S_1 population yields an activation energy of 117 ± 4 meV (Figure 7.3c), in very good agreement with the estimate from above. This puts E_{CS} again at around 1.31 eV, as shown schematically in Figure 7.4. Our estimate for E_{CS} challenges recent measurements of the energies of the frontier orbitals of the neat layers and in the blend with cyclophotovoltammetry or photoelectron spectroscopy, which predict values for E_{CS} between 1.0 eV and 1.62 eV.[29, 34, 66] These conflicting results motivate a comprehensive analysis of the energetics in this blend. Because of the large quadrupole moment of Y6, the frontier orbital offset in the blend may, indeed, differ significantly from the difference between the ionization energy of the neat donor and the electron affinity of the neat acceptor.[97]

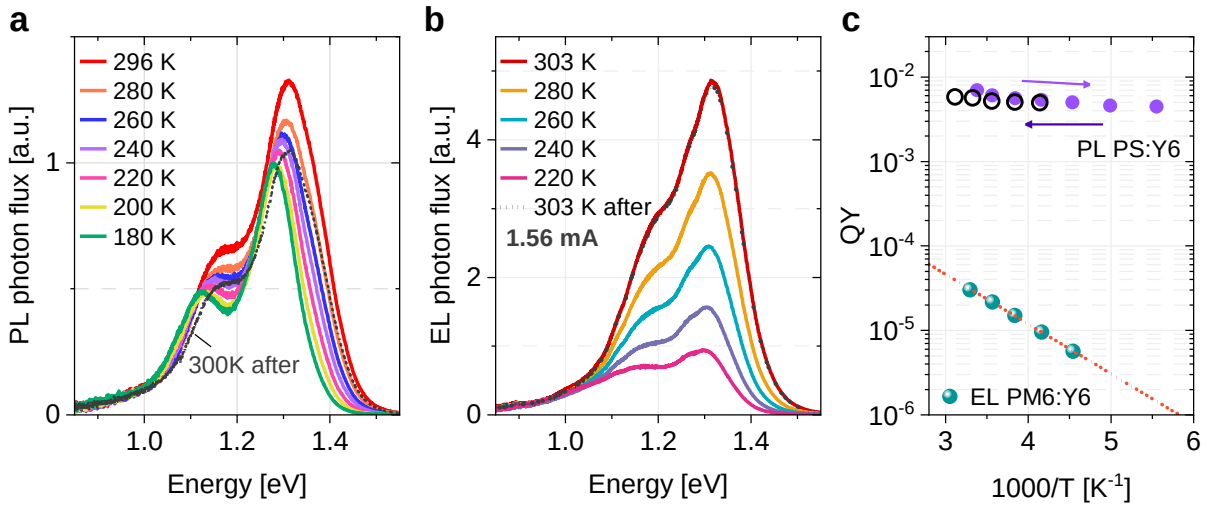

Figure 7.3: Emission properties as a function of temperature. a Steady-state photoluminescence (PL) spectra as a function of temperature of a thin film of PS:Y6 on glass. **b** Electroluminescence (EL) spectra as a function of temperature of a regular PM6:Y6 device measured at a constant current of 1.56 mA. **c** Temperature dependence of the PL intensity of a PS:Y6 film and the EL peak intensity of a PM6:Y6 device. The PLQY data was normalized to the value measured at room temperature in the integrating sphere. The full purple dots are the values obtained upon cooling while the open black dots were obtained when heating back up the sample. The ELQY data was normalized to the absolute measurement as well. The red dashed line is a fit to $\mathrm{ELQY} = \exp\left(-\frac{\Delta E}{k_B T}\right)$, which gives an activation energy $\Delta E = 117$ meV.

With $E_{S_1} - E_{CS} \cong 120$ meV, the PM6:Y6 system is, indeed, a low energy offset blend, though the offset is large enough to ensure efficient dissociation of excitons into free carriers as observed experimentally.[99] It is the reason why this blend generates charges so efficiently. On the other hand, reformation of singlet excitons from free charge generation is rather insignificant. To determine the fraction of charge carrier recombination events proceeding through exciton formation and recombination, we related the ELQY of PM6:Y6 (4×10^{-5}) to the PLQY of the PS:Y6 film (7×10^{-3}), where the latter is the probability that an exciton formed on Y6 emits a photon out. We estimate this fraction to be 0.6 %. All other recombination must proceed via other decay channels, involving state manifolds with very low radiative efficiency, most likely being CT states (see Figure 7.4).

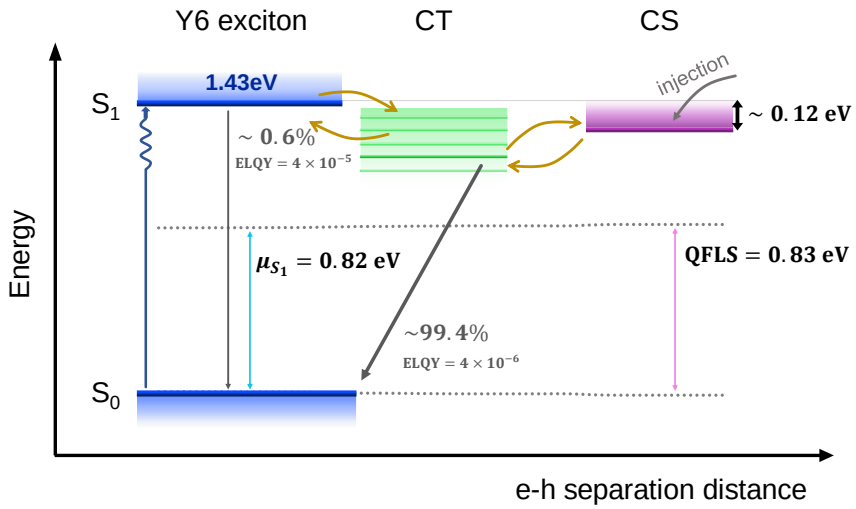

Figure 7.4: Energy scheme summarizing the findings in Chapter 7. In PM6:Y6 devices, the chemical potential of the Y6 singlet exciton, μ_{S_1}, is almost equal to the QFLS in the bulk, thus singlet excitons are in dynamic equilibrium with free carriers in the CS state, and most likely with the CT state as well. Most of the photon emission of the excited blend originates from the Y6 exciton. However, most nongeminate recombination occurs through a very weakly-emitting state different from the Y6 singlet. We can relate the ELQY of the singlet excitons in the device to the PLQY of the PS:Y6 film, and conclude that less than 0.6% of injected charges are re-formed into excitons. The low yield of reformation can be explained by the barrier between the singlet energy and the effective transport gap (CS state).

Our results show that the $\mathrm{EQE_{PV}}$, and with that the radiative loss, $\Delta V_{\mathrm{OC,rad}}$, is entirely determined by the strongly absorbing Y6 excitons. However, the state manifold through which most recombination proceeds has a much lower absorption strength and is most likely the CT state manifold. Being the dominant decay channel for charge carriers, it is the energetics and kinetics of the CT state which determines the V_{OC} of the PM6:Y6 blend, irrespective of the position and emission properties of the singlet state (see Ref.[289] and Note A4.4, Appendix A4). In fact, in the limit of $\mathrm{S_1}$-CT-CS equilibrium as explained above, the V_{OC} is given by

$$qV_{\mathrm{OC}} = E_{\mathrm{CT}} + k_{\mathrm{BT}} \ln\left(\frac{J_{\mathrm{SC}}}{qd\left(1+\frac{R_{\mathrm{S_1}}}{R_{\mathrm{CT}}}\right)k_{\mathrm{CT}}N_{\mathrm{CT}}}\right), \qquad (7.3)$$

where $R_{\mathrm{S_1}} = k_{\mathrm{S_1}} n_{\mathrm{S_1}}$ and $R_{\mathrm{CT}} = k_{\mathrm{CT}} n_{\mathrm{CT}}$ are the $\mathrm{S_1}$ and CT recombination rates, respectively, with $k_{\mathrm{S_1}}$ and k_{CT} the respective decay coefficients to the ground state. We have shown that $\frac{R_{\mathrm{S_1}}}{R_{\mathrm{CT}}} < 1\ \%$ in the PM6:Y6 blend, meaning that the properties of the Y6 singlets are almost irrelevant for the V_{OC} of the PM6:Y6 devices, which is instead dominated by the CT population and decay properties. It is only if singlets dominate the total recombination rate that the occupation and energetics of the $\mathrm{S_1}$ state become relevant for the V_{OC}.[289] Unfortunately, reliable information on the CT energetics cannot be gained from the EL and ELQY spectra as discussed earlier, though we expect an appreciable offset to the $\mathrm{S_1}$ state from the efficient exciton splitting. It is, therefore, instructive to consider the total V_{OC} loss in terms of the energy and recombination properties of free charges. Our analysis puts the charge-separated state at ca. 1.31 eV, only 70 meV below the photovoltaic gap of ca. 1.38 eV, which may indeed be the reason for the fairly small open-circuit voltage loss of this blend. The main $\mathrm{S_1}$ loss comes from the difference between E_{CS} and the QFLS, which is 0.47 eV. In case of negligible trapping and recombination via low energy states, this difference is given

by $E_{\mathrm{CS}} - qV_{\mathrm{OC}} = \mp k_{\mathrm{B}}T\ln\left(\frac{qdk_2N_{\mathrm{CS}}^2}{J_{\mathrm{SC}}}\right)$, where k_2 is the coefficient for nongeminate free charge recombination.[52, 111] It was shown recently that the PM6:Y6 blend benefits from a low tail state energetics disorder and exceptionally weak charge trapping.[34] Therefore, the V_{OC} loss originates mainly from a fairly high k_2, which we determined to be $k_2 = (1-2) \times 10^{-11}$ cm^{3}s^{-1}.[99] This is only ≅ 50 times suppressed to the Langevin coefficient for encounter-limited recombination, suggesting additional recombination pathways such as triplet formation or the recombination through midgap-states.[130, 289, 290] Recent work presented promising concepts to reduce the nongeminate recombination in PM6:Y6-based blends, e.g. through the use of solvent additives,[35] or by employing ternary blends.[291, 292]

7.6. Conclusions

In conclusion, we find that most nongeminate recombination in PM6:Y6 occurs through a very weakly-emitting (or even dark) low energy state that is different from the Y6 S_1 state from which almost all radiation originates. The chemical potential of the Y6 S_1 state is found to be almost equal to the QFLS in the bulk, meaning that the singlet excitons are in dynamic equilibrium with the free carriers (and most likely with the CT state). This is the exact reason why Rau's reciprocity works so well for PM6:Y6 solar cells. We estimate the singlet energy to lie ca. 120 meV above the effective transport gap, which explains efficient free charge formation and the low yield of exciton reformation. In fact, less than 1% of the recombination proceeds through exciton reformation and decay. As such, the V_{OC} of the PM6:Y6 blend is almost entirely determined by the energetics and kinetics of the CT state, irrespective of the position and emission properties of the singlet state. It is only when the density and/or the recombination properties of the interfacial CT are substantially reduced that a large gain in V_{OC} can be expected.

Chapter 8. Understanding the Role of Order in Y-series Non-Fullerene Solar Cells to Realize High Open-Circuit Voltages

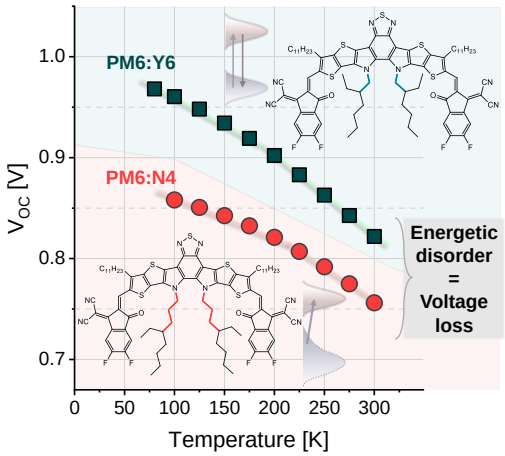

In this chapter, the role of structural and energetic disorder in the photovoltaic performance of PM6:Y6 solar cells is addressed. This is done by a detailed temperature dependent study of charge transport and recombination in comparison to the structurally similar but less ordered PM6:N4 blend. For both materials, energetic disorder has a substantial effect on the open-circuit voltage at room temperature, and also on its progression with temperature. However, PM6:Y6 benefits from superior morphological order and lower energetic disorder of the charge-separated states. As such, the gathered results highlight the need to understand the reasons behind energetic disorder in high-efficiency non-fullerene blends, with the goal to further reduce open-circuit voltage losses.

This chapter is an adapted preprint of:

L. Perdigón-Toro, L. Quang Phuong, F. Eller, G. Freychet, E. Saglamkaya, J. I. Khan, Q. Wei, S. Zeiske, D. Kroh, S. Wedler, A. Köhler, A. Armin, F. Laquai, E. M. Herzig, Y. Zou, S. Shoaee, and D. Neher. Understanding the Role of Order in Y-Series Non-Fullerene Solar Cells to Realize High Open-Circuit Voltages. *Adv. Energy Mater.* **2022**, 2103422.

8.1. Abstract

Non-fullerene acceptors (NFAs) as used in state-of-the-art organic solar cells feature highly crystalline layers that go along with low energetic disorder. Here, we study the crucial role of energetic disorder in blends of the donor polymer PM6 with two Y-type NFAs, Y6 and N4. By performing temperature-dependent charge transport and recombination studies, we come to a consistent picture of the shape of the density of state distributions for free charges in the two blends, which allows us to analytically describe the dependence of the open-circuit voltage V_{OC} on temperature and illumination intensity. We find that disorder influences the value of the V_{OC} at room temperature, but also its progression with temperature. Here, the PM6:Y6 blend benefits substantially from its narrower state distributions. Our analysis also shows that the energy of the equilibrated free charge population is well below the energy of the NFA singlet excitons for both blends and possibly below the energy of the populated charge transfer (CT) manifold, indicating a down-hill driving force for free charge formation. We conclude that energetic disorder of charge-separated states has to be considered in the analysis of the photovoltaic properties, even for the more ordered PM6:Y6 blend.

8.2. Introduction

Organic solar cells (OSCs) stand out because of their easy processability, flexibility, light weight and the abundance of materials that can act as electron donor (D) or acceptor (A) in the active layer of such devices. Great effort is put into the development of even a larger library of materials, and the appearance of new non-fullerene acceptors (NFAs) has injected new life into the technology.[24] Highest efficiencies are reported for single junction of ternary blends in which one of the components is the NFA Y6, or one of its close derivatives.[45, 46, 293–295] When blended with the polymer donor PM6, PM6:Y6 devices have high and reproducible power conversion efficiencies (PCEs), thus many studies have focused on elucidating what makes this blend so special.[29] On the one hand, free charge generation was shown to be essentially barrierless (Chapter 4) which was attributed to the molecular structure of Y6 and its large quadrupole moment, which causes band-bending across the heterojunction and drives charge separation.[99] The unique molecular packing of Y6 has also been pointed out as responsible for electron delocalization at the DA interface and consequent charge separation.[32] In comparison to NFAs reported earlier, neat films of Y6 have more preferential *face-on* orientation,[29, 36, 38] and clusters of Y6 are better connected, promoting faster transport of electrons, holes and excitons.[121] Despite a favorable morphology, the PM6:Y6 blend lags in terms of charge extraction,[296] given its fairly high bimolecular recombination coefficient and moderate mobility.[34, 35, 99] Both properties are known to be related to the energetic disorder of the charge transporting states, as previously seen in section 2.4. of the fundamentals.[102, 107, 297, 298] In addition, energetic disorder will reduce the open-circuit voltage (V_{OC}) because carriers accumulate in the tail of the electronic density of states (DOS).[52, 111, 299] Therefore, detailed knowledge of the interplay between energetic disorder and the physical processes determining the photovoltaic response is needed.

Compared to inorganics, organic semiconductors have a larger positional and energetic disorder (Chapter 2, section 2.4.1). In bulk heterojunction (BHJ) solar cells, this is primarily a result of molecular and interfacial interactions and the multiple possible morphologies upon mixing of the donor and acceptor. Research spanning over a decade attempted to link energetic disorder to the photovoltaic parameters of polymer:fullerene OSCs.[52, 110, 111, 204, 206, 300–303] Fullerene-based blends have large energetic disorder with values that can even exceed 100 meV.[100, 197,

304–306] This is because of the small aggregate size of substituted fullerenes such as PCBM but also the significant orientational and conformational disorder even within these ordered domains.[65, 307, 308] Modern NFAs as used in state-of-the-art OSCs exhibit layers with a well-defined intermolecular nanostructure.[36, 38, 309] For OSCs with Y-series acceptors, both the lowest unoccupied molecular orbital (LUMO) and the highest occupied molecular orbital (HOMO) exhibit energetic disorder values typically between 50 and 70 meV.[34, 35, 310, 311] As discussed in section 2.4.3, the effect of energetic disorder is often described through a Gaussian or exponential model of the density of states and the V_{OC} can be analytically derived from the splitting of the quasi-Fermi levels in each model, while considering whether recombination occurs between free charges via bound states to the ground state, or between free charges and traps.[52, 110, 112] The different mechanisms can be discerned experimentally by determining the recombination parameters from the V_{OC} dependence on carrier density (m-factor) and generation current (ideality factor, n_{id}), and the recombination current dependence on carrier density (recombination order δ), as detailed in Refs.[112, 206] and Chapter 2, section 2.4.3. So far, though, few experimental studies have tried to link energetic disorder to the V_{OC} losses, the V_{OC} dependence on temperature or the main recombination mechanism in NFA blends.[310, 312, 313] An approach frequently used in literature to determine the disorder is to measure the Urbach energy from the slope of the tail of the external quantum efficiency ($\mathrm{EQE_{PV}}$) spectrum.[310, 314, 315] However, for a Gaussian disorder, this slope will always be equal to the thermal energy, independent of the width of the DOS, σ.[316] Very recently, Brus et al.[313] explained the V_{OC} as a function of temperature and light intensity for several polymer:NFA blends, using a combination of bimolecular and trap-assisted recombination in the bulk and at the surface. To take energetic disorder into account, the recombination rates were related to a temperature-dependent mobility according to the Gaussian disorder model.[102] This yielded values of σ between 46 meV and 70 meV, depending on this system. Thereby, the same disorder was assumed for the HOMO and the LUMO. As for work on the PM6:Y6 blend, information on the energetic disorder was derived from temperature-dependent space charge-limited currents (SCLC) measurements but no corresponding measurement of the V_{OC} in relation to disorder was performed.[35] Interestingly, V_{OC} as a function of temperature data reported so far reveals a charge transfer (CT) energy, E_{CT}, of ca. 1.1 eV when extrapolated to 0 K,[99, 317, 318] which is less than 0.3 eV above qV_{OC}. This points to energetic disorder affecting the V_{OC} of PM6:Y6 solar cells, even at room temperature.

In this chapter, we highlight the role of energetic disorder in NFA solar cells, by comparing Y6 to a close derivative, namely, N4. Grazing-incidence wide-angle X-ray scattering (2D-GIWAXS) reveals distinct differences of the molecular orientation and order for the two acceptors blended with PM6, while temperature-dependent SCLC measurements show a significantly smaller energetic disorder in PM6:Y6. Temperature-dependent bias-assisted charge extraction (BACE) measurements reveal that the recombination mechanism is different in both blends. In PM6:Y6, recombination occurs between charges in a Gaussian HOMO DOS and a Gaussian LUMO DOS, both of narrow width, while the main recombination mechanism in PM6:N4 is of carriers in a broader Gaussian LUMO DOS recombining with carriers in a Gaussian HOMO DOS with an exponential tail. As a consequence, the V_{OC} of PM6:N4 is considerably lower compared to PM6:Y6. The effect of disorder on the V_{OC} as a function of temperature is quantitatively described by analytical models considering the shape and disorder of the HOMO and LUMO site distributions. Because of the higher disorder, the CT emission is well discernible in electroluminescence (EL) at low temperatures in PM6:N4, which we assign to emission from lower-lying states in a broad DOS distribution, again consistent with the larger voltage loss of this blend. Finally, for a given generation rate, the free carrier density increases with decreasing temperature in both PM6:Y6 and PM6:N4. This contrasts the view that charge separation is temperature-assisted or entropy-

driven. Instead, this finding supports the model that band bending in combination with energetic disorder provides a down-hill driving force for free charge formation.

8.3. Device Characteristics

Since it is well established that PM6:Y6 has a desirable morphology and thereby low energetic disorder, we aimed at having an in-depth comparison with an alternative blend that features a different molecular packing but has a similar molecular structure, that is, a Y-derivative. N4 is a small molecule acceptor that has an aromatic backbone identical to that of Y6 but different alkyl chains elongation, with 4th-position branching on the nitrogen atoms of the pyrrole motif of the backbone (instead of 2nd-position as in Y6, see Figure 8.1a). This increases the solubility of the N4 molecule.[42] Morphology studies performed by Jiang et. al showed that the PM6:N4 blend has a preferential *edge-on* orientation in contrast to the predominant *face-on* orientation of PM6:Y6. Moreover, R-SoXs experiments revealed larger but less pure domains in PM6:N4, pointing to more intermixing. As it turns out, the different molecular design and packing result in a poorer performance for the PM6:N4 devices, which have a lower V_{OC}, slightly lower fill factor (FF) but similar short-circuit current density (J_{SC}) when compared to PM6:Y6. The typical current density-voltage (*J-V*) characteristics of regular devices with a 100 nm layer of PM6:Y6 (1:1.2, wt%) and PM6:N4 (1:1.25, wt%) are shown in Figure 8.1b. Table A5.1 (Appendix A5) contains the averaged photovoltaic parameters of regular devices prepared in this work, while Figure A5.1 compares in more detail the statistics of both regular and inverted devices. The device fabrication details are found in Note A5.1, Appendix A5. Our regular PM6:Y6 devices exhibit a PCE average value of 14% whereas the PCE of PM6:N4 is at 12%. Inspection of the photovoltaic parameters shows that the PM6:Y6 produces on average 1 mAcm^{-2} more in J_{SC} than the PM6:N4 (24.9 mAcm^{-2} vs 23.9 mAcm^{-2}) for the same active layer thickness (Figure A5.2, Appendix A5, shows the photovoltaic external quantum efficiency, $\mathrm{EQE_{PV}}$, including the integrated J_{SC} for PM6:Y6 and PM6:N4). In addition, the FF is 2% higher, with a value of 66.8%, in PM6:Y6 compared to an average of 64.7% in PM6:N4. The largest difference is in the V_{OC}, which on average is 0.84 V in PM6:Y6 and 0.77 V in PM6:N4.

The large difference in V_{OC} comes as a surprise as N4 has been reported to have a slightly deeper HOMO and higher LUMO than Y6.[319] In accordance, the comparison in Figure 8.1c of the sensitive photovoltaic external quantum efficiency (s-$\mathrm{EQE_{PV}}$) spectra shows that the absorption is blue-shifted in PM6:N4 with respect to PM6:Y6. The same holds for the peak of the EQE derivative, which gives a photovoltaic gap of 1.38 eV and 1.43 eV for PM6:Y6 and PM6:N4, respectively. These results indicate that the PM6:N4 blend suffers overall from larger voltage losses. This is indeed observed in measurements of the external quantum efficiency of electroluminescence (ELQY), in Figure A5.3 (Appendix A5). PM6:N4 suffers from larger non-radiative losses given that its ELQY is more than one order of magnitude lower compared to PM6:Y6.

For a given energetics, a smaller V_{OC} would originate from faster geminate and/or nongeminate non-radiative recombination. Our previous measurements of time-delayed collection field (TDCF) on PM6:Y6 devices demonstrated that free charge generation is very efficient and independent of the electric field, pointing to small geminate losses in the blend (see Chapter 4). Similar results were obtained now for PM6:N4 (Figure A5.4, Appendix A5).

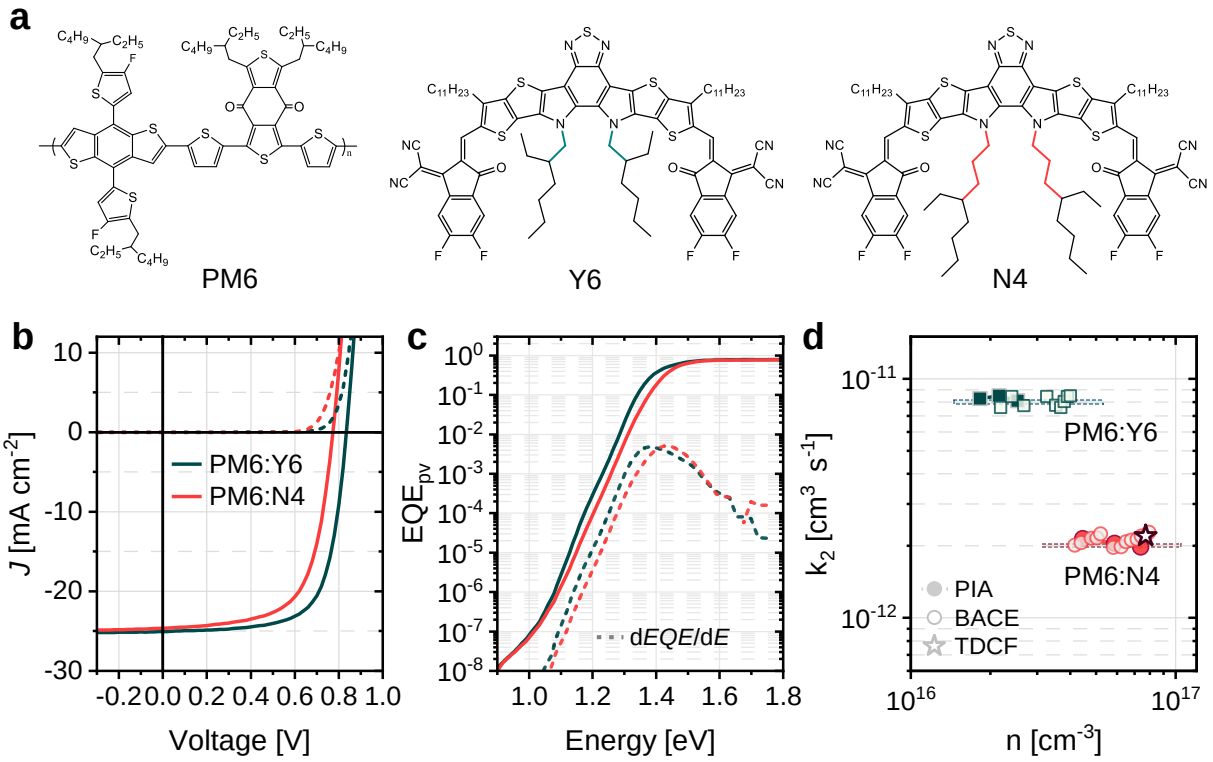

Figure 8.1: Photovoltaic characterization of PM6:Y6 and PM6:N4 solar cells. a Chemical structures of PM6, Y6 and N4. **b** Current density-voltage (*J-V*) characteristics of PM6:Y6 and PM6:N4 regular devices measured under simulated AM1.5G light (solid lines) and in the dark (dashed lines). **c** Sensitive photovoltaic external quantum efficiency (s-$\mathrm{EQE_{PV}}$) of PM6:Y6 and PM6:N4 devices (solid lines). The derivative $\mathrm{dEQE}/\mathrm{d}E$ is shown in dashed lines and the photovoltaic gap E_g^{PV} is determined from its maximum. The obtained E_g^{PV} is 1.38 eV for PM6:Y6 and 1.43 eV for PM6:N4. **d** Bimolecular recombination coefficient k_2 as a function of charge carrier density of PM6:Y6 and PM6:N4 devices measured via PIA (full symbols) and BACE (open symbols). For PM6:N4, the value of k_2 from TDCF-delay measurements is also plotted (star symbol).

We investigated nongeminate recombination of regular PM6:Y6 and PM6:N4 devices with a semi-transparent back electrode by means of charge extraction and spectroscopy techniques under steady-state conditions, namely bias-assisted charge extraction (BACE) and quasi-steady-state photoinduced absorption (PIA). In BACE, the device is held at V_{OC} under steady-state illumination and as soon as the light is turned off, a high reverse bias is applied to extract all charges.[135, 205] Provided the recombination rate, R, follows a second order dependence on charge carrier density n, k_2 is directly calculated from $R = k_2 n^2$ (Equation 2.13, section 2.4.2). PIA measurements are also performed at V_{OC}, but the yield and dynamics of free carriers are recorded by measuring the differential absorption upon modulation of the intensity of the quasi-steady-state illumination.[134, 162] Further experimental details on both techniques are found in Chapter 3. The results from both methods point to second order recombination in the blends. The recombination coefficients as a function of carrier density are compared in Figure 8.1d, where we observe that $k_2 \approx 8 \times 10^{-12}$ $\mathrm{cm^3 s^{-1}}$ for PM6:Y6 and $k_2 \approx 2 \times 10^{-12}$ $\mathrm{cm^3 s^{-1}}$ for PM6:N4, meaning that recombination is ~4 times slower in PM6:N4. This comes initially as a surprise since it is on the contrary a higher k_2 which would explain increased V_{OC} losses.[52, 111] We note that the k_2 for the PM6:Y6 regular devices in this work is lower than in our previous report, which could be related to using a newer batch of the blend materials. To confirm the conclusions about the recombination loss in PM6:N4, we additionally performed transient recombination measurements with TDCF. TDCF has been already applied to PM6:Y6 and gave excellent agreement to BACE

results (see Chapter 4 and Chapter 5).[320] The corresponding TDCF transients for PM6:N4 are shown in Figure A5.5 (Appendix A5). Analysis of these transients with an established model yielded the same k_2 as obtained via BACE and PIA, as marked in Figure 8.1d. A further source of V_{OC} losses is non-radiative recombination at the electrodes due to non-ideal contacts. To rule out carrier losses due to surface recombination, we followed the same approach as for our PM6:Y6 devices in Chapter 7,[68] and measured PIA and electromodulation injection-induced absorption (EMIA) spectroscopy on the same PM6:N4 device with regular architecture. These two complementary techniques allow us to compare photogenerated and dark injected charges at equivalent recombination currents (Figure A5.6, Appendix A5). At 1 sun, the carrier concentration under dark injection is slightly lower than under photoexcitation, but this would only cause a ~15 meV difference in the quasi-Fermi level splitting (QFLS). Furthermore, we compared the photogenerated carrier concentration in a full device and a PM6:N4 bare film on glass (Figure A5.6, Appendix A5). Here, the PM6:N4 data on device and film agree very well, as was the case for PM6:Y6,[134] suggesting that little carriers are lost due to the incorporation of transport layers and electrodes (due to interfacial or surface recombination). Consequently, the reason for the lower V_{OC} of the PM6:N4 blend must lie in the details of the energetics and recombination mechanism in the bulk, which motivated a thorough study of the morphology and energetic disorder of the two blends and the resulting photovoltaic properties, as detailed in the following.

8.4. Morphology and Energetic Disorder

We employed 2D-GIWAXS to investigate the differences in the blend morphology of PM6:Y6 and PM6:N4 films. Figure 8.2a shows the 2D-GIWAXS images of PM6:Y6 and PM6:N4. In order to disentangle the contribution of the single components in the blend, we measured films of all neat materials. Figure 8.2b,c correspond to the horizontal and vertical line cuts, respectively, of the neat materials PM6, Y6 and N4 (2D data can be found in Figure A5.7, Appendix A5), while Figure 8.2d,e contain the horizontal and vertical line cuts of the blends (from panel a). In Figure 8.2b,c, neat Y6 shows predominantly *face-on* orientation, as we observe the $\pi-\pi$ stacking in the vertical direction while the lamellar peaks are identified in the horizontal direction, in line with previous reports.[29, 36, 38] The Gaussian peak shape (coherence length of 6.4 nm) of the first lamellar peak suggests long range order within the Y6 network. On the contrary, the $\pi-\pi$ stacking in neat N4 is in the horizontal direction, pointing to preferential *edge-on* orientation. In addition, the lamellar stacking of N4 shows well defined, multiple structure peaks into specified directions which are more pronounced in comparison to the N4 $\pi-\pi$ stacking signal. Thus, the lamellar stacking seems to be the more dominant stacking mechanism for neat N4. The length of the side-chain before the branching point seems to be decisive in this competition, as a result of steric hindrance and/or the better solubility of N4.[321, 322] Overall, neat N4 is highly ordered but, in comparison to neat Y6, the $\pi-\pi$ stacking is less pronounced and the width of the peak is larger due to stronger cumulative disorder in the $\pi-\pi$ stacking of N4. For the neat PM6, there is strong lamellar stacking in the vertical direction, i.e. *edge-on* preferential orientation, while there is only evidence of a very weak $\pi-\pi$ stacking (Figure A5.7, Appendix A5). The corresponding data for the blends are shown in Figure 8.2a,d,e. For PM6:Y6, we notice that the first lamellar peak at $q_{xy}=0.29$ Å^{-1} is contributed by both PM6 and Y6 (making it hard to distinguish them), but the second lamellar peak at $q_{xy}=0.42$ Å^{-1} must have a Y6 contribution, meaning there is long range order of Y6 present within the blend. We attribute the $\pi-\pi$ stacking in the vertical direction at $q_z=1.7$ Å^{-1} almost solely to Y6 since the peak shape is nearly identical to the neat Y6 and PM6 has a weak $\pi-\pi$ stacking. Conclusively, Y6 maintains its preferential *face-on* packing when blended with PM6 and spincoated from CF with 0.5% v/v CN. In PM6:N4, the N4 lamellar ordering ($q_{xy}=0.33$

Å^{-1} and $q_{xy} = 0.41$ Å^{-1}) appears to have completely vanished, since the observed lamellar peaks in the blend resemble those of PM6 in position and shape. The lamellar peak at $q_{xy} = 0.29$ Å^{-1} of the PM6:N4 blend has a larger isotropic contribution than in the PM6:Y6 blend, i.e. PM6 is more isotropic if blended with N4. Interestingly, the $\pi - \pi$ stacking in the PM6:N4 blend is stronger in the vertical direction. It is unlikely that this signal is dominated by the PM6 which has a slightly preferred orientation of the lamellar stacking in the vertical. This in turn indicates that N4 is partially re-oriented to *face-on* in our PM6:N4 blend. This contrasts with previous morphology studies,[42] where no significant $\pi - \pi$ stacking could be observed for PM6:N4, while the lamellar stacking appeared to be similarly dominated by PM6 and thus no information on the N4 orientation in the blend could be obtained. This difference could be a result of using a different PM6 batch, with e.g. different molecular weight and/or polydispersity, or slightly different processing conditions. The addition of PM6 changes the environment of the N4 leading to a clearly altered aggregation behavior of the N4 including changes in the final orientation of the $\pi - \pi$ stacking and a loss in regular nanostructure between N4 molecules. Taking a closer look at the $\pi - \pi$ stacking, the intensity of the peaks is larger in PM6:Y6 compared to PM6:N4, meaning quantitatively that more NFA $\pi - \pi$ stacking in *face-on* direction is present in our Y6 blend. We finally performed Pseudo-Voigt fits to the $\pi - \pi$ peak and the disordered contribution in the vertical direction (see Figure A5.8 and Note A5.2, Appendix A5).[323, 324] The ratio between the area of $\pi - \pi$ peak and amorphous contribution is ~2.5 for PM6:N4 and ~5.4 for PM6:Y6, revealing a larger amorphous fraction in the PM6:N4 blend in comparison to the PM6:Y6 in the $\pi - \pi$ stacking direction. Thus, all the morphological features collected here indicate a lower degree and quality of stacking of N4 in the PM6:N4 blend in comparison to the neat N4 film, as well as in comparison to the Y6 in the PM6:Y6 blend. Here, stacking refers to the lamellar as well as the $\pi - \pi$ stacking. Particularly in the vertical direction, it becomes apparent that the PM6:N4 blend shows less order than PM6:Y6 on the short length scales that are decisive for the electronic interactions of the materials.

We noted earlier that PM6:N4 has a lower domain purity.[42] To conveniently examine this, we measured time-resolved photoluminescence (TRPL) on films of the neat acceptors blended with the inert polymer polystyrene (PS) and on the blends with PM6, as shown in Figure 8.2f,g. The PS:NFA data are fitted using a single exponential decay, whilst the PM6:NFA blends are fitted using two exponentials, see Note A5.3 and Table A5.2 (Appendix A5) for details. As expected, the blends with PM6 exhibit shorter lifetimes due to exciton quenching. In Figure 8.2f, the singlet exciton lifetime obtained for PS:Y6 is 723 ps and the weighted-average lifetime of PM6:Y6 is 88 ps, which gives a quenching efficiency of 88%. For the N4 blends, PS:N4 has a lifetime of 800 ps and PM6:N4 has 60 ps, thus the quenching efficiency is higher at 93%. Stronger exciton quenching is consistent with more intermixing in PM6:N4, i.e., more interfacial area between donor and acceptor. This in turn could be a potential source for a broadening of the DOS. For example, the presence of the other molecule disrupts the intermolecular order of the majority phase, going along with a larger energetic disorder. Also, all Y-shaped acceptor molecules exhibit quite large electrical dipole and quadrupole moments which, when mixed at low concentrations into PM6, could increase the energetic disorder in the donor phase.[325, 326] In general, more intermixing will create larger DA interfaces and a larger density of CT states, discerned by a broader and more significant low energy tail in $\mathrm{EQE_{PV}}$ measurements.[327, 328] However, as we have previously shown for PM6:Y6 in Chapter 7,[68] the tail of the sensitive $\mathrm{EQE_{PV}}$ is dominated by the Y6 exciton and there is no discernible evidence for CT absorption. We concluded this by measuring the photoluminescence (PL) spectrum of the blend, which is largely dominated by emission from the Y6 singlet exciton and using the optoelectronic reciprocity by Rau[145] to calculate the $\mathrm{EQE_{PV}}$ spectrum due to exciton absorption. We performed the same characterization for PM6:N4 in

Figure A5.9 (Appendix A5) where we observe that emission and absorption are dominated by N4 singlets. The reciprocity of the PL perfectly reproduces the tail of the measured s- EQE_{PV} except from ~1.2 eV and below, which indeed indicates additional absorption due to a low energy CT population.

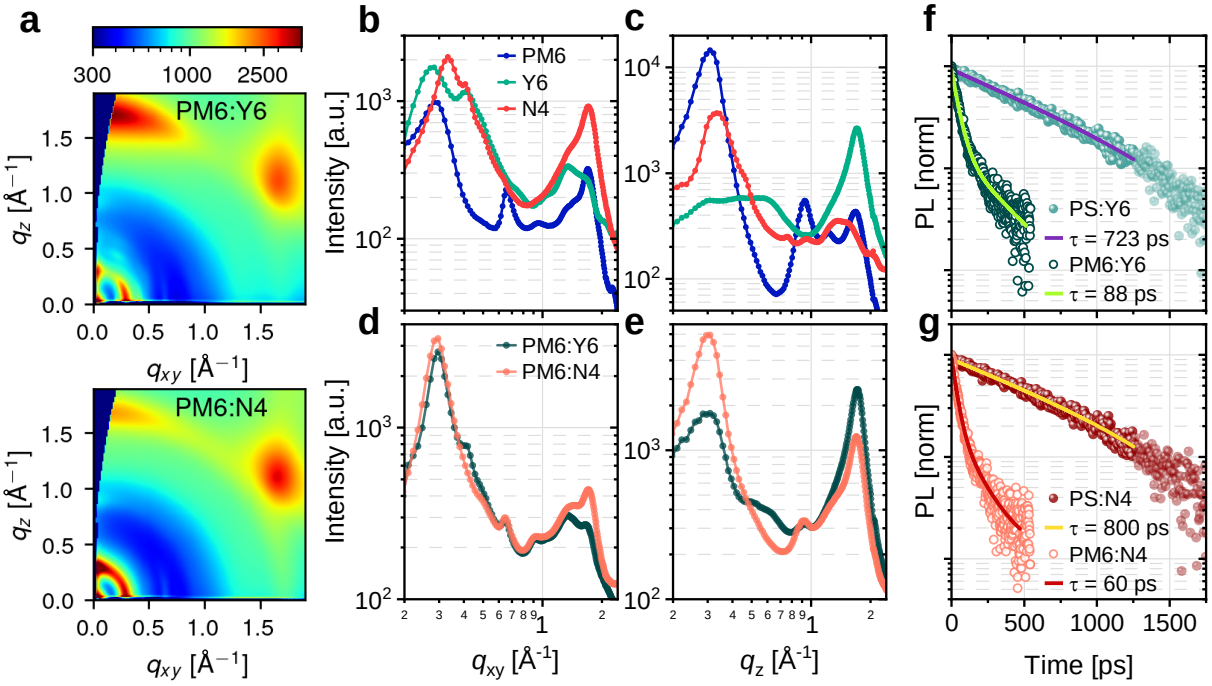

Figure 8.2: Morphology studies of the neat materials PM6, Y6 and N4, and the blends PM6:Y6 and PM6:N4. a 2D-GIWAXS images of PM6:Y6 (top) and PM6:N4 (bottom) measured on Si substrates (the strong diffraction signal at about q_{xy} = 1.7 Å^{-1}, q_z = 1.2 Å^{-1} is due to substrate scattering). **b** Horizontal and **c** vertical line cuts of the neat materials PM6, Y6 and N4. **d** Horizontal and **e** vertical line cuts of the blends PM6:Y6 and PM6:N4. Time-resolved photoluminescence measured on **f** PS:Y6 and PM6:Y6 films and **g** PS:N4 and PM6:N4 films, from which a quenching efficiency of 88% and 93%, respectively, were determined.

To establish the effect of the different morphologies on the energetic properties, we measured space charge limited currents (SCLC) of electron-only and hole-only devices as a function of temperature (see Note A5.4 and Figure A5.10-11, Appendix A5).[329] This approach has been shown to be sensitive to the shape and width of the DOS. We note that in order to avoid the effect of diffusion enhanced transport,[330] devices thicker than our typical solar cells were needed (typically larger than 150 nm). The temperature dependence of the zero-field mobility μ_0 for the PM6:Y6 and PM6:N4 blends is shown in Figure A5.12 (Appendix A5). Table 8.1 summarizes the values of μ_0 at 300 K and the energetic disorders for the HOMO, $\sigma_{H,D}$, and the LUMO, $\sigma_{L,A}$, obtained using the Gaussian disorder model (GDM), see Note A5.4 (Appendix A5). When it comes to the LUMO, the disorder is slightly larger PM6:N4, at 66 meV, while it is only 60 meV in the PM6:Y6. The electron mobility is then 5 times lower in PM6:N4 compared to PM6:Y6. It is in the HOMO where striking differences in disorder values are observed. The $\sigma_{H,D}$ increases from 74 meV in PM6:Y6 to 90 meV in PM6:N4, going along with 10 times decrease of the zero-field mobility. It seems that the lower molecular order of PM6:N4 leads to a slight increase of disorder in the LUMO while affecting to a greater extent the DOS of the HOMO. From the earlier TRPL results, we speculate that N4 molecules mix into PM6 domains.

In addition, it becomes meaningful to plot the logarithmic slope of the *J-V* curves, $\text{slope} = \text{d}(\log J)/\text{d}(\log V)$, to reveal the SCLC regime and the presence of energetic traps.[102, 203, 331, 332] This is done in Figure A5.10 and Figure A5.11 (Appendix A5) in dependence of the applied voltage for PM6:Y6 and PM6:N4 electron- and hole-only devices. The electron-only devices of both blends follow a slope between 2 and 2.5 at higher voltages. The slight increase, especially at lower temperatures, is most likely due to a field-dependence of the mobility. The situation is the same for the PM6:Y6 hole-only data. The device that behaves differently is the hole-only PM6:N4. Here, the slope saturates at higher fields and the saturation value increases with decreasing temperature, reaching close to 4 at 223 K. This behavior is characteristic for an exponential distribution of tail states.[333, 334] For SCLCs in a pure exponential DOS, $J \propto V^{2l+1}$, with $l = T_0/T$ and T_0 being the characteristic distribution temperature of the exponential DOS (see Note A5.5 Appendix A5). The best fit of the PM6:N4 hole-only data is shown in Figure A5.13 (Appendix A5) and yields $T_0 = 585$ K. The true width may, however, be different as this analysis does not consider an explicit voltage dependence of the free carrier mobility.

Table 8.1: Energetic disorder parameters. Disorder in the LUMO ($\sigma_{L,A}$) and the HOMO ($\sigma_{H,D}$), and zero-field electron (μ_e) and hole (μ_h) mobilities in the blends PM6:Y6 and PM6:N4.

Blend	$\sigma_{\text{L,A}}$ [meV]	$\sigma_{\text{H,D}}$ [meV]	μ_e [$\times 10^{-4}$ cm^{2}V^{-1}s^{-1}]	μ_h [$\times 10^{-4}$ cm^{2}V^{-1}s^{-1}]
PM6:Y6	60	74	8.4	1.3
PM6:N4	66	90	1.6	0.1

8.5. Nongeminate Recombination

As presented in section 2.4.3, the shape of the DOS does not only affect the free carrier transport but also its nongeminate recombination characteristics.[122, 206, 299, 335, 336] In brief, the recombination rate R is defined as the decay of charge carriers n with time (Equation 2.12), $R = -dn/dt = \gamma n^{\delta}$, where δ is the recombination order and γ the recombination coefficient. As introduced earlier, bimolecular recombination gives $\delta = 2$ and the recombination coefficient is then denoted as k_2. At V_{OC} conditions, recombination equals generation, while the generation rate G can be expressed in terms of the generation current J_{G} as in Equation 2.16 (section 2.4.3):

$$J_{\text{G}} = qdR = qd\gamma n^{\delta},$$

where q is the elementary charge and d is the film thickness. The steady-state recombination current is connected to the applied voltage, V, via the ideality factor, n_{id}, according to $J_R = J_0 \exp\left(\frac{qV}{n_{\text{id}} k_{\text{B}} T}\right)$, with J_0 being the dark recombination current, T temperature and k_{B}, the Boltzmann constant. Then, at open-circuit conditions (V_{OC}), we obtain Equation 2.17 (section 2.4.3):

$$J_{\text{G}}(V_{\text{OC}}) = J_{\text{R}}(V_{\text{OC}}) = J_0 \exp\left(\frac{qV_{\text{OC}}}{n_{\text{id}} k_{\text{B}} T}\right).$$

In absence of surface recombination, the V_{OC} is equal to the quasi-Fermi level splitting in the bulk which in turn, for equilibrated electrons and holes, is a function of the electron and hole densities. For an ideal intrinsic semiconductor with sharp bands, $n = p \propto \exp\left(\frac{qV_{\text{OC}}}{2k_{\text{B}}T}\right)$. In general, the relation between V_{OC} and n is re-written according to Equation 2.19 (section 2.4.3):

$$n = p = N_0 \exp\left(\frac{qV_{\text{OC}}}{2mk_{\text{B}}T}\right),$$

where the m-factor is introduced to describe the degree of disorder and N_0 is the effective density of states. In case of two Gaussians, $\delta = 2$, $n_{\mathrm{id}} = 1$ and $m = 1$, with all parameters being independent of temperature (see Table 2.1 in Chapter 2).[112] We already note here that for a Gaussian DOS, these considerations are only correct in the non-degenerate limit (see Note A5.6 Appendix A5).[142] As we will show later, the approximation holds for $T \gtrsim 200$ K in the PM6:Y6 blend. In contrast, once an exponential DOS is involved in recombination, at least two of the above parameters depend on l, and with that on temperature,[112] given that $l = T_0/T$ as introduced earlier in this chapter. Moreover, it makes a difference whether free or trapped carriers are involved. The reason is that for an exponential DOS the free carrier density is a nonlinear function of the total carrier density according to $n_f \propto n_T^l$ (this was introduced in section 2.4.3 with $l = \alpha$).

Following the above equations, we measured J-Vs and $n(V_{\mathrm{OC}})$ at different illumination intensities and as a function of temperature. Figure 8.3a,b show the recombination rate R as a function of carrier density, measured using BACE, to determine δ for PM6:Y6 and PM6:N4. For both blends, we were able to fit the entire temperature range with a slope close to 2 (see the solid lines in the plots). We also notice that the recombination is slowed down at lower temperatures and the carrier density increases in both blends, which we will discuss in greater detail below. Differences between the blends appear in the charge carrier dependence on V_{OC} as shown in Figure 8.3c,d. While the slope of $\log(n)$ versus V_{OC} becomes larger with lower temperatures in the PM6:Y6 blend, it is nearly constant in PM6:N4. Remarkably, the PM6:N4 data points seem to merge onto one line, which is clearly not the case for PM6:Y6. The same effect is seen in the $\log(J_{\mathrm{G}})$ vs V_{OC} plots in Figure 8.3e,f where we observe a weak (if any) T-dependence of the slope for PM6:N4.

These findings are summarized in Figure 8.4a, where the parameters δ, m and n_{id} taken from the fits in Figure 8.3 are plotted as a function of temperature. The values of the recombination order δ assemble around 2 for both blends, with no appreciable dependence on temperature. As anticipated for the PM6:Y6 device, m and n_{id} remain constant at values of around 1.2 in the range of 300 K down to 200 K. The temperature independence and values close to 1 support the picture that the recombination of free carriers in PM6:Y6 involves mainly two Gaussians, as we argued before in Chapter 4.[99] This situation is sketched in Figure 8.4b. A possible cause for n_{id} being slightly above one is additional recombination through midgap traps.[337] At 300 K, PM6:N4 has similar values of m and n_{id} as PM6:Y6, close to 1, but as the sample is cooled down, both parameters increase to above 1.4 at 225 K. According to Hofacker and Neher (Table 2.1),[112] it is only when free charges in a Gaussian recombine with trapped charges in an exponential that the recombination order is equal to 2 and independent of temperature, but m and n_{id} depend on T. For this case, $n_{id} = m = \frac{1}{2}\left(1 + \frac{T_0}{T}\right)$. This equation gives a reasonable fit to the experimental data (dashed grey line in Figure 8.4a), yielding $T_0 = 435$ K. We will discuss the discrepancy to the value from the T-dependent SCLC measurements below. According to SCLC results of PM6:N4 we assign a purely Gaussian shape to the density of electron-transporting states, while the density of hole-transporting states is characterized by an exponential tail (see Figure 8.4c for a schematic presentation of this situation). A possible scenario is that holes become immobilized in the exponential tail of the PM6 HOMO, while electrons move more freely in the Gaussian-shaped DOS of the N4 LUMO. Recombination takes place either at the interdiffused D:A heterojunction or electrons penetrate into the PM6-rich phase via dissolved N4 molecules. As mentioned above, R-SoXS revealed a smaller domain purity in the PM6:N4 blend compared to PM6:Y6, and GIWAXS showed no significant nanostructure between different N4 molecules when blended with PM6 apart from $\pi - \pi$ stacking.

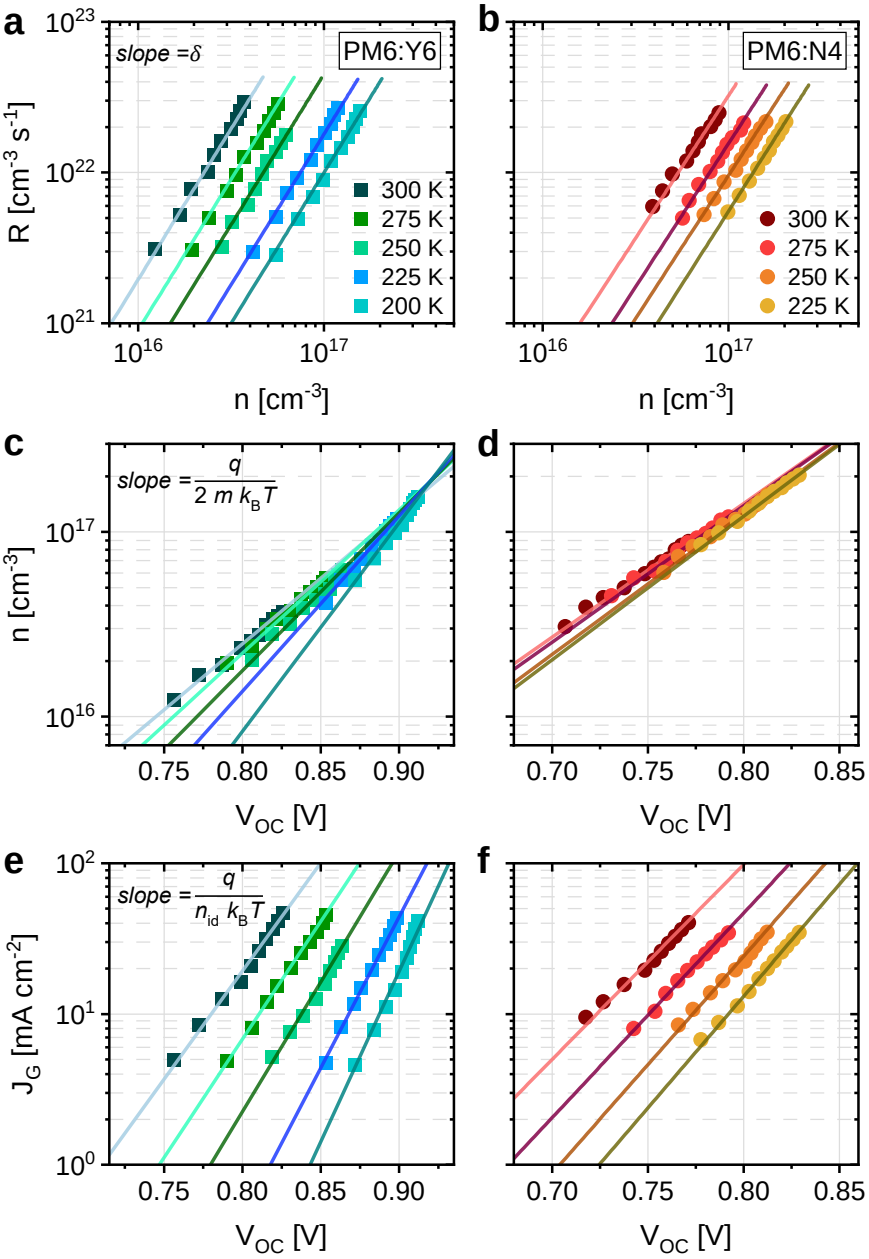

Figure 8.3: Recombination data for PM6:Y6 and PM6:N4 solar cells. Recombination rate as a function of charge carrier density to determine the recombination order δ at different temperatures for **a** PM6:Y6 and **b** PM6:N4 devices. Charge carrier density as a function of V_{OC} to determine the m-factor at different temperatures for **c** PM6:Y6 and **d** PM6:N4 devices. Generation current density as a function of V_{OC} to determine the ideality factor n_{id} at different temperatures for **e** PM6:Y6 and **f** PM6:N4 devices. δ, the m-factor and n_{id} were extracted from the slope of the solid line fits (see equations in the left side panels).

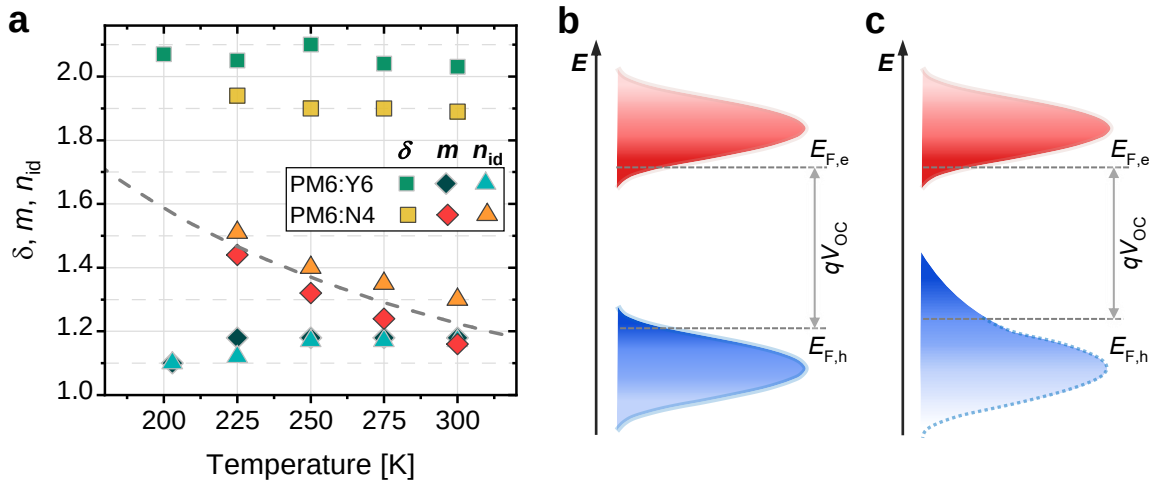

Figure 8.4: Recombination models. a Dependencies of the parameters δ, the m-factor and n_{id} on temperature for PM6:Y6 and PM6:N4 devices. δ and the m-factor were obtained from temperature-dependent BACE and n_{id} from temperature-dependent J-Vs. The dashed line is a fit to the PM6:N4 data according to the equation $n_{id} = m = \frac{1}{2}\left(1 + \frac{T_0}{T}\right)$, as predicted for free-trapped recombination in the Gaussian-exponential model. **b** Scheme of HOMO and LUMO density distributions for a Gaussian-Gaussian model. c Model of the HOMO and LUMO for PM6:N4, where recombination is dominated by holes in an exponential tail. $E_{\mathrm{F},e}$ and $E_{\mathrm{F},h}$ are the quasi-Fermi levels for electrons and holes, respectively.

8.6. Predicting the Open-Circuit Voltage as a Function of Temperature

The models proposed in Figure 8.4b,c suggest that the two blends will differ in their quasi-Fermi level splitting, $\mathrm{QFLS} = E_{\mathrm{F},e} - E_{\mathrm{F},h}$, and with that in their V_{OC} and its dependence on temperature and illumination intensity. From Equation 2.22 (section 2.5.), we know that for a Gaussian-type HOMO and LUMO, $E_{F,e} = E_{\mathrm{L,}A} - \frac{\sigma_{\mathrm{L,A}}^2}{2k_{\mathrm{B}}T} + k_{\mathrm{B}}T\ln\frac{n}{N_0}$ and $E_{F,h} = E_{\mathrm{H,D}} + \frac{\sigma_{\mathrm{H,D}}^2}{2k_{\mathrm{B}}T} - k_{\mathrm{B}}T\ln\frac{p}{N_0}$, with $E_{\mathrm{L,A}}$ and $E_{\mathrm{H,D}}$ being the center of the respective DOSs. Under the assumption that the electron and hole densities are equal ($n = p$) under illumination at open-circuit conditions, the V_{OC} can be described analytically with Equation 2.23:

$$qV_{\mathrm{OC}} = E_{\mathrm{F},e} - E_{\mathrm{F},h} = E_{\mathrm{g}} - \frac{\sigma_{\mathrm{L,A}}^2 + \sigma_{\mathrm{H,D}}^2}{2k_{\mathrm{B}}T} + 2k_{\mathrm{B}}T\ln\frac{n}{N_0},$$

where $E_{\mathrm{g}} = E_{\mathrm{L,A}} - E_{\mathrm{H,D}}$. As discussed in section 2.5. and further in Note A5.6 (Appendix A5), the above expression holds in the limit of an equilibrated population at high enough temperature, where the state population can be described by a Boltzmann distribution. This is the case when the quasi-Fermi levels are more than $3k_{\mathrm{B}}T$ away from the so-called equilibrium energies of the Gaussian DOSs. To predict the V_{OC} at low temperatures, the degenerate case has to be considered, for which Paatsch et al.[142] provided an analytical approximation (Note A5.6 and Figure A5.14, Appendix A5).

In contrast, for holes in an exponential DOS, there is no distinction between non-degenerate and degenerate regions and $E_{\mathrm{F},h} \cong E_{\mathrm{H,D}} - k_{\mathrm{B}}T_0\ln\frac{p}{N_0}$ (see Equation 2.21, section 2.4.3).[116] Then, assuming again $n = p$, the V_{OC} expression for the Gaussian-exponential model in the non-degenerate limit is

$$qV_{\mathrm{OC}} = E_{\mathrm{F},e} - E_{\mathrm{F},h} = E_{\mathrm{g}} - \frac{\sigma_{\mathrm{L,A}}^2}{2k_{\mathrm{B}}T} + k_{\mathrm{B}}(T + T_0)\, ln\frac{n}{N_0}, \qquad (8.1)$$

(see the Note A5.6 in Appendix A5 for the corresponding equation in the degenerate regime).

Equation 2.23 predicts that for the combination of two Gaussians, the increase of V_{OC} with decreasing temperature due to the entropic contribution becomes partially compensated by the reduction of the effective bandgap, $E_{\mathrm{g}}^{\mathrm{eff}} = E_{\mathrm{g}} - \frac{\sigma_{\mathrm{L,A}}^2 + \sigma_{\mathrm{H,D}}^2}{2k_{\mathrm{B}}T}$, especially at low temperatures. For the Gaussian-exponential case, the temperature dependence of both terms is reduced because $E_{\mathrm{F},h}$ does not depend explicitly on temperature.

These trends are indeed observed in the experimental $V_{\mathrm{OC}}(T)$ data plotted in Figure 8.5a. Not only is the V_{OC} higher for PM6:Y6, due to smaller disorder, but it also displays a steeper slope of the $V_{\mathrm{OC}}(T)$ dependence at higher temperatures. For low temperatures, the temperature dependence of V_{OC} becomes smaller for both systems, indicating the transition to the degenerate regime. The analytical description of the experimental $V_{\mathrm{OC}}(T)$ data requires knowledge of the temperature-dependent carrier density. Determination of n at low temperatures with BACE is problematic as this method relies on the extraction of charges. We have therefore applied PIA spectroscopy, which is an extraction-less technique, with the results shown in Figure 8.5b for 1 sun illumination conditions. First, we observe that the carrier density n is consistently higher in PM6:N4, in agreement with the smaller k_2 reported above. More importantly, for both blends there is an increase of n over the entire temperature range, being stronger at first from 300 K to 200 K.

With $n(T)$ at hand, we are now in a position to analytically describe the progression of the V_{OC} with temperature (Figure 8.5a). For PM6:Y6 with two Gaussian distributions, $V_{\mathrm{OC}}(T)$ was fitted with a combination of Equation 2.23 and Equation A5.1, Appendix A5 (see Note A5.6 for the discussion of the applicability of the equations). The fitting parameters are collected in Table A5.3 (Appendix A5). N_0 was set to the number density of Y6/N4 molecules in the blend ($N_{\mathrm{Y6/N4}} = 2.4\text{x}10^{20}$ cm^{-3}), [68] and the values of $\sigma_{\mathrm{L,A}}$ and $\sigma_{\mathrm{H,D}}$ were fixed as obtained from SCLC, leaving the HOMO-LUMO gap as the only free parameter. As shown by the solid lines in Figure 8.5a, this approach explains well the temperature dependence of V_{OC}, yielding a reasonable value for the bandgap, $E_{\mathrm{g}} = 1.42 \pm 0.015$ eV. Notably, when the system has fully entered the degenerate regime, the temperature does not appear as an independent variable anymore but influences V_{OC} only through the temperature dependence of the carrier density. Therefore, without knowledge of $n(T)$, the analysis of $V_{\mathrm{OC}}(T)$ will likely lead to wrong conclusions. We note a small discontinuity of the predicted $V_{\mathrm{OC}}(T)$ from Equation 2.23 and Equation A5.1 (Appendix A5) at the transition from the non-degenerate to the degenerate regions at around 200 K. The reason is that Equation 2.23 becomes inaccurate at this transition, but unfortunately, there is no analytical approximation to provide a description of the entire transition region. For the same reason, the bandgap from the fit is slightly different for the high and low temperature regimes.

The fit to the PM6:N4 device with the Gaussian-Gaussian model and the disorder values deduced from SCLC works well in the non-degenerate regime, but the model fails to explain the data in the low temperature region, where it predicts a stronger temperature dependence (Figure 8.5a). In contrast, the Gaussian-exponential model (Equation 8.1 and Equation A5.2, Appendix A5), marked in the plot with dashed lines, reproduces the V_{OC} over the entire temperature range. As detailed above, the lack of a temperature dependence of the (quasi-)Fermi level causes a smaller dependence of the V_{OC} on temperature, exactly as we observe in the PM6:N4 experimental data. The data could be well fitted using $T_0 = 435$ K, the value predicted from the $m(T)$ and $n_{\mathrm{id}}(T)$ data (Figure 8.4a). We notice that the V_{OC} does not increase as much as the models would predict

towards lower temperatures, in neither PM6:Y6 and PM6:N4 devices. To ensure that the reduction of the V_{OC} is not a consequence of high leakage current,[338] we compared the light and dark *J-V*s in Figure A5.15 (Appendix A5). The dark current decreases with temperature, and it is much lower than the photocurrent at low temperatures. For both systems, at 100 K, subtracting the leakage current from the photocurrent increases the V_{OC} by less than 5 mV, thus we conclude that the leakage effect is negligible. Another potential source of V_{OC} saturation is a low built-in voltage, e.g. due to a too small difference between the electrodes or an injection barrier.[52, 136, 180] We, therefore, measured $V_{OC}(T)$ for different illumination intensities (Figure A5.16, Appendix A5). Instead of converging towards a fixed V_{OC}, changing the intensity leads to a horizontal shift of the $V_{OC}(T)$, with little distortion of the shape. In fact, we could reproduce the entire data set with the parameters determined from the fit to the 1 sun $V_{OC}(T)$ data and assuming that recombination is bimolecular for all temperatures (the carrier density depends strictly on the square root of the intensity). We, therefore, believe that the slight deviation of the measured and predicted V_{OC} at low temperatures has other reasons. We, finally, point out that all published $V_{OC}(T)$ data for the PM6:Y6 blend exhibit very similar behavior, implying that the underlying phenomena are intrinsic to the blend.

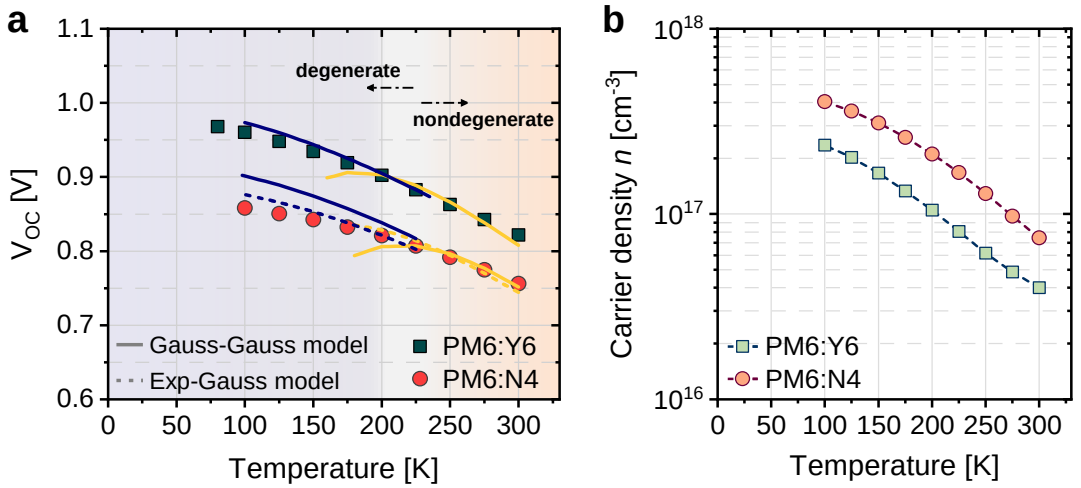

Figure 8.5: Temperature dependence of the open-circuit voltage and the carrier density in PM6:Y6 and PM6:N4 solar cells. a Open-circuit voltage V_{OC} as a function of temperature for PM6:Y6 and PM6:N4 devices (full symbols). The experimental data were fitted according to the Gaussian-Gaussian model (full lines) or the Gaussian-exponential model (dashed lines) using the expressions in the non-degenerate and degenerate regions, with the transition marked between 200 and 250 K depending on the blend and charge carrier density. The fitting parameters can be found in Table A5.3 (Appendix A5). **b** Temperature dependence of the charge carrier density n for the blends PM6:Y6 and PM6:N4 devices (symbols), obtained via PIA. Dashed lines are a guide to the eye.

8.7. Discussion and Conclusions

Our data show that energetic disorder has a pronounced effect on the absolute value of the V_{OC} but also on the steepness of its temperature dependence, already at room temperature. Consequently, disorder affects the interpretation of the linear extrapolation of the $V_{OC}(T)$ to $T = 0$, which is typically assigned to the energy of the recombining state; the charge transfer (CT) state (in organic solar cells). For PM6:Y6, the extrapolation gives $qV_{OC}(T = 0K) \cong 1.1$ eV. Because of the strong contribution of the NFA singlet excitons to the absorption and emission of this blend, there is yet no accurate value of the CT energy of PM6:Y6. Moreover, because of the energetic disorder, the mean energy of the populated CT state manifold is itself a function of temperature

and referring to one CT state energy is meaningless.[129, 339] The situation is similar for PM6:N4, where $qV_{\mathrm{OC}}(T = 0K) \cong 1.0$ eV is an unreasonably low value. Therefore, the extrapolation of qV_{OC} will not provide a reasonable estimate of the mean energy of the CT state manifold in these blends.

For PM6:Y6, the temperature-dependent charge transport can be consistently described by a Gaussian-type donor HOMO and acceptor LUMO, with a width of 74 and 60 meV, respectively. This picture is confirmed by the recombination analysis, which yielded n_{id} and m independent of temperature and close to one. Importantly, the very same disorder parameters deduced from transport measurements explain the course of the temperature-dependent V_{OC}. It has been proposed that OSCs are non-equilibrium hot carrier devices, where photo-generated carriers leave the device before they equilibrate in the DOS.[197, 305] While there is consistent proof that hot carriers assist charge extraction for highly disordered blends,[227] there is a current debate whether the same mechanism is functional at open-circuit conditions.[204] Very recently, kinetic Monte Carlo (kMC) simulations on a PM6:Y6 blend suggested a 130 meV increase in V_{OC} compared to the case of fully equilibrated charges.[340] It was also suggested that photo-generated charge carriers exit the device via one of the contacts, followed by reinjection and recombination of equilibrated charge. While we cannot fully rule out that non-equilibrated carriers affect the measured V_{OC} in our devices, we argue that experiments on PM6:Y6 blends without and with electrodes gave the same recombination rate.[134] Also, our steady-state approach reproduces the $V_{\mathrm{OC}}(T)$ on the basis of the measured carrier densities and disorders, for different illumination intensities, with the HOMO-LUMO splitting as the only unknown parameter. We see this as a strong proof that the QFLS and with that the V_{OC} is mostly determined by equilibrated carriers.

For the PM6:N4 blend, the combination of two Gaussians yields a good prediction for $V_{\mathrm{OC}}(T)$ at higher temperatures but does not provide a good fit of the low temperature regime. Here, the combination of a Gaussian-shaped N4 LUMO with a broader PM6 HOMO that has an exponential tail gives a much better description. Again, we find a very similar dependence of the carrier density on fluence for the neat PM6:N4 film and device (Figure A5.5, Appendix A5), meaning that the recombination properties are not affected by the presence of the electrodes. It is, however, unlikely that the replacement of Y6 by N4 transforms the entire PM6 HOMO into an exponential DOS. Rather than that, we presume that the larger distortion of the PM6 phase in the PM6:N4 blend but also the mixing of N4 molecules into the polymer phase broadens the tail of the DOS. As N4 and Y6 have the same conjugated core, we expect the same electric dipole and quadrupole moment for both molecules. It has been shown that a small concentration of randomly oriented electric dipoles creates a Lorentzian DOS.[325] Similarly, a random distribution of point charges creates exponential band tails.[326] Such tail broadening has been experimentally observed in doped organic molecules and polymers.[341] Further experiments and simulations are needed to reveal the true origin and shape of the PM6 HOMO, which is however beyond the scope of this paper. As a side note, such non-uniform DOS explains why T_0 from the analysis of the SCLC transport is different from the value extracted from the recombination studies. The reason is that the SCLC current is proportional to the density of free charges while, in our model, the recombination concerns mainly charges in the tail of the distribution.

The lower V_{OC} of the PM6:N4 blend is consistent with a picture of equilibrated charges in a broader density of states distribution. This raises the questions whether a similar broadening concerns the CT state manifold. Because of additional disorder of the electrostatic interaction, it is predicted that the distribution of the CT energies is wider than that of the charge separated states.[342] Also, the larger morphological disorder at the donor-acceptor interface would potentially broaden the CT DOS.[303] Unfortunately, the presence of a strong absorption and

emission from Y6 excitons prevents the determination of the spectral position and width of the CT emission in PM6:Y6.[68] In EL measurements, this is observed by injected free charges that are reformed into singlet excitons. Figure A5.17, Appendix A5 shows the EL spectra of a PM6:N4 device as a function of temperature. At 300 K, the peak at 1.32 eV corresponds to the N4 singlet but we observe that, as the sample is cooled down, a low energy contribution becomes discernible. The peak is at 1.10 eV at 300 K and it overcomes the singlet below 240 K. This is different in PM6:Y6, where the low energy peak is at ca. 1.15 eV at 300 K, but the singlet emission dominates at all temperatures.[68] For both cases, the intensity of the low energy emission is independent of temperature for a given injection current, implying that it originates from the radiative recombination of the main recombining state – the CT state. These results point to a lower energy of the populated CT manifold in PM6:N4, e.g. due to an overall lower CT energy or by more pronounced state broadening. Energetic disorder is indicated by the red-shift of the low energy emission peak in Figure A5.17 (Appendix A5) with decreasing temperature. With respect to this, recent kMC simulations suggested that free charge encounter forms an athermal CT population, whose mean energy is not simply determined by the CT state properties but in addition by the energy of the encountering charges, which itself is a function of temperature.[109] Irrespective of the exact mechanism, the data show that for PM6:N4, the offset between the populated CT and singlet state is larger, which explains the lower contribution by singlet emission and why the ELQY is more than one order of magnitude lower in PM6:N4 compared to PM6:Y6 (Figure A5.3, Appendix A5). This, in turn, explains the non-radiative voltage losses in PM6:N4.

Finally, we find that the free carrier density increases with decreasing temperature in both blends. At V_{OC}, CT states and free carriers (in the charge-separated, CS, state) are in dynamic equilibrium.[62] Our data suggest that the CT-CS balance shifts towards free charges for a lower T. In other words, the reformation of CT states by free charge encounter is more affected by the lowering of the temperature than the re-dissociation of these states into free charges. Recent transient absorption and time-resolved photoluminescence experiments suggested that charges in PM6:Y6 have to overcome a substantial Coulomb-barrier to form free carriers, which would favor CT reformation at lower temperatures.[343] On the other hand, recent simulations showed that this barrier due to mutual Coulomb attraction can be fully compensated by strong band bending across the DA heterojunction.[66] Energetic disorder will add complexity to these models as it provides additional low-lying states to host free charges.[95, 344] From the parameters deduced above, we conclude that the mean energy of the populated CS states is never larger than 1.1 eV in PM6:Y6 (see Note A5.6 and Figure A5.14, Appendix A5). This is significantly smaller than the Y6 singlet energy and, according to the EL spectra, lower than the populated CT energy. As such, energetic disorder is likely to contribute to free charge formation in such high-performance NFA-based blends.

In summary, by comparing the temperature-dependent charge transport and recombination properties of PM6 blended with two Y-shaped NFAs, Y6 and N4, we show that energetic disorder plays an important role even in high-efficiency organic solar cells. Studies of the blend morphology reveal a different packing and larger structural disorder in the PM6:N4 blend, which translates into a larger energetic disorder but also different shape of the density of states distributions. This is confirmed by temperature dependent BACE and *J-V* measurements, which reveal that the blends exhibit different nongeminate recombination mechanism: in PM6:Y6, recombination occurs between carriers in two rather narrow Gaussian state distributions while in PM6:N4, recombination is predominantly between carriers in a Gaussian-shaped LUMO DOS with carriers in the tail of a broader HOMO DOS with a more exponential character of tail states. This information combined with the carrier densities from photoinduced absorption allows us to

analytically describe the V_{OC} as a function of temperature and illumination intensity. Hereby, we find that the free carrier density increases with decreasing temperatures in both PM6:Y6 and PM6:N4, indicative of a down-hill driving force for free charge formation assisted by energetic disorder. Regarding the CT properties, electroluminescence measurements reveal a red-shifted CT emission in PM6:N4 compared to PM6:Y6, which becomes predominant over the singlet at low temperatures. This points to a lower energy of the populated CT state manifold, possibly due to a wider distribution of the CT energies in this more disordered blend, which goes along with a larger non-radiative voltage loss in PM6:N4. We conclude that energetic disorder has to be taken into account when considering the absolute value of the V_{OC} but also the steepness of its temperature dependence, and that the treatment of recombination and related properties with single CT and charge transporting levels is inappropriate. In this regard, PM6:Y6 benefits substantially from a narrower Gaussian-type density of state distribution, giving promise for the development of NFA-based solar cells with even smaller V_{OC} losses once the origin of energetic disorder is properly understood.

Conclusion and Outlook

The commencement of this thesis coincided with a turning point in the research field of organic solar cells: the appearance of newly developed small molecules named non-fullerene acceptors (NFAs). This work focuses on the generation and fate of free charge carriers in organic solar cells, with the aim to link these crucial physical processes to the unique attributes of NFA molecules and related blends. At the center of our investigations lies the PM6:Y6 blend as a model system for high-efficiency bulk-heterojunction (BHJ) solar cells.

Firstly, an important feature of polymer:NFA blends are low energy offsets at the donor-acceptor interface. In this picture, our initial goal was to study free charge generation in PM6:Y6. In particular, we aimed to address the long-standing question of "hot" vs "cold" processes by looking at a system with a low driving force for charge generation. Accordingly, in Chapter 4, the efficiency of free charge generation has been thoroughly investigated as a function of field, excitation energy and temperature. With time-delayed collection field (TDCF) measurements, we observed field-independent charge transfer (CT) dissociation upon excitation of both donor (channel I) and acceptor (channel II). This experimental result is complemented by the modeling of the internal quantum efficiency, which was also found to be independent of excitation energy. We, therefore, concluded that charge generation proceeds through a cold pathway, that is, a thermalized CT state manifold. It was at this point, however, that we realized the difficulties of identifying the energy of the CT state, E_{CT}, in PM6:Y6 using established methods for fullerene blends. Without knowledge of E_{CT}, it is not possible to obtain the value or magnitude of the driving force for hole transfer from the acceptor, $\Delta E_{\mathrm{S_1-CT}}$. Various reports including our own assigned values of E_{CT} in the range 1.29-1.31 eV or >1.40 eV,[214, 345] the latter case implying a driving force of almost zero. Very recently, Wan et al.[318] used a combination of electro-absorption and ultraviolet photoelectron spectroscopy measurements to conclusively put the E_{CT} of PM6:Y6 at 1.27 eV and the driving force for charge generation at 0.14 eV, which suggets that a small yet non-negligible $\Delta E_{\mathrm{S_1-CT}}$ may assist in charge generation. We continued with a detailed analysis of temperature-dependent external quantum efficiency (EQE) and TDCF experiments. We found that the activation energy for CT dissociation is very small at ~6 meV, which essentially implied barrierless free charge generation in PM6:Y6. This result has been recently challenged by the kinetic model employed in the work by Li et al.[128] which yielded an activation energy of ca. 100 meV for charge dissociation in PM6:Y6. The authors argue that free charge generation is in effect kinetically driven despite being energetically disadvantaged, because the dissociation rate of bound states to free charges is faster than their decay rate. This phenomenon would explain near-unity charge generation yield in PM6:Y6, which Li et al. also observed. Indeed, kinetics may contribute to efficient charge generation in PM6:Y6 but we have shown in Chapter 4 that the A-D-A molecular architecture and aggregation of Y6 are of vital importance as well. One may recall that TDCF measurements in diluted blends of PM6:Y6 (10:1 wt%) revealed field- and temperature-dependent free charge generation. This suggested that ordered Y6 clusters are needed to ensure CT separation, as also pointed out by Zhang et al.[32] and Natsuda et al.[33] In fact, theoretical modeling evidenced the presence of an electrostatic interfacial field resulting from the interaction between charges and the large quadrupole moments of Y6 molecules. The calculated interfacial bias potential leads to band bending across the DA interface and destabilizes the CT state, which can also be viewed as the E_{CT} increasing in energy and becoming less (or not) bound relative to the charge-separated state. This effectively lowers the barrier for free charge generation. Although the actual picture in the blends' solid film may differ from the modeling, there exists a correlation between photocurrent generation and the bias potential.[74] Surely, the experimental observation of barrierless free charge generation with near-unity efficiency is the first important

finding in this thesis, as it inspired many other studies on the mechanisms of CT separation in PM6:Y6 and closely related blends.

Having realized that photocurrent generation and the yield of free charges are not limiting factors in PM6:Y6, we turn our attention to other parameters that can cause a deviation from ideal performance. In Chapter 4, we reported that nongeminate recombination in PM6:Y6 is bimolecular in nature, with a bimolecular recombination coefficient $k_2 = 1.7 \times 10^{-17}$ m^3s^{-1} at one sun illumination conditions. Similar values have been since confirmed by other groups in literature.[34, 346, 347] Importantly, such values mean that recombination is only ca. 50 times suppressed compared to the Langevin model. This fact together with the moderate mobilities (in the range of 10^{-4}-10^{-3} $cm^2V^{-1}s^{-1}$) found in PM6:Y6 support that this blend predominantly suffers from extraction losses following very successful charge generation.

Our conclusions on the order and coefficient of recombination are primarily based on charge extraction techniques, i.e., TDCF and bias-assisted charge extraction (BACE). Therefore, our simulation work in Chapter 5 became key to support our view on recombination losses in PM6:Y6. In this chapter, we presented drift-diffusion simulations on TDCF and BACE to learn under which conditions these methods provide reliable information. It was important to recognize that the analysis of BACE and TDCF data assumes a homogeneous charge carrier density profile in the active layer prior to extraction. On the one hand, BACE measurements provide accurate values of the recombination order and k_2 in the absence of surface recombination. In this case, if the photogenerated carrier density is large enough (e.g., at high illumination intensities), the total (injected plus photogenerated) carrier density profiles become homogenous except close to the electrodes. This holds particularly for thick active layers (> 200 nm). On the contrary, at low illumination intensities and for thin layers, the recombination order was greater than 2 when only bimolecular recombination was implemented in the simulations. In the presence of surface recombination, results obtained via BACE did no longer represent the bulk of the active layer due to a significant charge carrier density reduction near the contacts. This also resulted in higher recombination order and values of k_2. To distinguish surface recombination, we recommended to perform BACE experiments at different layer thicknesses. On the other hand, we demonstrated that TDCF is more robust against surface recombination as the laser pulse excitation allows for homogenous and high carrier densities. Furthermore, we found that surface recombination is strongest at early times, but the recombination data measured at different fluences merged at longer times representing exclusively bulk recombination (either between photogenerated carriers or between photogenerated and dark-injected carriers). Surface recombination should then become evident when comparing experimental data from BACE and TDCF. In this regard, TDCF experiments were performed in a 100 nm PM6:Y6 device at different prebias (i.e., different background dark-injected charge) to compliment the simulations. This set of data was fitted with a bias- and fluence independent bimolecular recombination coefficient, $k_2 = 1.7 \times 10^{-17}$ m^3s^{-1}, as also obtained via BACE. The remarkable agreement between TDCF and BACE led us to conclude that nongeminate losses in thin PM6:Y6 devices are dominated by processes in the bulk and that surface recombination is of minor importance.

In Chapter 5, the influence of dark-injected charges in charge extraction methods was already discussed. In TDCF, we observed that at low illumination intensities, recombination between photogenerated charges and the background charge dominates, as the slope of the recombination rate versus charge carrier density plot is 1. The recombination order of 1 became more dominant at prebias close to the open-circuit voltage (V_{OC}). In Chapter 6, we unequivocally ascribed first order losses with respect to light intensity in the steady state to bimolecular recombination between photogenerated and dark-injected charges in the bulk of the active layer.

This observation was made possible by a combination of experimental data and numerical simulations of photocurrent and charge carrier density profiles at different conditions. We demonstrated that the “pseudo"-first order losses are more predominant as the forward bias increases, because the dark excess charge is pushed deeper into the active layer. As such, this type of recombination may be entirely responsible for fill factor (FF) losses in OSCs at intensities up to 1 sun equivalent. Also, the first order losses depended on the slower carrier mobility and decreased for lower recombination coefficients while, expectedly, second order losses in the bulk had a larger contribution as the active layer thickness increased. Notably, we revealed that ohmic contacts are the most beneficial configuration for the device performance as the surface recombination is reduced (i.e., the built-in field increases) despite having stronger recombination of photogenerated and dark charges close to the contacts. However, we note that this is the case for solar cells with significant surface recombination velocities with ohmic contacts. The findings in Chapter 6 are valuable because linear losses in OSCs have been mistakenly interpreted as geminate CT or trap-assisted recombination, but these losses were not implemented in our simulations. Therefore, we advised to be cautious when disentangling monomolecular and bimolecular losses by only measuring photocurrent as a function of intensity at 0 V. In turn, this work inspired the Bachelor thesis of Fabian Rohne titled “Intensity dependent photocurrents of organic solar cells", at the University of Potsdam. Fabian Rohne measured intensity-dependent photocurrent in PM6:Y6 solar cells. The results in the thesis for a 100 nm PM6:Y6 device closely resemble those of the FTAZ:ITIC blend in Chapter 6. At 1 sun illumination conditions, there is a small first order loss from 0 V to 0.7 V (ca. 15%), which doubles when going from 0 V to 0.8 V (close to V_{OC}). At 0.8 V, there is already a slight deviation from linearity, meaning that second order losses (recombination between photogenerated charges) are also present. This shows that first order recombination dominates the loss in FF close to maximum power point. The conclusions gathered together from Chapter 5 and Chapter 6 corroborate our views on recombination in PM6:Y6 solar cells. Decidedly, improving the performance of such devices will require to address recombination losses in the bulk.

Thus far, we have established that recombination losses limit the FF of PM6:Y6 solar cells while photogeneration losses are minimal. Therefore, we turn our attention to the V_{OC} losses. In particular, the second attribute of NFAs we were interested in was the rather high luminescence yield of the neat films, as it was proposed in the literature that the higher emission efficiency of the NFA singlet can reduce the non-radiative loss of the blend. Accordingly, we aimed to investigate the impact of Y6's emission on the radiative efficiency of the PM6:Y6 blend. In Chapter 7, we determined that the photoluminescence (PL) flux of the PM6:Y6 blend is almost the same at short-circuit and open-circuit conditions. This means that the PL of the blend is dominated by the radiative decay of Y6 excitons which are not prone to dissociation (most likely far from the interface). Thereafter, we made use of the reciprocity relation between absorption and emission, and we were able to reproduce the photovoltaic external quantum efficiency ($\mathrm{EQE_{PV}}$) of PM6:Y6 simply on the basis of the Y6 optical properties. This had the important implication that the Y6 excitons also dominate the blend absorption and consequently, there is no discernible evidence for CT absorption in the $\mathrm{EQE_{PV}}$ spectrum, confirming our previous suspicions. Additional revelations arose upon comparison of the PL and the electroluminescence (EL) spectra. We found that the EL emission peaks at the same energy as the PL and has a similar spectral shape; revealing that most radiative emission in EL originates from Y6 singlet excitons, which are reformed upon free charge recombination either directly or via the CT states. In the normalized spectra, upon subtraction of the PL from the EL, a broad low energy emission appeared peaking at 1.15 eV. We attributed this extra emission in the blend to the radiative decay of lower lying states, most likely the CT state manifold. However, the radiative recombination of CT states

contributed at maximum 10% to the total EL quantum yield (ELQY). In order to draw more conclusions from EL regarding free charge recombination, we had to assess whether the EL spectra represented the state population in the PM6:Y6 active layer under photoexcitation at V_{OC}. This was confirmed when the same free carrier density was obtained under steady-state illumination at 1 sun conditions and upon dark injection of an equivalent recombination current via photoinduced absorption and electromodulation injection absorption, respectively. These results once again corroborated that surface recombination losses in PM6:Y6 are negligible. In the following, we were able to use the ELQY to determine the chemical potential of the singlets μ_{S_1}. Given that the value was very close to the V_{OC} of the device, our study also provided proof of a dynamic equilibrium between excitons and free charges, and probably the CT states as well. As part of Chapter 7, we then measured EL spectra as a function of temperature to learn about the energetic offset between the Y6 singlet excitons and the charge-separated (CS) states, which was ~120 meV. As such, our results revealed that $E_{\mathrm{CS}} \sim 1.31$ eV. The offset of 120 meV between the singlet energy and E_{CS} explained efficient free charge formation but also pointed to a low yield of exciton reformation. Indeed, our estimate was that less than 1% of the recombination proceeds through exciton reformation and decay. In turn, most recombination proceeds through the CT state which has a lower radiative efficiency. This leads to the important conclusion that the S_1 state dominates the radiative recombination flux but this does not help the V_{OC}, as this parameter is almost entirely determined by the non-radiative recombination of the CT state. Inevitably, it is the energetics and kinetics of the CT state which define the V_{OC} of PM6:Y6 solar cells. Hence, we propose to put the focus on reducing the density and/or recombination of the interfacial CT or on improving its radiative efficiency. In addition, the yield of singlet reformation should be considered in high-efficiency polymer:NFA blends with low energy offsets.

Another important feature of NFAs that prompted the work in Chapter 8 is their high crystallinity in solid films. Due to the superior molecular ordering of NFAs, the blends exhibit a low energetic disorder. The specific goal was to understand to what extent disorder plays a role in high-efficiency polymer:NFA solar cells, especially for the V_{OC} of such blends. To this end, we performed morphology measurements, and temperature-dependent charge transport and recombination studies in the blend of PM6 with two Y-series NFAs, Y6 and N4. These blends were chosen because despite similar energetics the V_{OC} was 50 mV lower in the PM6:N4 devices. The morphology measurements revealed a different molecular orientation and less structural order in PM6:N4. This resulted in a larger energetic disorder and lower mobilities in PM6:N4 as obtained from temperature-dependent space-charge limited currents. For PM6:Y6, the electron mobility is $\sim 8 \times 10^{-4}$ $\mathrm{cm^2V^{-1}s^{-1}}$ and it decreases down to $\sim 2 \times 10^{-4}$ $\mathrm{cm^2V^{-1}s^{-1}}$ when replacing Y6 by N4. The hole mobility of PM6:Y6 is $\mu_h = 1.3 \times 10^{-4}$ $\mathrm{cm^2V^{-1}s^{-1}}$ and $\mu_h = 1.3 \times 10^{-5}$ $\mathrm{cm^2V^{-1}s^{-1}}$ of PM6:N4 (i.e. 10x lower). This large difference is a direct consequence of the different shape and width of the density of states (DOS) distribution. Temperature-dependent BACE and *J-V* measurements demonstrated that the nongeminate recombination mechanism is also different in these blends. In PM6:Y6, recombination occurs between charges in a Gaussian HOMO DOS and Gaussian LUMO DOS, both of narrow width. On the other hand, the main nongeminate loss mechanism in PM6:N4 involves carriers in a broader LUMO DOS recombining with carriers in the tail of a HOMO DOS with a more exponential character. This information together with the measured energetic disorder in the HOMO and LUMO and the free charge carrier density in the device (from photoinduced absorption as a function of temperature), allowed us to reproduce the V_{OC} as a function of temperature and illumination intensity for PM6:Y6 and PM6:N4 devices. This analysis demonstrated that energetic disorder lowers the V_{OC} value at room temperature, while also influencing its progression with temperature. In this respect, PM6:Y6 benefits considerably from narrower DOS distributions pointing yet again to the important role of morphological order.

Another key finding in this chapter was that the free carrier density increased with decreasing temperature in both PM6:Y6 and PM6:N4. This suggested that the CT-CS balance under equilibrium at V_{OC} shifts towards free charges at lower temperatures. This basically means that the reformation of CT states by free charge encounter is more affected by decreasing T than the re-dissociation into free charges, but we note that this picture becomes more complex when energetic disorder is considered. The fact that we could successfully reproduce the $V_{OC}(T)$ data with our steady-state model is a strong indication that the V_{OC} is mostly determined by equilibrated carriers. Based on this, we predict that the equilibrium energy of the populated CS states is not larger than 1.10 eV in PM6:Y6 at 300 K. Since the Y6 singlet energy is significantly larger at ~1.43 eV and the populated CT states are also higher in energy (if we take the maximum of the CT states emission in EL at ~1.15 eV from Chapter 7), we noticed that energetic disorder is likely to assist in free charge formation by providing lower-lying states, even in the highly ordered PM6:Y6 blend. This contrasted with our initial assumptions in Chapter 4. In addition, the absorption and emission studies discussed in Chapter 7 were also performed on the PM6:N4 blend. Interestingly, EQE_{PV}, PL and EL spectra all hint at an additional contribution from CT states at a lower energy (maximum at ~1.10 eV) than in PM6:Y6. In temperature dependent EL measurements of PM6:N4, the low energy emission became predominant over the singlet at low temperatures (unlike in PM6:Y6), while the intensity was independent of temperature for a given injected current (as in PM6:Y6). This finally indicated that this emission was originating from the main recombination state, that is, the CT state. The fact that the populated CT state manifold was found at a lower energy in PM6:N4 suggests a broadening of the CT states as well and explains the larger non-radiative voltage loss in this more disordered blend. Conclusively, the analysis of recombination, V_{OC}, and related properties with single CT and CS energy levels becomes inaccurate once energetic disorder is considered.

Evidently, non-fullerene acceptors have rightfully earnt a central place in the research field of organic solar cells, owing to several desirable properties as detailed throughout the thesis and in this conclusion. Despite the striking success of NFAs, this work has also identified key fundamental processes that must be addressed in order to bring the efficiency of NFA OSCs over 20%. First of all, to reduce extraction losses, the dominant bimolecular recombination pathway in the active layer needs to be reduced. To achieve lower values of k_2, we propose that a less interpenetrating blend morphology may be beneficial, which is feasible due to the large diffusion lengths of NFAs. In fact, pseudo-bilayer films prepared from sequential deposition have started to draw considerable attention,[348] because their processability is compatible with large-area blade-coating for up-scaling, as already applied to PM6:Y6 solar cells.[349, 350] In addition, the charge carrier mobilities need to be increased in order to improve charge transport. Increasing the mobility of the slower carrier (holes in PM6:Y6) is also expected to reduce recombination between photogenerated and dark-injected carriers. Higher mobilities go hand-in-hand with a lower energetic disorder, which has the potential to reduce the voltage losses, even when the morphological order in the blend is seemingly high. It was already demonstrated that the molecular packing and high crystallinity of state-of-the-art NFAs are crucial for efficient free charge generation. Strategies to improve the order of NFA solar cells even further usually begin at the basic processing conditions, including the use of additives and temperature or solvent annealing. Still, a more fundamental understanding of the origin of disorder in polymer:NFA blends is required. Finally, we believe the field requires deeper insight on the interplay between excitons, CT states and free charges in connection to radiative and non-radiative voltage losses, with an especial focus on improving the radiative properties of the CT state. Although challenging, this final endeavor will undoubtedly benefit from a consensus on the determination and analysis of the energy levels of all involved states in the photocurrent generation in OSCs.

Bibliography

[1] COP26 conclusion (2021). Available at: https://ec.europa.eu/commission/presscorner/detail/en/IP_21_6021 (accessed 02/27/2022).

[2] IEA (2021), *Net Zero by 2050*, IEA, Paris.

[3] IRENA (2019), *Global Energy Transformation: A Roadmap to 2050 (2019 Edition)*, International Renewable Energy Agency, Abu Dhabi.

[4] IEA (2021), *Key World Energy Statistics 2021*, IEA, Paris.

[5] P. Breeze. *Power generation technologies*. Elsevier, 2019.

[6] C. Battaglia, A. Cuevas, S. De Wolf. High-efficiency crystalline silicon solar cells: status and perspectives. *Energy Environ. Sci.* **9** (2016), 1552–1576.

[7] O. Almora, D. Baran, G. C. Bazan, et al. Device Performance of Emerging Photovoltaic Materials (Version 2). *Adv. Energy Mater.* **11** (2021), 2102526.

[8] B. Kippelen, J. L. Brédas. Organic photovoltaics. *Energy Environ. Sci.* **2** (2009). pp. 251–261.

[9] S. I. Na, Y. H. Seo, Y. C. Nah, et al. High Performance Roll-to-Roll Produced Fullerene-Free Organic Photovoltaic Devices via Temperature-Controlled Slot Die Coating. *Adv. Funct. Mater.* **29** (2019), 1805825.

[10] A. S. Gertsen, M. F. Castro, R. R. Søndergaard, J. W. Andreasen. Scalable fabrication of organic solar cells based on non-fullerene acceptors. *Flex. Print. Electron.* **5** (2020), 014004.

[11] R. Sun, Q. Wu, J. Guo, et al. A Layer-by-Layer Architecture for Printable Organic Solar Cells Overcoming the Scaling Lag of Module Efficiency. *Joule*. **4** (2020), 407–419.

[12] C. J. M. Emmott, J. A. Röhr, M. Campoy-Quiles, et al. Organic photovoltaic greenhouses: a unique application for semi-transparent PV? *Energy Environ. Sci.* **8** (2015), 1317–1328.

[13] E. Ravishankar, R. E. Booth, C. Saravitz, H. Sederoff, H. W. Ade, B. T. O'Connor. Achieving Net Zero Energy Greenhouses by Integrating Semitransparent Organic Solar Cells. *Joule*. **4** (2020), 490–506.

[14] M. B. Upama, M. Wright, N. K. Elumalai, et al. High-Efficiency Semitransparent Organic Solar Cells with Non-Fullerene Acceptor for Window Application. *ACS Photonics*. **4** (2017), 2327–2334.

[15] R. Xia, C. J. Brabec, H. L. Yip, Y. Cao. High-Throughput Optical Screening for Efficient Semitransparent Organic Solar Cells. *Joule*. **3** (2019), 2241–2254.

[16] N. C. Davy, M. Sezen-Edmonds, J. Gao, et al. Pairing of near-ultraviolet solar cells with electrochromic windows for smart management of the solar spectrum. *Nat. Energy*. **2** (2017), 1–11.

[17] X. Wu, Y. Liu, F. Qi, et al. Improved stability and efficiency of perovskite/organic tandem solar cells with an all-inorganic perovskite layer. *J. Mater. Chem. A*. **9** (2021), 19778–19787.

[18] P. Wang, W. Li, O. J. Sandberg, et al. Tuning of the Interconnecting Layer for Monolithic Perovskite/Organic Tandem Solar Cells with Record Efficiency Exceeding 21%. *Nano Lett.* **21** (2021), 7845–7854.

[19] C. W. Tang, A. C. Albrecht. Photovoltaic effects of metal–chlorophyll-a–metal sandwich cells. *J. Chem. Phys.* **62** (2008), 2139.

[20] G. Yu, J. Gao, J. C. Hummelen, F. Wudl, A. J. Heeger. Polymer photovoltaic cells: Enhanced efficiencies via a network of internal donor-acceptor heterojunctions. *Science.* **270** (1995), 1789.

[21] G. Dennler, M. C. Scharber, C. J. Brabec. Polymer-Fullerene Bulk-Heterojunction Solar Cells. *Adv. Mater.* **21** (2009), 1323–1338.

[22] J. A. Bartelt, Z. M. Beiley, E. T. Hoke, et al. The Importance of Fullerene Percolation in the Mixed Regions of Polymer–Fullerene Bulk Heterojunction Solar Cells. *Adv. Energy Mater.* **3** (2013), 364–374.

[23] C. Yan, S. Barlow, Z. Wang, et al. Non-fullerene acceptors for organic solar cells. *Nat. Rev. Mater.* **3** (2018). pp. 1–19.

[24] A. Armin, W. Li, O. J. Sandberg, et al. A History and Perspective of Non-Fullerene Electron Acceptors for Organic Solar Cells. *Adv. Energy Mater.* **11** (2021). p. 2003570.

[25] P. Meredith, W. Li, A. Armin. Nonfullerene Acceptors: A Renaissance in Organic Photovoltaics? *Adv. Energy Mater.* **10** (2020), 2001788.

[26] W. Zhao, S. Li, H. Yao, et al. Molecular Optimization Enables over 13% Efficiency in Organic Solar Cells. *J. Am. Chem. Soc.* **139** (2017), 7148–7151.

[27] J. Zhao, C. Yao, M. U. Ali, J. Miao, H. Meng. Recent advances in high-performance organic solar cells enabled by acceptor–donor–acceptor–donor–acceptor (A–DA'D–A) type acceptors. *Mater. Chem. Front.* **4** (2020), 3487–3504.

[28] J. Hou, O. Inganäs, R. H. Friend, F. Gao. Organic solar cells based on non-fullerene acceptors. *Nat. Mater.* **17** (2018), 119–128.

[29] J. Yuan, Y. Zhang, L. Zhou, et al. Single-Junction Organic Solar Cell with over 15% Efficiency Using Fused-Ring Acceptor with Electron-Deficient Core. *Joule*. **3** (2019), 1140–1151.

[30] J. Kniepert, M. Schubert, J. C. Blakesley, D. Neher. Photogeneration and recombination in P3HT/PCBM solar cells probed by time-delayed collection field experiments. *J. Phys. Chem. Lett.* **2** (2011), 700–705.

[31] D. Qian, Z. Zheng, H. Yao, et al. Design rules for minimizing voltage losses in high-efficiency organic solar cells. *Nat. Mater.* **17** (2018), 703–709.

[32] G. Zhang, X. K. Chen, J. Xiao, et al. Delocalization of exciton and electron wavefunction in non-fullerene acceptor molecules enables efficient organic solar cells. *Nat. Commun.* **11** (2020), 3943.

[33] S. Natsuda, T. Saito, R. Shirouchi, et al. Cascaded energy landscape as a key driver for slow yet efficient charge separation with small energy offset in organic solar cells. *Energy Environ. Sci.* (2022), doi:10.1039/d1ee03565g.

[34] J. Wu, J. Lee, Y. C. Chin, et al. Exceptionally low charge trapping enables highly efficient organic bulk heterojunction solar cells. *Energy Environ. Sci.* **13** (2020), 2422–2430.

[35] S. M. Hosseini, N. Tokmoldin, Y. W. Lee, et al. Putting Order into PM6:Y6 Solar Cells to Reduce the Langevin Recombination in 400 nm Thick Junction. *Sol. RRL*. **4** (2020), 2000498.

[36] Z. Bi, K. Chen, L. Gou, et al. Observing long-range non-fullerene backbone ordering in real-space to improve the charge transport properties of organic solar cells. *J. Mater. Chem. A*. **9** (2021), 16733–16742.

[37] S. Leng, T. Hao, G. Zhou, et al. Correlating Electronic Structure and Device Physics with Mixing Region Morphology in High-Efficiency Organic Solar Cells. *Adv. Sci.* **9** (2022), 2104613.

[38] L. Zhu, M. Zhang, G. Zhou, et al. Efficient Organic Solar Cell with 16.88% Efficiency Enabled by Refined Acceptor Crystallization and Morphology with Improved Charge Transfer and Transport Properties. *Adv. Energy Mater.* **10** (2020), 1904234.

[39] K. Li, Y. Wu, Y. Tang, et al. Ternary Blended Fullerene-Free Polymer Solar Cells with 16.5% Efficiency Enabled with a Higher-LUMO-Level Acceptor to Improve Film Morphology. *Adv. Energy Mater.* **9** (2019), 1901728.

[40] M. Zhang, L. Zhu, G. Zhou, et al. Single-layered organic photovoltaics with double cascading charge transport pathways: 18% efficiencies. *Nat. Commun.* **12** (2021), 1–10.

[41] Y. Cui, H. Yao, J. Zhang, et al. Over 16% efficiency organic photovoltaic cells enabled by a chlorinated acceptor with increased open-circuit voltages. *Nat. Commun.* **10** (2019), 2515.

[42] K. Jiang, Q. Wei, J. Y. L. Lai, et al. Alkyl Chain Tuning of Small Molecule Acceptors for Efficient Organic Solar Cells. *Joule*. **3** (2019), 3020–3033.

[43] Y. Cui, Y. Xu, H. Yao, et al. Single-Junction Organic Photovoltaic Cell with 19% Efficiency. *Adv. Mater.* **33** (2021), 2102420.

[44] K. Chong, X. Xu, H. Meng, et al. Realizing 19.05% Efficiency Polymer Solar Cells by Progressively Improving Charge Extraction and Suppressing Charge Recombination. *Adv. Mater.* (2022), 2109516.

[45] Q. Liu, Y. Jiang, K. Jin, et al. 18% Efficiency organic solar cells. *Sci. Bull.* **65** (2020), 272–275.

[46] T. Zhang, C. An, P. Bi, et al. A Thiadiazole-Based Conjugated Polymer with Ultradeep HOMO Level and Strong Electroluminescence Enables 18.6% Efficiency in Organic Solar Cell. *Adv. Energy Mater.* **11** (2021), 2101705.

[47] D. Baran, R. S. Ashraf, D. A. Hanifi, et al. Reducing the efficiency–stability–cost gap of organic photovoltaics with highly efficient and stable small molecule acceptor ternary solar cells. *Nat. Mater. 2016 163*. **16** (2016), 363–369.

[48] W. Peng, Y. Lin, S. Y. Jeong, et al. Over 18% ternary polymer solar cells enabled by a terpolymer as the third component. *Nano Energy*. **92** (2022), 106681.

[49] A. Karki, A. J. Gillett, R. H. Friend, T. Nguyen. The Path to 20% Power Conversion Efficiencies in Nonfullerene Acceptor Organic Solar Cells. *Adv. Energy Mater.* **11** (2021), 2003441.

[50] A. Köhler, H. Bässler. *Electronic processes in organic semiconductors: An introduction*. Wiley-VCH Verlag, 2015.

[51] R. E. Peierls. *Quantum Theory of Solids*. Oxford University Press, 2007.

[52] J. C. Blakesley, D. Neher. Relationship between energetic disorder and open-circuit voltage in bulk heterojunction organic solar cells. *Phys. Rev. B*. **84** (2011), 075210.

[53] T. M. Clarke, J. R. Durrant. Charge Photogeneration in Organic Solar Cells. *Chem. Rev.* **110** (2010), 6736–6767.

[54] E. Nardon, A. Matsuyama, D. Hu, et al. Efficient charge generation at low energy losses in organic solar cells: a key issues review. *Reports Prog. Phys.* **83** (2020), 082601.

[55] M. Knupfer. Exciton binding energies in organic semiconductors. *Appl. Phys. A 2003 775*. **77** (2003), 623–626.

[56] L. Zhu, Y. Yi, Z. Wei. Exciton Binding Energies of Nonfullerene Small Molecule Acceptors: Implication for Exciton Dissociation Driving Forces in Organic Solar Cells. *J. Phys. Chem. C*. **122** (2018), 22309–22316.

[57] O. V. Mikhnenko, P. W. M. Blom, T. Q. Nguyen. Exciton diffusion in organic semiconductors. *Energy Environ. Sci.* **8** (2015), 1867–1888.

[58] Y. Firdaus, V. M. Le Corre, S. Karuthedath, et al. Long-range exciton diffusion in molecular non-fullerene acceptors. *Nat. Commun.* **11** (2020), 1–10.

[59] C. Deibel, V. Dyakonov. Polymer–fullerene bulk heterojunction solar cells. *Reports Prog. Phys.* **73** (2010), 096401.

[60] C. Deibel, T. Strobel, V. Dyakonov,] C Deibel, T. Strobel, V. Dyakonov. Role of the Charge Transfer State in Organic Donor–Acceptor Solar Cells. *Adv. Mater.* **22** (2010), 4097–4111.

[61] T. Unger, S. Wedler, F.-J. Kahle, U. Scherf, H. Bässler, A. Köhler. The Impact of Driving Force and Temperature on the Electron Transfer in Donor–Acceptor Blend Systems. *J. Phys. Chem. C.* **121** (2017), 22739–22752.

[62] O. J. Sandberg, A. Armin. Energetics and Kinetics Requirements for Organic Solar Cells to Break the 20% Power Conversion Efficiency Barrier. *J. Phys. Chem. C.* **125** (2021), 15590–15598.

[63] K. Vandewal, S. Albrecht, E. T. Hoke, et al. Efficient charge generation by relaxed charge-transfer states at organic interfaces. *Nat. Mater.* **13** (2014), 63–68.

[64] S. Albrecht, K. Vandewal, J. R. Tumbleston, et al. On the Efficiency of Charge Transfer State Splitting in Polymer:Fullerene Solar Cells. *Adv. Mater.* **26** (2014), 2533–2539.

[65] J. Kurpiers, T. Ferron, S. Roland, et al. Probing the pathways of free charge generation in organic bulk heterojunction solar cells. *Nat. Commun.* **9** (2018), 2038.

[66] S. Karuthedath, J. Gorenflot, Y. Firdaus, et al. Intrinsic efficiency limits in low-bandgap non-fullerene acceptor organic solar cells. *Nat. Mater.* **20** (2021), 378–384.

[67] Y. Zhong, M. Causa', G. J. Moore, et al. Sub-picosecond charge-transfer at near-zero driving force in polymer:non-fullerene acceptor blends and bilayers. *Nat. Commun.* **11** (2020), 833.

[68] L. Perdigón-Toro, L. Quang Phuong, S. Zeiske, et al. Excitons Dominate the Emission from PM6:Y6 Solar Cells, but This Does Not Help the Open-Circuit Voltage of the Device. *ACS Energy Lett.* **6** (2021), 557–564.

[69] G. Grancini, M. Maiuri, D. Fazzi, et al. Hot exciton dissociation in polymer solar cells. *Nat. Mater.* **12** (2013), 29–33.

[70] A. A. Bakulin, A. Rao, V. G. Pavelyev, et al. The role of driving energy and delocalized states for charge separation in organic semiconductors. *Science.* **335** (2012), 1340–1344.

[71] G. Grancini, N. Martino, M. R. Antognazza, M. Celebrano, H. J. Egelhaaf, G. Lanzani. Influence of blend composition on ultrafast charge generation and recombination dynamics in low band gap polymer-based organic photovoltaics. *J. Phys. Chem. C.* **116** (2012), 9838–9844.

[72] S. Athanasopoulos, F. Schauer, V. Nádaždy, et al. What is the Binding Energy of a Charge Transfer State in an Organic Solar Cell? *Adv. Energy Mater.* **9** (2019), 1900814.

[73] M. Saladina, P. Simón Marqués, A. Markina, et al. Charge Photogeneration in Non-Fullerene Organic Solar Cells: Influence of Excess Energy and Electrostatic Interactions. *Adv. Funct. Mater.* **31** (2021), 2007479.

[74] A. Markina, K.-H. Lin, W. Liu, et al. Chemical Design Rules for Non-Fullerene Acceptors in Organic Solar Cells. *Adv. Energy Mater.* **11** (2021), 2102363.

[75] L. Benatto, C. A. M. Moraes, G. Candiotto, et al. Conditions for efficient charge generation preceded by energy transfer process in non-fullerene organic solar cells. *J. Mater. Chem. A.* **9** (2021), 27568–27585.

[76] S. Shoaee, T. M. Clarke, C. Huang, et al. Acceptor Energy Level Control of Charge Photogeneration in Organic Donor/Acceptor Blends. *J. Am. Chem. Soc.* **132** (2010), 12919–12926.

[77] S. D. Dimitrov, J. R. Durrant. Materials Design Considerations for Charge Generation in Organic Solar Cells. *Chem. Mater.* **26** (2013), 616–630.

[78] S. Shoaee, S. Subramaniyan, H. Xin, et al. Charge Photogeneration for a Series of Thiazolo-Thiazole Donor Polymers Blended with the Fullerene Electron Acceptors PCBM and ICBA. *Adv. Funct. Mater.* **23** (2013), 3286–3298.

[79] A. Tang, B. Xiao, Y. Wang, et al. Simultaneously Achieved High Open-Circuit Voltage and Efficient Charge Generation by Fine-Tuning Charge-Transfer Driving Force in Nonfullerene Polymer Solar Cells. *Adv. Funct. Mater.* **28** (2018), 1704507.

[80] H. Cha, C.-H. Tan, J. Wu, et al. An Analysis of the Factors Determining the Efficiency of Photocurrent Generation in Polymer:Nonfullerene Acceptor Solar Cells. *Adv. Energy Mater.* **8** (2018), 1801537.

[81] K. Nakano, Y. Chen, B. Xiao, et al. Anatomy of the energetic driving force for charge generation in organic solar cells. *Nat. Commun.* **10** (2019), 2520.

[82] G. Zhou, M. Zhang, Z. Chen, et al. Marcus Hole Transfer Governs Charge Generation and Device Operation in Nonfullerene Organic Solar Cells. *ACS Energy Lett.* **6** (2021), 2971–2981.

[83] C. H. Tan, J. Gorman, A. Wadsworth, et al. Barbiturate end-capped non-fullerene acceptors for organic solar cells: tuning acceptor energetics to suppress geminate recombination losses. *Chem. Commun.* **54** (2018), 2966–2969.

[84] S. Li, L. Zhan, C. Sun, et al. Highly Efficient Fullerene-Free Organic Solar Cells Operate at Near Zero Highest Occupied Molecular Orbital Offsets. *J. Am. Chem. Soc.* **141** (2019), 3073–3082.

[85] R. Jasiu Nas, H. Zhang, J. Yuan, et al. From Generation to Extraction: A Time-Resolved Investigation of Photophysical Processes in Non-fullerene Organic Solar Cells. *J. Phys. Chem. C*. **124** (2020), 21283–21292.

[86] S. Shoaee, M. Stolterfoht, D. Neher. The Role of Mobility on Charge Generation, Recombination, and Extraction in Polymer-Based Solar Cells. *Adv. Energy Mater.* **8** (2018), 1703355.

[87] Y. Puttisong, Y. Xia, X. Chen, et al. Charge Generation via Relaxed Charge-Transfer States in Organic Photovoltaics by an Energy-Disorder-Driven Entropy Gain. *J. Phys. Chem. C*. **122** (2018), 12640–12646.

[88] T. M. Burke, M. D. McGehee. How High Local Charge Carrier Mobility and an Energy Cascade in a Three-Phase Bulk Heterojunction Enable >90% Quantum Efficiency. *Adv. Mater.* **26** (2014), 1923–1928.

[89] A. Devižis, K. Meerholz, D. Hertel, V. Gulbinas. Hierarchical charge carrier motion in conjugated polymers. *Chem. Phys. Lett.* **498** (2010), 302–306.

[90] A. C. Jakowetz, M. L. Böhm, J. Zhang, et al. What Controls the Rate of Ultrafast Charge Transfer and Charge Separation Efficiency in Organic Photovoltaic Blends. *J. Am. Chem. Soc.* **138** (2016), 11672–11679.

[91] M. Casalegno, R. Pastore, J. Idé, R. Po, G. Raos. Origin of Charge Separation at Organic Photovoltaic Heterojunctions: A Mesoscale Quantum Mechanical View. *J. Phys. Chem. C*. **121** (2017), 16693–16701.

[92] F.-J. Kahle, C. Saller, S. Olthof, et al. Does Electron Delocalization Influence Charge Separation at Donor–Acceptor Interfaces in Organic Photovoltaic Cells? *J. Phys. Chem. C*. **122** (2018), 21792–21802.

[93] H. Bässler, A. Kohler. "hot or cold": How do charge transfer states at the donor-acceptor interface of an organic solar cell dissociate? *Phys. Chem. Chem. Phys.* **17** (2015), 28451–28462.

[94] P. Peumans, S. R. Forrest. Separation of geminate charge-pairs at donor–acceptor interfaces in disordered solids. *Chem. Phys. Lett.* **398** (2004), 27–31.

[95] S. N. Hood, I. Kassal. Entropy and Disorder Enable Charge Separation in Organic Solar Cells. *J. Phys. Chem. Lett.* **7** (2016), 4495–4500.

[96] C. Poelking, M. Tietze, C. Elschner, et al. Impact of mesoscale order on open-circuit voltage in organic solar cells. *Nat. Mater.* **14** (2015), 434–439.

[97] M. Schwarze, W. Tress, B. Beyer, et al. Band structure engineering in organic semiconductors. *Science*. **352** (2016), 1446–9.

[98] M. Schwarze, K. S. Schellhammer, K. Ortstein, et al. Impact of molecular quadrupole moments on the energy levels at organic heterojunctions. *Nat. Commun.* **10** (2019), 2466.

[99] L. Perdigón-Toro, H. Zhang, A. Markina, et al. Barrierless Free Charge Generation in the High-Performance PM6:Y6 Bulk Heterojunction Non-Fullerene Solar Cell. *Adv. Mater.* **32** (2020), 1906763.

[100] J. I. Khan, M. A. Alamoudi, N. Chaturvedi, et al. Impact of Acceptor Quadrupole Moment on Charge Generation and Recombination in Blends of IDT-Based Non-Fullerene Acceptors with PCE10 as Donor Polymer. *Adv. Energy Mater.* **11** (2021), 2100839.

[101] J. M. Hodgkiss. No free lunch for non-fullerene acceptors. *Nat. Mater. 2020 203*. **20** (2020), 289–290.

[102] H. Bässler. Charge Transport in Disordered Organic Photoconductors a Monte Carlo Simulation Study. *Phys. status solidi*. **175** (1993), 15–56.

[103] C. Wang, X. Zhang, H. Dong, X. Chen, W. Hu. Challenges and Emerging Opportunities in High-Mobility and Low-Energy-Consumption Organic Field-Effect Transistors. *Adv. Energy Mater.* **10** (2020), 2000955.

[104] A. Miller, E. Abrahams. Impurity Conduction at Low Concentrations. *Phys. Rev.* **120** (1960), 745.

[105] N. Tessler, Y. Preezant, N. Rappaport, Y. Roichman. Charge Transport in Disordered Organic Materials and Its Relevance to Thin-Film Devices: A Tutorial Review. *Adv. Mater.* **21** (2009), 2741–2761.

[106] J. O. Oelerich, D. Huemmer, S. D. Baranovskii. How to find out the density of states in disordered organic semiconductors. *Phys. Rev. Lett.* **108** (2012), 226403.

[107] S. D. Baranovskii. Theoretical description of charge transport in disordered organic semiconductors. *Phys. status solidi*. **251** (2014), 487–525.

[108] A. Karki, G. A. H. Wetzelaer, G. N. M. Reddy, et al. Unifying Energetic Disorder from Charge Transport and Band Bending in Organic Semiconductors. *Adv. Funct. Mater.* **29** (2019), 1901109.

[109] G. Zuo, S. Shoaee, M. Kemerink, D. Neher. General Rules for the Impact of Energetic Disorder and Mobility on Nongeminate Recombination in Phase-Separated Organic Solar Cells. *Phys. Rev. Appl.* **16** (2021), 034027.

[110] T. Kirchartz, B. E. Pieters, J. Kirkpatrick, U. Rau, J. Nelson. Recombination via tail states in polythiophene:fullerene solar cells. *Phys. Rev. B*. **83** (2011), 115209.

[111] S. D. Collins, C. M. Proctor, N. A. Ran, T.-Q. Nguyen. Understanding Open-Circuit Voltage Loss through the Density of States in Organic Bulk Heterojunction Solar Cells. *Adv. Energy Mater.* **6** (2016), 1501721.

[112] A. Hofacker, D. Neher. Dispersive and steady-state recombination in organic disordered semiconductors. *Phys. Rev. B*. **96** (2017), 245204.

[113] B. Xiao, P. Calado, R. C. I. MacKenzie, T. Kirchartz, J. Yan, J. Nelson. Relationship between fill factor and light intensity in solar cells based on organic disordered semiconductors: The role of tail states. *Phys. Rev. Appl.* **14** (2020), 024034.

[114] W. F. Pasveer, J. Cottaar, C. Tanase, et al. Unified description of charge-carrier mobilities in disordered semiconducting polymers. *Phys. Rev. Lett.* **94** (2005), 206601.

[115] A. V. Nenashev, J. O. Oelerich, S. D. Baranovskii. Theoretical tools for the description of charge transport in disordered organic semiconductors. *J. Phys. Condens. Matter*. **27** (2015), 093201.

[116] P. Mark, W. Helfrich. Space-charge-limited currents in organic crystals. *J. Appl. Phys.* **33** (1962), 205–215.

[117] C. Liu, K. Huang, W. T. Park, et al. A unified understanding of charge transport in organic semiconductors: The importance of attenuated delocalization for the carriers. *Mater. Horizons*. **4** (2017), 608–618.

[118] S. Fratini, M. Nikolka, A. Salleo, G. Schweicher, H. Sirringhaus. Charge transport in high-mobility conjugated polymers and molecular semiconductors. *Nat. Mater.* **19** (2020). pp. 491–502.

[119] H. Sirringhaus, P. J. Brown, R. H. Friend, et al. Two-dimensional charge transport in self-organized, high-mobility conjugated polymers. *Nature*. **401** (1999), 685–688.

[120] A. M. Hiszpanski, Y. L. Loo. Directing the film structure of organic semiconductors via post-deposition processing for transistor and solar cell applications. *Energy Environ. Sci.* **7** (2014). pp. 592–608.

[121] G. Kupgan, X. K. Chen, J. L. Brédas. Molecular packing of non-fullerene acceptors for organic solar cells: Distinctive local morphology in Y6 vs. ITIC derivatives. *Mater. Today Adv.* **11** (2021), 100154.

[122] D. Rauh, C. Deibel, V. Dyakonov. Charge density dependent nongeminate recombination in organic bulk heterojunction solar cells. *Adv. Funct. Mater.* **22** (2012), 3371–3377.

[123] W. Shockley, W. T. Read. Statistics of the recombinations of holes and electrons. *Phys. Rev.* **87** (1952), 835–842.

[124] P. Würfel. *Physics of Solar Cells: From Principles to New Concepts*. Wiley-VCH, 2007.

[125] P. Langevin. The recombination and mobilities of ions in gases. *Ann. Chim. Phys.* **28** (1903), 433–530.

[126] A. Armin, Z. Chen, Y. Jin, K. Zhang, F. Huang, S. Shoaee. A Shockley-Type Polymer: Fullerene Solar Cell. *Adv. Energy Mater.* **8** (2018), 1701450.

[127] S. Wilken, D. Scheunemann, S. Dahlström, M. Nyman, J. Parisi, R. Österbacka. How to Reduce Charge Recombination in Organic Solar Cells: There are Still Lessons to Learn from P3HT:PCBM. *Adv. Electron. Mater.* **7** (2021), 2001056.

[128] W. Li, S. Zeiske, O. J. Sandberg, D. B. Riley, P. Meredith, A. Armin. Organic solar cells with near-unity charge generation yield. *Energy Environ. Sci.* **14** (2021), 6484–6493.

[129] T. M. Burke, S. Sweetnam, K. Vandewal, M. D. McGehee. Beyond Langevin Recombination: How Equilibrium Between Free Carriers and Charge Transfer States Determines the Open-Circuit Voltage of Organic Solar Cells. *Adv. Energy Mater.* **5** (2015), 1500123.

[130] S. Shoaee, A. Armin, M. Stolterfoht, S. M. Hosseini, J. Kurpiers, D. Neher. Decoding Charge Recombination through Charge Generation in Organic Solar Cells. *Sol. RRL*. **3** (2019), 1900184.

[131] A. Rahimi Chatri, S. Torabi, V. M. Le Corre, L. J. A. Koster. Impact of Electrodes on Recombination in Bulk Heterojunction Organic Solar Cells. *ACS Appl. Mater. Interfaces*. **10** (2018), 12013–12020.

[132] D. J. Wehenkel, L. J. A. Koster, M. M. Wienk, R. A. J. Janssen. Influence of injected charge carriers on photocurrents in polymer solar cells. *Phys. Rev. B - Condens. Matter Mater. Phys.* **85** (2012), 1–12.

[133] J. Reinhardt, M. Grein, C. Bühler, M. Schubert, U. Würfel. Identifying the Impact of Surface Recombination at Electrodes in Organic Solar Cells by Means of Electroluminescence and Modeling. *Adv. Energy Mater.* **4** (2014), 1400081.

[134] L. Q. Phuong, S. M. Hosseini, O. J. Sandberg, et al. Quantifying Quasi-Fermi Level Splitting and Open-Circuit Voltage Losses in Highly Efficient Nonfullerene Organic Solar Cells. *Sol. RRL*. **5** (2021), 2000649.

[135] J. Kniepert, I. Lange, N. J. van der Kaap, L. J. A. Koster, D. Neher. A Conclusive View on Charge Generation, Recombination, and Extraction in As-Prepared and Annealed P3HT:PCBM Blends: Combined Experimental and Simulation Work. *Adv. Energy Mater.* **4** (2014), 1301401.

[136] A. Spies, M. List, T. Sarkar, U. Würfel. On the Impact of Contact Selectivity and Charge Transport on the Open-Circuit Voltage of Organic Solar Cells. *Adv. Energy Mater.* **7** (2017), 1601750.

[137] B. P. Rand, D. P. Burk, S. R. Forrest. Offset energies at organic semiconductor heterojunctions and their influence on the open-circuit voltage of thin-film solar cells. *Phys. Rev. B - Condens. Matter Mater. Phys.* **75** (2007), 115327.

[138] I. Lange, J. Kniepert, P. Pingel, et al. Correlation between the open circuit voltage and the energetics of organic bulk heterojunction solar cells. *J. Phys. Chem. Lett.* **4** (2013), 3865–3871.

[139] U. Rau, B. Blank, T. C. M. Müller, T. Kirchartz. Efficiency Potential of Photovoltaic Materials and Devices Unveiled by Detailed-Balance Analysis. *Phys. Rev. Appl.* **7** (2017), 044016.

[140] A. Jungbluth, P. Kaienburg, M. Riede. Charge transfer state characterization and voltage losses of organic solar cells. *J. Phys. Mater.* **5** (2022), 024002.

[141] M. Azzouzi, T. Kirchartz, J. Nelson. Factors Controlling Open-Circuit Voltage Losses in Organic Solar Cells. *Trends Chem.* **1** (2019), 49–62.

[142] G. Paasch, S. Scheinert. Charge carrier density of organics with Gaussian density of states: Analytical approximation for the Gauss-Fermi integral. *J. Appl. Phys.* **107** (2010), 104501.

[143] G. Kirchhoff. Ueber das Verhältniss zwischen dem Emissionsvermögen und dem Absorptionsvermögen der Körper für Wärme und Licht. *Ann. der Phys. und Chemie*. **185** (1860), 275–301.

[144] W. Shockley, H. J. Queisser. Detailed Balance Limit of Efficiency of *p-n* Junction Solar Cells. *J. Appl. Phys.* **32** (1961), 510–519.

[145] U. Rau. Reciprocity relation between photovoltaic quantum efficiency and electroluminescent emission of solar cells. *Phys. Rev. B - Condens. Matter Mater. Phys.* **76** (2007), 085303.

[146] J. Benduhn, K. Tvingstedt, F. Piersimoni, et al. Intrinsic non-radiative voltage losses in fullerene-based organic solar cells. *Nat. Energy.* **2** (2017), 17053.

[147] Y. Wang, D. Qian, Y. Cui, et al. Optical Gaps of Organic Solar Cells as a Reference for Comparing Voltage Losses. *Adv. Energy Mater.* **8** (2018), 1801352.

[148] K. Vandewal, K. Tvingstedt, A. Gadisa, O. Inganäs, J. V. Manca. On the origin of the open-circuit voltage of polymer-fullerene solar cells. *Nat. Mater.* **8** (2009), 904–909.

[149] A. Classen, C. L. Chochos, L. Lüer, et al. The role of exciton lifetime for charge generation in organic solar cells at negligible energy-level offsets. *Nat. Energy*. **5** (2020), 711–719.

[150] T. F. Hinrichsen, C. C. S. Chan, C. Ma, et al. Long-lived and disorder-free charge transfer states enable endothermic charge separation in efficient non-fullerene organic solar cells. *Nat. Commun.* **11** (2020), 1–10.

[151] X. K. Chen, D. Qian, Y. Wang, et al. A unified description of non-radiative voltage losses in organic solar cells. *Nat. Energy*. **6** (2021), 799–806.

[152] M. Azzouzi, J. Yan, T. Kirchartz, et al. Nonradiative Energy Losses in Bulk-Heterojunction Organic Photovoltaics. *Phys. Rev. X*. **8** (2018), 031055.

[153] F. D. Eisner, M. Azzouzi, Z. Fei, et al. Hybridization of Local Exciton and Charge-Transfer States Reduces Nonradiative Voltage Losses in Organic Solar Cells. *J. Am. Chem. Soc.* **141** (2019), 6362–6374.

[154] M. Azzouzi, N. P. Gallop, F. Eisner, et al. Reconciling models of interfacial state kinetics and device performance in organic solar cells: impact of the energy offsets on the power conversion efficiency. *Energy Environ. Sci.* (2022), doi:10.1039/d1ee02788c.

[155] Y. Dong, H. Cha, H. L. Bristow, et al. Correlating Charge-Transfer State Lifetimes with Material Energetics in Polymer:Non-Fullerene Acceptor Organic Solar Cells. *J. Am. Chem. Soc.* **143** (2021), 7599–7603.

[156] Q. Zhang, L. Yan, X. Jiao, et al. Fluorinated Thiophene Units Improve Photovoltaic Device Performance of Donor-Acceptor Copolymers. *Chem. Mater.* **29** (2017), 5990–6002.

[157] Y. Lin, F. Zhao, S. K. K. Prasad, et al. Balanced Partnership between Donor and Acceptor Components in Nonfullerene Organic Solar Cells with >12% Efficiency. *Adv. Mater.* **30** (2018), 1706363.

[158] J. Kniepert. "Correlation between Dynamic Parameters and Device Performance of Organic Solar Cells." PhD thesis. University of Potsdam, 2016.

[159] P. Caprioglio. "Non-Radiative Recombination Losses in Perovskite Solar Cells: From Fundamental Understanding to High Efficiency Devices." PhD thesis. University of Potsdam, 2020.

[160] S. Zeiske, C. Kaiser, P. Meredith, A. Armin. Sensitivity of Sub-Bandgap External Quantum Efficiency Measurements of Solar Cells under Electrical and Light Bias. *ACS Photonics*. **7** (2020), 256–264.

[161] J. Kurpiers. "Probing the Pathways of Free Charge Generation and Recombination in Organic Solar Cells: The Role of Excess Energy and Dispersive Effects." PhD thesis. University of Potsdam, 2019.

[162] L. Q. Phuong, S. M. Hosseini, C. W. Koh, H. Y. Woo, S. Shoaee. Measuring Competing Recombination Losses in a Significantly Reduced Langevin System by Steady-State Photoinduced Absorption and Photocurrent Spectroscopy. *J. Phys. Chem. C*. **123** (2019), 27417–27422.

[163] L. J. A. Koster, E. C. P. Smits, V. D. Mihailetchi, P. W. M. Blom. Device model for the operation of polymer/fullerene bulk heterojunction solar cells. *Phys. Rev. B*. **72** (2005), 085205.

[164] M. Burgelman, P. Nollet, S. Degrave. Modelling polycrystalline semiconductor solar cells. *Thin Solid Films*. **361**–**362** (2000), 527–532.

[165] V. M. Le Corre, A. R. Chatri, N. Y. Doumon, L. J. A. Koster. Charge Carrier Extraction in Organic Solar Cells Governed by Steady-State Mobilities. *Adv. Energy Mater.* **1701138** (2017), 1701138.

[166] H. K. Gummel. A Self-Consistent Iterative Scheme for One-Dimensional Steady State Transistor Calculations. *IEEE Trans. Electron Devices*. **11** (1964), 455–465.

[167] X. Xu, K. Feng, Z. Bi, W. Ma, G. Zhang, Q. Peng. Single-Junction Polymer Solar Cells with 16.35% Efficiency Enabled by a Platinum(II) Complexation Strategy. *Adv. Mater.* **31** (2019), 1901872.

[168] S. Xiong, L. Hu, L. Hu, et al. 12.5% Flexible Nonfullerene Solar Cells by Passivating the Chemical Interaction Between the Active Layer and Polymer Interfacial Layer. *Adv. Mater.* **31** (2019), 1806616.

[169] J. Yuan, T. Huang, P. Cheng, et al. Enabling low voltage losses and high photocurrent in fullerene-free organic photovoltaics. *Nat. Commun.* **10** (2019), 570.

[170] D. Baran, T. Kirchartz, S. Wheeler, et al. Reduced voltage losses yield 10% efficient fullerene free organic solar cells with >1 V open circuit voltages. *Energy Environ. Sci.* **9** (2016), 3783–3793.

[171] R. S. Gurney, D. G. Lidzey, T. Wang. A review of non-fullerene polymer solar cells: from device physics to morphology control. *Reports Prog. Phys.* **82** (2019), 036601.

[172] C. L. Braun. Electric field assisted dissociation of charge transfer states as a mechanism of photocarrier production. *J. Chem. Phys.* **80** (1984), 4157–4161.

[173] J. Shi, A. Isakova, A. Abudulimu, et al. Designing high performance all-small-molecule solar cells with non-fullerene acceptors: comprehensive studies on photoexcitation dynamics and charge separation kinetics. *Energy Environ. Sci.* **11** (2018), 211–220.

[174] J. Liu, S. Chen, D. Qian, et al. Fast charge separation in a non-fullerene organic solar cell with a small driving force. *Nat. Energy*. **1** (2016), 16089.

[175] H. Yao, Y. Cui, D. Qian, et al. 14.7% Efficiency Organic Photovoltaic Cells Enabled by Active Materials with a Large Electrostatic Potential Difference. *J. Am. Chem. Soc.* **141** (2019), 7743–7750.

[176] R. Scholz, R. Luschtinetz, G. Seifert, et al. Quantifying charge transfer energies at donor–acceptor interfaces in small-molecule solar cells with constrained DFTB and spectroscopic methods. *J. Phys. Condens. Matter*. **25** (2013), 473201.

[177] H. Tamura, I. Burghardt. Ultrafast Charge Separation in Organic Photovoltaics Enhanced by Charge Delocalization and Vibronically Hot Exciton Dissociation. *J. Am. Chem. Soc.* **135** (2013), 16364–16367.

[178] A. Y. Sosorev, D. Y. Godovsky, D. Y. Paraschuk. Hot kinetic model as a guide to improve organic photovoltaic materials. *Phys. Chem. Chem. Phys.* **20** (2018), 3658–3671.

[179] D. Di Nuzzo, L. J. A. Koster, V. S. Gevaerts, S. C. J. Meskers, R. A. J. Janssen. The Role of Photon Energy in Free Charge Generation in Bulk Heterojunction Solar Cells. *Adv. Energy Mater.* **4** (2014), 1400416.

[180] F. Gao, W. Tress, J. Wang, O. Inganäs. Temperature Dependence of Charge Carrier Generation in Organic Photovoltaics. *Phys. Rev. Lett.* **114** (2015), 128701.

[181] J. Zhang, A. C. Jakowetz, G. Li, et al. On the energetics of bound charge-transfer states in organic photovoltaics. *J. Mater. Chem. A*. **5** (2017), 11949–11959.

[182] M. Gerhard, A. P. Arndt, M. Bilal, U. Lemmer, M. Koch, I. A. Howard. Field-induced exciton dissociation in PTB7-based organic solar cells. *Phys. Rev. B*. **95** (2017), 195301.

[183] Y. Dong, H. Cha, J. Zhang, et al. The binding energy and dynamics of charge-transfer states in organic photovoltaics with low driving force for charge separation. *J. Chem. Phys.* **150** (2019), 104704.

[184] E. Collado-Fregoso, S. N. Pugliese, M. Wojcik, et al. Energy-Gap Law for Photocurrent Generation in Fullerene-Based Organic Solar Cells: The Case of Low-Donor-Content Blends. *J. Am. Chem. Soc.* **141** (2019), 2329–2341.

[185] X.-K. Chen, V. Coropceanu, J.-L. Brédas. Assessing the nature of the charge-transfer electronic states in organic solar cells. *Nat. Commun.* **9** (2018), 5295.

[186] S. D. Dimitrov, M. Azzouzi, J. Wu, et al. Spectroscopic Investigation of the Effect of Microstructure and Energetic Offset on the Nature of Interfacial Charge Transfer States in Polymer: Fullerene Blends. *J. Am. Chem. Soc.* **141** (2019), 4634–4643.

[187] M. S. Vezie, M. Azzouzi, A. M. Telford, et al. Impact of Marginal Exciton–Charge-Transfer State Offset on Charge Generation and Recombination in Polymer:Fullerene Solar Cells. *ACS Energy Lett.* **4** (2019), 2096–2103.

[188] K. Vandewal, J. Benduhn, V. C. Nikolis. How to determine optical gaps and voltage losses in organic photovoltaic materials. *Sustain. Energy Fuels*. **2** (2018), 538–544.

[189] J. Kurpiers, D. Neher. Dispersive Non-Geminate Recombination in an Amorphous Polymer:Fullerene Blend. *Sci. Rep.* **6** (2016), 26832.

[190] L. Onsager. Initial Recombination of Ions. *Phys. Rev.* **54** (1938), 554–557.

[191] O. Alqahtani, M. Babics, J. Gorenflot, et al. Mixed Domains Enhance Charge Generation and Extraction in Bulk-Heterojunction Solar Cells with Small-Molecule Donors. *Adv. Energy Mater.* **8** (2018), 1702941.

[192] S. Chandrabose, K. Chen, A. J. Barker, et al. High Exciton Diffusion Coefficients in Fused Ring Electron Acceptor Films. *J. Am. Chem. Soc.* **141** (2019), 6922–6929.

[193] A. J. Moulé, D. Neher, S. T. Turner. P3HT-based solar cells: Structural properties and photovoltaic performance. *Adv. Polym. Sci.* **265** (2014), 181–232.

[194] T. M. Clarke, A. M. Ballantyne, J. Nelson, D. D. C. Bradley, J. R. Durrant. Free Energy Control of Charge Photogeneration in Polythiophene/Fullerene Solar Cells: The Influence of Thermal Annealing on P3HT/PCBM Blends. *Adv. Funct. Mater.* **18** (2008), 4029–4035.

[195] A. A. Bakulin, Y. Xia, H. J. Bakker, O. Inganäs, F. Gao. Morphology, Temperature, and Field Dependence of Charge Separation in High-Efficiency Solar Cells Based on Alternating Polyquinoxaline Copolymer. *J. Phys. Chem. C*. **120** (2016), 4219–4226.

[196] J. Bergqvist, C. Lindqvist, O. Bäcke, et al. Sub-glass transition annealing enhances polymer solar cell performance. *J. Mater. Chem. A*. **2** (2014), 6146–6152.

[197] A. Melianas, V. Pranculis, Y. Xia, et al. Photogenerated Carrier Mobility Significantly Exceeds Injected Carrier Mobility in Organic Solar Cells. *Adv. Energy Mater.* **7** (2017), 1602143.

[198] C. Deibel, T. Strobel, V. Dyakonov. Origin of the Efficient Polaron-Pair Dissociation in Polymer-Fullerene Blends. *Phys. Rev. Lett.* **103** (2009), 036402.

[199] C. Groves. Developing understanding of organic photovoltaic devices: kinetic Monte Carlo models of geminate and non-geminate recombination, charge transport and charge extraction. *Energy Environ. Sci.* **6** (2013), 3202.

[200] S. Shoaee, S. Subramaniyan, H. Xin, et al. Charge Photogeneration for a Series of Thiazolo-Thiazole Donor Polymers Blended with the Fullerene Electron Acceptors PCBM and ICBA. *Adv. Funct. Mater.* **23** (2013), 3286–3298.

[201] O. Rubel, S. D. Baranovskii, W. Stolz, F. Gebhard. Exact Solution for Hopping Dissociation of Geminate Electron-Hole Pairs in a Disordered Chain. *Phys. Rev. Lett.* **100** (2008), 196602.

[202] S. Hood, N. Zarrabi, P. Meredith, I. Kassal, A. Armin. Measuring Energetic Disorder in Organic Semiconductors Using the Photogenerated Charge-Separation Efficiency. *J. Phys. Chem. Lett.* **10** (2019), 3863–3870.

[203] N. Felekidis, A. Melianas, M. Kemerink. Automated open-source software for charge transport analysis in single-carrier organic semiconductor diodes. *Org. Electron.* **61** (2018), 318–328.

[204] S. Roland, J. Kniepert, J. A. Love, et al. Equilibrated Charge Carrier Populations Govern Steady-State Nongeminate Recombination in Disordered Organic Solar Cells. *J. Phys. Chem. Lett.* **10** (2019), 1374–1381.

[205] S. M. Hosseini, S. Roland, J. Kurpiers, et al. Impact of Bimolecular Recombination on the Fill Factor of Fullerene and Nonfullerene-Based Solar Cells: A Comparative Study of Charge Generation and Extraction. *J. Phys. Chem. C*. **123** (2019), 6823–6830.

[206] T. Kirchartz, J. Nelson. Meaning of reaction orders in polymer:fullerene solar cells. *Phys. Rev. B*. **86** (2012), 165201.

[207] G. Lakhwani, A. Rao, R. H. Friend. Bimolecular Recombination in Organic Photovoltaics. *Annu. Rev. Phys. Chem.* **65** (2014), 557–581.

[208] H. Cha, G. Fish, J. Luke, et al. Suppression of Recombination Losses in Polymer:Nonfullerene Acceptor Organic Solar Cells due to Aggregation Dependence of Acceptor Electron Affinity. *Adv. Energy Mater.* **9** (2019), 1901254.

[209] C. Poelking, D. Andrienko. Design Rules for Organic Donor–Acceptor Heterojunctions: Pathway for Charge Splitting and Detrapping. *J. Am. Chem. Soc.* **137** (2015), 6320–6326.

[210] C. Poelking, D. Andrienko. Long-Range Embedding of Molecular Ions and Excitations in a Polarizable Molecular Environment. *J. Chem. Theory Comput.* **12** (2016), 4516–4523.

[211] G. D'Avino, L. Muccioli, F. Castet, et al. Electrostatic phenomena in organic semiconductors: fundamentals and implications for photovoltaics. *J. Phys. Condens. Matter*. **28** (2016), 433002.

[212] N. B. Kotadiya, A. Mondal, P. W. M. Blom, D. Andrienko, G.-J. J. A. H. Wetzelaer. A window to trap-free charge transport in organic semiconducting thin films. *Nat. Mater.* **18** (2019). pp. 1182–1186.

[213] D. Abbaszadeh, A. Kunz, N. B. Kotadiya, et al. Electron Trapping in Conjugated Polymers. *Chem. Mater.* **31** (2019), 6380–6386.

[214] A. Karki, J. Vollbrecht, A. L. Dixon, et al. Understanding the High Performance of over 15% Efficiency in Single-Junction Bulk Heterojunction Organic Solar Cells. *Adv. Mater.* **31** (2019), 1903868.

[215] H. Mangold, A. A. Bakulin, I. A. Howard, et al. Control of charge generation and recombination in ternary polymer/polymer:fullerene photovoltaic blends using amorphous and semi-crystalline copolymers as donors. *Phys. Chem. Chem. Phys.* **16** (2014), 20329–20337.

[216] J. Kniepert, I. Lange, J. Heidbrink, et al. Effect of Solvent Additive on Generation, Recombination, and Extraction in PTB7:PCBM Solar Cells: A Conclusive Experimental and Numerical Simulation Study. *J. Phys. Chem. C*. **119** (2015), 8310–8320.

[217] C. M. Proctor, M. Kuik, T.-Q. Nguyen. Charge carrier recombination in organic solar cells. *Prog. Polym. Sci.* **38** (2013), 1941–1960.

[218] M. Stolterfoht, A. Armin, B. Philippa, et al. Photocarrier drift distance in organic solar cells and photodetectors. *Sci. Rep.* **5** (2015), 9949.

[219] D. Bartesaghi, I. del C. Pérez, J. Kniepert, et al. Competition between recombination and extraction of free charges determines the fill factor of organic solar cells. *Nat. Commun.* **6** (2015), 7083.

[220] F. S. U. Fischer, D. Trefz, J. Back, et al. Highly crystalline films of PCPDTBT with branched side chains by solvent vapor crystallization: Influence on opto-electronic properties. *Adv. Mater.* **27** (2015), 1223–1228.

[221] P. Kaienburg, U. Rau, T. Kirchartz. Extracting Information about the Electronic Quality of Organic Solar-Cell Absorbers from Fill Factor and Thickness. *Phys. Rev. Appl.* **6** (2016), 024001.

[222] C. G. Shuttle, B. O'Regan, A. M. Ballantyne, J. Nelson, D. D. C. Bradley, J. R. Durrant. Bimolecular recombination losses in polythiophene: Fullerene solar cells. *Phys. Rev. B - Condens. Matter Mater. Phys.* **78** (2008), 1–4.

[223] J. Guo, H. Ohkita, S. Yokoya, H. Benten, S. Ito. Bimodal Polarons and Hole Transport in Poly(3-hexylthiophene):Fullerene Blend Films. *J. Am. Chem. Soc.* **132** (2010), 9631–9637.

[224] S. M. Menke, A. Sadhanala, M. Nikolka, et al. Limits for Recombination in a Low Energy Loss Organic Heterojunction. *ACS Nano*. **10** (2016), 10736–10744.

[225] L. M. Andersson, A. Melianas, Y. Infahasaeng, et al. Unified Study of Recombination in Polymer:Fullerene Solar Cells Using Transient Absorption and Charge-Extraction Measurements. *J. Phys. Chem. Lett.* **4** (2013), 2069–2072.

[226] A. J. Mozer, N. S. Sariciftci, L. Lutsen, et al. Charge transport and recombination in bulk heterojunction solar cells studied by the photoinduced charge extraction in linearly increasing voltage technique. *Appl. Phys. Lett.* **86** (2005), 1–3.

[227] N. Gasparini, M. Salvador, T. Heumueller, et al. Polymer:Nonfullerene Bulk Heterojunction Solar Cells with Exceptionally Low Recombination Rates. *Adv. Energy Mater.* **7** (2017), 1701561.

[228] C. G. Shuttle, B. O'Regan, A. M. Ballantyne, et al. Experimental determination of the rate law for charge carrier decay in a polythiophene: Fullerene solar cell. *Appl. Phys. Lett.* **92** (2008), 2008–2010.

[229] R. Hamilton, C. G. Shuttle, B. O'Regan, T. C. Hammant, J. Nelson, J. R. Durrant. Recombination in annealed and nonannealed polythiophene/fullerene solar cells: Transient photovoltage studies versus numerical modeling. *J. Phys. Chem. Lett.* **1** (2010), 1432–1436.

[230] D. Baran, N. Gasparini, A. Wadsworth, et al. Robust nonfullerene solar cells approaching unity external quantum efficiency enabled by suppression of geminate recombination. *Nat. Commun.* **9** (2018), 1–9.

[231] D. Kiermasch, A. Baumann, M. Fischer, V. Dyakonov, K. Tvingstedt. Revisiting lifetimes from transient electrical characterization of thin film solar cells; a capacitive concern evaluated for silicon, organic and perovskite devices. *Energy Environ. Sci.* **11** (2018), 629–640.

[232] O. J. Sandberg, K. Tvingstedt, P. Meredith, A. Armin. Theoretical Perspective on Transient Photovoltage and Charge Extraction Techniques. *J. Phys. Chem. C*. **123** (2019), 14261–14271.

[233] C. G. Shuttle, A. Maurano, R. Hamilton, B. O'Regan, J. C. De Mello, J. R. Durrant. Charge extraction analysis of charge carrier densities in a polythiophene/fullerene solar cell: Analysis of the origin of the device dark current. *Appl. Phys. Lett.* **93** (2008), 2008–2010.

[234] C. M. Proctor, C. Kim, D. Neher, T. Q. Nguyen. Nongeminate recombination and charge transport limitations in diketopyrrolopyrrole-based solution-processed small molecule solar cells. *Adv. Funct. Mater.* **23** (2013), 3584–3594.

[235] C. Deibel, A. Wagenpfahl, V. Dyakonov. Origin of reduced polaron recombination in organic semiconductor devices. *Phys. Rev. B - Condens. Matter Mater. Phys.* **80** (2009), 1–7.

[236] F. Deledalle, P. Shakya Tuladhar, J. Nelson, J. R. Durrant, T. Kirchartz. Understanding the Apparent Charge Density Dependence of Mobility and Lifetime in Organic Bulk Heterojunction Solar Cells. *J. Phys. Chem. C*. **118** (2014), 8837–8842.

[237] S. Albrecht, S. Janietz, W. Schindler, et al. Fluorinated copolymer PCPDTBT with enhanced open-circuit voltage and reduced recombination for highly efficient polymer solar cells. *J. Am. Chem. Soc.* **134** (2012), 14932–14944.

[238] W. Li, S. Albrecht, L. Yang, et al. Mobility-controlled performance of thick solar cells based on fluorinated copolymers. *J. Am. Chem. Soc.* **136** (2014), 15566–15576.

[239] S. Roland, L. Yan, Q. Zhang, et al. Charge Generation and Mobility-Limited Performance of Bulk Heterojunction Solar Cells with a Higher Adduct Fullerene. *J. Phys. Chem. C*. **121** (2017), 10305–10316.

[240] T. Ferron, M. Waldrip, M. Pope, B. A. Collins. Increased charge transfer state separation *via* reduced mixed phase interface in polymer solar cells. *J. Mater. Chem. A*. **7** (2019), 4536–4548.

[241] U. Würfel, L. Perdigón-Toro, J. Kurpiers, et al. Recombination between Photogenerated and Electrode-Induced Charges Dominates the Fill Factor Losses in Optimized Organic Solar Cells. *J. Phys. Chem. Lett.* **10** (2019), 3473–3480.

[242] S. A. Hawks, B. Y. Finck, B. J. Schwartz. Theory of Current Transients in Planar Semiconductor Devices: Insights and Applications to Organic Solar Cells. *Phys. Rev. Appl.* **3** (2015), 044014.

[243] O. J. Sandberg, A. Sundqvist, M. Nyman, R. Österbacka. Relating Charge Transport, Contact Properties, and Recombination to Open-Circuit Voltage in Sandwich-Type Thin-Film Solar Cells. *Phys. Rev. Appl.* **5** (2016), 044005.

[244] A. Pivrikas, G. Juška, A. J. Mozer, et al. Bimolecular Recombination Coefficient as a Sensitive Testing Parameter for Low-Mobility Solar-Cell Materials. *Phys. Rev. Lett.* **94** (2005), 176806.

[245] U. Würfel, M. Unmüssig. Apparent Field-Dependence of the Charge Carrier Generation in Organic Solar Cells as a Result of (Bimolecular) Recombination. *Sol. RRL*. **2** (2018), 1800229.

[246] H. Zhou, Y. Zhang, J. Seifter, et al. High-Efficiency Polymer Solar Cells Enhanced by Solvent Treatment. *Adv. Mater.* **25** (2013), 1646–1652.

[247] L. Lu, T. Zheng, Q. Wu, A. M. Schneider, D. Zhao, L. Yu. Recent Advances in Bulk Heterojunction Polymer Solar Cells. *Chem. Rev.* **115** (2015). pp. 12666–12731.

[248] Y. Firdaus, V. M. Le Corre, J. I. Khan, et al. Key Parameters Requirements for Non-Fullerene-Based Organic Solar Cells with Power Conversion Efficiency >20%. *Adv. Sci.* **6** (2019), 1802028.

[249] U. Würfel, D. Neher, A. Spies, S. Albrecht. Impact of charge transport on current-voltage characteristics and power-conversion efficiency of organic solar cells. *Nat Commun*. **6** (2015), 6951.

[250] D. Neher, J. Kniepert, A. Elimelech, L. J. A. Koster. A New Figure of Merit for Organic Solar Cells with Transport-limited Photocurrents. *Sci. Rep.* **6** (2016), 24861.

[251] T. Kirchartz, T. Agostinelli, M. Campoy-Quiles, W. Gong, J. Nelson. Understanding the Thickness-Dependent Performance of Organic Bulk Heterojunction Solar Cells: The Influence of Mobility, Lifetime, and Space Charge. *J. Phys. Chem. Lett.* **3** (2012), 3470–3475.

[252] M. Stolterfoht, A. Armin, B. Philippa, D. Neher. The Role of Space Charge Effects on the Competition between Recombination and Extraction in Solar Cells with Low-Mobility Photoactive Layers. *J. Phys. Chem. Lett.* **7** (2016), 4716–4721.

[253] L. J. A. Koster, M. Kemerink, M. M. Wienk, M. Klará, R. A. J. Janssen. Quantifying Bimolecular Recombination Losses in Organic Bulk Heterojunction Solar Cells. *Adv. Mater.* **23** (2011), 1670–1674.

[254] S. R. Cowan, A. Roy, A. J. Heeger. Recombination in polymer-fullerene bulk heterojunction solar cells. *Phys. Rev. B*. **82** (2010), 245207.

[255] Z. Li, C. R. McNeill. Transient photocurrent measurements of PCDTBT:PC70BM and PCPDTBT:PC70BM Solar Cells: Evidence for charge trapping in efficient polymer/fullerene blends. *J. Appl. Phys.* **109** (2011), 74513.

[256] R. a. Street, M. Schoendorf, A. Roy, J. H. Lee. Interface state recombination in organic solar cells. *Phys. Rev. B*. **81** (2010), 205307.

[257] M. Stolterfoht, S. Shoaee, A. Armin, et al. Electric Field and Mobility Dependent First-Order Recombination Losses in Organic Solar Cells. *Adv. Energy Mater.* **7** (2017), 1601379.

[258] H. Bin, L. Gao, Z. G. Zhang, et al. 11.4% Efficiency non-fullerene polymer solar cells with trialkylsilyl substituted 2D-conjugated polymer as donor. *Nat. Commun.* **7** (2016), 1–11.

[259] J. Yuan, Y. Zhang, S. Xie, X. Zhang, X. Zuo, H. Zhou. Understanding charge transport and recombination losses in high performance polymer solar cells with non-fullerene acceptors. *J. Mater. Chem. A*. **5** (2017), 17230–17239.

[260] A. K. K. Kyaw, D. H. Wang, V. Gupta, et al. Intensity dependence of current-voltage characteristics and recombination in high-efficiency solution-processed small-molecule solar cells. *ACS Nano*. **7** (2013), 4569–4577.

[261] S. R. Cowan, J. Wang, J. Yi, Y. J. Lee, D. C. Olson, J. W. P. Hsu. Intensity and wavelength dependence of bimolecular recombination in P3HT:PCBM solar cells: A white-light biased external quantum efficiency study. *J. Appl. Phys.* **113** (2013), doi:10.1063/1.4801920.

[262] S. R. Cowan, W. L. Leong, N. Banerji, G. Dennler, A. J. Heeger. Identifying a Threshold Impurity Level for Organic Solar Cells: Enhanced First-Order Recombination Via Well-Defined PC84BM Traps in Organic Bulk Heterojunction Solar Cells. *Adv. Funct. Mater.* **21** (2011), 3083–3092.

[263] Z. Li, G. Lakhwani, N. C. Greenham, C. R. McNeill. Voltage-dependent photocurrent transients of PTB7:PC70BM solar cells: Experiment and numerical simulation. *J. Appl. Phys.* **114** (2013), 34502.

[264] G. F. A. Dibb, T. Kirchartz, D. Credgington, J. R. Durrant, J. Nelson. Analysis of the Relationship between Linearity of Corrected Photocurrent and the Order of Recombination in Organic Solar Cells. *J. Phys. Chem. Lett.* **2** (2011), 2407–2411.

[265] V. D. Mihailetchi, L. J. A. Koster, J. C. Hummelen, P. W. M. Blom. Photocurrent Generation in Polymer-Fullerene Bulk Heterojunctions. *Phys. Rev. Lett.* **93** (2004), 216601.

[266] M. Lenes, M. Morana, C. J. Brabec, P. W. M. Blom. Recombination-Limited Photocurrents in Low Bandgap Polymer/Fullerene Solar Cells. *Adv. Funct. Mater.* **19** (2009), 1106–1111.

[267] T. Hahn, S. Tscheuschner, F. J. Kahle, et al. Monomolecular and Bimolecular Recombination of Electron–Hole Pairs at the Interface of a Bilayer Organic Solar Cell. *Adv. Funct. Mater.* **27** (2017), 1604906.

[268] R. Mauer, I. A. Howard, F. F. Laquai. Effect of External Bias on Nongeminate Recombination in Polythiophene/Methanofullerene Organic Solar Cells. *J. Phys. Chem. Lett.* **2** (2011), 1736–1741.

[269] A. Foertig, J. Kniepert, M. Gluecker, et al. Nongeminate and Geminate Recombination in PTB7:PCBM Solar Cells. *Adv. Funct. Mater.* **24** (2013), 1306.

[270] S. Gélinas, A. Rao, A. Kumar, et al. Ultrafast Long-Range Charge Separation in Organic Semiconductor Photovoltaic Diodes. *Science.* **343** (2014), 512–516.

[271] G. F. A. Dibb, F. C. Jamieson, A. Maurano, J. Nelson, J. R. Durrant. Limits on the Fill Factor in Organic Photovoltaics: Distinguishing Nongeminate and Geminate Recombination Mechanisms. *J. Phys. Chem. Lett.* **4** (2013), 803–808.

[272] M. Stolterfoht, A. Armin, S. Shoaee, I. Kassal, P. Burn, P. Meredith. Slower carriers limit charge generation in organic semiconductor light-harvesting systems. *Nat. Commun.* **7** (2016), 11944.

[273] M. Stolterfoht, B. Philippa, S. Shoaee, et al. Charge Transport without Recombination in Organic Solar Cells and Photodiodes. *J. Phys. Chem. C*. **119** (2015), 26866–26874.

[274] Y. Liang, Z. Xu, J. Xia, et al. For the bright future-bulk heterojunction polymer solar cells with power conversion efficiency of 7.4%. *Adv. Mater.* **22** (2010), E135–E138.

[275] S. C. Price, A. C. Stuart, L. Yang, H. Zhou, W. You. Fluorine Substituted Conjugated Polymer of Medium Band Gap Yields 7% Efficiency in Polymer–Fullerene Solar Cells. *J. Am. Chem. Soc.* **133** (2011), 4625–4631.

[276] Synopsys. Synopsys TCAD, release L-2016.03-SP2. 2016. Available: http://www.synopsys.com.

[277] B. Philippa, M. Stolterfoht, P. L. Burn, et al. The impact of hot charge carrier mobility on photocurrent losses in polymer-based solar cells. *Sci. Rep.* **4** (2015), 5695.

[278] G. A. H. Wetzelaer, P. W. M. Blom. Ohmic current in organic metal-insulator-metal diodes revisited. *Phys. Rev. B - Condens. Matter Mater. Phys.* **89** (2014), 1–5.

[279] M. C. Heiber, C. Baumbach, V. Dyakonov, C. Deibel. Encounter-Limited Charge-Carrier Recombination in Phase-Separated Organic Semiconductor Blends. *Phys. Rev. Lett.* **114** (2015), 136602.

[280] M. A. Green, E. D. Dunlop, J. Hohl-Ebinger, M. Yoshita, N. Kopidakis, X. Hao. Solar cell efficiency tables (version 56). *Prog. Photovoltaics Res. Appl.* **28** (2020), 629–638.

[281] B. Siegmund, A. Mischok, J. Benduhn, et al. Organic narrowband near-infrared photodetectors based on intermolecular charge-transfer absorption. *Nat. Commun.* **8** (2017), 1–6.

[282] M. List, T. Sarkar, P. Perkhun, J. Ackermann, C. Luo, U. Würfel. Correct determination of charge transfer state energy from luminescence spectra in organic solar cells. *Nat. Commun.* **9** (2018), 1–8.

[283] A. Armin, N. Zarrabi, O. J. Sandberg, et al. Limitations of Charge Transfer State Parameterization Using Photovoltaic External Quantum Efficiency. *Adv. Energy Mater.* **10** (2020), 2001828.

[284] S. Ullbrich, J. Benduhn, X. Jia, et al. Emissive and charge-generating donor–acceptor interfaces for organic optoelectronics with low voltage losses. *Nat. Mater.* **18** (2019), 459–464.

[285] K. Vandewal, S. Mertens, J. Benduhn, Q. Liu. The Cost of Converting Excitons into Free Charge Carriers in Organic Solar Cells. *J. Phys. Chem. Lett.* **11** (2019), 129–135.

[286] X. Zou, G. Wen, R. Hu, et al. An Insight into the Excitation States of Small Molecular Semiconductor Y6. *Molecules*. **25** (2020), 4118.

[287] Y. Gu, Y. Liu, T. P. Russell. Fullerene-Based Interlayers for Breaking Energy Barriers in Organic Solar Cells. *Chempluschem*. **85** (2020), 751–759.

[288] N. Zarrabi, O. J. Sandberg, S. Zeiske, et al. Charge-generating mid-gap trap states define the thermodynamic limit of organic photovoltaic devices. *Nat. Commun.* **11** (2020), 1–10.

[289] T. Linderl, U. Hörmann, S. Beratz, et al. Temperature dependent competition between different recombination channels in organic heterojunction solar cells. *J. Opt. (United Kingdom)*. **18** (2016), 024007.

[290] A. J. Gillett, A. Privitera, R. Dilmurat, et al. The role of charge recombination to triplet excitons in organic solar cells. *Nature*. **597** (2021), 666–671.

[291] T. Yan, W. Song, J. Huang, R. Peng, L. Huang, Z. Ge. 16.67% Rigid and 14.06% Flexible Organic Solar Cells Enabled by Ternary Heterojunction Strategy. *Adv. Mater.* **31** (2019), 1902210.

[292] N. Gasparini, S. H. K. Paleti, J. Bertrandie, et al. Exploiting Ternary Blends for Improved Photostability in High-Efficiency Organic Solar Cells. *ACS Energy Lett.* **5** (2020), 1371–1379.

[293] Y. Cui, H. Yao, J. Zhang, et al. Single-Junction Organic Photovoltaic Cells with Approaching 18% Efficiency. *Adv. Mater.* **32** (2020), 1908205.

[294] Y. Lin, Y. Firdaus, F. H. Isikgor, et al. Self-assembled monolayer enables hole transport layer-free organic solar cells with 18% efficiency and improved operational stability. *ACS Energy Lett.* **5** (2020), 2935–2944.

[295] F. Liu, L. Zhou, W. Liu, et al. Organic Solar Cells with 18% Efficiency Enabled by an Alloy Acceptor: A Two-in-One Strategy. *Adv. Mater.* **33** (2021), 2100830.

[296] N. Tokmoldin, J. Vollbrecht, S. M. Hosseini, et al. Explaining the Fill-Factor and Photocurrent Losses of Nonfullerene Acceptor-Based Solar Cells by Probing the Long-Range Charge Carrier Diffusion and Drift Lengths. *Adv. Energy Mater.* **11** (2021), 2100804.

[297] A. Hofacker, J. O. Oelerich, A. V. Nenashev, F. Gebhard, S. D. Baranovskii. Theory to carrier recombination in organic disordered semiconductors. *J. Appl. Phys.* **115** (2014), 223713.

[298] V. Coropceanu, J. L. Brédas, S. Mehraeen. Impact of Active Layer Morphology on Bimolecular Recombination Dynamics in Organic Solar Cells. *J. Phys. Chem. C*. **121** (2017), 24954–24961.

[299] D. Credgington, J. R. Durrant. Insights from transient optoelectronic analyses on the open-circuit voltage of organic solar cells. *J. Phys. Chem. Lett.* **3** (2012), 1465–1478.

[300] A. Foertig, A. Baumann, D. Rauh, V. Dyakonov, C. Deibel. Charge carrier concentration and temperature dependent recombination in polymer-fullerene solar cells. *Appl. Phys. Lett.* **95** (2009), 052104.

[301] G. Garcia-Belmonte, J. Bisquert. Open-circuit voltage limit caused by recombination through tail states in bulk heterojunction polymer-fullerene solar cells. *Appl. Phys. Lett.* **96** (2010), 113301.

[302] F. Etzold, I. A. Howard, R. Mauer, et al. Ultrafast exciton dissociation followed by nongeminate charge recombination in PCDTBT:PCBM photovoltaic blends. *J. Am. Chem. Soc.* **133** (2011), 9469–9479.

[303] W. Kaiser, A. Gagliardi. Kinetic Monte Carlo Study of the Role of the Energetic Disorder on the Open-Circuit Voltage in Polymer/Fullerene Solar Cells. *J. Phys. Chem. Lett.* **10** (2019), 6097–6104.

[304] A. Melianas, V. Pranculis, A. Devižis, V. Gulbinas, O. Inganäs, M. Kemerink. Dispersion-Dominated Photocurrent in Polymer:Fullerene Solar Cells. *Adv. Funct. Mater.* **24** (2014), 4507–4514.

[305] A. Melianas, F. Etzold, T. J. Savenije, F. Laquai, O. Inganäs, M. Kemerink. Photo-generated carriers lose energy during extraction from polymer-fullerene solar cells. *Nat. Commun.* **6** (2015), 1–8.

[306] T. Upreti, Y. Wang, H. Zhang, D. Scheunemann, F. Gao, M. Kemerink. Experimentally Validated Hopping-Transport Model for Energetically Disordered Organic Semiconductors. *Phys. Rev. Appl.* **12** (2019), 064039.

[307] N. R. Tummala, S. Mehraeen, Y. T. Fu, C. Risko, J. L. Brédas. Materials-scale implications of solvent and temperature on [6,6]-phenyl-C61-butyric acid methyl ester (PCBM): A theoretical perspective. *Adv. Funct. Mater.* **23** (2013), 5800–5813.

[308] N. R. Tummala, Z. Zheng, S. G. Aziz, V. Coropceanu, J. L. Brédas. Static and Dynamic Energetic Disorders in the C60, PC61BM, C70, and PC71BM Fullerenes. *J. Phys. Chem. Lett.* **6** (2015), 3657–3662.

[309] H. Cha, Y. Zheng, Y. Dong, et al. Exciton and Charge Carrier Dynamics in Highly Crystalline PTQ10:IDIC Organic Solar Cells. *Adv. Energy Mater.* **10** (2020), 2001149.

[310] S. Liu, J. Yuan, W. Deng, et al. High-efficiency organic solar cells with low non-radiative recombination loss and low energetic disorder. *Nat. Photonics*. **14** (2020), 300–305.

[311] J. Yuan, C. Zhang, H. Chen, et al. Understanding energetic disorder in electron-deficient-core-based non-fullerene solar cells. *Sci. China Chem.* **63** (2020), 1159–1168.

[312] S. Xie, Y. Xia, Z. Zheng, et al. Effects of Nonradiative Losses at Charge Transfer States and Energetic Disorder on the Open-Circuit Voltage in Nonfullerene Organic Solar Cells. *Adv. Funct. Mater.* **28** (2018), 1705659.

[313] V. V. Brus, N. Schopp, S. Ko, et al. Temperature and Light Modulated Open-Circuit Voltage in Nonfullerene Organic Solar Cells with Different Effective Bandgaps. *Adv. Energy Mater.* **11** (2021), 2003091.

[314] C. He, Y. Li, Y. Liu, et al. Near infrared electron acceptors with a photoresponse beyond 1000 nm for highly efficient organic solar cells. *J. Mater. Chem. A*. **8** (2020), 18154–18161.

[315] C. Zhang, J. Yuan, K. L. Chiu, et al. A disorder-free conformation boosts phonon and charge transfer in an electron-deficient-core-based non-fullerene acceptor. *J. Mater. Chem. A*. **8** (2020), 8566–8574.

[316] C. Kaiser, O. J. Sandberg, N. Zarrabi, W. Li, P. Meredith, A. Armin. A universal Urbach rule for disordered organic semiconductors. *Nat. Commun.* **12** (2021), 1–9.

[317] A. Karki, J. Vollbrecht, A. J. Gillett, et al. The role of bulk and interfacial morphology in charge generation, recombination, and extraction in non-fullerene acceptor organic solar cells. *Energy Environ. Sci.* **13** (2020), 3679–3692.

[318] P. Wan, X. Chen, Q. Liu, et al. Direct Observation of the Charge Transfer States from a Non-Fullerene Organic Solar Cell with a Small Driving Force. *J. Phys. Chem. Lett.* **12** (2021), 10595–10602.

[319] S. Li, C.-Z. Li, M. Shi, H. Chen. New Phase for Organic Solar Cell Research: Emergence of Y-Series Electron Acceptors and Their Perspectives. *ACS Energy Lett.* (2020), 1554–1567.

[320] J. Kniepert, A. Paulke, L. Perdigón-Toro, et al. Reliability of charge carrier recombination data determined with charge extraction methods. *J. Appl. Phys.* **126** (2019), 205501.

[321] S. Dong, T. Jia, K. Zhang, J. Jing, F. Huang. Single-Component Non-halogen Solvent-Processed High-Performance Organic Solar Cell Module with Efficiency over 14%. *Joule*. **4** (2020), 2004–2016.

[322] L. Hong, H. Yao, Z. Wu, et al. Eco-Compatible Solvent-Processed Organic Photovoltaic Cells with Over 16% Efficiency. *Adv. Mater.* **31** (2019), 1903441.

[323] T. J. Prosa, J. Moulton, A. J. Heeger, M. J. Winokur. Diffraction line-shape analysis of poly(3-dodecylthiophene): a study of layer disorder through the liquid crystalline polymer transition. *Macromolecules*. **32** (1999), 4000–4009.

[324] J. Rivnay, R. Noriega, R. J. Kline, A. Salleo, M. F. Toney. Quantitative analysis of lattice disorder and crystallite size in organic semiconductor thin films. *Phys. Rev. B - Condens. Matter Mater. Phys.* **84** (2011), 045203.

[325] A. Dieckmann, H. Bässler, P. M. Borsenberger. An assessment of the role of dipoles on the density-of-states function of disordered molecular solids. *J. Chem. Phys.* **99** (1993), 8136–8141.

[326] M. Silver, L. Pautmeier, H. Bässler. On the origin of exponential band tails in amorphous semiconductors. *Solid State Commun.* **72** (1989), 177–180.

[327] K. Vandewal, J. Widmer, T. Heumueller, et al. Increased open-circuit voltage of organic solar cells by reduced donor-acceptor interface area. *Adv. Mater.* **26** (2014), 3839–3843.

[328] A. Zusan, K. Vandewal, B. Allendorf, et al. The Crucial Influence of Fullerene Phases on Photogeneration in Organic Bulk Heterojunction Solar Cells. *Adv. Energy Mater.* **4** (2014), 1400922.

[329] P. N. Murgatroyd. Theory of space-charge-limited current enhanced by Frenkel effect. *J. Phys. D. Appl. Phys.* **3** (1970), 151–156.

[330] N. I. Craciun, J. J. Brondijk, P. W. M. Blom. Diffusion-enhanced hole transport in thin polymer light-emitting diodes. *Phys. Rev. B - Condens. Matter Mater. Phys.* **77** (2008), 035206.

[331] G. Zuo, Z. Li, O. Andersson, H. Abdalla, E. Wang, M. Kemerink. Molecular Doping and Trap Filling in Organic Semiconductor Host–Guest Systems. *J. Phys. Chem. C*. **121** (2017), 7767–7775.

[332] G. Zuo, M. Linares, T. Upreti, M. Kemerink. General rule for the energy of water-induced traps in organic semiconductors. *Nat. Mater.* **18** (2019), 588–593.

[333] P. W. M. Blom, M. J. M. de Jong, J. J. M. Vleggaar. Electron and hole transport in PPV devices. *Appl. Phys. Lett.* **63** (1996), 3308–3310.

[334] R. Steyrleuthner, S. Bange, D. Neher. Reliable electron-only devices and electron transport in n -type polymers. *J. Appl. Phys.* **105** (2009), 064509.

[335] G. A. H. Wetzelaer, M. Kuik, H. T. Nicolai, P. W. M. Blom. Trap-assisted and Langevin-type recombination in organic light-emitting diodes. *Phys. Rev. B - Condens. Matter Mater. Phys.* **83** (2011), 165204.

[336] T. Ripolles-Sanchis, S. R. Raga, A. Guerrero, et al. Molecular electronic coupling controls charge recombination kinetics in organic solar cells of low bandgap diketopyrrolopyrrole, carbazole, and thiophene polymers. *J. Phys. Chem. C*. **117** (2013), 8719–8726.

[337] N. Zarrabi, O. J. Sandberg, S. Zeiske, et al. Charge-generating mid-gap trap states define the thermodynamic limit of organic photovoltaic devices. *Nat. Commun.* **11** (2020), 5567.

[338] Y. Tang, J. M. Bjuggren, Z. Fei, M. R. Andersson, M. Heeney, C. R. McNeill. Origin of Open-Circuit Voltage Turnover in Organic Solar Cells at Low Temperature. *Sol. RRL*. **4** (2020), 2000375.

[339] J. Yan, E. Rezasoltani, M. Azzouzi, F. Eisner, J. Nelson. Influence of static disorder of charge transfer state on voltage loss in organic photovoltaics. *Nat. Commun.* **12** (2021), 1–12.

[340] T. Upreti, S. Wilken, H. Zhang, M. Kemerink. Slow Relaxation of Photogenerated Charge Carriers Boosts Open-Circuit Voltage of Organic Solar Cells. *J. Phys. Chem. Lett.* **12** (2021), 9874–9881.

[341] P. Pingel, D. Neher. Comprehensive picture of p-type doping of P3HT with the molecular acceptor F4TCNQ. *Phys. Rev. B - Condens. Matter Mater. Phys.* **87** (2013), 1–9.

[342] Z. Zheng, N. R. Tummala, T. Wang, V. Coropceanu, J. Brédas. Charge-Transfer States at Organic–Organic Interfaces: Impact of Static and Dynamic Disorders. *Adv. Energy Mater.* **9** (2019), 1803926.

[343] C. C. S. Chan, C. Ma, X. Zou, et al. Quantification of Temperature-Dependent Charge Separation and Recombination Dynamics in Non-Fullerene Organic Photovoltaics. *Adv. Funct. Mater.* **31** (2021), 2107157.

[344] S. Athanasopoulos, H. Bässler, A. Köhler. Disorder vs Delocalization: Which Is More Advantageous for High-Efficiency Organic Solar Cells? *J. Phys. Chem. Lett.* **10** (2019), 7107–7112.

[345] Q. Liu, Y. Wang, J. Fang, et al. Synergistically minimized nonradiative energy loss and optimized morphology achieved via the incorporation of small molecule donor in 17.7% efficiency ternary polymer solar cells. *Nano Energy*. **85** (2021), 105963.

[346] M. Zhang, L. Zhu, T. Hao, et al. High-Efficiency Organic Photovoltaics using Eutectic Acceptor Fibrils to Achieve Current Amplification. *Adv. Mater.* **33** (2021), 2007177.

[347] Y. Zeng, D. Li, Z. Xiao, et al. Exploring the Charge Dynamics and Energy Loss in Ternary Organic Solar Cells with a Fill Factor Exceeding 80%. *Adv. Energy Mater.* **11** (2021), 2101338.

[348] K. Jiang, J. Zhang, Z. Peng, et al. Pseudo-bilayer architecture enables high-performance organic solar cells with enhanced exciton diffusion length. *Nat. Commun.* **12** (2021), 1–9.

[349] R. Sun, Q. Wu, J. Guo, et al. A Layer-by-Layer Architecture for Printable Organic Solar Cells Overcoming the Scaling Lag of Module Efficiency. *Joule*. **4** (2020), 407–419.

[350] Y. Zheng, R. Sun, M. Zhang, et al. Baseplate Temperature-Dependent Vertical Composition Gradient in Pseudo-Bilayer Films for Printing Non-Fullerene Organic Solar Cells. *Adv. Energy Mater.* **11** (2021), 2102135.

Appendix

A1. Supporting Material to Chapter 4

Note A1.1: Supplementary methods

Device preparation

The devices were fabricated with a structure ITO/ZnO/PM6:Y6/MoOx/Ag. Patterned ITO (Lumtec) substrates were cleaned in an ultrasonic bath with acetone, Hellmanex, deionized water and isopropanol for 10 min, followed by microwave plasma treatment (4 min at 200 W). Subsequently, ZnO nanoparticles (Avantama N-10) dissolved on isopropanol were filtered through a 0.45 µm PTFE filter and spin coated onto ITO at 4000 rpm under ambient conditions. The ZnO substrates were thermally annealed at 120°C for 30 min, followed by exposition to UV light inside a nitrogen-filled glovebox for 10 min. PM6 and Y6 were dissolved in chloroform ($CHCl_3$) to a total concentration of 16 $mgmL^{-1}$ with a 1 to 1.2 weight ratio and 0.5% chloronaphthalene (v/v, CN/$CHCl_3$) as additive. The $CHCl_3$ and the additive CN were purchased from Carl Roth and Alfa Aesar, respectively. The solution was stirred for 3 hours inside the glovebox. Then, the blend was spin coated (2500-3000 rpm) onto the ZnO layer to obtain a photoactive layer of thickness ~100 nm. To complete the devices, 10 nm of MoO_3 as the anode interlayer and 100 nm of Ag as the top electrode were evaporated under a 10^{-6}-10^{-7} mbar vacuum. The resulting active area was 0.55 or 1.1 mm^2 for TDCF and BACE experiments and 6 mm^2 for EQE, RPV and *J-V* measurements.

Resistance Dependent Photovoltage (RPV)

The laser pulse to generate charges comes from a diode pumped, Q-switched Nd:YAG laser (NT242, EKSPLA) with 5 ns pulse duration at a repetition rate of 50 Hz. Photovoltage transients were recorded with an oscilloscope (Agilent DSO9104H) with a load resistance of 1MOhm. External voltages were applied to the sample when needed with a pulse generator (Agilent 81150A). Low laser pulse fluences were used to prevent screening of the internal field and a built-up of charges inside the device.

Temperature-dependent measurements

For TDCF measurements at different temperatures, the device was placed on the cooling finger of a closed cycle helium cryostat (ARS-CS202-X1.AL). The cryostat was heated and evacuated to ~$1x10^{-4}$ mbar (Pfeiffer TCP121 Turbo pump and Edwards XDS-10 scroll pump). Electrical connection was done through a home-built amplifier which was directly attached as close as possible to the sample outside the cryostat.

For the *J-V* and EQE measurements as function of temperature at Linköping University, the sample was placed in a closed cycle helium cryostat (bought from ASR together with the compressor).

Table A1.1: Average photovoltaic parameters and standard deviations for control batches of PM6:Y6 (1:1.2 w/w CF, additive CN 0.5% v/v, as cast) devices with structure ITO/ZnO/PM6:Y6/MoO_x/Ag and A=6 mm^2.

V_{OC} [V]	J_{SC} [mA cm^{-2}]	FF [%]	PCE [%]
0.856 ±0.005	22.4 ±0.2	71.3 ±0.1	13.7 ±0.001

Seite 3/9
Page

Fraunhofer ISE

1002092UPO0519

CalLab PV Cells

Die Rückführung der Spektralmessung auf SI-Einheiten erfolgte über den Vergleich mit einer Standardlampe.
The traceability of the measurement of the spectral distribution to SI-Units is achieved using a standard lamp for the calibration of the spectroradiometer.

Identitäts-Nr. / *Identity-Nr.* :	Kalibrierschein-Nr./ *Certificate-Nr.* :	Rückführung/ *Traceability* :
BN-9101-451	40002-14-PTB	PTB

3. Messbedingungen
Measurement conditions

Standardtestbedingungen (STC) / *Standard Testing Conditions (STC)* :

Absolute Bestrahlungsstärke / *Total irradiance* :	1000	W/m²
Temperatur des Messobjektes / *Temperature of the DUT* :	25	°C
Spektrale Bestrahlungsstärke / *Spectral irradiance distribution* :	AM1.5G Ed.4 (2019)	

Die Messung der IV-Kennlinie (Strom-Spannungs-Kennlinie) des Messobjektes erfolgt mit Hilfe eines Vierquadranten-Netzteiles und eines Kalibrierwiderstandes.
The measurement of the IV-curve is performed with a 4-quadrant power amplifier and a calibration resistor.

4. Messergebnis
Measurement results

Mismatch-Faktor / *Mismatch factor* : = 1.0098

(Spektral-Korrektur / *spectral correction*)

Fläche / Area (da)[1]: = (1.0229 ± 0.0063) cm²

[1] : *(t) = total area, (ap) = aperture area, (da) = designated illumination area /7/*

Kennlinienparameter des Messobjektes unter Standardtestbedingungen (STC) / *IV-curve parameter under Standard Testing Conditions (STC)* :

V_{OC}	=	(842.2	±	3.4	) mV
I_{SC} (Ed.4 - 2019)/3/	=	(23.81	±	0.33	) mA
J_{SC}	=	(23.28	±	0.32	) mA/cm²
I_{MPP}	=	20.06			mA
V_{MPP}	=	685.9			mV
P_{MPP}	=	(13.76	±	0.20	) mW
FF	=	(68.62	±	0.32	) %
η	=	(13.45	±	0.21	) %

Figure A1.1: Fraunhofer certificate for a 1 cm2 device prepared in this work. The corresponding current-voltage characteristics are shown in Figure A1.2.

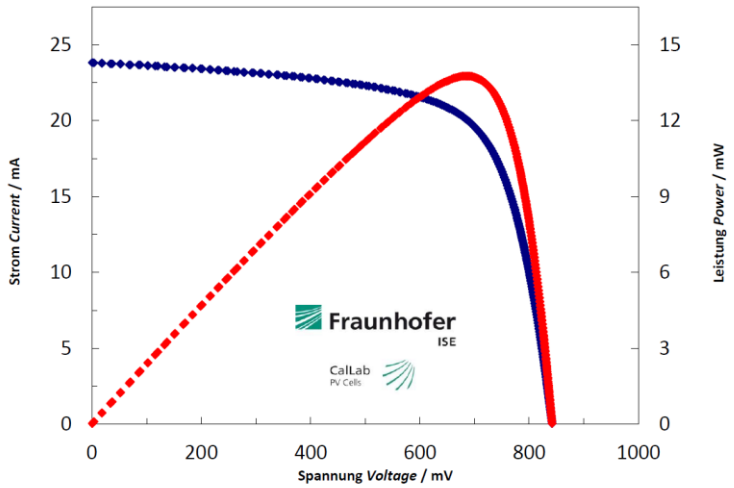

Figure A1.2: Certified current-voltage characteristics for a 1 cm^2 device prepared in this work. A power conversion efficiency of 13.45% was achieved for an aperture area of 1.0229 cm^2 as stated in the certificate in Figure A1.1.

Note A1.2: Energy levels of PM6:Y6

We note that the energy levels used to select each excitation are based on cyclic voltammetry (CV) results take from Ref.[29] In this work, the measurements were performed after spin coating the polymer donor or the NFA on Pt to form thin films as the electrode, and then put in acetonitrile solution. Acetonitrile is a poor solvent for both the polymer and the small molecule and therefore the measured energy levels closely reflect those in solid-state.

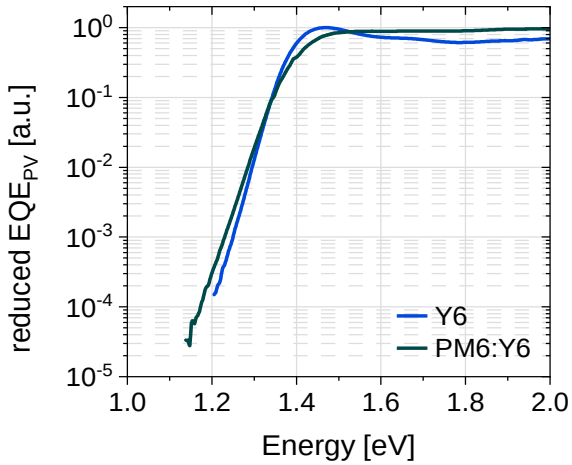

Figure A1.3: Fourier-transform photocurrent spectroscopy spectra of the PM6:Y6 blend and the pristine Y6. There is very little difference between the normalized $\mathbf{EQE_{PV}}$ spectra of the neat NFA and the blend. This is in strong favor of a small HOMO energy offset at the D/A interface, meaning that the energy of the NFA singlet exciton and of the interfacial CT state are nearly indistinguishable.

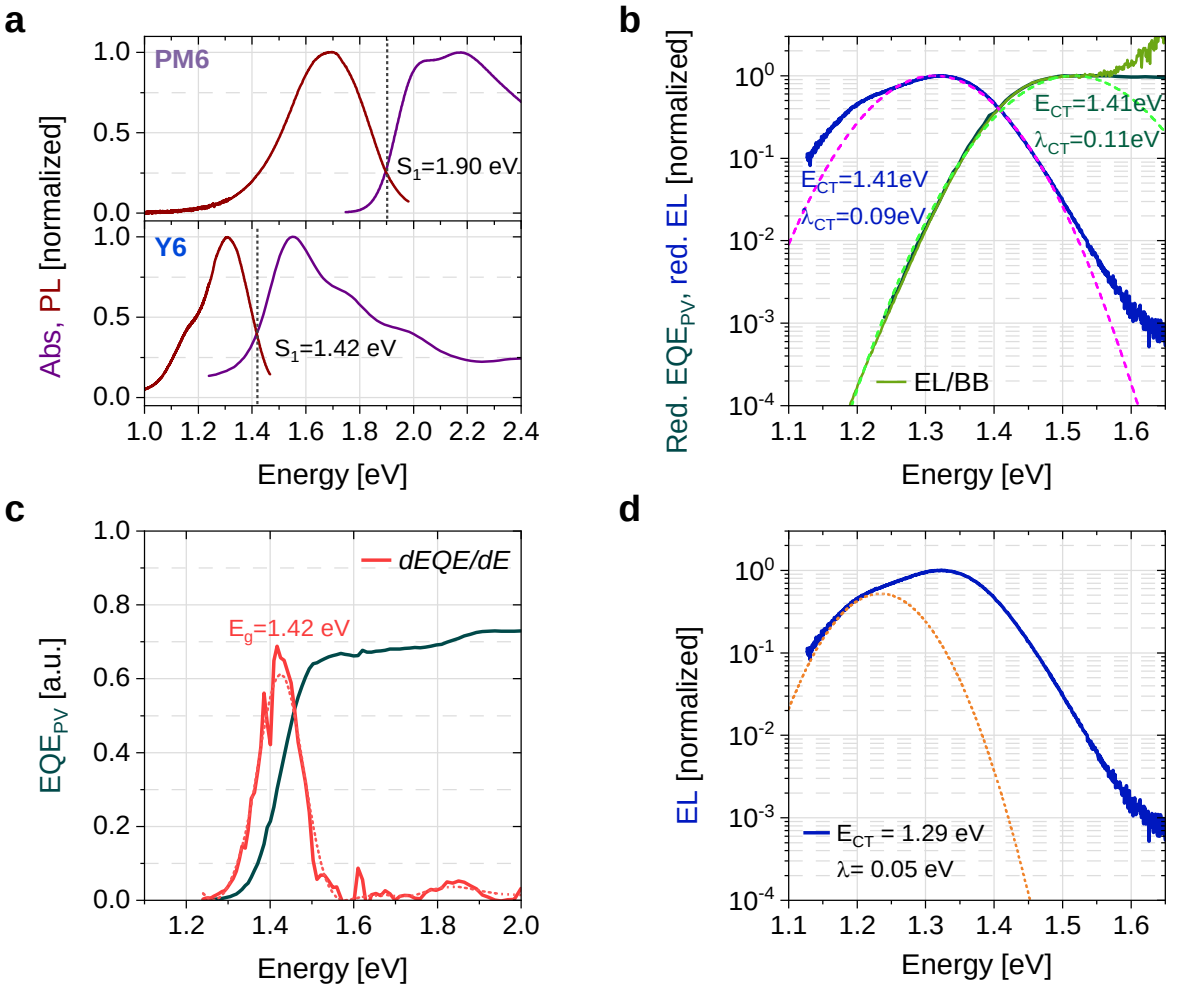

Figure A1.4: a Absorption and photoluminescence (PL) spectra of PM6 and Y6 pristine films. The crossing point of both spectra gives the singlet exciton energy S_1. **b** Normalized reduced $\mathrm{EQE_{PV}}$ and reduced emission (EL) of the PM6:Y6 blend device. The dashed lines correspond to fits to equations $\mathrm{EQE_{PV}}(E) = E\ \exp\left(-\frac{(E_{\mathrm{CT}}+\lambda-E)^2}{4\lambda k_{\mathrm{B}}T}\right)$ and $EL(E) = E^3 \exp\left(-\frac{(E_{\mathrm{CT}}-\lambda-E)^2}{4\lambda k_{\mathrm{B}}T}\right)$, according to Ref.[188] The fitting parameters are given in the inset. **c** $\mathrm{EQE_{PV}}$ and its derivative $\mathrm{dEQE}/\mathrm{d}E$ for the PM6:Y6 blend. E_{g} is determined from the maximum of the derivative, as in Ref.[147] **d** Normalized EL spectra of the PM6:Y6 blend. As an attempt to differentiate the singlet and CT contributions on the emission, the dashed line corresponds to a fit to the low-energy peak of the EL using the equation $EL(E) = \frac{Ef}{\sqrt{4\pi\lambda k_{\mathrm{B}}T}} \exp\left(-\frac{(E_{\mathrm{CT}}-\lambda-E)^2}{4\lambda k_B T}\right)$, as done previously in Ref.[79] We observe that the methods employed in b and c give similar results for the CT energy and we obtain a nearly negligible driving force $\Delta E_{S_1(\mathrm{A})-\mathrm{CT}}$, given that S_1(A) and E_{CT} are very similar in energy. If we consider the result in d and the low energy peak as CT emission contribution, $\Delta E_{S_1(\mathrm{A})-\mathrm{CT}}$ is 0.13 eV, which is still a very small driving force.

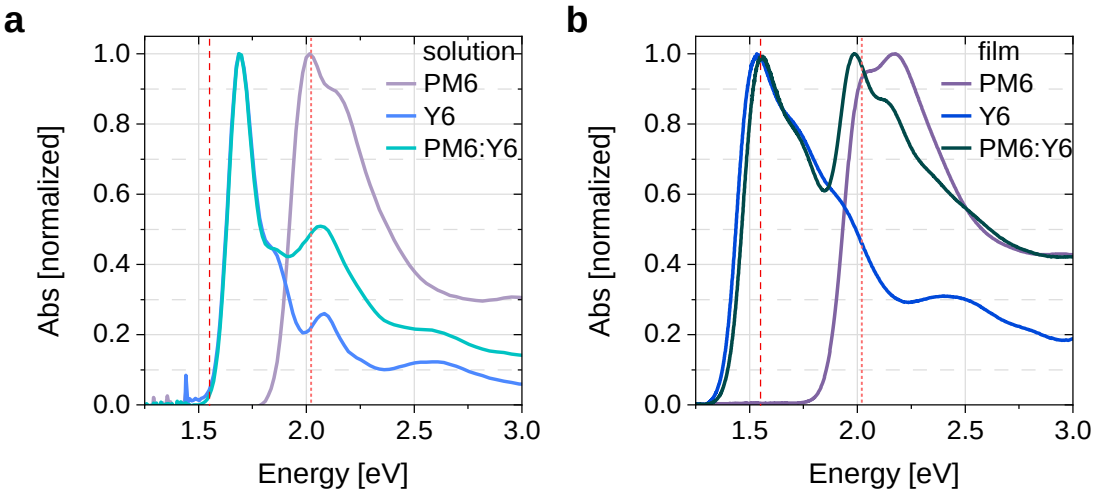

Figure A1.5: Absorption spectra of PM6, Y6 and PM6:Y6 (1:1.2 w/w, CN 0.5% v/v) in a solution and b solid-state (thin films as cast). The dotted lines represent the low energy absorption peaks of films of neat PM6 and Y6 for reference when comparing to the solution and the blend. Clearly, the absorption of Y6 is strongly red-shifted when going from solution to solid-state. Also, in thin films, the absorption of the blend resembles very accurately the superposition of PM6 and Y6 solid-state absorption.

Note A1.3: Internal quantum efficiency and internal generation efficiency

To calculate the internal photovoltaic quantum efficiency (IQE) and the internal generation efficiency (IGE), the fraction of absorption in the active layer was simulated using the transfer matrix method, which takes into account the multiple reflections and interference of all layers in the solar cell stack. To apply the transfer matrix method, the optical constants n and k were modelled for the PM6:Y6 (1:1.2, 0.5% CN) blend as cast, from reflection and transmission measurements performed in the layer using an integrating sphere (see Figure A1.6a). Subsequently, in Figure A1.6c, the losses due to reflection R (dashed line) and parasitic absorption PA (dotted line) were calculated by considering the thickness of each layer in the stack. The IQE was determined by dividing the experimental EQE (open dots) by the fraction of absorption in the active layer, i.e. $IQE = EQE/1 - R - PA$.[64] The simulation rendered a generation current $J_{\mathrm{sim}} =$ 21.2 mAcm^{-2}, very close to the integrated value from EQE of J_{sim} =20.9 mAcm^{-2} in the range from 1.25 eV to 3.1 eV. The IGE is calculated similarly by defining EGE as the ratio of the charges extracted by TDCF to the photons incident on the device at each used excitation energy.[184] Therefore, the IGE corresponds to the scenario without transport or nongeminate recombination losses.

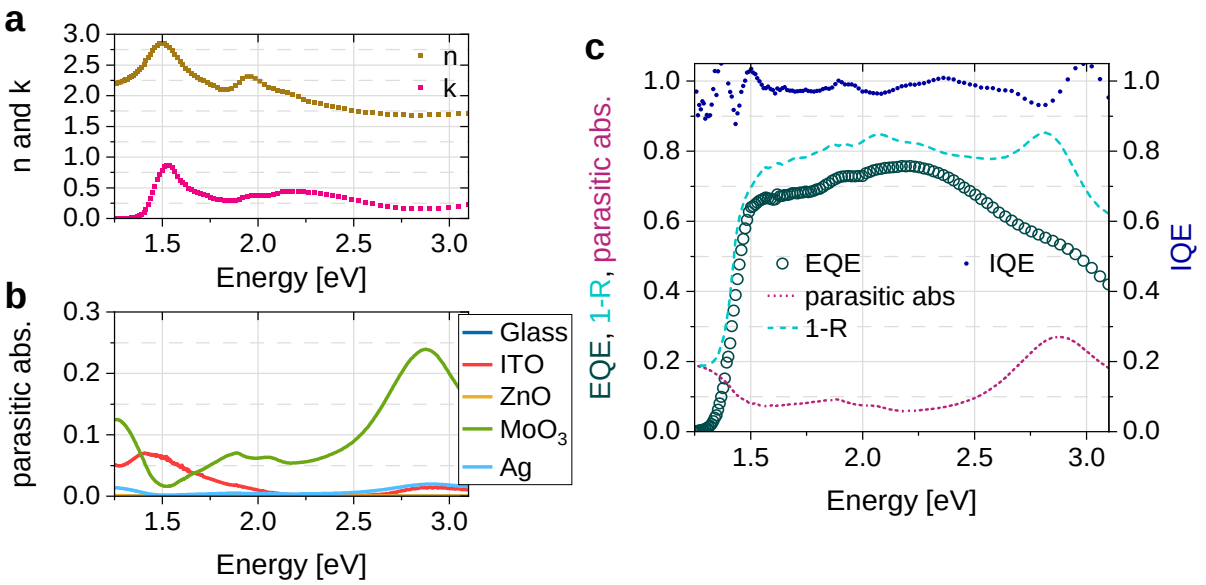

Figure A1.6: a Extinction coefficient k and refractive index n for the PM6:Y6 (1:1.2 w/w, CN 0.5% v/v) blend as cast. These optical constants are needed to model the optical field inside the stack of layers of a full device with PM6:Y6 as the active layer, which was done using the transfer matrix method. **b** Contribution of the different layers in the stack device to the parasitic absorption. c Reflection and parasitic absorption losses are added to the EQE in order to obtain IQE.

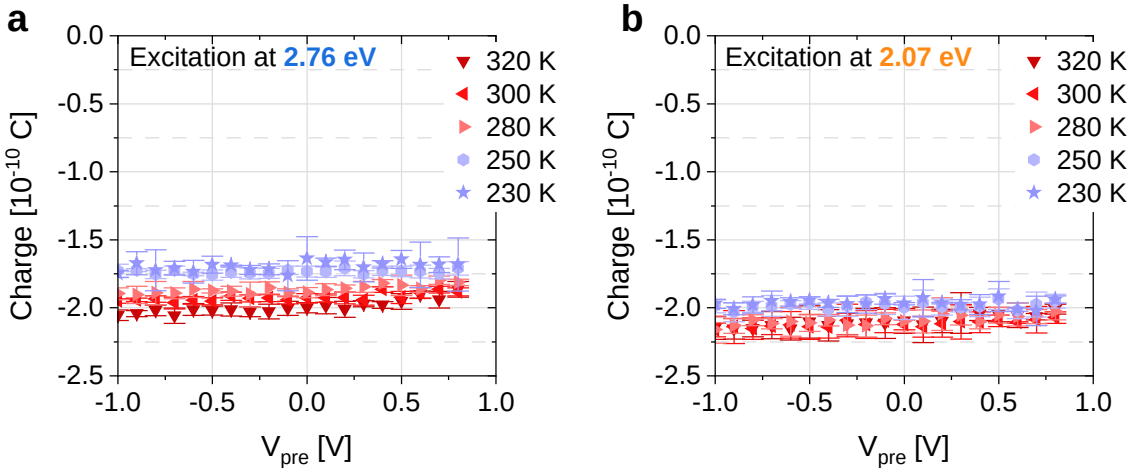

Figure A1.7: Bias-dependent charge generation for a PM6:Y6 device measured at different temperatures by TDCF for **a** excitation energy of 2.76 eV with a fluence of 0.13 μJcm^{-2} and **b** excitation energy of 2.07 eV with a fluence of 0.09 μJcm^{-2}. For all measurements, V_{coll} = -2.5 V. Charge generation remains field-independent for all proved temperatures and the total charge Q does not drop substantially at lower temperature.

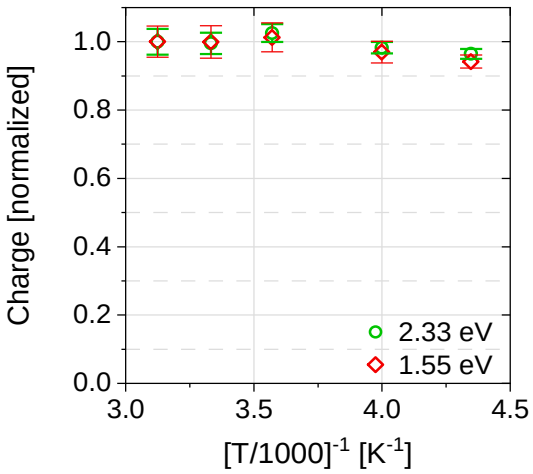

Figure A1.8: Total extracted charge Q_{tot} as function of temperature from the bias- and temperature-dependent TDCF data in Figure 4.2a, normalized to the value at 320 K. To reduce noise, we averaged the TDCF data over the entire bias range for each temperature. Error bars indicate the standard deviation. The extracted charge is virtually temperature independent, down to temperatures of 230 K, pointing to a very small activation energy for CT dissociation.

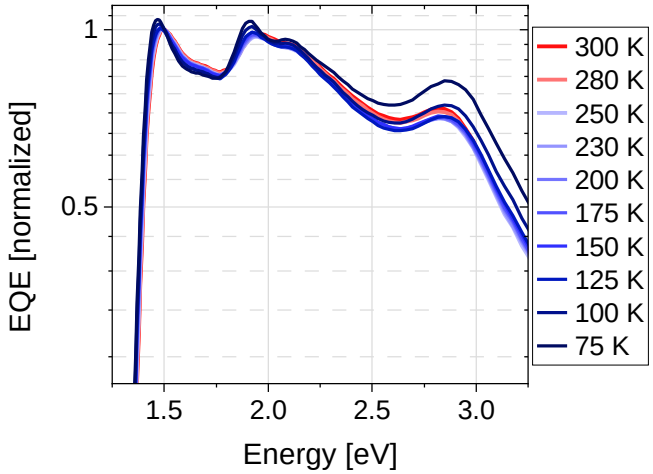

Figure A1.9: Normalized EQE spectra to the Y6 absorption peak at 1.5 eV. Considerable changes in the shape of the spectrum start to appear below 125 K.

Note A1.4: Temperature dependence of open-circuit voltage

Analytically, the open-circuit voltage V_{OC} can be described and related to free charge carrier density in OSCs by Equation 2.23 (section 2.5. in fundamentals). This equation therefore defines a linear increase of V_{OC} with decreasing T, provided the free charge carrier density in the device is constant, and the extrapolation to $T = 0$ K gives the value of E_g.[289] Figure 4.2d in the main text shows the temperature dependence of V_{OC} for a PM6:Y6 device and the fit to Equation 2.23 is indicated by dashed line (without considering disorder and taking a constant free carrier density), corresponding to E_g =1.12 eV. The plot shows a deviation from linearity starting at ~100 K for all light intensities. Gao et al.[180] simulated in their work that the saturation of V_{OC} at low temperatures can be attributed to disorder. We note that the reduction by disorder at a given temperature can be overestimated when we extrapolate the linear points of the high temperature regime, and highly depend on the actual temperature range measured and delimited as linear thereafter. We believe that this, together with the fact that the CT energy can vary with

temperature, lead to underestimate E_g in the V_{OC} *vs.* T plot. However, this does not change our conclusions on charge generation, since they are based exclusively on increasing V_{OC} with decreasing temperature as predicted by Equation 2.23 for a constant charge generation np. Furthermore, Gao et al.[180] showed that non-selective contacts result in a detrimental built-in potential which limits the maximum achievable V_{OC} and can lead to saturation at low temperatures as well. They observed a decrease of V_{OC} for some blends with decreasing temperature and concluded that this came in fact from decreased charge carrier densities in the device, that is, geminate losses. In our case, we do not observe a decrease in V_{OC} even down to 75 K.

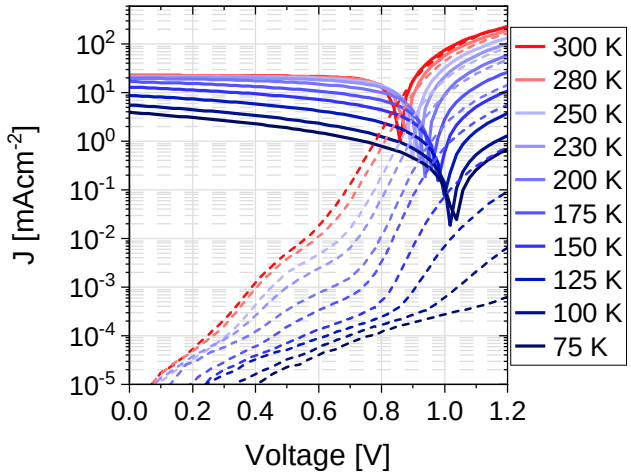

Figure A1.10: Light (solid lines) current density-voltage characteristics of PM6:Y6 cells illuminated to a 1 sun equivalent with a LED (470 nm). The dark current (dashed lines) is much lower than the photocurrent at low temperatures, which indicates that the V_{OC} is not limited by leakage current in this regime.

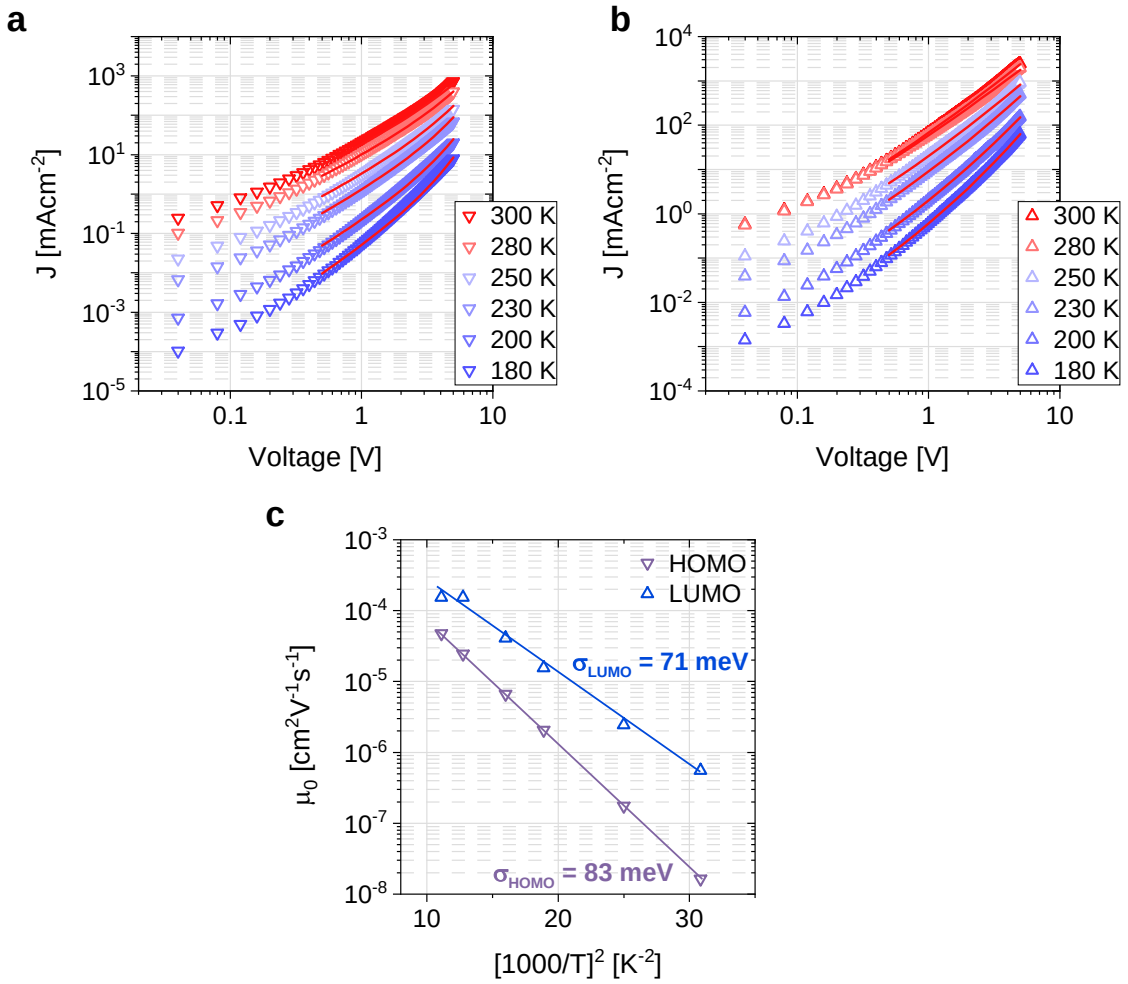

Figure A1.11: **a** Space-charge limited currents (SCLC) for a hole-only device (ITO/PEDOT:PSS/PM6:Y6/MoO_3/Al) and **b** electron-only device (ITO/ZnO/PM6:Y6/LiF/Al). **c** Zero-field charge carrier mobility μ_0 of holes (HOMO) and electrons (LUMO). The energetic disorder σ can be from $\mu_0(T) = \mu_\infty \exp\left[-\left(\frac{2\sigma}{3k_BT}\right)^2\right]$.[203]

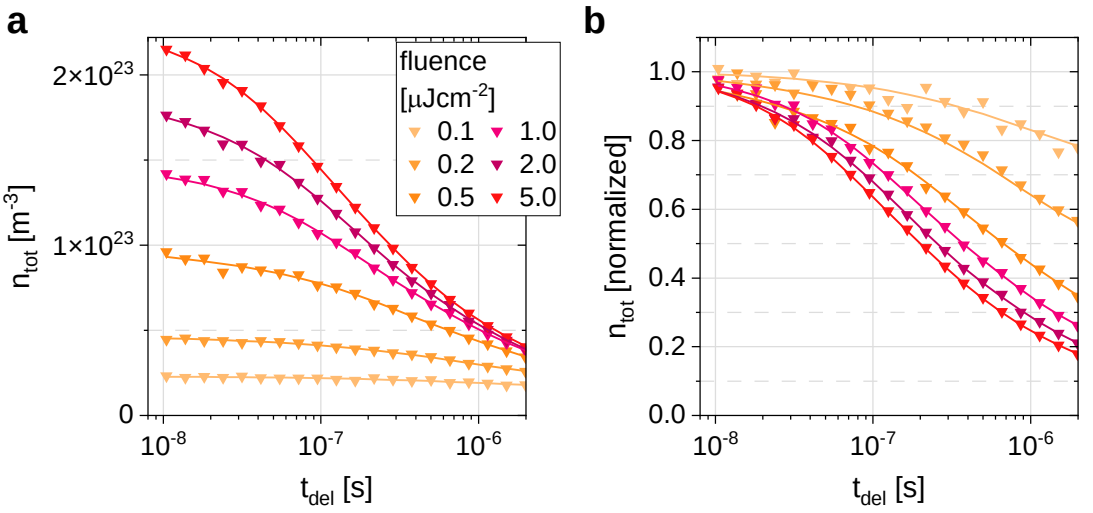

Figure A1.12: a Total charge carrier density (n_{tot}) and **b** normalized data plotted as a function of the delay time (t_{del}) for a PM6:Y6 (1:1.2 w/w, CN 0.5% v/v) device, measured by TDCF for an excitation of 2.07 eV. Results correspond to six different fluences, with V_{pre} =0.6 V and V_{coll} =-2.5 V. At the given pre-bias, the background charge is n_{BG} =1.8x10^{21} m^{-3}. At early times, the total charge is constant for lower fluences, which reassures that there is no significant geminate recombination of long lived CT states or first order losses due to recombination of dark charge with photogenerated charge. After that time, charges decay via a bimolecular recombination process (solid line fits). The recombination rate is calculated from this plot following Equation 2.12 (section 2.4.2), which results in Figure 4.3a.

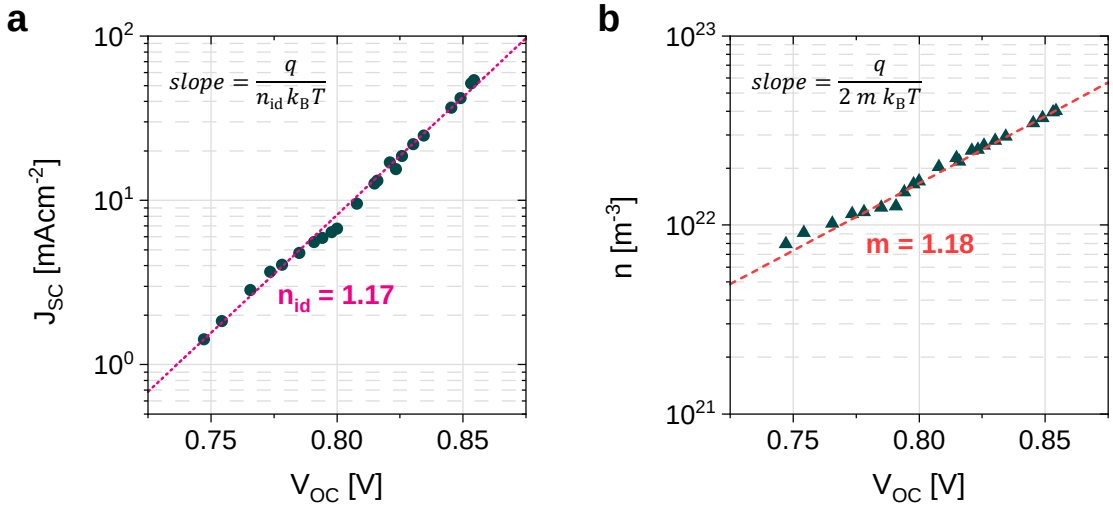

Figure A1.13: a Short-circuit current density (J_{SC}) as a function of open-circuit voltage (V_{OC}) to determine the ideality factor n_{id} from the slope (see equation in the graph). **b** Charge carrier density n as a function of V_{OC} to determine the m-factor from the slope (see equation in the graph). n_{id} and m close to 1 support that nongeminate losses originate from recombination of carriers in a Gaussian density of states (DOS).[112]

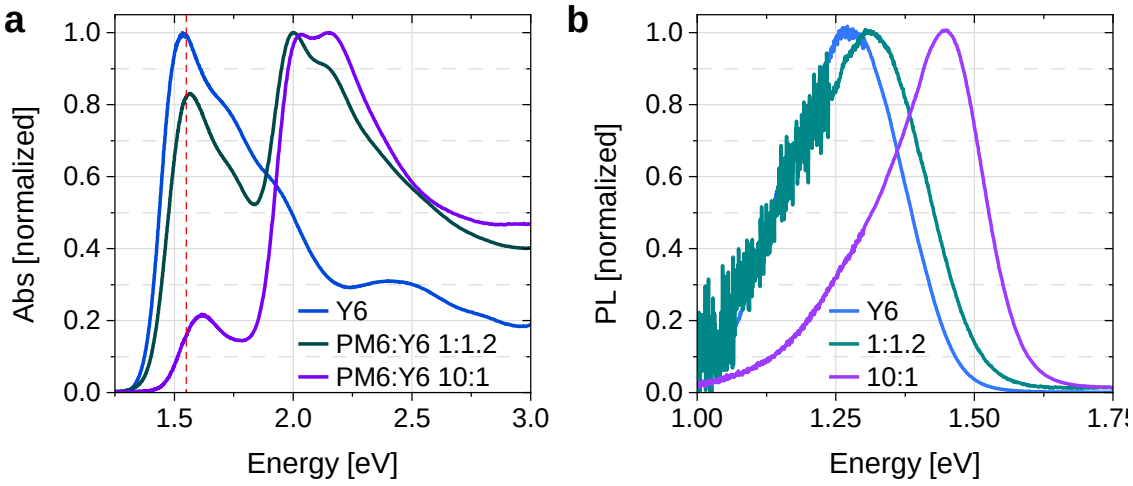

Figure A1.14: a Absorption spectra of Y6 compared to PM6:Y6 at different weight ratios of donor:acceptor (1:1.2 and 10:1 w/w, without additives) in solid-state (thin films). The main absorption peak of the NFA is shifted to a higher energy for the 10:1 ratio, which is closer to the Y6 absorption in solution (Figure A1.5). **b** Photoluminescence spectra of Y6 compared to PM6:Y6 at different weight ratios of donor:acceptor (1:1.2 and 10:1 w/w, without additives) in solid-state (thin films). The emission is blue-shifted for the 10:1 ratio in accordance to the absorption spectra. These measurements suggest that Y6 is de-aggregated in this "diluted" blend.

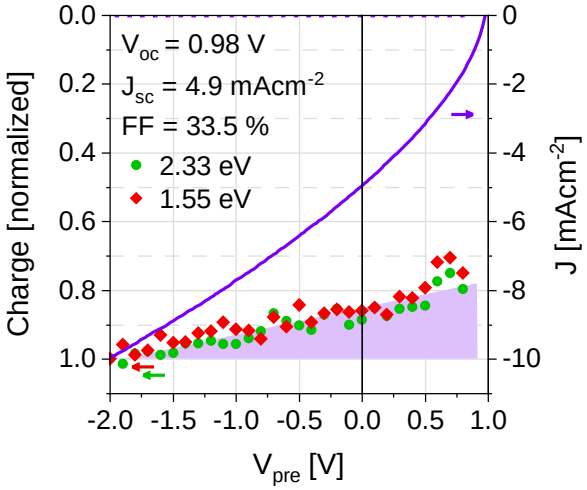

Figure A1.15: Bias-dependent normalized charge generation (symbols, left axis) for a "diluted" PM6:Y6 (10:1, w/w) device measured by TDCF for an excitation of 2.33 eV and 1.55 eV with a low fluence of 0.05 μJcm^{-2} and V_{coll}=-2.5 V. For both excitation energies, the field-dependence of charge generation is 20% (shaded area), as defined by the ratio of Q at V_{OC} and high reverse bias. Larger geminate losses seem to appear at lower fields. For comparison, the current density-voltage characteristics of the device under simulated AM1.5G light are also shown (solid lines, right axis) and the photovoltaic parameters are given in the inset. The low FF can be explained by a combination of the above-mentioned geminate losses, large bimolecular losses (see next Figure A1.16) and possibly imbalanced mobilities due to the low content of NFA.

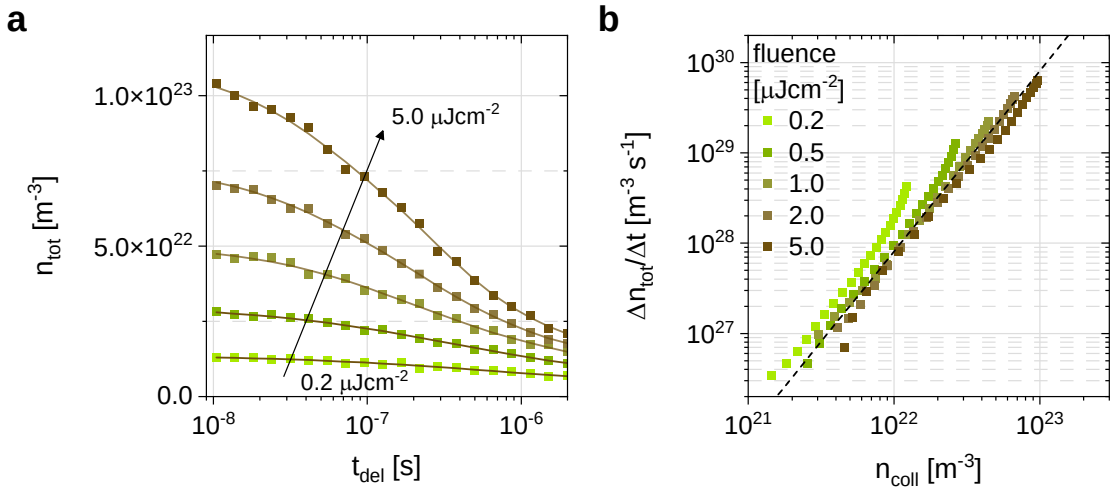

Figure A1.16: a Total charge carrier density (n_{tot}) plotted as a function of the delay time (t_{del}) for a "diluted" PM6:Y6 (10:1, w/w) device measured by TDCF for an excitation of 2.33 eV. Results correspond to five different fluences, with V_{pre} =0.6 V and V_{coll} =-2.5 V (see the main text for more details on the measurement of recombination dynamics with TDCF). At early times, the total charge is constant for lower fluences, which reassures that there is no significant geminate recombination of long lived CT states or first order losses due to recombination of dark charge with photogenerated charge. After that time, charges decay via a bimolecular recombination process (solid line fits). **b** Recombination rate versus photogenerated charge carrier density (squared symbols). The dashed line is calculated from $R = k_2 n_{coll}^2$, with k_2=8.0x10^{-17} $m^3 s^{-1}$, that is a ~5 times larger recombination coefficient compared to the 1:1.2 blend (see Figure 4.3). A slope of 2 indicates that free charge bimolecular recombination is predominant and is higher than in the 1:1.2 blend given that free holes are most likely to find a free electron at a dispersed NFA domain, which cannot be extracted.

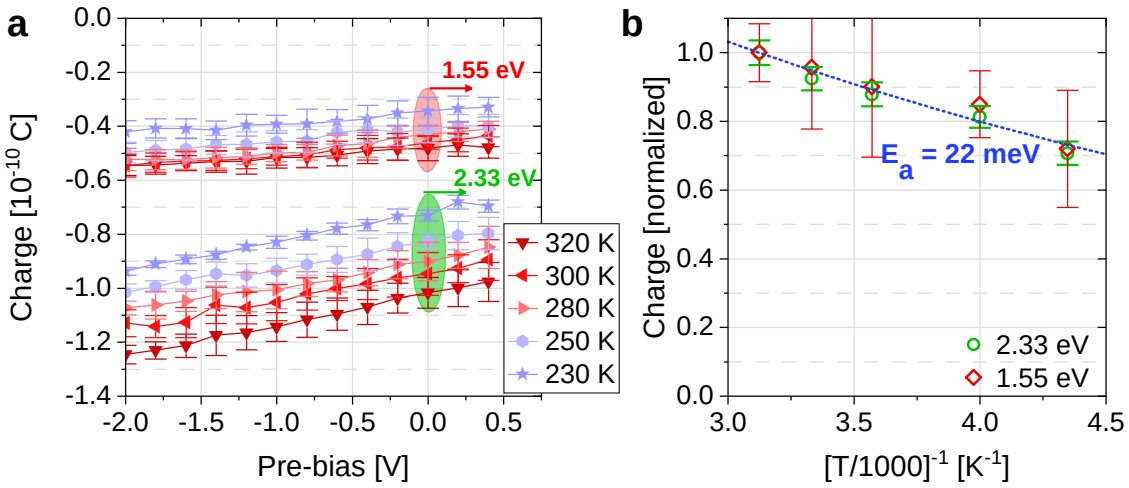

Figure A1.17: a Bias-dependent charge generation for a "diluted" PM6:Y6 (10:1, w/w) measured at different temperatures by TDCF. The data includes excitation of primarily PM6 at 2.33 eV and of Y6 at 1.55 eV with a fluence of 0.1 µJcm^{-2} and V_{coll} =-2.5 V. **b** Extracted Q_{tot} as function of temperature, normalized to the value at 320 K for two different excitation energies. To reduce noise, we averaged the experimental data in Figure A1.17a between V_{pre} = -0.4 V and V_{pre} = 0.4 V for each temperature. Error bars indicate the standard deviation. The dashed line is a fit for Arrhenius-type temperature dependence, which yields an activation energy (E_a) for free charge generation of 22 meV. Clearly, the devices containing a low content of the acceptor Y6 show temperature- and bias-dependent generation.

Note A1.5: Computer simulations on Y6

The simulation approach consists of the following steps: (i) quantum chemical calculations of Y6 in a gas phase, (ii) force-field parameterization and molecular dynamics (MD) simulations, (iii) calculations of the electrostatic contribution to the gas phase energy (crystal field).

(i) Gas-phase quantum chemical calculations:

We perform density functional theory (DFT) calculations using B3LYP functional and 6-311g(d,p) basis set.[351] Some of the solubilizing groups were removed to reduce the computational effort. Obtained ground state configuration, electrical potential and atomic quadruple tensor are shown in Figure 4.4a. The optimized configuration was used for calculation of atomic partial charges via the CHELPG[352] scheme and parameterization of a polarizable force field for the step ii.

(ii) Force-field parameterization and molecular dynamics simulations:

Morphology simulations were performed using the GROMACS simulation package. In our approach, we first adapt the OPLS-AA force-field,[353–355] by reparameterizing missing improper and torsional potentials. This is done by scanning the cross-sections of the potential energy surfaces using DFT (at B3LYP/6-31g(d,p) level). An example of such dihedral potential parametrization is shown in Figure A1.18, were the fit with a polynomial of 5th order is used to parameterize the difference of energies of quantum and classical calculations. All Lennard–Jones parameters are taken from the OPLS-AA, the combination rules and the fudge-factor of 0.5 are used for 1–4 interactions. The long-range electrostatic interactions are treated by using a smooth particle mesh Ewald technique. All calculations are performed in the NPT ensemble using the canonical velocity-rescaling thermostat[356] and the Berendsen barostat,[357] as implemented in the GROMACS simulation package.[358, 359]

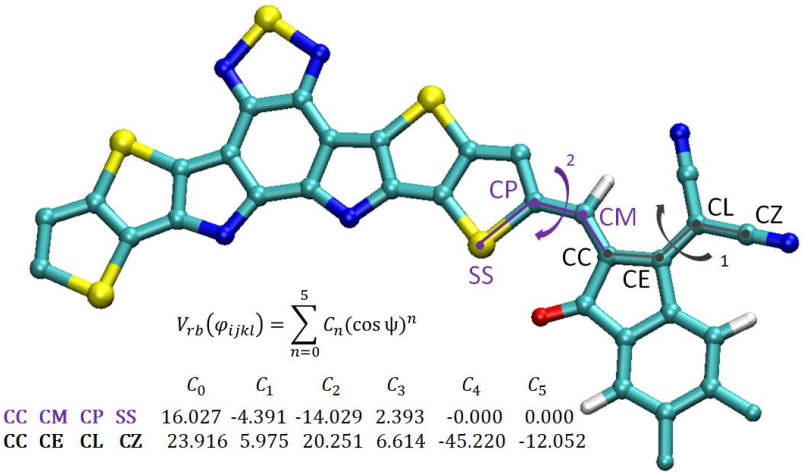

Figure A1.18: Parametrization of missing in OPLS-AA parameters of dihedral potential.

The initial guess of a crystalline arrangement of 192 molecules is equilibrated in the NPT ensemble at T = 400K using the canonical velocity-rescaling thermostat[356] and the Berendsen barostat.[357] After the equilibration step, the simulation box has a correct experimental density of $\rho = 1.08\ g/cm^3$. Figure A1.19a and b show the lamellar packing of Y6 dimers, which is depicted in Figure A1.19c.

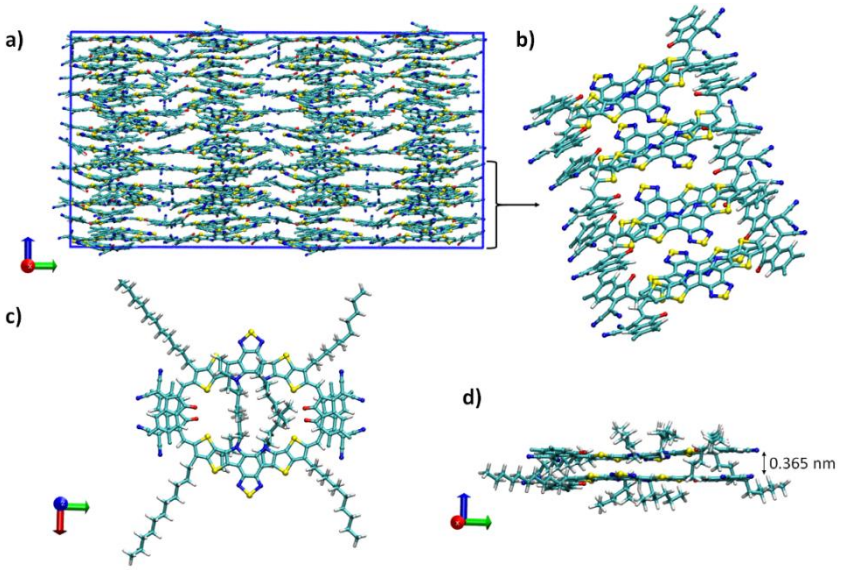

Figure A1.19: a Snapshot of the simulation cell of Y6 lamellar packing (9.5x9.5x5 nm) after 5ns of simulations in NPT ensemble (side chains are omitted for simplifying visualization); b) a lamella formed with Y6 dimers; c) Y6 dimers, the average distance between molecules is 0.365 nm.

(iii) Solid-state electrostatic contribution

Using the molecular dynamics trajectories, the site energies are evaluated in a perturbative way, starting from the gas-phase quantum chemical calculations and then taking into account environmental effects as a perturbation. The total site energies are obtained by adding the electrostatic and induction energies to the gas phase ionization potential of a molecule. The electrostatic and induction contributions to site energies were calculated self-consistently using the Thole model[358, 359] on the basis of the atomic polarizabilities and distributed multipoles obtained by using GDMA program[360] for a cation and a neutral molecule. This approach, in combination with an aperiodic inclusion of charges to a neutral periodic morphology, is available in the VOTCA.[361] Figure 4.4b of the main text shows the distribution of electron affinities and ionization energies in a solid state.

The electrostatic bias potential is defined as $B = \Delta_h^A + \Delta_e^A$, where Δ_e^A and Δ_h^A are solid-state contributions to the ionization energy of an electron and a hole.

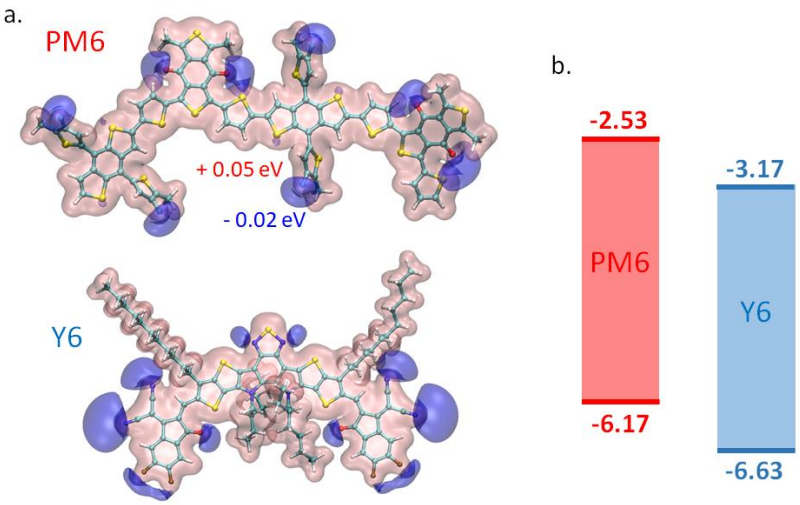

Figure A1.20: Electrostatic potential surfaces and gas-phase ionization energies and electron affinities calculated at the B3LYP 6-311g(d,p) level of theory.

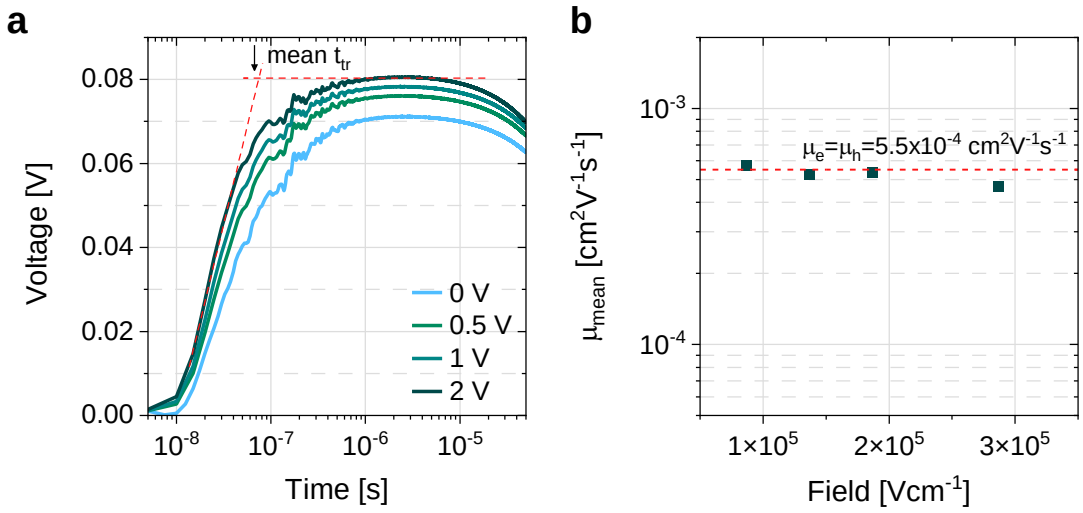

Figure A1.21: a Resistance dependent photovoltage (RPV) results for a PM6:Y6 device at the maximum load resistance of 1 MΩ and varying the applied external voltage. Broad mean transit times (t_{tr}) for all fields indicate that photogenerated carriers have similar arrival times to the electrodes and thus balanced mobilities. **b** The mean mobility (μ_{mean}) is calculated at each field with $\mu = d^2/t_{tr}V_{BI}$, where d is the active layer thickness and V_{BI} is the built-in-voltage.

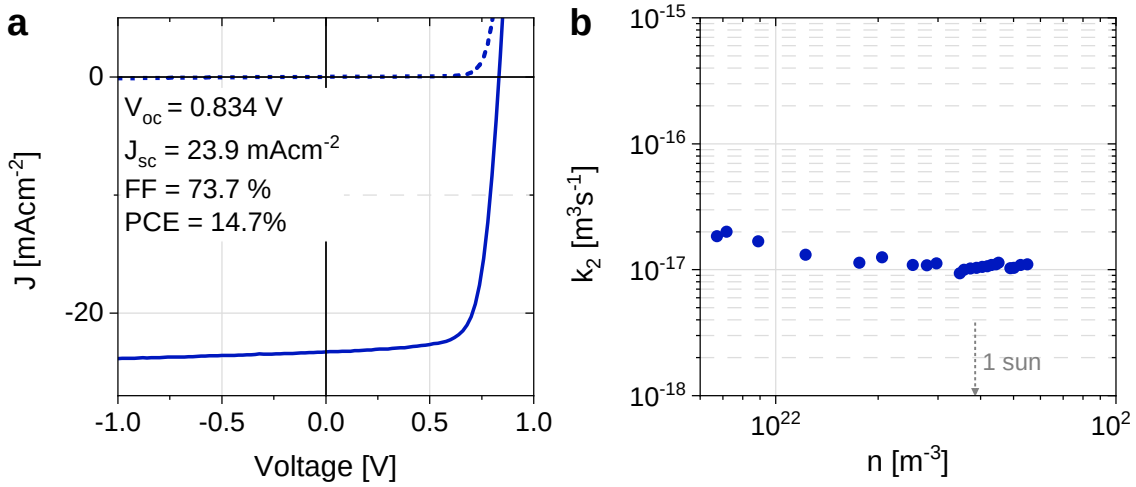

Figure A1.22: a Current density-voltage characteristics (*J-V*) of a PM6:Y6 device in regular structure under simulated AM1.5G light. The devices were fabricated with a structure ITO/PEDOT:PSS/PM6:Y6/PDINO/Ag with a final active layer thickness of 100 nm. **b** Bimolecular recombination coefficient as function of charge carrier density calculated from BACE measurements on the same device. The obtained values are very close to those of our inverted devices in Figure 4.3.

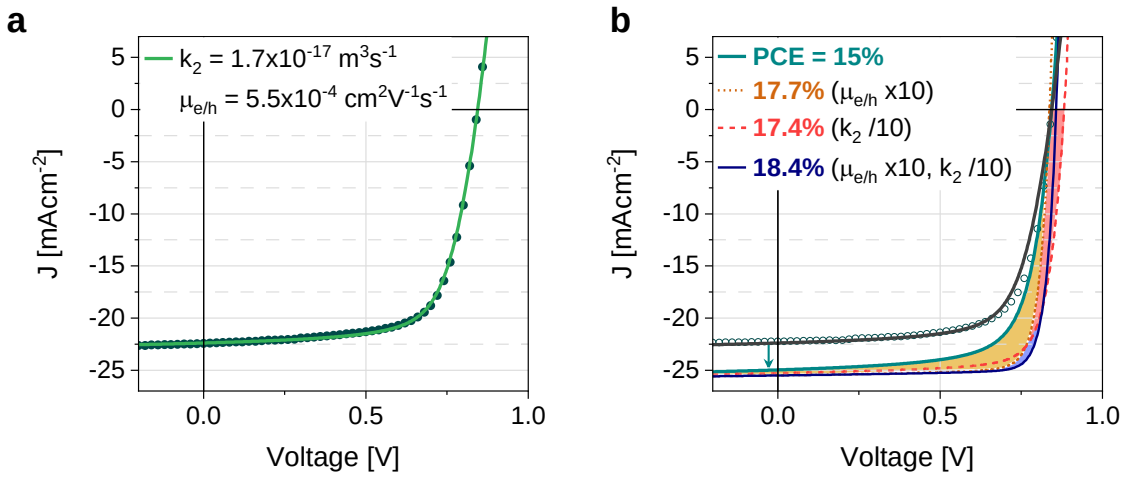

Figure A1.23: a Current density-voltage characteristics of the 1 cm² device under simulated AM1.5G light (V_{OC} = 0.844 V, J_{SC} =22.4 mAcm^{-2}, FF =69.9%, PCE=13.2%) at 25°C. Open dots are the experimental data and the solid line is the drift-diffusion simulation result using the parameters k_2 and $\mu_{e/h}$ as determined experimentally (and shown in the inset). **b** Simulation results by varying the key parameters k_2 and $\mu_{e/h}$. The green solid line depicts a simulated *JV*-curve where the light absorption was optimized with respect to the cell shown in panel (a) which results in a PCE of 15%. In the simulation corresponding to the orange dotted line, the charge carrier mobility was increased one order of magnitude, while all other parameters were kept the same, which already increases the FF to over 80% (shaded area). In the simulation corresponding to the dashed red line, only the recombination coefficient was reduced, which increased both the V_{OC} and FF. The overall performance can be increased to 18.4% provided that $\mu_{e/h}$ is increased and k_2 decreased (blue solid line) by a factor of 10. Simulations were performed using the open-source code SCAPS, which can be obtained from https://users.elis.ugent.be/ELISgroups/solar/projects/scaps upon the conditions requested by the developers Marc Burgelman et al.

Table A1.2: Simulation parameters for a 1 cm² PM6:Y6 device (Figure A1.23).

Parameter	Value	Unit
E_g	1.27	eV
Thickness absorber	100	nm
Effective density of states (active layer)	1×10^{20}	cm^{-3}
Relative dielectric constant	3.5	-
Generation rate („1 sun“)	$\sim 1 \times 10^{22}$	cm^{-3}s^{-1}
Recombination coefficient (k_2)	1.7×10^{-11}	cm^{3}s^{-1}
Electron mobility (μ_e)	5.5×10^{-4}	cm^2 V^{-1} s^{-1}
Hole mobility (μ_h)	5.5×10^{-4}	cm^2 V^{-1} s^{-1}
Electron/hole injection barrier	0	eV
Anode hole surface rec. velocity	10^7	cm s^{-1}
Anode electron surface rec. velocity	10^2	cm s^{-1}
Cathode electron surface rec. velocity	10^7	cm s^{-1}
Cathode hole surface rec. velocity	10^2	cm s^{-1}

The red-shaded values for the recombination coefficient and electron and hole mobility correspond to the initial simulation using the experimental values determined in this work (Figure A1.23a). The values were changed accordingly to obtain the curves in Figure A1.23b. We note that only bimolecular and surface recombination were implemented, since there was no indication of trap-assisted recombination in the experimental recombination dynamics (see Figure 4.3 and Chapter 4). The surface recombination for minority carriers was added to mimic the blocking effect that interlayers will have in a full device. Also, shunt resistance ($R_{\text{shunt}} = 3 \times 10^3\ \Omega cm^2$) and series resistance ($R_{\text{series}} =$

$1.5\ \Omega cm^2$) were implemented to account for the slight shunt we observed in the large area devices and the lower FF with respect to the small-area device ($\sim$ 2% loss).

References:

[351] C. Poelking, E. Cho, A. Malafeev, et al. Characterization of Charge-Carrier Transport in Semicrystalline Polymers: Electronic Couplings, Site Energies, and Charge-Carrier Dynamics in Poly(bithiophene- *alt* -thienothiophene) [PBTTT]. *J. Phys. Chem. C*. **117** (2013), 1633–1640.

[352] C. M. Breneman, K. B. Wiberg. Determining atom-centered monopoles from molecular electrostatic potentials. The need for high sampling density in formamide conformational analysis. *J. Comput. Chem.* **11** (1990), 361–373.

[353] W. L. Jorgensen, J. Tirado-Rives. Potential energy functions for atomic-level simulations of water and organic and biomolecular systems. *Proc. Natl. Acad. Sci. U. S. A.* **102** (2005), 6665–70.

[354] W. L. Jorgensen, J. Tirado-Rives. The OPLS [optimized potentials for liquid simulations] potential functions for proteins, energy minimizations for crystals of cyclic peptides and crambin. *J. Am. Chem. Soc.* **110** (1988), 1657–1666.

[355] W. L. Jorgensen, D. S. Maxwell, J. Tirado-Rives. Development and testing of the OPLS all-atom force field on conformational energetics and properties of organic liquids. *J. Am. Chem. Soc.* **118** (1996), 11225–11236.

[356] G. Bussi, D. Donadio, M. Parrinello. Canonical sampling through velocity rescaling. *J. Chem. Phys.* **126** (2007), 014101.

[357] H. J. C. Berendsen, J. P. M. Postma, W. F. van Gunsteren, A. DiNola, J. R. Haak. Molecular dynamics with coupling to an external bath. *J. Chem. Phys.* **81** (1984), 3684–3690.

[358] B. T. Thole. Molecular polarizabilities calculated with a modified dipole interaction. *Chem. Phys.* **59** (1981), 341–350.

[359] P. T. Van Duijnen, M. Swart. Molecular and atomic polarizabilities: Thole's model revisited. *J. Phys. Chem. A*. **102** (1998), 2399–2407.

[360] A. J. Stone. Distributed multipole analysis: Stability for large basis sets. *J. Chem. Theory Comput.* **1** (2005), 1128–1132.

[361] V. Rühle, A. Lukyanov, F. May, et al. Microscopic Simulations of Charge Transport in Disordered Organic Semiconductors. *J. Chem. Theory Comput.* **7** (2011), 3335–3345.

A2. Supporting Material to Chapter 5

Carrier density profiles for different generation rates and layer thicknesses, with and without surface recombination:

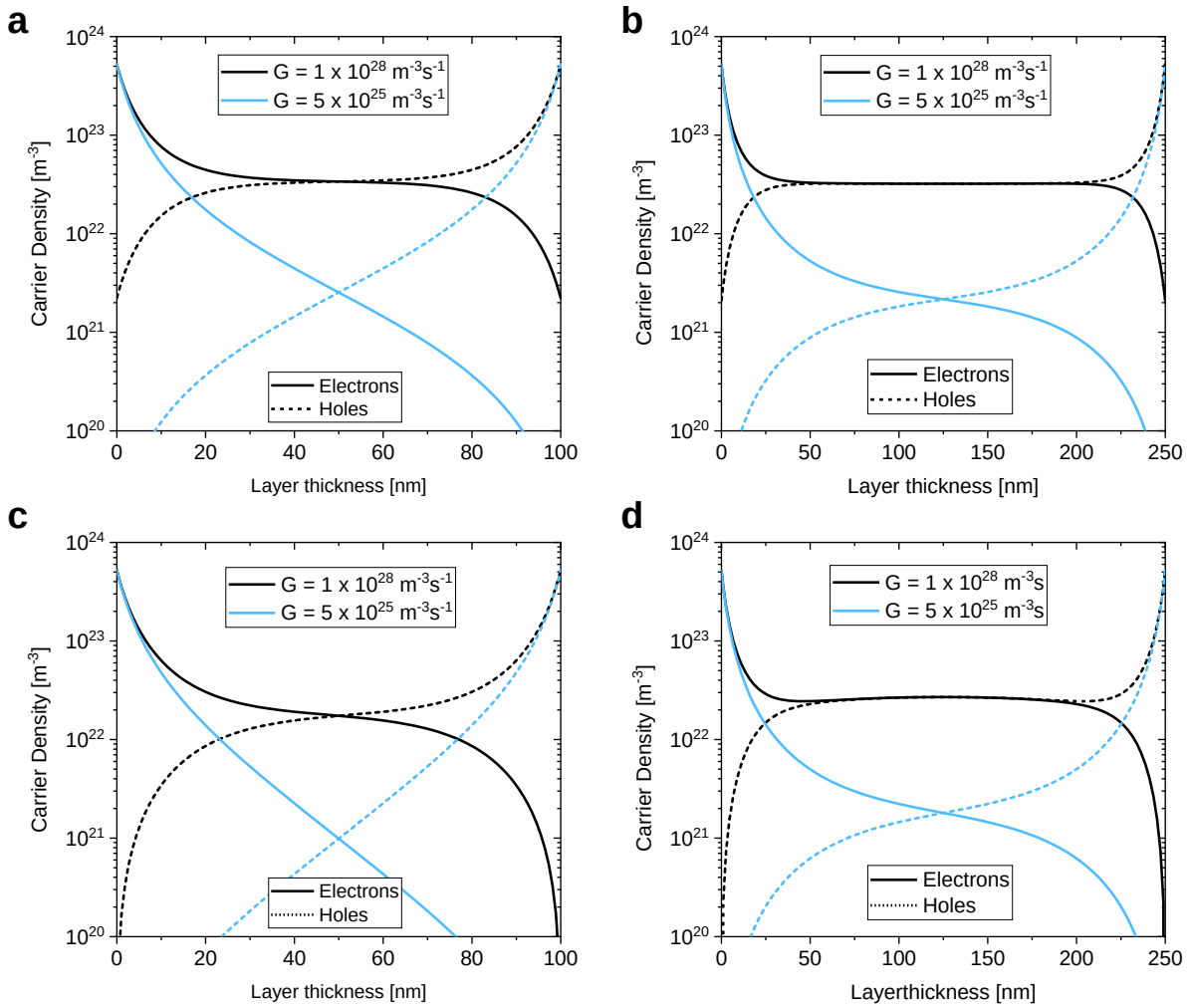

Figure A2.1: Mobilities and recombination coefficient are the same for all simulations ($\mu_e = \mu_h = 10^{-3}$ cm^{2}V^{-1}s^{-1} and $k_2 = 1 \times 10^{-17}$ m^{3}s^{-1}, respectively). **a** and **b** no surface recombination. **c** and **d** infinite surface recombination. Homogeneity of the carrier density profiles increases with generation rate, layer thickness and in the absence of surface recombination.

Influence of prebias and decay kinetics:

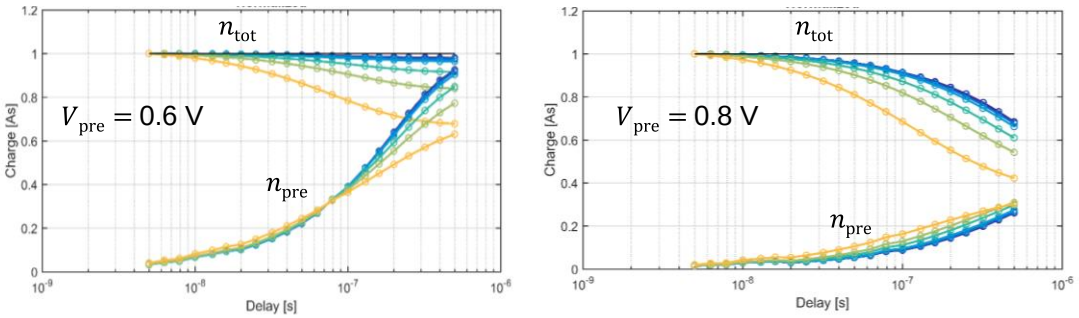

Figure A2.2: n_{tot} and n_{pre} normalized to the initial n_{tot} (for a delay of 5 ns) as a function of the delay time for two different prebias. All other conditions are as in Figure 5.3. Also, the color code is the same as in Figure 5.3, with the initial carrier density increasing from blue to orange.

Equitemporal fits to the differential decay data:

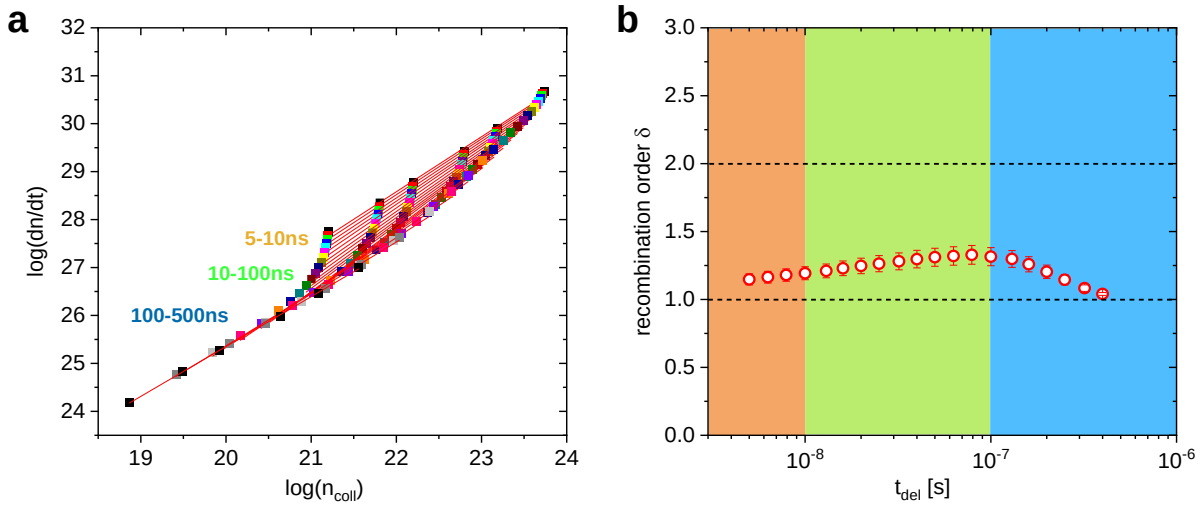

Figure A2.3: a Differential decay data for the 100 nm device with infinite surface recombination at both contacts (data from Figure 5.7a). The thin red lines are power law – type fits of the recombination rates for the same delay time. **b** The recombination order δ derived from the fits of the equitemporal recombination rates in panel a.

A3. Supporting Material to Chapter 6

Note A3.1: Recombination order with respect to light intensity

As explained in section 2.4.2, bimolecular recombination refers to the recombination between free charge carriers regardless of whether they are photogenerated, injected or originate from doping. Bimolecular recombination is a second-order process ($R \sim np$) with respect to the density of these charges, however, as we discuss throughout Chapter 6 can be of first- or second order with respect to the light intensity. In Chapter 6, we study the recombination order with respect to the light intensity as this dependence is directly accessible through intensity dependent photocurrent measurements. Monomolecular recombination on the other hand refers to traps-assisted, CT-state or exciton recombination and is a first order recombination process with respect to the density of the species involved. Monomolecular recombination processes are not implemented in the simulations in Chapter 6, however, we note that it has been previously shown that trap-assisted recombination cannot cause a significant loss in the linear IPC regime (see Ref.[273]).

Note A3.2: Supplementary methods

Device preparation

Substrates with an ~150 nm indium tin oxide (ITO) layer (Lumtec) were cleaned in an ultrasonic bath with acetone, Hellmanex, deionized water and 2-propanol for 10 min, respectively, and UV-plasma treated. Subsequently, the substrates were coated with 30 nm PEDOT:PSS (Baytron P VPAl4083). Blends of PTB7 and $PC_{70}BM$ were prepared from a 1,2-dichlorobenzene (DCB) solution using a total concentration of 31 $mgcm^{-3}$. The optimized blend ratio by weight of 1 to 1.5 was used. We note that no 1,8-diodooctane (DIO) was used which can increase the efficiency for this blend.[274] The solution was spin coated onto the substrates and the resulting layer was not annealed. The active layer thicknesses were measured with a DekTak 150 profilometer. The PTB7:$PC_{70}BM$ devices were completed by vacuum evaporation of 15 nm of calcium followed by 75 nm of aluminium under a pressure of 10^{-6} mbar. The device area was 16 mm^2. FTAZ:IDIC devices were fabricated ITO/ZnO/FTAZ:IDIC/MoO_3/Ag architecture. ZnO nanoparticles (Avantama) were filtered through a 0.45 µm PTFE filter and spin coated on ITO at 3600 rpm under ambient conditions. Then the ZnO substrates were thermally annealed at 120°C for 30 min, followed by exposition to UV light inside the glovebox for 10 min. FTAZ and IDIC were dissolved in chloroform ($CHCl_3$) to a total concentration of 12 $mgmL^{-1}$ with a 1 to 1.5 weight ratio and 0.25% DIO (v/v, DIO/$CHCl_3$) as additive. The blend was subsequently spin coated (2000 rpm) onto the ZnO layer to obtain a photoactive layer of thickness ~110 nm. To complete the devices, 10 nm of MoO_3 as the anode interlayer and 100 nm of Ag as the top electrode were evaporated under 10^{-6} mbar vacuum. The devices were encapsulated for the IPC and TDCF measurements.

Drift-diffusion simulations

The numerical simulations presented in this study were performed with the semiconductor simulation tool SCAPS (see Chapter 3, section 3.6.). We also compared the results as obtained from SCAPS to results obtained from Sentaurus Device,[276] using the same input parameter files which provided identical results.

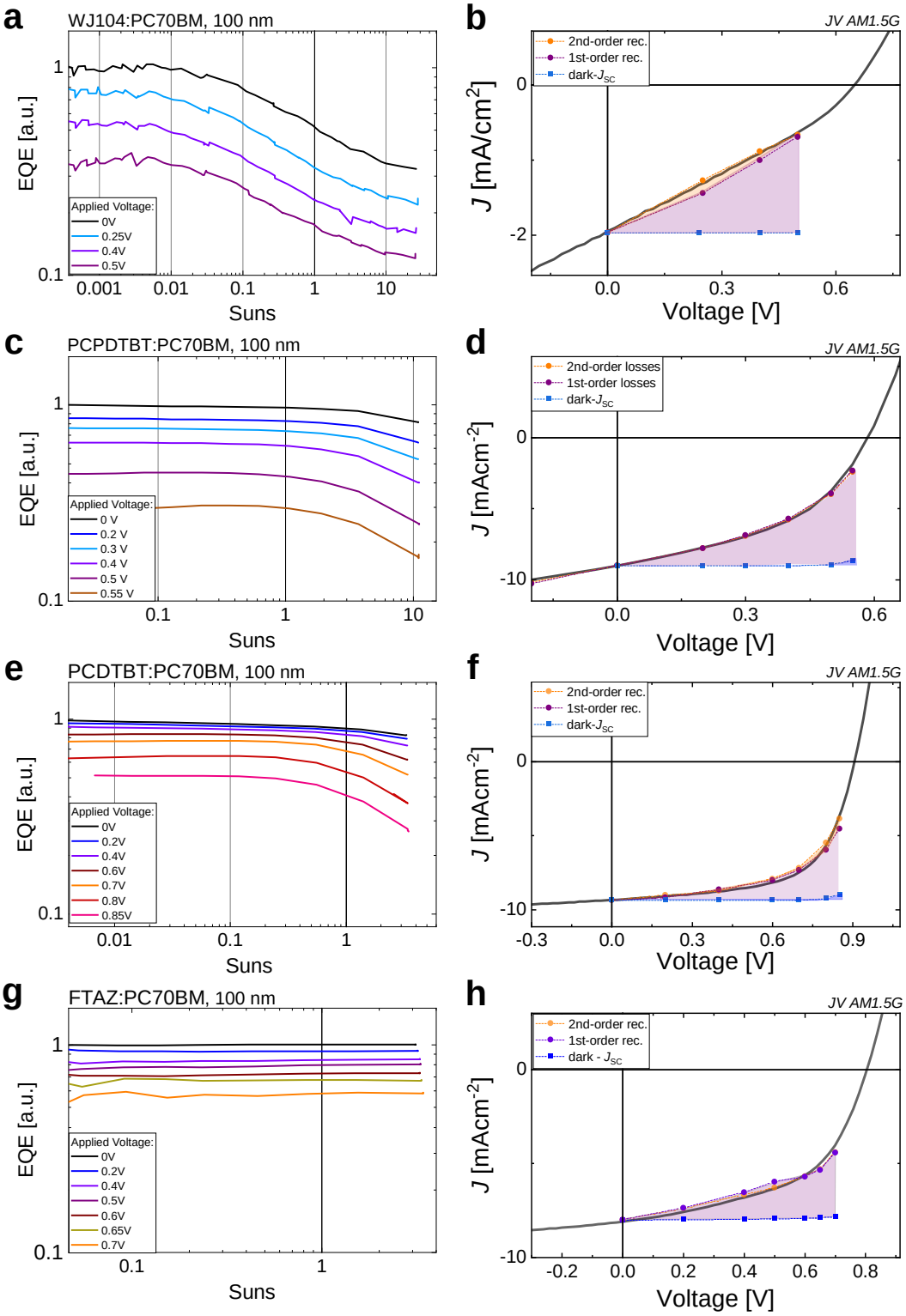

Figure A3.1: The order of recombination with respect to the light intensity throughout the power generating regime as deduced from IPC measurements for various organic solar cells with optimized film thickness. Notably, also in less efficient cells which are already limited by second order recombination at 0V, the losses scale linearly in forward bias as shown in in panels **a** and **b**.

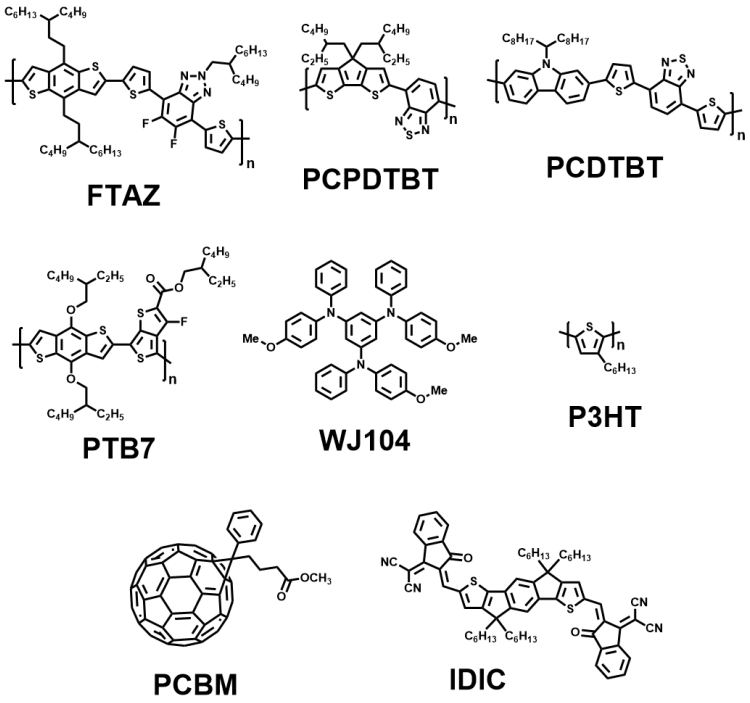

Figure A3.2: The chemical structures of each material used in Chapter 6.

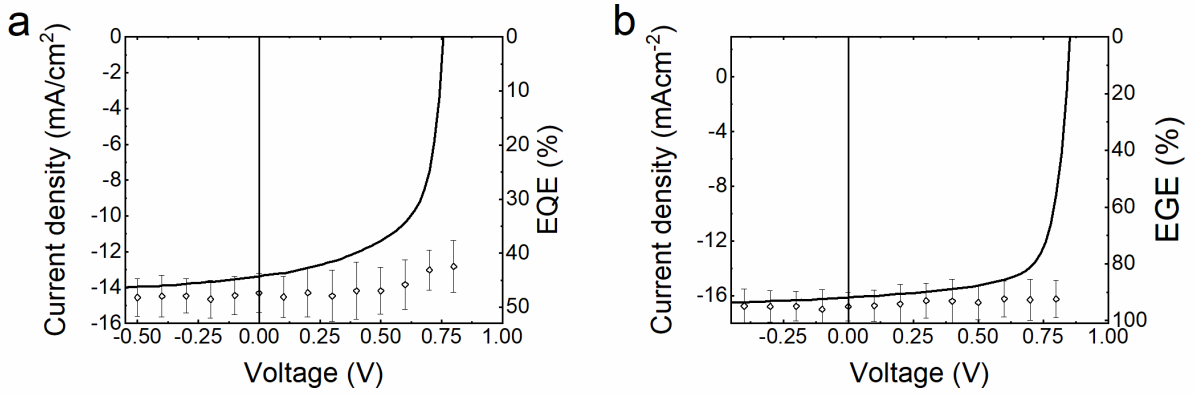

Figure A3.3: Time-delayed collection field experiments. The bias dependent external generation efficiency (EGE, diamonds) on the right y-axis demonstrates field-independent generation in the blends shown in Figure 6.1. For PTB7:PCBM an excitation wavelength of 450 nm was chosen, a delay time of 6 ns, a collection voltage of -2V, and a fluence of 0.05 μJcm^{-2}. For FTAZ:IDIC an excitation wavelength of 600 nm was chosen, a delay time of 2 ns, a collection voltage of -1V, and a fluence of 0.15 μJcm^{-2}.

Table A3.1: Simulation parameters for PTB7:$PC_{70}BM$

Parameter	Value	Unit
E_g	1.25	eV
Thickness absorber	80	nm
Effective density of states (active layer)	1×10^{20}	cm^{-3}
Relative dielectric constant	4	-
Generation rate („1 sun“)	$\sim 1 \times 10^{22}$	$cm^{-3}s^{-1}$
Recombination coefficient (k_2)	6×10^{-11}	cm^3s^{-1}
Electron mobility (μ_e)	3×10^{-4}	$cm^2 V^{-1} s^{-1}$
Hole mobility (μ_h)	3×10^{-4}	$cm^2 V^{-1} s^{-1}$
Electron/hole injection barrier	0.0	eV
Anode hole surface rec. velocity	10^7	$cm\ s^{-1}$
Anode electron surface rec. velocity	10^2	$cm\ s^{-1}$
Cathode electron surface rec. velocity	10^7	$cm\ s^{-1}$
Cathode hole surface rec. velocity	10^2	$cm\ s^{-1}$

We note that no trap-assisted recombination was implemented, only bimolecular recombination between free charges and surface recombination. We further note that the low surface recombination velocity (S) for minority carriers (10^2 cms^{-1}) was implemented to mimic an interlayer with some blocking behavior for the minority carrier. We note that the precise value of S does not change the conclusions as shown in Figure A3.7, while the effect of interlayers is further discussed in Figure A3.8.

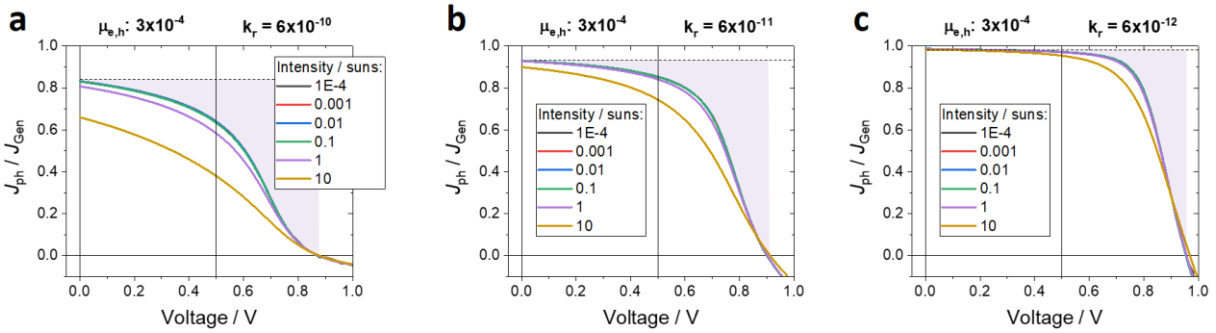

Figure A3.4: The impact of the recombination coefficient on the first- (purple shade) and higher order recombination losses and the fill factor.

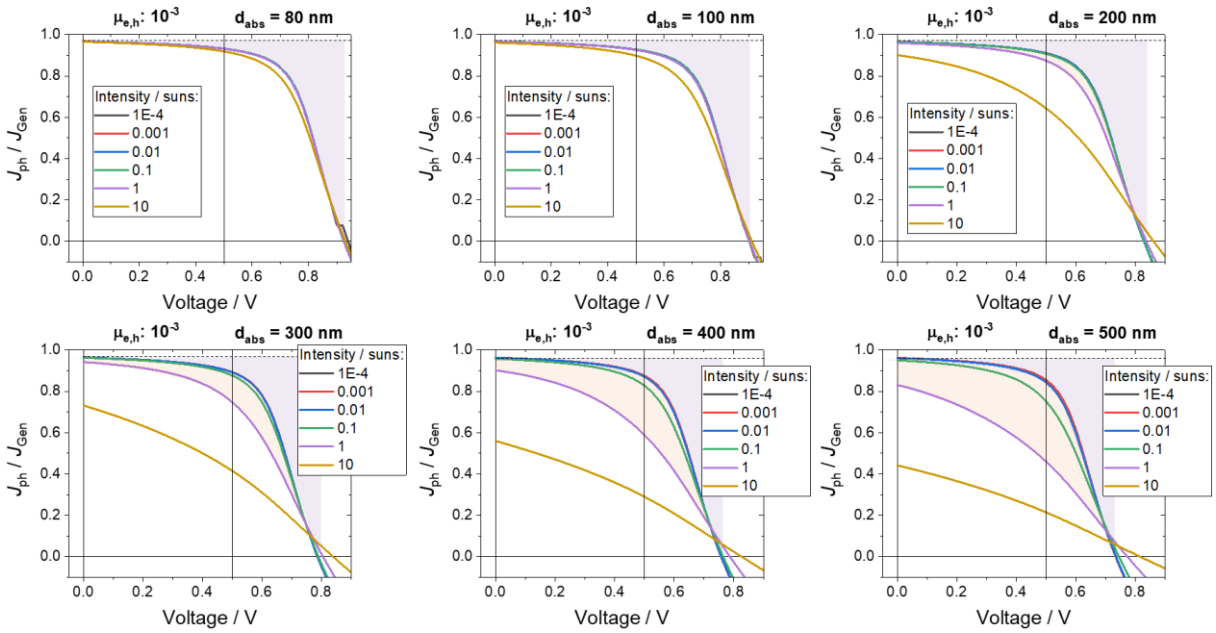

Figure A3.5: The impact of the film thickness on the relative contribution of first- (purple shade) and second order (orange shade) losses in the power generating regime of the *J-V* curve. While the first order losses (at low intensities) remain similar when the active layer thickness is increased from 80 nm to 500 nm, the contribution of second order recombination increases comparatively. However, first order recombination clearly dominates in blends with optimized FF and active layer thicknesses.

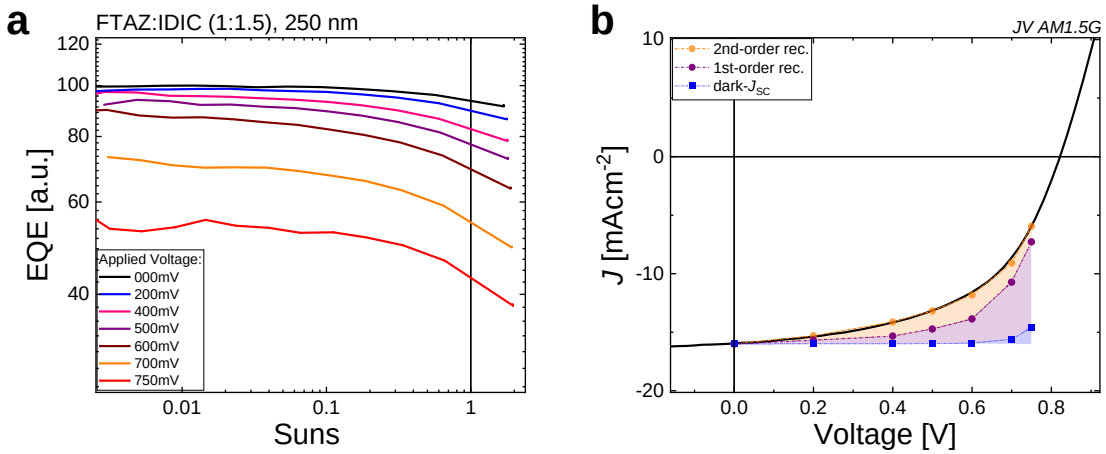

Figure A3.6: Intensity dependent EQE curves at different applied voltages from short-circuit close to open-circuit conditions for a FTAZ:IDIC (1:1.5 w/w) blend with non-optimal active layer thickness of approximately 250 nm. As expected from the simulations in Figure A3.5, the higher film thickness results in a significant contribution of second order recombination losses in the power generating *J-V* regime which further deteriorates the fill factor.

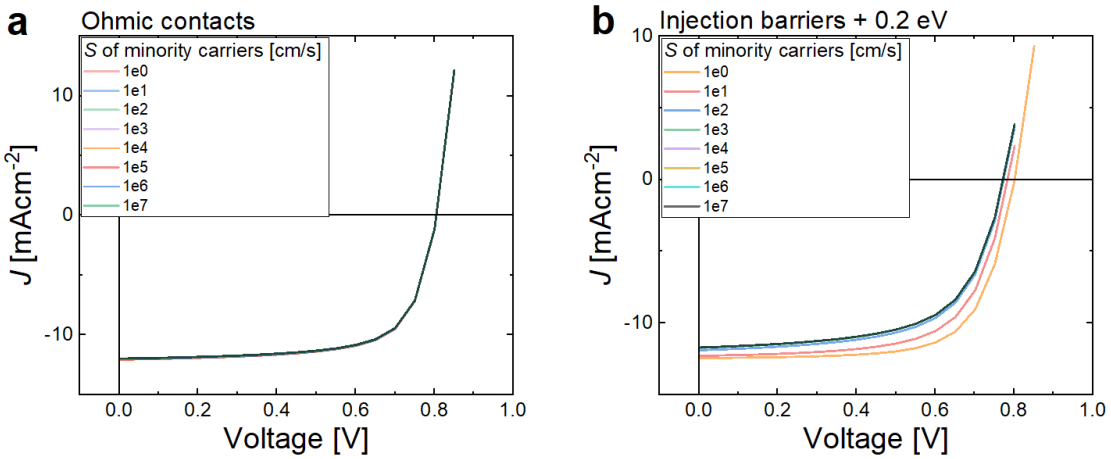

Figure A3.7: The impact of the surface recombination velocity (S) for minority carriers at both metal contacts on the J-V characteristics. As discussed in Chapter 6, surface recombination plays no role in case of ohmic contacts (**a**). However, in case of injection barriers (**b**), reduced surface recombination is beneficial which, in the limit of 0 surface recombination allows to regain the performance of ohmic contact.

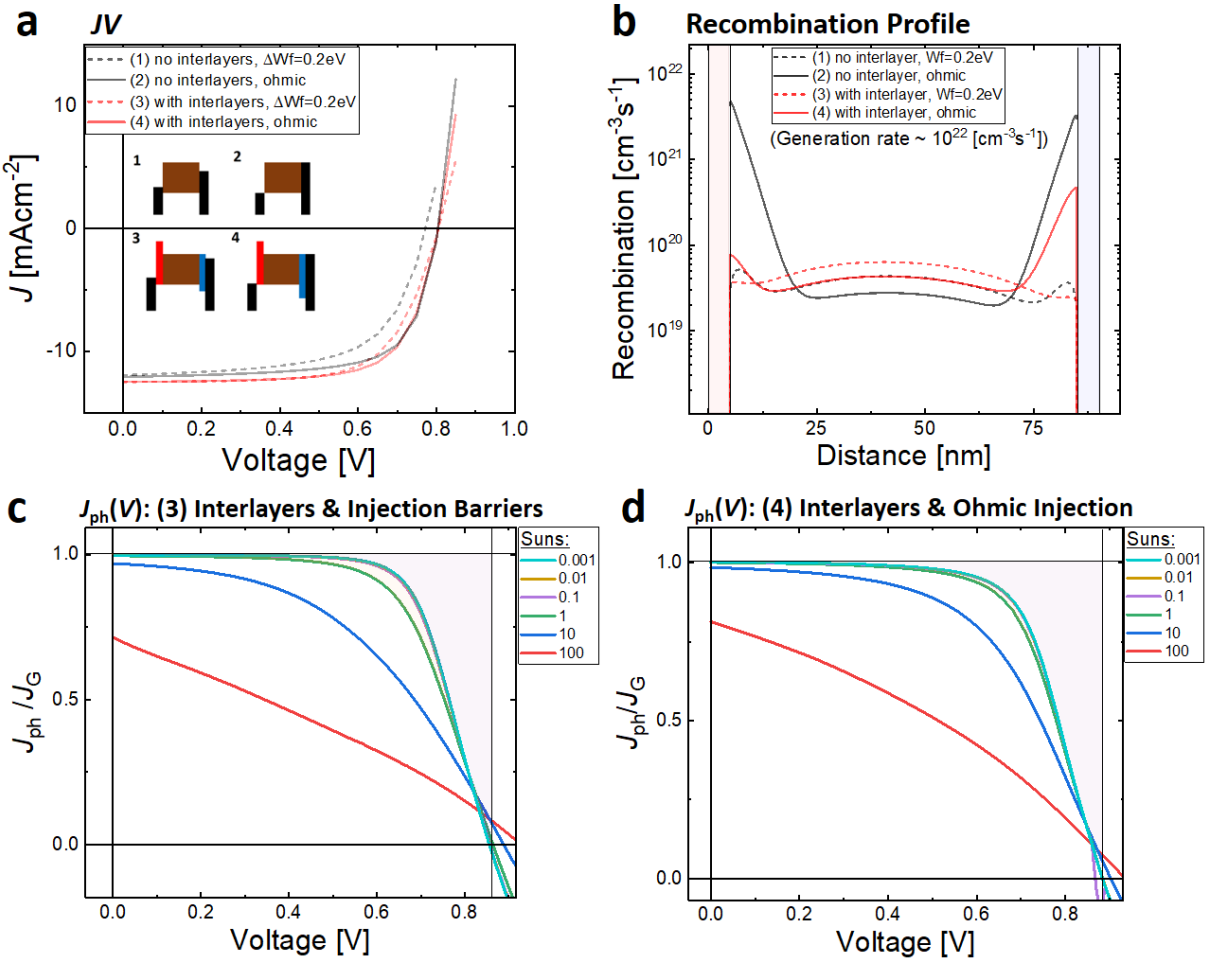

Figure A3.8: a *J-V* characteristics of cells with and without interlayers in case of ohmic contacts ($\Delta W_f = $ 0.0 eV) and injection barriers ($\Delta W_f = 0.2$ eV). The interlayers were optimized in order to avoid FF losses, i.e. they are very thin ~5 nm, they allow a high enough majority carrier mobility ~1x10^{-3} cm^2 V^{-1}s^{-1}, the energy levels for majority carriers are aligned with respect to the active layer and they do not cause interfacial recombination. In case of ohmic contacts (black), the implementation of such optimized interlayers can slightly increase the short-circuit current (J_{SC}) which leads to a small efficiency improvement from 6.8% to 7.1%. In case of injection barriers (red), the implementation of these interlayers can lead to larger improvements due to suppressed surface recombination (the PCE increases from 5.8% to 6.8%). **b** shows the corresponding recombination profiles at 0V. The reason for the improved J_{SC} in case of interlayers (which are shown by the red and blue shaded regions) is the suppressed recombination rate close the interfaces. In case of ohmic contacts & interlayers, the recombination shifts from the metal contacts to close to the interlayers in the bulk, while in case of injection barriers & interlayers, the recombination happens throughout the whole bulk. **c** and **d** The corresponding normalized photocurrent vs. voltage plots for different light intensities show that the recombination order remains also in case of interlayers largely of first order with respect to the light intensity.

A4. Supporting Material to Chapter 7

Note A4.1: Supplementary methods

Device preparation

The devices with regular configuration were fabricated as ITO/PEDOT:PSS/PM6:Y6/PDINO/Ag. Patterned ITO (Lumtec) substrates were cleaned in an ultrasonic bath with acetone, Hellmanex, deionized water and isopropanol for 10 min, followed by microwave plasma treatment (4 min at 200 W). Subsequently, PEDOT:PSS (Clevios AI 4083) was filtered through a 0.2 µm PA filter and spin coated onto ITO at 5000 rpm under ambient conditions to obtain a ~30 nm layer. The PEDOT:PSS coated substrates were thermally annealed at 150°C for 10 min. PM6 and Y6 were dissolved in $CHCl_3$ to a total concentration of 16 $mgmL^{-1}$ with a 1 to 1.2 weight ratio and 0.5% CN (v/v, CN/ $CHCl_3$) as additive. The solution was stirred for 3 hours inside the glovebox. Then, the blend was spin coated (between 800 and 2500 rpm) onto the PEDOT:PSS layer to obtain a photoactive layer of thickness between 100 nm and 200 nm. To complete the devices, a very thin layer (~10 nm) of PDINO (1-Material Inc.) was spin coated onto the active layer, from a 1 $mgmL^{-1}$ solution in methanol (2000 rpm), and 100 nm of Ag as the top electrode were evaporated under a 10^{-6}-10^{-7} mbar vacuum. For devices with semi-transparent cathode, only 45 nm of Ag were evaporated at this stage. In the case of inverted devices, the structure was ITO/ZnO/PM6:Y6/MoO_3/Ag. After following the same cleaning procedure as above, ZnO nanoparticles (Avantama N-10) dissolved on isopropanol were filtered through a 0.45 µm PTFE filter and spin coated onto ITO at 5000 rpm under ambient conditions. The ZnO substrates were thermally annealed at 120°C for 30 min. The active layer of the device was prepared as for regular devices. To complete the devices, 8 nm of MoO_3 as the anode interlayer and 100 nm of Ag as the top electrode were evaporated. The resulting active area for all devices in this work was 6 mm^2.

For absorption and photoluminescence measurements of films, solutions of Y6, PS:Y6 and PM6:Y6 were spin coated on glass directly. Afterwards they were covered with another glass substrate using encapsulation only on the edges, prior to the measurements. PM6:Y6 solutions were prepared as explained above. Y6 and PS (Sigma Aldrich, 35 kDa) were dissolved on CF as well. The weight ratio 1 to 1.2 was maintained for the PS:Y6 blend.

Temperature-dependent measurements

For photoluminescence and electroluminescence measurements at different temperatures, the devices were loaded into a liquid nitrogen-cooled cryostat (Janis) and the temperature was adjusted in a range of 180 K to 300 K using a temperature controller (Lakeshore 335). The cryostat was placed in front of the lenses that focus the emission onto the spectrograph (Andor Solis SR393i-B spectrograph with a silicon DU420A-BR-DD detector and an Indium Gallium Arsenide DU491A-1.7 detector, see Chapter 3). For EL measurements, the device was hold at a constant voltage, using a Keithley 2400, for 1 s.

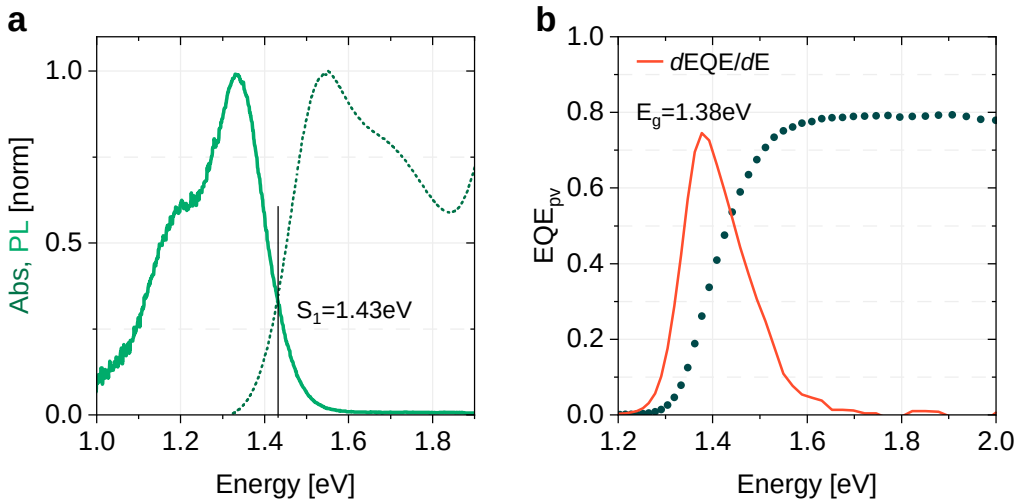

Figure A4.1: a Normalized absorption and photoluminescence (PL) spectra of a PM6:Y6 film. The crossing point of both spectra gives the Y6 exciton singlet energy, E_{S_1}, in the blend. **b** Photovoltaic external quantum efficiency ($\mathrm{EQE_{PV}}$) of a regular PM6:Y6 device and its derivative $\mathrm{d}EQE/\mathrm{d}E$. The photovoltaic gap E_g of the blend is determined from the maximum of the derivative, as in Ref.[147]

Table A4.1: Photovoltaic parameters for the different configurations considered in this work with PM6:Y6 as the active layer. The corresponding current density-voltage characteristics can be found in Figure A4.2 panel a.

Device	***d* [nm]**	**V_{OC} [V]**	**J_{SC} [mA cm^{-2}]**	**FF [%]**	**PCE [%]**
Regular	100	0.84	26.0	69.2	15.1
Regular	145	0.834	25.0	68.8	14.3
Semi-transparent	135	0.828	23.2	66.1	12.7
Semi-transparent	200	0.817	22.6	61.1	11.3
Inverted	110	0.825	23.4	69.7	13.5

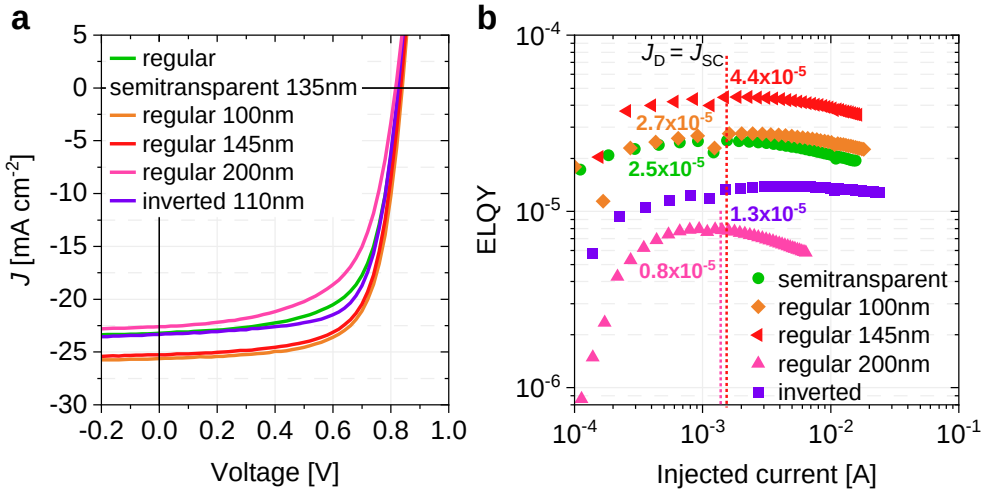

Figure A4.2: a Current density-voltage (*J-V*) characteristics of the different configurations considered in this work with PM6:Y6 as the active layer, measured under simulated AM1.5G light. Regular structure is ITO/PEDOT:SS/PM6:Y6/PDINO/Ag. For semi-transparent devices only 45 nm of Ag (top cathode) were evaporated. Inverted structure consists of ITO/ZnO/PM6:Y6/MoO_3/Ag. The legend specifies the thickness of the active layer in each configuration. **b** Electroluminescence quantum efficiency (ELQY) as a function of injected current for the same devices as in panel a. The values given for each data set correspond to the ELQY value when the injected current (J_D) equals short-circuit current density (J_{SC}) at 1 sun.

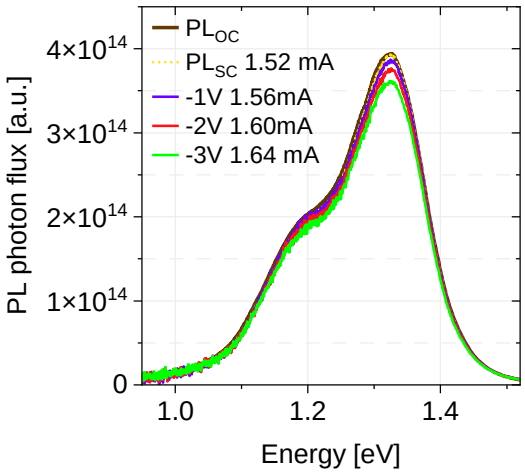

Figure A4.3: Photoluminescence (PL) spectra recorded at open-circuit (OC), short-circuit (SC) conditions and at 3 different reverse biases under a 1 sun equivalent illumination for a 100 nm regular PM6:Y6 device with fully reflecting back electrode. We observe that the PL intensity is reduced by less than 10% when going from OC to -3V and the shape of the spectra remains unchanged.

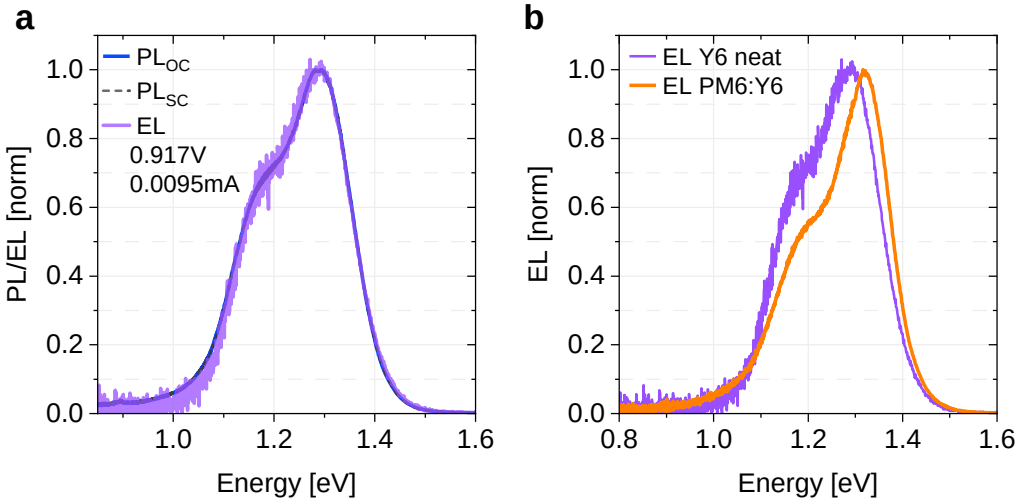

Figure A4.4: a Normalized steady-state photoluminescence (PL) and electroluminescence (EL) spectra of a 50 nm neat Y6 regular device with fully reflecting cathode. PL was recorded at open-circuit (OC) and short-circuit (SC) conditions under a 1 sun equivalent illumination. In EL, the injected current matched the 1 sun photocurrent density at an applied voltage of 0.917 V. **b** Comparison of the EL spectra measured for the neat Y6 device in panel a and the EL measured for a 100 nm PM6:Y6 regular device with fully reflecting cathode.

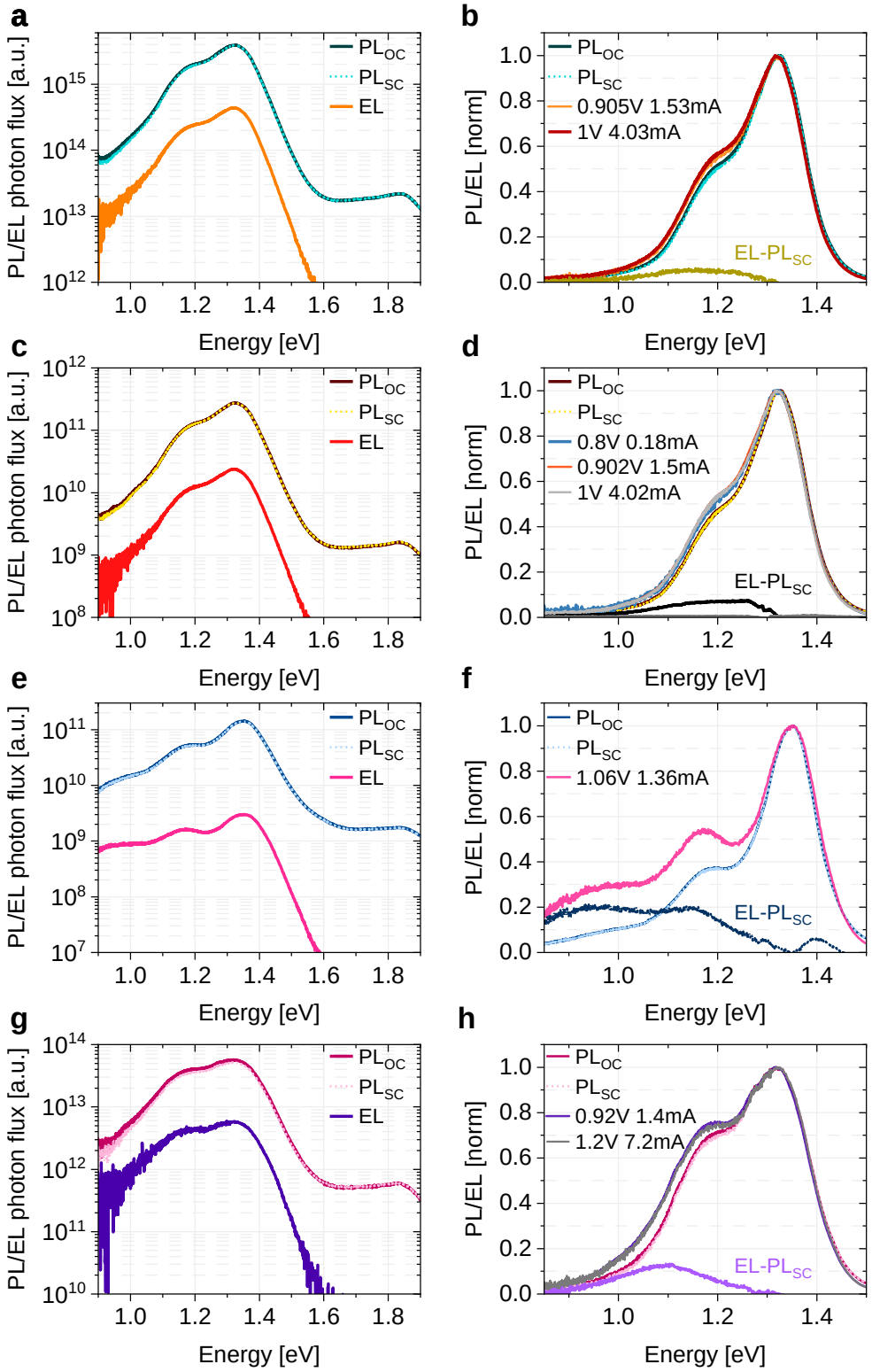

Figure A4.5: PL and EL spectra measured for the different configurations considered in this work with PM6:Y6 as the active layer. PL was recorded at open-circuit (OC) and short-circuit (SC) conditions under a 1 sun equivalent illumination and EL was measured at the driving currents specified in the legend. **a** and **b** for a 100 nm PM6:Y6 regular device with fully reflecting cathode. **c** and **d** for a 145 nm PM6:Y6 regular device with fully reflecting cathode. **e** and **f** for a 200 nm PM6:Y6 regular device with semi-transparent cathode. **g** and **h** for a 110 nm PM6:Y6 inverted device with fully reflecting cathode. The normalized right-side panels show for all device configurations that the shape of the EL spectra do not vary at different driving currents. Moreover, a broad emission appears upon subtracting PL_{SC} from EL, but the spectral shape and strength of the emission depends largely on the active layer thickness and device configuration.

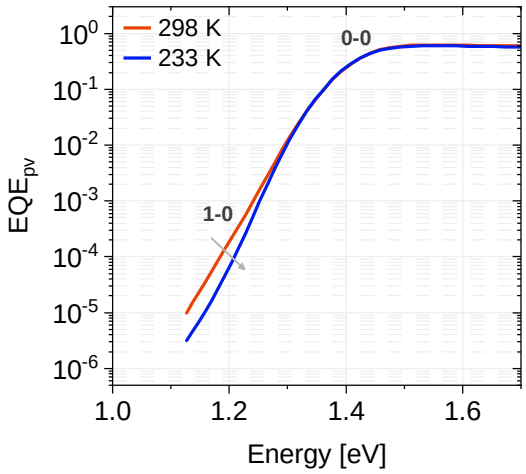

Figure A4.6: Photovoltaic external quantum efficiency ($\mathrm{EQE_{PV}}$) of a PM6:Y6 device measured at 298 K and upon cooling down to 233 K. At 233 K the shoulder corresponding to the transition 1-0, i.e. the transition from thermally excited vibronic states of S_0 to the vibronic ground state of S_1, becomes supressed.

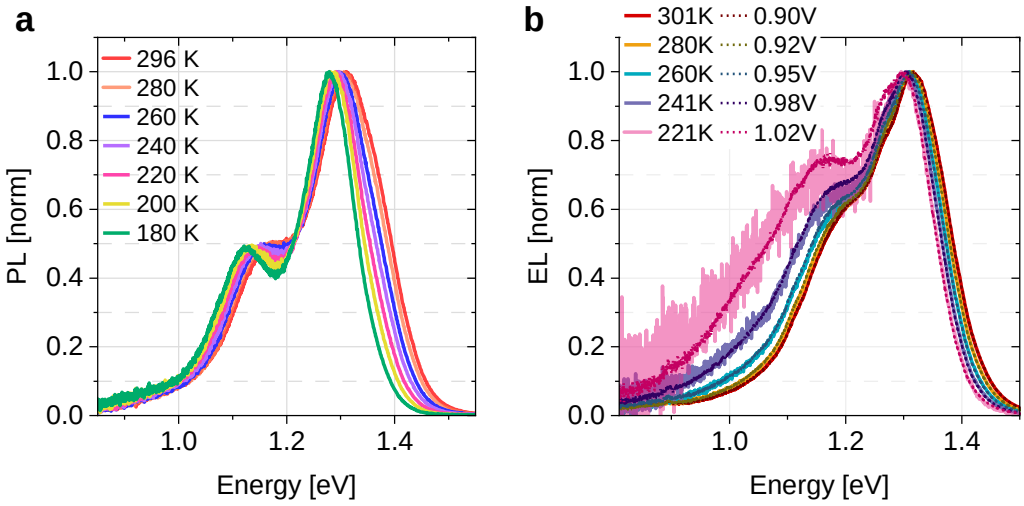

Figure A4.7: a Normalized photoluminescence (PL) spectra as a function of temperature of a thin film of PS:Y6 on glass, to observe the red-shift of the main emission peak. The data corresponds to that showed in Figure 7.3a. **b** Electroluminescence (EL) spectra as a function of temperature of a regular PM6:Y6 device measured at constant current of 1.56 mA, generated by applying the specified driving voltages (dotted lines). The full lines correspond to the spectra measured for each temperature at a constant voltage of 0.90 V. We observe that the driving conditions do not change the shape of the spectra.

Note A4.2: Chemical potential and photon flux

According to Burke et al.,[129] the density of CT excitons n_{CT} at energy E_{CT} in an optically or electrical driven sample is $n_{\mathrm{CT}} = N_{\mathrm{CT}} \exp\left(-\frac{E_{\mathrm{CT}}}{k_{\mathrm{B}}T}\right) \exp\left(\frac{\mu_{\mathrm{CT}}}{k_{\mathrm{B}}T}\right)$. Here, μ_{CT} is the chemical potential of the non-thermal CT state population and N_{CT} is the number density of sites where CT excitons can form. This equation was derived under the assumption of a low excitation density, $n_{CT} \ll N_{\mathrm{CT}}$, and that no site can be populated with more than one CT exciton. At thermal equilibrium, $\mu_{\mathrm{CT}} = 0$, resulting in the thermally excited CT population in the dark: $n_{\mathrm{CT}}^{0} = N_{\mathrm{CT}} \exp\left(-\frac{E_{\mathrm{CT}}}{k_{\mathrm{B}}T}\right)$. This leads to $n_{\mathrm{CT}} = n_{\mathrm{CT}}^{0} \exp\left(\frac{\mu_{\mathrm{CT}}}{k_{\mathrm{B}}T}\right)$. The same holds for the population of singlet excitons on Y6 for relevant

illumination (injection) conditions: $n_{S_1} = N_{S_1} \exp\left(-\frac{E_{S_1}}{k_B T}\right) \exp\left(\frac{\mu_{S_1}}{k_B T}\right) = n_{S_1}^0 \exp\left(\frac{\mu_{S_1}}{k_B T}\right)$. Related to that, the emitted photon flux from Y6 excitons relative to the excitonic photon emission in the dark is $\phi_{S_1} = \phi_{S_1}^0 \exp\left(\frac{\mu_{S_1}}{k_B T}\right)$.

We determined ϕ_{S_1} by assuming that at least 90 % of the total EL photon flux stems from Y6 exciton recombination: $\phi_{S_1} \geq 0.9 \times \mathrm{ELQY} \times \frac{J_R}{q}$

With the recombination current density being $J_R = J_{SC} = 25\ mAcm^{-2}$ and the $\mathrm{ELQY} = 4.4 \times 10^{-5}$ for the 145 nm thick device considered here, (see Table A4.3 for all values), we obtain $\phi_{S_1}(EL) \geq 6.2 \times 10^{12}$ cm^{-2}s^{-1}.

To calculate the emission of photons due to exciton population from free charges, we employed Rau's reciprocity (see Equation 2.26), but now aligning the optical reciprocity of the device PL (and not the EL) with the tail of the $\mathrm{EQE_{PV}}$ to obtain $\mathrm{EQE_{PV,S_1}}(E)$. Then, $\phi_{S_1}^0$ was calculated with

$$\phi_{S_1}^0 = \int \mathrm{EQE_{PV,S_1}}(E) \phi_{BB}(E) \mathrm{d}E$$

For our 145 nm regular device and the spectra in Figure 7.2d this yields $\phi_{S_1}^0 = 0.11$ cm^{-2}s^{-1} and with ϕ_{S_1} from above, $\mu_{S_1} \geq 0.821$ eV.

Note A4.3: Calculation of the number density of Y6 molecules

The number density of Y6 molecules in the blend, $N_{Y6} = 2.4 \times 10^{20}$ cm^{-3} was calculated from the molar mass of Y6 ($M = 1452$ g/mol), a PS:Y6 weight fraction of 1:1.2, and assuming a density of the blend $\rho = 1.08$ g/mol.[58]

Note A4.4: Contribution of the S_1 energetics and recombination properties to V_{OC}

In the limit of a Boltzmann population of the S_1 and the CT state (see above Note A4.2):

$$n_{S_1} = N_{S_1} \exp\left(-\frac{E_{S_1}}{k_B T}\right) \exp\left(\frac{\mu_{S_1}}{k_B T}\right) \text{ and } n_{CT} = N_{CT} \exp\left(-\frac{E_{CT}}{k_B T}\right) \exp\left(\frac{\mu_{CT}}{k_B T}\right).$$

We have shown that the S_1 state population is in dynamic equilibrium with the CT state population, meaning that $\mu_{S_1} = \mu_{CT}$. This results in

$$n_{S_1} = \frac{N_{S_1}}{N_{CT}} \exp\left(-\frac{E_{S_1} - E_{CT}}{k_B T}\right) n_{CT}.$$

The total recombination rate (including exciton reformation and decay) is then

$$R = R_{S_1} + R_{CT} = k_{S_1} n_{S_1} + k_{CT} n_{CT} = \left[\frac{k_{S_1} N_{S_1}}{k_{CT} N_{CT}} \exp\left(-\frac{E_{S_1} - E_{CT}}{k_B T}\right) + 1\right] k_{CT} n_{CT}.$$

Here, k_{S_1} and k_{CT} are the decay rates of the S_1 and the CT state, respectively, to the ground state. With $J_{SC} = qdR$, this leads to

$$n_{CT} = \frac{J_{SC}}{qd\left[1 + \frac{k_{S_1} N_{S_1}}{k_{CT} N_{CT}} \exp\left(-\frac{E_{S_1} - E_{CT}}{k_B T}\right)\right] k_{CT}}.$$

We now use again that all populations (S_1, CT and free charges) are in a dynamic equilibrium, meaning that $\mu_{CT} = E_{CT} + k_B T ln\left(\frac{n_{CT}}{N_{CT}}\right) \cong qV_{OC}$.

Combining these equations finally leads to

$$qV_{OC} = E_{CT} + k_B T \ln\left(\frac{J_{SC}}{qd\left[k_{CT}N_{CT} + k_{S_1}N_{S_1}\exp\left(-\frac{E_{S_1}-E_{CT}}{k_B T}\right)\right]}\right).$$

On the other hand, the ratio between the S_1 and the CT recombination is

$$\frac{R_{S_1}}{R_{CT}} = \frac{k_{S_1}N_{S_1}}{k_{CT}N_{CT}} = \frac{k_{S_1}N_{S_1}}{k_{CT}N_{CT}}\exp\left(-\frac{E_{S_1}-E_{CT}}{k_B T}\right).$$

Then,

$$qV_{OC} = E_{CT} + k_B T \ln\left(\frac{J_{SC}}{qd(1+\frac{R_{S_1}}{R_{CT}})k_{CT}N_{CT}}\right).$$

In our PM6:Y6 sample, $R_{S_1}/R_{CT} < 0.01$, meaning that the exciton recombination properties (related to the population and decay rate of the singlet excitons are of no importance for the V_{OC} of this blend. It is only for the case that singlet recombination dominates ($k_{S_1}N_{S_1}\exp\left(-\frac{E_{S_1}-E_{CT}}{k_B T}\right) > k_{CT}N_{CT}$) that

$$qV_{OC} = E_{S_1} + k_B T ln\left(\frac{J_{SC}}{qdk_{S_1}N_{S_1}}\right)$$

Table A4.2: Voltage losses for the different configurations considered in Chapter 7 with PM6:Y6 as the active layer

Device	d [nm]	V_{OC} [V]	E_g^{opt}/q	V_{OC}^{SQ}	$E_g^{opt}/q - V_{OC}^{SQ}$	$V_{OC,rad}$	$V_{OC}^{SQ} - V_{OC,rad}$	$V_{OC,rad} - V_{OC}$	$\Delta V_{OC,nrad}$ (ELQY)
Regular	100	0.84	1.38	1.119	0.261	1.081	0.038	0.241	0.273
Regular	145	0.834	1.38	1.119	0.261	1.082	0.037	0.248	0.26
Semi-transparent	135	0.828	1.38	1.119	0.261	1.075	0.044	0.247	0.275
Inverted	110	0.825	1.41	1.147	0.263	1.098	0.049	0.273	0.292

Table A4.3: Important parameters measured and calculated for the different configurations considered in in Chapter 7 with PM6:Y6 as the active layer (same as in the previous Table A4.2. The emission currents and chemical potentials are calculated as described above in Note A4.2.

Device	J_{SC} [A cm^{-2}]	$J_{0,rad}$ [A cm^{-2}]	ELQY	$\phi_{S_1}^0$ [cm^{-2}s^{-1}]	ϕ_{S_1} [cm^{-2}s^{-1}]	μ_{S_1} [eV]	E_{S_1} [eV]	n_{S_1} [cm^{-2}s^{-1}]	$E_{S_1} - E_{CS}$ [eV]
Regular	0.026	2.0x10^{-20}	2.7x10^{-5}	0.11	3.9x10^{12}	0.809	1.43	9.6x10^{9}	0.113±0.01
Regular*	0.025	1.9x10^{-20}	4.4x10^{-5}	0.11	6.2x10^{12}	0.821	1.43	15x10^{9}	0.119±0.01
Semi-transparent	0.0232	2.3x10^{-20}	2.5x10^{-5}	0.14	3.3x10^{12}	0.798	1.43	6.3x10^{9}	0.125±0.01
Inverted	0.234	0.9x10^{-20}	1.3x10^{-5}	0.06	1.7x10^{12}	0.804	1.435	6.5x10^{9}	0.133±0.01

* for this device, the photovoltaic external quantum efficiency was measured with the highly sensitive EQE_{PV} setup in Swansea University, with the EQE_{PV} spectrum plotted in Figure 7.2d of the main document. For all other samples, the EQE_{PV} spectrum was measured with setup in Potsdam.

A5. Supporting Material to Chapter 8

Note A5.1: Supplementary methods

Device preparation

The devices with a regular configuration were fabricated with a structure ITO/PEDOT:PSS/active layer/PDINO/Ag. Patterned ITO (Lumtec) substrates were cleaned in an ultrasonic bath with acetone, Hellmanex, deionized water and isopropanol for 10 min, followed by microwave plasma treatment (4 min at 200 W). Subsequently, PEDOT:PSS (Clevios AI 4083) was filtered through a 0.2 µm PA filter and spin coated onto ITO at 5000 rpm under ambient conditions to obtain a ~30 nm layer. Th PEDOT:PSS coated substrates were thermally annealed at 150°C for 10 min. PM6 and Y6 were dissolved in $CHCl_3$ to a total concentration of 16 mgmL^{-1} with a 1 to 1.2 weight ratio, and 0.5% CN (v/v, CN/ $CHCl_3$) for the devices with additive. In case of PM6 and N4, the materials were dissolved in $CHCl_3$ to a total concentration of 16 mgmL^{-1} with a 1 to 1.25 weight ratio and 0.5% CN (v/v, CN/ $CHCl_3$) as additive. The solutions were stirred for 3 hours inside the glovebox. Then, blends were spin coated (at 2500 rpm for PM6:Y6 and 2000 rpm for PM6:N4) onto the PEDOT:PSS layer to obtain a photoactive layer of thickness of ca. 110 nm, and annealed at 90°C for 5 min. To complete the devices, a very thin layer (~10 nm) of PDINO (1-Material Inc.) was spin coated onto the active layer, from a 1 mgmL^{-1} solution in methanol (2000 rpm), and 100 nm of Ag as the top electrode were evaporated under a 10^{-6}-10^{-7} mbar vacuum. For devices with semi-transparent cathode, only 45 nm of Ag were evaporated at this stage. The active area of the cells is A = 1.1 mm^2 for BACE measurement and A = 6 mm^2 for all other measurements.

For photoluminescence measurements of films, solutions of PS:NFA and PM6:NFA were spin coated on glass directly. PM6:NFA solutions were prepared as explained above. NFA and PS (Sigma Aldrich, 35 kDa) were dissolved on CF as well. The weight ratio 1 to 1.2 for the PS:Y6 blend and the ratio 1 to 1.25 for the PS:N4 were maintained.

Temperature-dependent measurements

For PIA, SCLC and V_{OC} measurements at different temperatures, the devices were loaded into a liquid nitrogen-cooled cryostat (Janis) and the temperature was adjusted in a range of 80 K to 300 K using a temperature controller (Lakeshore 335). *J-V* data were measured using a Keithley 2400 Source Meter in a two-wire configuration. Photoluminescence and electroluminescence were measured as in Chapter 7. For BACE measurements as a function of temperature, the device was placed on the cooling finger of a closed cycle helium cryostat (ARS-CS202-X1.AL). The cryostat was heated and evacuated to ~1x10^{-4} mbar (Pfeiffer TCP121 Turbo pump and Edwards XDS-10 scroll pump). Electrical connection was done through a home-built amplifier which was directly attached as close as possible to the sample outside the cryostat.

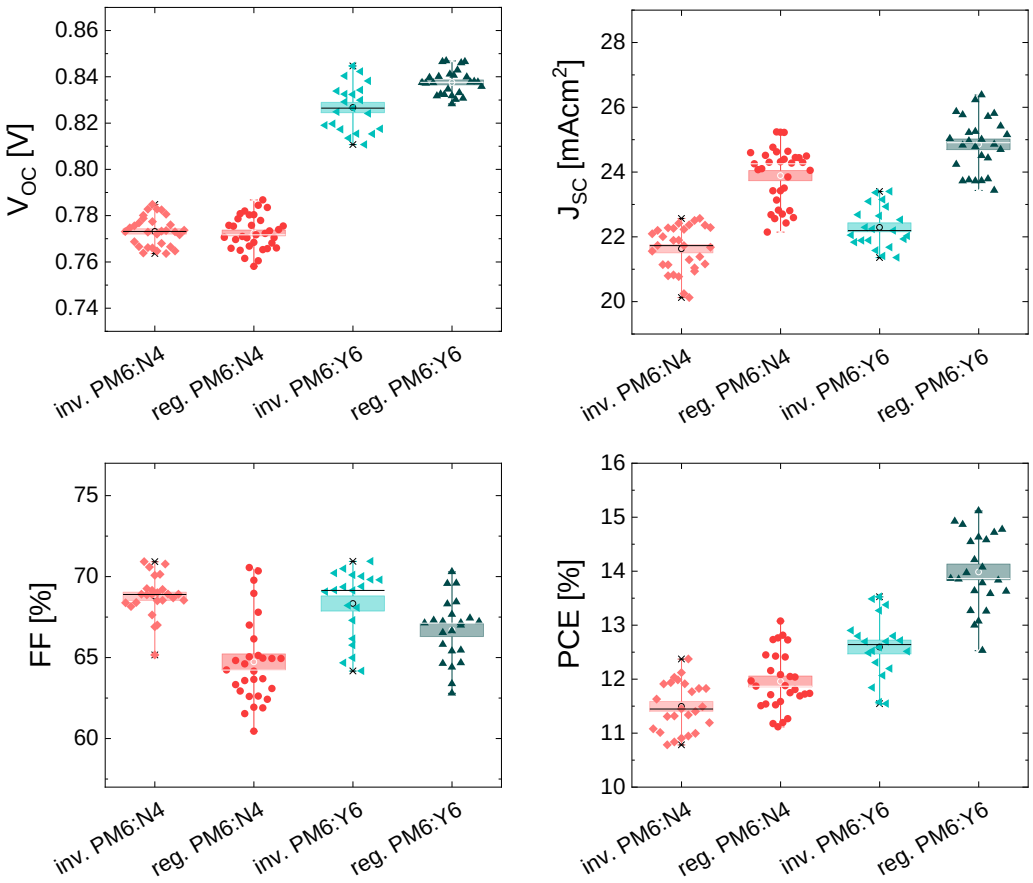

Figure A5.1: Photovoltaic performance parameters and cell statistics of PM6:Y6 and PM6:N4 in regular and inverted device architecture with fully reflecting electrode (100 nm Ag).

Table A5.1: Average photovoltaic parameters and standard deviations for PM6:Y6 (1:1.2 w/w CF, additive CN 0.5% v/v, 90°C for 5 min) and PM6:N4 (1:1.25 w/w CF, additive CN 0.5% v/v, 90°C for 5 min) devices with structure ITO/PEDOT:PSS/PM6:NFA/PDINO/Ag(fully reflecting 100nm). Active layer thickness is ca. 110 nm and A=6 mm^2.

Blend	V_{OC} [V]	J_{SC} [mA cm^{-2}]	FF [%]	PCE [%]
PM6:Y6	0.838 ±0.005	24.9 ±0.8	66.8 ±1.9	14.0 ±0.7
PM6:N4	0.773 ±0.007	23.9 ±0.9	64.7 ±2.6	12.0 ±0.5

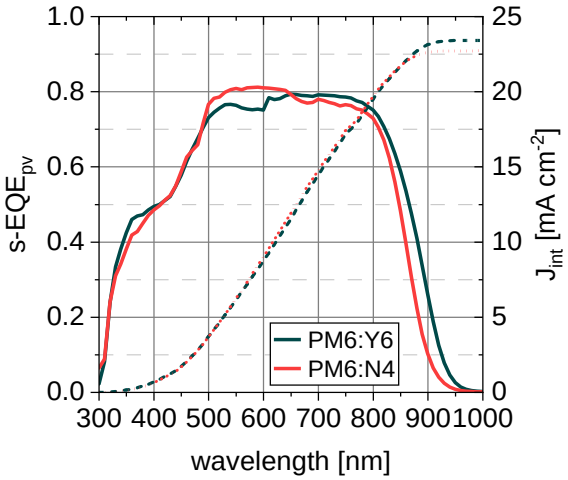

Figure A5.2: Linear photovoltaic external quantum efficiency ($\mathrm{EQE_{PV}}$), left axis, and the integrated J_{SC}, right axis. The J_{int} for PM6:Y6 is 23.4 mAcm^{-2}, and for PM6:N4 22.7 mAcm^{-2}. The lower integrated values in comparison to those in Table A5.1 might be due to slight degradation of the samples sent to for sensitive measurements to Swansea.

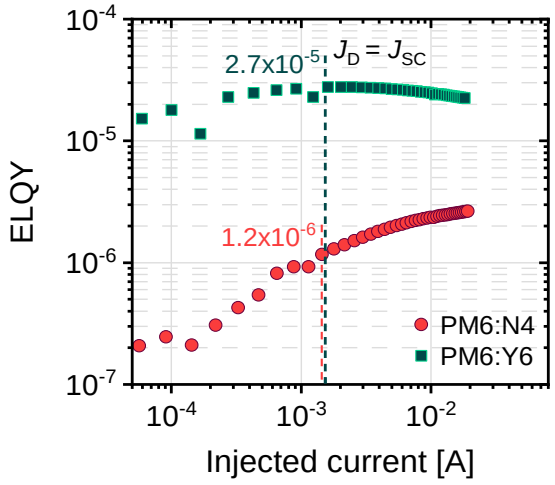

Figure A5.3: Electroluminescence quantum efficiency (ELQY) as a function of injected current for PM6:Y6 and PM6:N4 regular devices.

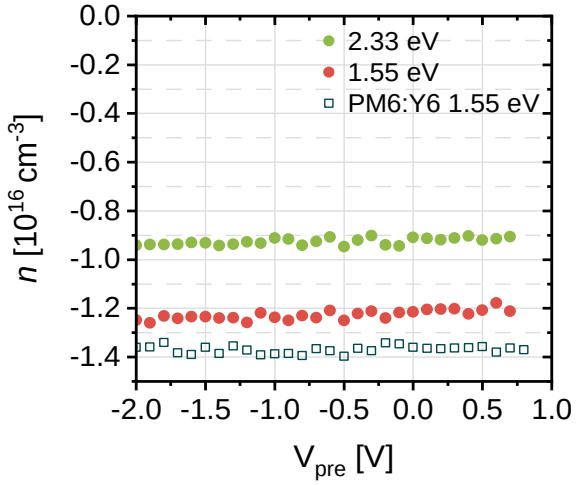

Figure A5.4: Bias-dependent free charge generation for PM6:N4 measured by TDCF for an excitation of 2.33 eV and 1.55 eV with a low fluence of 0.05 µJcm^{-2} and V_{coll} =-2.5 V. For comparison, the equivalent measurement of PM6:Y6 at 1.55 eV is shown.

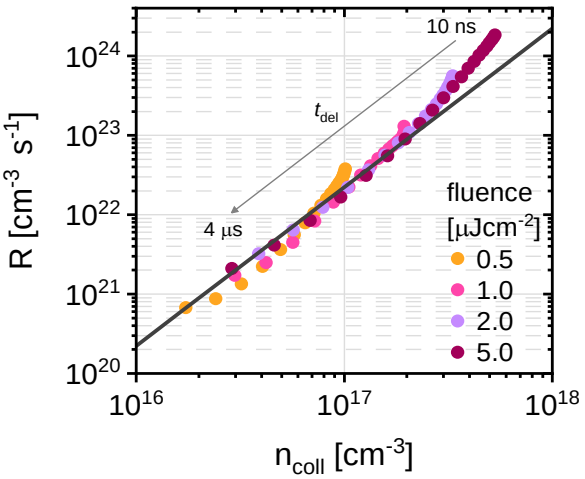

Figure A5.5: Recombination rate R as a function of the remaining charge in the device (n_{coll}) after a given certain delay time (t_{del}) for a PM6:N4 device by TDCF, for an excitation of 2.0 eV and V_{pre} =0.6 V, V_{coll} =-2.5 V. The dark line is a fit to $R = k_2 n^2$, with $k_2 = 2.2 \times 10^{-12}$ cm^{3}s^{-1}.

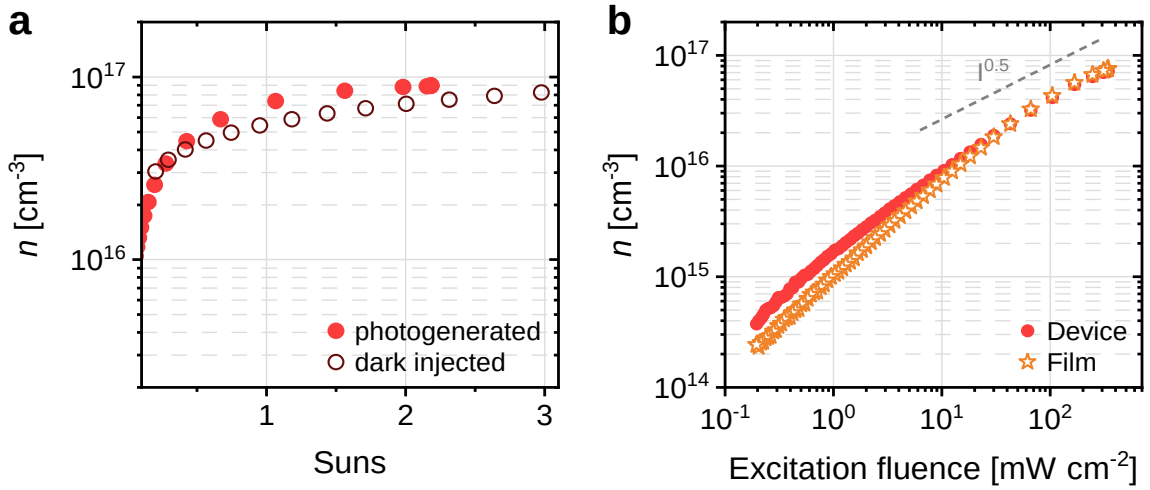

Figure A5.6: a Charge carrier density obtained from excitation-intensity-dependent photoinduced absorption (PIA) spectroscopy (photogenerated, full dots) and electromodulation injection absorption (EMIA) measurements (dark injected charges, open dots) measured for a PM6:N4 regular device with a semi-transparent cathode, both at a photon energy of 1.25 eV. The difference in the carrier concentration under photoexcitation and under dark injection is very little, causing only ~15 meV difference in QFLS at 1 sun. **b** Excitation-intensity-dependent photoinduced absorption (PIA) signals measured for a PM6:N4 regular device and on a PM6:N4 film on glass. The PIA data of the film is calibrated with a factor due to the back reflection from the Ag electrode. The calibration factor is evaluated by measuring the PIA signals with and without the Ag electrode. At 1 sun, we observe bimolecular recombination for both data sets and the agreement in carrier concentration points to small losses of carriers at the transport layer interfaces in the full device.

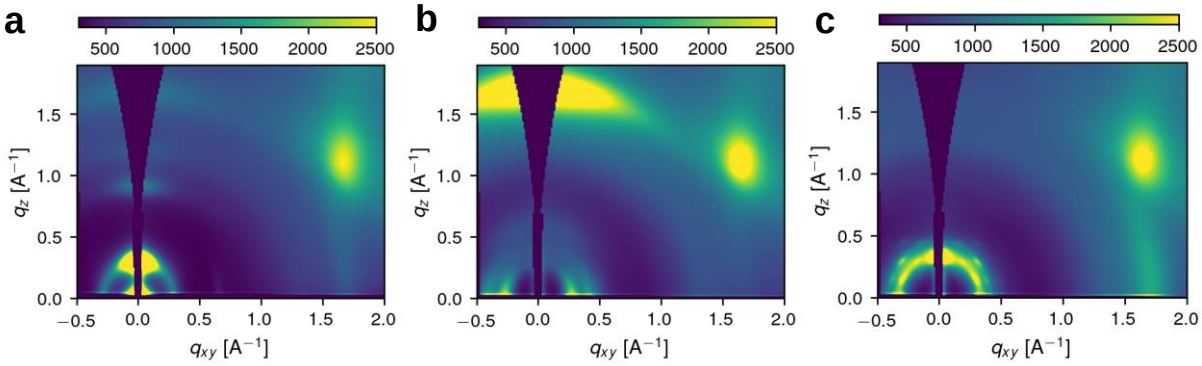

Figure A5.7: 2D-GIWAXS images of **a** neat PM6, **b** neat Y6 and **c** neat N4, measured on Si substrates (the strong diffraction signal at about q_{xy} =1.7 Å^{-1}, q_z =1.2 Å^{-1} is due to substrate scattering).

Note A5.2: GIWAXS measurements and Pseudo-Voigt fits

Grazing-incidence wide-angle X-ray scattering (2D GIWAXS) measurements were performed in vacuum at the Soft Matter Interfaces beamline (12-ID) at the National Synchrotron Lightsource II (NSLS-II) at Brookhaven National Laboratory at an energy of 16.1 keV and an angle of incidence of 0.18° (clearly above the critical angle for all materials to probe the bulk). The FWHM of the beam profile was 25 µm vertically and 250 µm horizontally. A Pilatus300KW detector with a sample to detector distance of 275 mm was used at different rotational angles to cover a larger q-range. The single pictures were merged and converted into a linear q scale. The samples were prepared on PEDOT:PSS coated Si substrates. Neat films were spin-coated from CF and blends from CN/CF (0.5%v/v), to a thickness of ca. 100 nm. All measurements are averages over 6 positions on the sample each measured for 20 s to reduce effects due to inhomogeneities. Changes in intensity profiles with time were tested for all samples and no beam damage was determined for 20 s of exposure. The presented q-profiles in the vertical and horizontal direction are cake cuts covering a range of 20° being background corrected by the corresponding rescaled cuts of PEDOT:PSS on Si.

All performed fits are Pseudo-Voigt fits, described by the following expression for a single peak:

$$f(q) = A[\eta L(q) + (1-\eta)G(q)] \; with \; 0 < \eta < 1$$

$$G(q) = \exp\left[-\ln(2)\left(\frac{q-c}{b}\right)^2\right], \qquad L(q) = \frac{1}{1+\left(\frac{q-c}{b}\right)^2},$$

where A is the peak amplitude, c is the peak position, $2b$ is the full width at half maximum of the Pseudo-Voigt peak and η the Pseudo-Voigt mixing parameter. When several peaks were overlapping the sum of several Pseudo-Voigt peaks was fitted. Moreover, an additional constant background was fitted.

The Pseudo-Voigt mixing parameter η describes the contribution of cumulative disorder (described by a Lorentzian) while the other contribution is due to non-cumulative disorder (described by a Gaussian).[324] When cumulative as well as non-cumulative contribute, the peak shape is described by a Voigt profile (convolution of Gaussian and Lorentzian), which can be approximated by a Pseudo-Voigt profile.[323, 324] For η close to 0, non-cumulative disorder is dominating and a coherence length can be calculated with the Scherrer equation:

$$L_c = \frac{2\pi \mathrm{K}}{\Delta q} = \frac{2\pi \mathrm{K}}{2b}$$

Where Δq is the full width at half maximum and $\mathrm{K} = 0.94$ was chosen as shape factor. For higher η (especially the case for $\pi - \pi$ peaks) the peak width is strongly influenced by cumulative disorder leading to significant deviation of the calculated coherence length.[323, 324]

In Figure A5.8 below, the peak areas of the $\pi - \pi$ peak and the amorphous contribution are calculated by integrating the Pseudo-Voigt function obtained by fitting the contributions (fit curves also displayed in Figure A5.8). Then the ratios between the peak areas of the $\pi - \pi$ peak and the amorphous contribution are calculated.

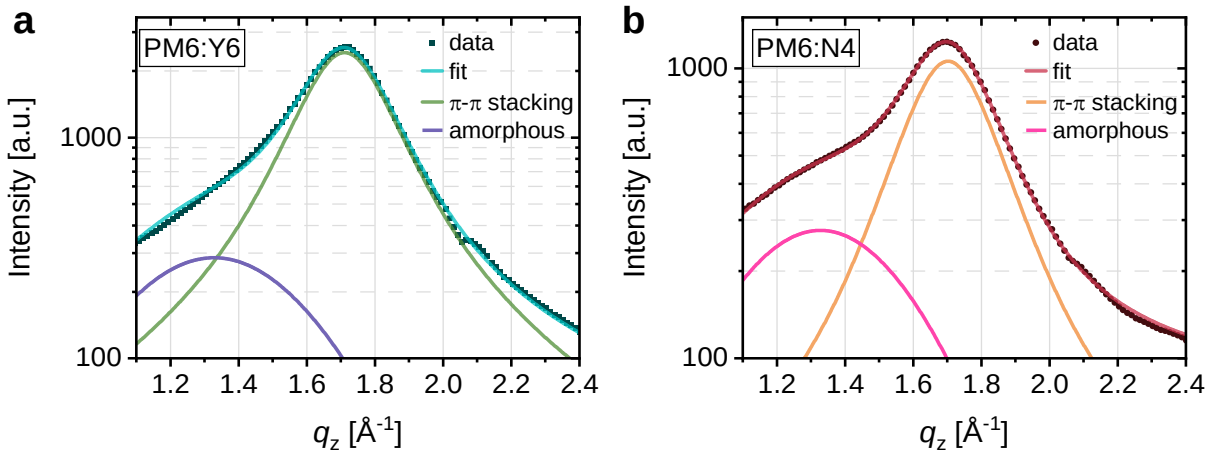

Figure A5.8: Pseudo-Voigt fits to the normalized vertical $\pi - \pi$ stacking peak and the disordered contribution of **a** PM6:Y6 and **b** PM6:N4. The ratio in the vertical direction between the area of the $\pi - \pi$ peak and the amorphous contribution is approximately 2.5 for PM6:N4 and 5.4 for PM6:Y6.

Note A5.3: Fitting the time-resolved photoluminescence (TRPL) kinetics

Time-resolved photoluminescence (TRPL) measurements were performed by Jafar I. Khan in the Kaust Solar Center (KSC) of the King Abdullah University of Science and Technology. The experiments were carried out using the output of a Chameleon (Coherent AG) fs laser operating at 80 MHz repetition rate. During measurements, thin films were kept in a small nitrogen-filled chamber, and the excitation laser fluence was kept around 500 nJcm^{-2} at 710 nm wavelength. The PL of the samples was collected by an optical telescope (consisting of two plano-convex lenses) and focused onto the slit of a grating spectrograph (PI Spectra Pro SP2300) and detected with a Streak Camera (Hamamatsu C10910) system with a temporal resolution of about 15 ps. The data was acquired in the photon counting mode using the Streak Camera software (HPDTA) and exported to Origin Pro 2020 for further analysis.

To calculate exciton quenching, PL lifetimes of the PM6:NFA blends are parametrized by fitting the experimental data with exponential decay curves. The TRPL of the two PS:NFA can be described by a monoexponential decay, representing the intrinsic lifetime of the exciton. In contrast, the blend TRPL consists of a fast decay, assigned to the quenching of the NFA exciton due to charge transfer at the D:A interface as well as a slow component. The latter may be due to the reformation of NFA excitons from the CT state but also due to the decay of excitons formed within large acceptors clusters which exhibit a longer lifetime. We have shown recently that the steady state PL of the PM6:Y6 blend is governed by such remaining non-dissociated excitons (see Chapter 7). To take this into account, the PL decay properties of the blends were described by a weighted-average lifetime:[66]

$$t_{\mathrm{avg,wt}} = \frac{A_1 t_1 + A_2 t_2}{A_1 + A_2}$$

where A is the signal amplitude and t is the decay. The PL quenching efficiency is then calculated by: $1 - (t_{\mathrm{avg,blend}},/t_{1,\mathrm{neat}})$.

Table A5.2: Parameters obtained by fitting the time-resolved PL data. A is the signal amplitude and t is the decay. The weighted-average lifetime $t_{\mathrm{avg,wt}}$ is calculated as shown in Note A5.2 above.

Blend	A_1	A_2	t_1[ps]	t_2[ps]	$t_{\mathrm{avg,wt}}$[ps]
PS:Y6	0.98	-	723	-	723
PM6:Y6	0.78	0.15	47	304	88
PS:N4	0.98	-	800	-	800
PM6:N4	0.75	0.20	35	152	60

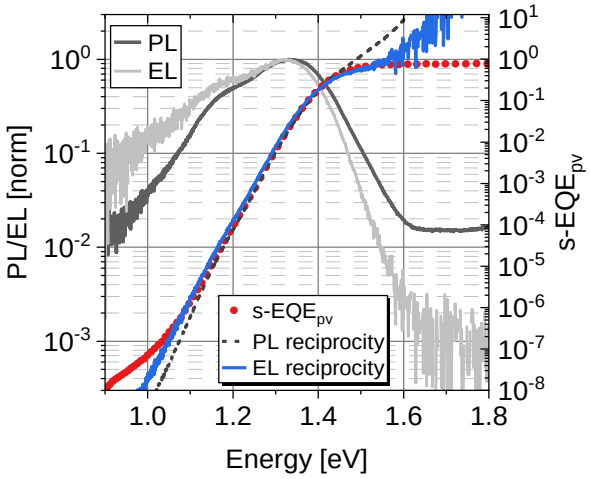

Figure A5.9: Normalized PL and EL spectra of a regular PM6:N4 device (gray lines, left axis), and sensitive photovoltaic external quantum efficiency (s-$\mathrm{EQE_{PV}}$) of the same PM6:N4 device (dots, right axis). The absorption spectra calculated via the reciprocity relation from the depicted PL and EL are given in dotted black and red lines, respectively.

Note A5.4: Space charge limited current (SCLC)

In the SCLC regime, the current density J depends quadratically on the voltage V, following the Mott-Gurney law:

$$J = \frac{9}{8}\varepsilon_0\varepsilon_r\mu\frac{V^2}{d^3},$$

where μ is the charge carrier mobility and d is the film thickness. ε_0 and ε_r are the vacuum and relative dielectric constants, respectively. In most cases, the slope of the J-V curve on a double log-scale is larger than 2, due to disorder, traps or field-dependent mobilities.[102, 203, 331] To account for the observed field enhancement, Murgatroyd and Gill (MG) extended the above equation, as:[329]

$$J = \frac{9}{8}\varepsilon_0\varepsilon_r\mu_0\frac{V^2}{d^3}\exp\left(0.891\gamma\sqrt{\frac{V}{d}}\right)$$

with μ_0 being the zero-field mobility and γ, the field enhancement factor. Assuming a Gaussian DOS, the Gaussian disorder model (GDM) can be used to describe the zero-field mobility dependence on temperature T by[102]

$$\mu_0(T) = \mu_\infty \exp\left[\left(\frac{2}{3}\frac{\sigma}{k_B T}\right)^2\right]$$

where μ_∞ is the mobility at infinite temperature and σ is the static Gaussian disorder. k_B is the Boltzmann constant.

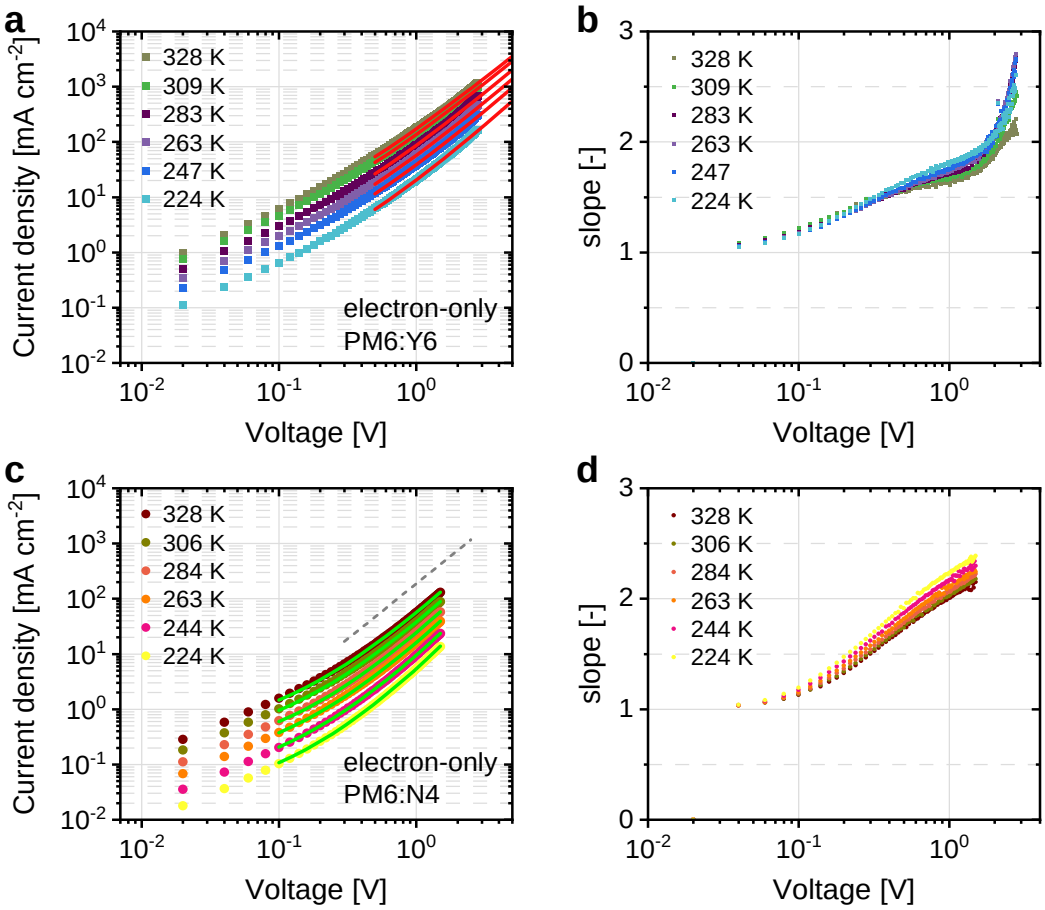

Figure A5.10: *J-V* characteristics of electron-only devices (ITO/ZnO/PM6:NFA/PDINO/Ag). **a** PM6:Y6, 150 nm layer (squares) and **c** PM6:N4, 150 nm layer (dots), and the corresponding $\text{slope} = \mathrm{d}(\log J)/\mathrm{d}(\log V)$ vs voltage of **b** PM6:Y6 and **d** PM6:N4. The solid lines in panels a and c are the SCLC fittings with the Murgatroyd and Gill equation.

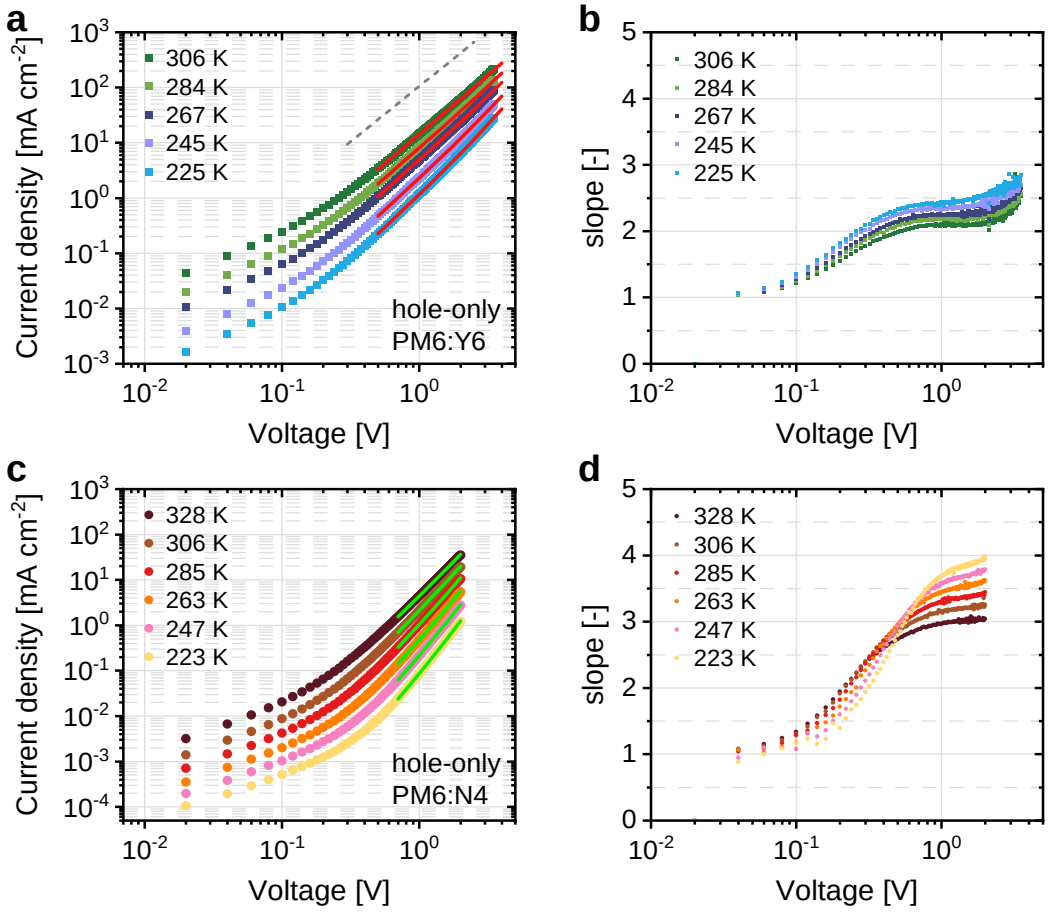

Figure A5.11: *J-V* characteristics of hole-only devices (ITO/MoO_3/PM6:NFA/ MoO_3/Ag). **a** PM6:Y6, 170 nm layer (squares) and **c** PM6:N4, 240 nm layer (dots), and the corresponding $\text{slope} = \mathrm{d}(\log J)/\mathrm{d}(\log V)$ vs voltage of **b** PM6:Y6 and **d** PM6:N4. The solid lines in panel a and c are the SCLC fittings with the Murgatroyd and Gill equation.

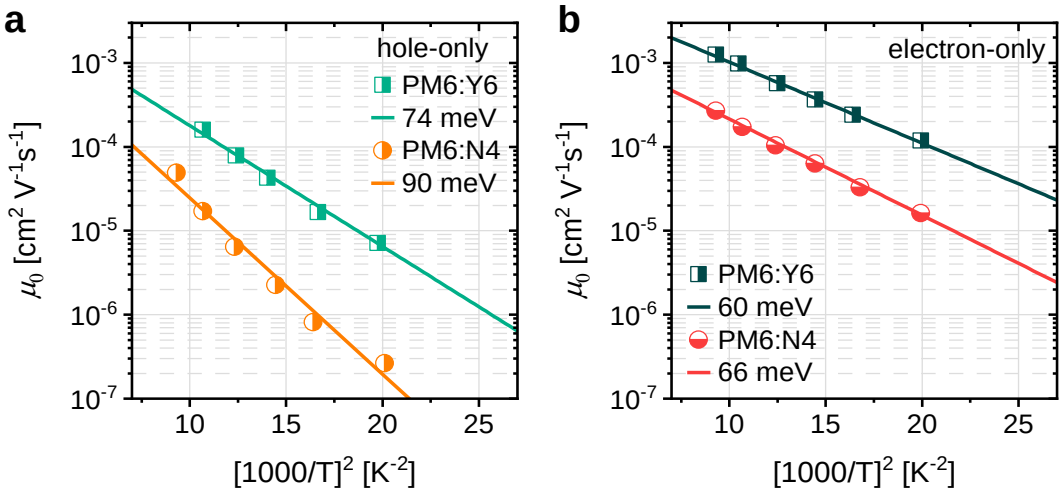

Figure A5.12: Zero-field charge carrier mobility μ_0 of a holes and b electrons in the blends PM6:Y6 and PM6:N4. The energetic disorder is calculated from the slope, following the GDM (see Note A5.4).

Note A5.5: Fits to space charge limited current (SCLC) for an exponential trap distribution

Mark and Helfrich[116] showed that under the assumption of an exponential trap distribution with a characteristic distribution temperature T_0, the SCLC current density measured in only-devices follows the equation

$$J = qN_0\mu\left(\frac{l}{l+1}\frac{\varepsilon_0\varepsilon_r}{qN_t}\right)^l\left(\frac{2l+1}{l+1}\right)^{l+1}\frac{U^{l+1}}{d^{2l+1}},$$

where q is the elementary charge, N_0 the effective density of states, N_t the total trap density and μ the trap-free charge mobility. Here, l is defined as $l = T_0/T$. N_t can be determined from the crossing point the J-V curves at all temperatures,[334] which is denoted as V_c and calculated as follows

$$V_c = \frac{qN_t d^2}{2\varepsilon_0\varepsilon_r}.$$

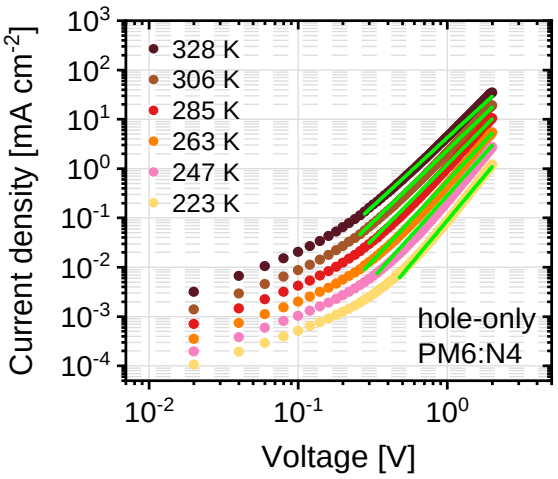

Figure A5.13: J-V characteristics of a PM6:N4 hole-only device (ITO/MoO_3/PM6:NFA/ MoO_3/Ag), same as in Figure A5.11c. The solid lines are fits using the Mark and Helfrich expression (see Note A5.5). The fitting parameters are N_0 = 2.4x10^{20} cm^{-3}, N_t = 5.5x10^{17} cm^{-3}, μ = 1.7x10^{-5} cm^{2}V^{-1}s^{-1} and T_0= 585 K.

Note A5.6: Open-circuit voltage (V_{OC}) for a Gaussian or an exponential DOS

The relation between the (quasi-) Fermi level position and the density of equilibrated charges in a Gaussian DOS is generally described by the Gauss-Fermi integral for which an analytical solution is not available. However, analytical approximations exist for different regimes, as discussed in detail in the paper by G. Paasch and S. Scheinert.[142] The case of high temperatures and low enough carrier densities can be described by the non-degenerate case. Here, carriers are situated at around the equilibrium energy, which is $E_{\infty,e} = E_{\mathrm{L},A} - \frac{\sigma_{L,A}^2}{k_B T}$ for electrons in the acceptor LUMO and $E_{\infty,h} = E_{\mathrm{H},D} + \frac{\sigma_{H,D}^2}{k_B T}$) for holes in the donor HOMO, respectively, as discussed in section 2.4.3. Also, the (quasi-) Fermi level for electrons (holes) is well below (above) the main carrier energy: $E_{\mathrm{F},e} < E_{\infty,e}$ and $E_{\mathrm{F},h} > E_{\infty,h}$. In this case, the Fermi-Dirac distribution can be approximated by the Boltzmann distribution and Equation 2.23 in section 2.5. of the fundamentals is valid for high enough temperatures. The transition to the degenerate case occurs when the (quasi-)Fermi levels cross the equilibrium energy. This is the case for low temperatures and/or high carrier densities.

As a consequence, the mean carrier energy will be no more the equilibrium energy but it will be rather determined by the positions of the quasi-Fermi levels. In the extreme case, $T = 0K$, the Fermi–Dirac distribution becomes a Heaviside step at the Fermi energy, which now must be situated deep in the DOS for a non-zero carrier density. Then, $E_{\mathrm{F},e} = E_{\mathrm{L,A}} - \sqrt{2}\sigma_{L,A}\,\mathrm{erfc}^{-1}\left(2\frac{n}{N_0}\right)$ and $E_{\mathrm{F},h} = E_{\mathrm{H,D}} + \sqrt{2}\sigma_{H,D}\,\mathrm{erfc}^{-1}\left(2\frac{p}{N_0}\right)$, with no dependence on temperature.

For $T > 0$. Paasch and Scheinert derived the following approximation for the degenerate regime:

$$E_{\mathrm{F},e} = E_{\mathrm{L,A}} - \frac{\sqrt{2}\sigma_{\mathrm{L,A}}}{H_{\mathrm{L,A}}}\,\mathrm{erfc}^{-1}\left(2\frac{n}{N_0}\right),$$

$$E_{\mathrm{F},h} = E_{\mathrm{H,D}} + \frac{\sqrt{2}\sigma_{\mathrm{H,D}}}{H_{\mathrm{H,D}}}\,\mathrm{erfc}^{-1}\left(2\frac{p}{N_0}\right).$$

The functions $H_{\mathrm{L,A}}$ and $H_{\mathrm{H,D}}$ for the acceptor and the donor are defined as

$$H_{\mathrm{L,A}} = \frac{\sqrt{2}}{\sigma_{\mathrm{L,A}}}k_{\mathrm{B}}T\,\mathrm{erfc}^{-1}\left[\exp\left(-\frac{1}{2}\left(\frac{\sigma_{\mathrm{L,A}}}{k_{\mathrm{B}}T}\right)^2\right)\right],$$

$$H_{\mathrm{H,D}} = \frac{\sqrt{2}}{\sigma_{H,D}}k_{\mathrm{B}}T\,\mathrm{erfc}^{-1}\left[\exp\left(-\frac{1}{2}\left(\frac{\sigma_{\mathrm{H,D}}}{k_{\mathrm{B}}T}\right)^2\right)\right].$$

Then, under the assumption that the electron and hole densities are equal ($n = p$) under illumination at open-circuit conditions, the V_{OC} can be approximated analytically as

$$qV_{\mathrm{OC}} = E_{\mathrm{F},e} - E_{\mathrm{F},h} = E_{\mathrm{g}} - \frac{\sqrt{2}\sigma_{\mathrm{L,A}}}{H_{\mathrm{L,A}}}\,\mathrm{erfc}^{-1}\left(2\frac{n}{N_0}\right) - \frac{\sqrt{2}\sigma_{H,D}}{H_{\mathrm{H,D}}}\,\mathrm{erfc}^{-1}\left(2\frac{n}{N_0}\right). \qquad (\mathrm{A5.1})$$

As pointed out above, the transition between the high temperature non-degenerate case (Equation 2.23) and low temperature approximation (Equation A5.1) occurs when the quasi-Fermi levels cross the equilibrium energy: $E_{\mathrm{F},e} = E_{\infty,e}$ and $E_{\mathrm{F},h} = E_{\infty,h}$. If $n = p$ and the acceptor LUMO has a similar width as the donor HOMO, this transition will occur at the same temperature and carrier density for both electrons and holes. Then, Equation 2.23 will be valid for $qV_{\mathrm{OC}} = E_{\mathrm{F},e} - E_{\mathrm{F},h} < E_{\infty,e} - E_{\infty,h}$ while Equation A5.1 must be applied if $qV_{\mathrm{OC}} = E_{\mathrm{F},e} - E_{\mathrm{F},h} > E_{\infty,e} - E_{\infty,h}$. In Figure A5.14 below, we have plotted $E_{\infty,e} - E_{\infty,h}$ and qV_{OC} as function of temperature for the parameters derived for the PM6:Y6 blend and simulated for 1 sun conditions. Because of the term $-\frac{\sigma^2}{2k_{\mathrm{B}}T}$, $E_{\infty,e} - E_{\infty,h}$ decreases strongly with decreasing temperature while $qV_{\mathrm{OC}} = E_{\mathrm{F},e} - E_{\mathrm{F},h}$ increases, also because of the increasing carrier density. The crossing point is around 200 K, moving to higher temperatures for a higher carrier density or a broader DOS.[142] Therefore, above 200 K, Equation 2.23 is suited to describe the temperature dependence of the V_{OC} but not below. We note here that Equation 2.23 is no more a good approximation of $V_{\mathrm{OC}}(T)$ very close to the transition point, where the Boltzmann-distribution is not valid anymore. In Ref.[142], Paasch and Scheinert have provided an analytical approximation for the non-degenerate regime, which relates the carrier density to the position of the Fermi-level and temperature. Unfortunately, this relation cannot be inversed to provide the QFLS as a function of n and T.

In the non-degenerate regime, carriers are located at $E_{\infty,e}$ and $E_{\infty,h}$, meaning that $E_{\infty,e} - E_{\infty,h}$ is the energy of the equilibrated electron-hole pair i.e., the energy of the charge separate state, E_{CS}. To provide an upper limit for E_{CS} in the degenerate regime, we have taken the carrier density at a given temperature, and calculated the QFLS for the given density in the approximation of a step-

wise state occupation ($T = 0K$), yielding $\left(E_{\mathrm{F},e} - E_{\mathrm{F},h}\right)_n$. As expected, qV_{OC} approximates $\left(E_{\mathrm{F},e} - E_{\mathrm{F},h}\right)_n$ for low temperatures in Figure A5.14, while the increase of $\left(E_{\mathrm{F},e} - E_{\mathrm{F},h}\right)_n$ with decreasing temperature mirrors the dependence of the carrier density on temperature.

In case of an exponential distribution, which has a shallower tail, the Fermi level will always dig into the DOS, the mean carrier energy is located close to the quasi-Fermi level and, for a given carrier density, is independent of temperature.[116] Then, for the case that electrons in a Gaussian DOS recombine with holes in an exponential DOS, only $E_{\mathrm{F},e}(n)$ is explicitly temperature dependent, which for the transition region yields:

$$qV_{\mathrm{OC}} = E_{\mathrm{F},e} - E_{\mathrm{F},h} = E_{\mathrm{g}} - \frac{\sqrt{2}\sigma_{\mathrm{L,A}}}{H_{\mathrm{L,A}}}\,\mathrm{erfc}^{-1}\left(2\frac{n}{N_0}\right) + k_B T_0\, ln\frac{n}{N_0}. \qquad (\text{A5.2})$$

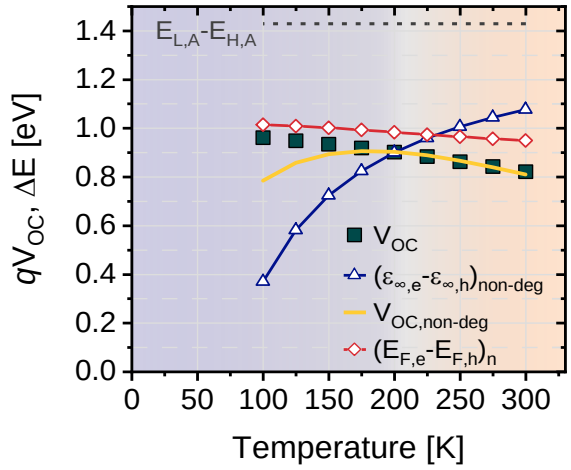

Figure A5.14: Temperature dependence of the relevant properties for the PM6:Y6 blend describing the transition between the non-degenerate and degenerate regime. $E_{\infty,e} - E_{\infty,h}$ is the energy difference between the equilibrium energy of the acceptor LUMO and donor HOMO, representing the energy of the charge-separated (CS) state. The transition to the degenerate regime occurs when this energy crosses the experimental qV_{OC}, representing the $\mathrm{QFLS} = E_{\mathrm{F},e} - E_{\mathrm{F},h}$. As expected, the non-degenerate model, Equation 2.23, fails to explain the experimental qV_{OC} below the transition temperature. Also shown is $\left(E_{\mathrm{F},e} - E_{\mathrm{F},h}\right)_n$, which for the given temperature dependence of the carrier density is the Fermi level for a hypothetical step-wise distribution function and serves as an upper limit of the CS energy in the degenerate regime (see above Note A5.6).

Table A5.3: Measured and fitted parameters used to predict the open-circuit voltage as a function of temperature data shown in Figure 8.5a. G-G stand for Gauss-Gauss model and G-Exp for exponential-Gauss. For each model the parameters are divided into the non-degenerate ($\mathrm{non}-\mathrm{deg}$) and degenerate ($\mathrm{deg}$) regimes. In all calculations, N_0 was set to the number density of Y6/N4 molecules in the blend (N_{Y6} = 2.4x10^{20} cm^{-3}).

PM6:Y6				PM6:N4				
Model	**E_g[eV]**[a)]	**$\sigma_{L,A}$[meV]**[b)]	**$\sigma_{H,D}$[meV]**[b)]	**Model**	**E_g[eV]**[a)]	**$\sigma_{L,A}$[meV]**[b)]	**$\sigma_{H,D}$[meV]**[b)]	**T_0[K]**[b)]
G-G non − deg	1.43	60	74	G-G non − deg	1.41	66	90	-
G-G deg	1.41	60	74	G-G deg	1.37	66	90	-
				G-exp non − deg	1.34	66	-	435
				G-exp deg	1.32	66	-	435

a) Fitted parameter;
b) Experimental data.

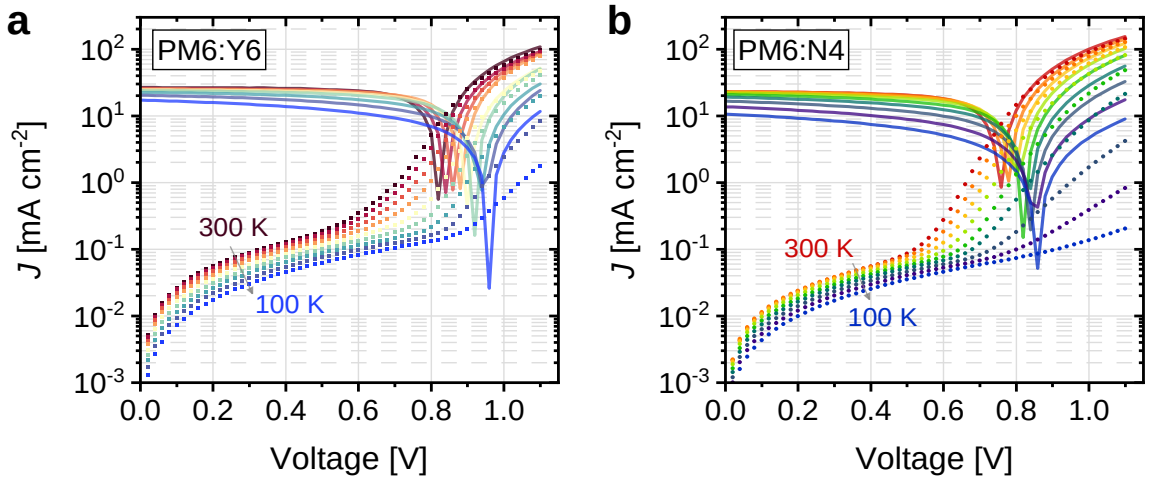

Figure A5.15: *J-V* characteristics measured at 1 sun equivalent (solid lines) with white light and in the dark (squares and dots) of **a** PM6:Y6 and **b** PM6:N4. The dark current decreases with temperature and is lower than the photocurrent at low temperatures, which shows that the V_{OC} is not limited by leakage current in this regime.

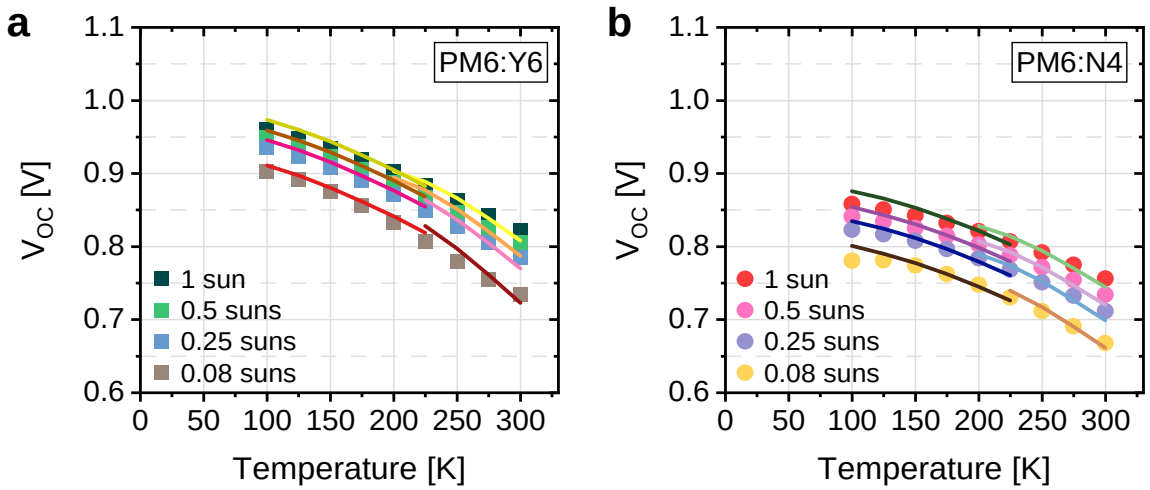

Figure A5.16: Open-circuit voltage V_{OC} as a function of illumination intensity and temperature for **a** PM6:Y6 and **b** PM6:N4 (full symbols). The experimental data were fitted at 1 sun according to the Gaussian-Gaussian model for PM6:Y6 and the Gaussian-exponential model for PM6:N4 using the expressions in the non-degenerate and degenerate regions, as shown in Figure 8.5 (see Note A5.6). To fit the lower intensities, the carrier density at 1 sun was simply reduced by the factor $F = \sqrt{\frac{I_{low}}{I_{1sun}}}$, which assumes bimolecular recombination over all temperatures.

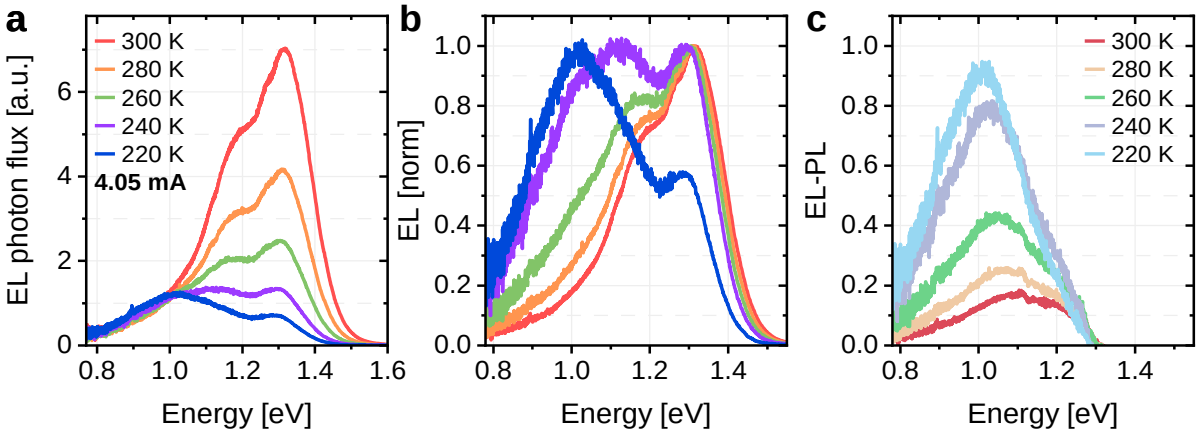

Figure A5.17: a Electroluminescence (EL) spectra as a function of temperature of a regular PM6:N4 device measured at a constant current of 4.05 mA. **b** Normalized EL spectra from panel a. **c** Resulting spectra after subtraction of the photoluminescence (PL) of the device from the normalized EL spectra in panel b. The subtraction reveals a broad emission with a maximum at 1.10 eV at 300 K.

List of Abbreviations and Symbols

Abbreviations

A	acceptor
BACE	bias-assisted charge extraction
BHJ	bulk heterojunction
BMR	bimolecular recombination
CN	chloronaphthalene
CS	charge-separated
CT	charge transfer
D	donor
DA	donor-acceptor
DOS	density of states
EA	electron affinity
EL	electroluminescence
ELQY	electroluminescence quantum yield
EMIA	electromodulation injection absorption
$\mathrm{EQE_{PV}}$	photovoltaic external quantum efficiency
ETL	electron transport layer
FF	fill factor
FREA	fused-ring electron acceptor
FTAZ	poly(benzodithiophene-alt-dithienyl difluorobenzotriazole)
GDM	Gaussian disorder model
GIWAXS	grazing-incidence wide-angle X-ray scattering
HOMO	highest occupied molecular orbital
HTL	hole transport layer
IDIC	2,2'-((2Z,2'Z)-((4,4,9,9-tetrahexyl-4,9-dihydro-s-indaceno[1,2-b:5,6-b']dithiophene-2,7-diyl)bis(methanylylidene))bis(3-oxo-2,3-dihydro-1H-indene-2,1-diylidene))dimalononitrile
IE	Ionization energy
IQE	internal quantum efficiency
ITIC	3,9-Bis(2-methylene-(3-(1,1-dicyanomethylene)-indanone))-5,5,11,11-tetrakis(4-hexylphenyl)-dithieno[2,3-d:2',3'-d']-s-indaceno[1,2-b:5,6-b']-dithiophene)
ITO	indium tin oxide
J-V	current density vs. voltage
LCAO	linear combination of atomic orbitals
LED	light emitting diode
LUMO	lowest unoccupied molecular orbital
MPP	maximum power point
NFA	non-fullerene acceptor

NGR	nongeminate recombination
NIR	near-infrared
OC	open circuit
OPV	organic photovoltaic
OSC	organic solar cell
P3HT	poly(3-hexylthiophene-2,5-diyl)
$PC_{70}BM$	[6,6]-Phenyl-C71-butyric acid methyl ester
PCE	power conversion efficiency
PDINO	N,N'-Bis(N,N-dimethylpropan-1-amine oxide)perylene-3,4,9,10-tetracarboxylic diimide
PEDOT:PSS	poly(3,4-ethylenedioxythiophene):poly(styrenesulfonate)
PIA	photoinduced absorption
PL	photoluminescence
PLQY	photoluminescence quantum yield
PM6	poly[(2,6-(4,8-bis(5-(2-ethylhexyl-3-fluoro)thiophen-2-yl)-benzo[1,2-b:4,5-b']dithiophene))-alt-(5,5-(1',3'-di-2-thienyl-5',7'-bis(2-ethylhexyl)benzo[1',2'-c:4',5'-c']dithiophene-4,8-dione)]
PTB7	poly[[4,8-bis[(2-ethylhexyl)oxy]benzo[1,2-b:4,5-b']dithiophene-2,6-diyl][3-fluoro-2-[(2-ethylhexyl)carbonyl]thieno[3,4-b]thiophenediyl]]
PV	photovoltaic
QFLS	quasi-Fermi level splitting
RPV	resistance dependent photovoltage
SC	short circuit
SCLC	space charge limited current
Si	silicon
SRH	Shockley-Read-Hall
TAS	transient absorption spectroscopy
TDCF	time-delayed collection field
TRPL	time-resolved photoluminescence
Y6	2,2'-((2Z,2'Z)-((12,13-bis(2-ethylhexyl)-3,9-diundecyl-12,13-dihydro-[1,2,5]thiadiazolo[3,4-e] thieno[2'',3'':4',5']thieno [2',3':4,5] pyrrolo[3,2-g]thieno[2',3':4,5]thieno[3,2-b]indole-2,10-diyl)bis(methanylylidene))bis(5,6-difluoro-3-oxo-2,3-dihydro-1H-indene-2,1-diylidene))dimalononitrile

Symbols

A	area
B	interfacial bias potential
c	velocity of light in vacuum
d	active layer thickness
D	diffusion constant
E_a	activation energy

$E_{\mathrm{b,CT}}$	Coulomb binding energy of the charge transfer state
$E_{\mathrm{b,S_1}}$	hole-electron binding energy of a Frenkel-type exciton
E_{CS}	energy of the charge-separated state
E_{CT}	energy of the charge transfer state
$E_{\mathrm{S_1}}$	energy of the singlet excited state
E_{tr}	effective transport energy
E_{∞}	equilibrium energy
$E_{\mathrm{F},e}$	electron quasi-Fermi level
$E_{\mathrm{F},h}$	hole quasi-Fermi level
E_{C}	conduction band energy
E_{V}	valence band energy
$E_{\mathrm{L,A}}$	center of the LUMO in the acceptor
$E_{\mathrm{H,D}}$	center the HOMO in the donor
E_{g}	bandgap of the donor-acceptor blend
$\boldsymbol{E_{\mathrm{g}}^{\mathrm{PV}}}$	photovoltaic gap
$\boldsymbol{E_{\mathrm{g}}^{\mathrm{opt}}}$	optical gap
F	electric field
G	generation rate
$\hbar$	reduced Planck constant
J_G	generation current density
J_R	recombination current density
J_0	dark recombination current density
J_{ph}	photocurrent
J_{SC}	short-circuit current
J_{surf}	surface recombination current
k_{B}	Boltzmann constant
k_{bt}	charge transfer-to-exciton back transfer rate constant
k_{d}	charge transfer state dissociation rare constant
k_{f}	charge transfer state recombination rate constant
k_{ht}	hole transfer rate constant of excitons in the acceptor
k_{S}	recombination rate constant of excitons in the acceptor
k_1	monomolecular recombination coefficient
k_2	bimolecular recombination coefficient
k_L	Langevin recombination coefficient
m	factor describing the degree of disorder
n_{id}	ideality factor
n	density of electrons
n_f	density of free electrons

n_t	density of trapped electrons
$\boldsymbol{n_{CS}}$	density of free carriers in the charge-separated state
$\boldsymbol{n_{CT}}$	density of charge transfer states
$\boldsymbol{n_{S_1}}$	density of excitons
N_0	density of available states
N_{Y6}	number density of Y6 molecules
N_{CS}	density of available states for free carriers
N_{CT}	density of available interfacial charge transfer states
N_{S_1}	density of available excitonic states
p	density of holes
p_f	density of free holes
p_t	density of trapped holes
P_{in}	sun spectrum power density
q	elementary charge
Q	charge
Q_{coll}	collected charge
Q_{extr}	extracted charge
Q_{pre}	pre-extracted charge
Q_{tot}	total charge
R	recombination rate
S_1	singlet exciton
S	surface recombination velocity (or entropy when specified)
t	time
t_{del}	delay time
T	temperature
T_0	characteristic distribution temperature of an exponential density of states
V	applied voltage
V_{coll}	collection bias
V_{pre}	prebias
V_{OC}	open-circuit voltage
$V_{OC,rad}$	radiative limit of the open-circuit voltage
$\Delta V_{OC,nrad}$	non-radiative voltage loss
V_{BI}	built-in voltage

Greek Symbols

β_{enc}	coefficient for bimolecular free charge encounter
γ	recombination coefficient
δ	recombination order
ΔE_{S_1-CT}	energetic driving force for charge generation

ΔE_{CS}	energetic driving force for charge separation
ΔW_{f}	work function energetic offset
ε	dielectric constant
ε_0	vacuum permittivity
η_{abs}	absorption efficiency
η_{ex}	exciton diffusion and dissociation efficiency
η_{CT}	charge transfer state dissociation efficiency
η_{CE}	free charge extraction efficiency
μ	Charge carrier mobility
μ_0	zero-field and infinite temperature mobility
$\mu_{e(h)}$	electron (hole) mobility
μ_{CT}	chemical potential of the charge transfer state
μ_{S_1}	chemical potential of the singlet state
ν	drift velocity
σ	Gaussian energetic disorder
$\sigma_{\mathrm{L,A}}$	energetic disorder of the charge-separated states in the LUMO of the acceptor
$\sigma_{\mathrm{H,D}}$	energetic disorder of the charge-separated states in the HOMO of the donor
φ_{B}	injection barrier
Φ	electrostatic potential
ϕ_{BB}	black body emission photon flux
ϕ_{em}	total emitted photon flux
ϕ_{sun}	solar emission photon flux
ϕ_{S_1}	external excitonic emission photon flux
$\phi_{\mathrm{S}_1}^0$	excitonic emission photon flux in the dark

List of Publications

1. M. Stolterfoht, C. M. Wolff, Y. Amir, A. Paulke, L. Perdigón-Toro, P. Caprioglio, and D. Neher. Approaching the fill factor Shockley-Queisser limit in stable, dopant-free triple cation perovskite solar cells. *Energy Environ. Sci*. **2017**, 10, 1530–1539.

2. C. M. Wolff, F. Zu, A. Paulke, L. Perdigón-Toro, N. Koch, and D. Neher. Reduced Interface-Mediated Recombination for High Open-Circuit Voltages in CH3NH3PbI3 Solar Cells. *Adv. Mater*. **2017**, 29, 1700159.

3. E. Collado-Fregoso, S. N. Pugliese, M. Wojcik, J. Benduhn, E. Bar-Or, L. Perdigón Toro, U. Hörmann, D. Spoltore, K. Vandewal, J. M. Hodgkiss, and D. Neher. Energy-Gap Law for Photocurrent Generation in Fullerene-Based Organic Solar Cells: The Case of Low-Donor-Content Blends. *J. Am. Chem. Soc*. **2019**, 141, 2329–2341.

4. U. Würfel, L. Perdigón-Toro, J. Kurpiers, C. M. Wolff, P. Caprioglio, J. J. Rech, J. Zhu, X. Zhan, W. You, S. Shoaee, D. Neher, and M. Stolterfoht. Recombination between Photogenerated and Electrode-Induced Charges Dominates the Fill Factor Losses in Optimized Organic Solar Cells. *J. Phys. Chem. Lett*. **2019**, 10, 3473–3480.

5. M. Schwarze, K. S. Schellhammer, K. Ortstein, J. Benduhn, C. Gaul, A. Hinderhofer, L. Perdigón Toro, R. Scholz, J. Kublitski, S. Roland, M. Lau, C. Poelking, D. Andrienko, G. Cuniberti, F. Schreiber, D. Neher, K. Vandewal, F. Ortmann, and K. Leo. Impact of molecular quadrupole moments on the energy levels at organic heterojunctions. *Nat. Commun*. **2019**, 10, 2466.

6. V. M. Le Corre, M. Stolterfoht, L. Perdigón Toro, M. Feuerstein, C. Wolff, L. Gil-Escrig, H. J. Bolink, D. Neher, and L. J. A. Koster. Charge Transport Layers Limiting the Efficiency of Perovskite Solar Cells: How to Optimize Conductivity, Doping, and Thickness. *ACS Appl. Energy Mater*. **2019**, 2, 6280–6287.

7. J. Kniepert, A. Paulke, L. Perdigón-Toro, J. Kurpiers, H. Zhang, F. Gao, J. Yuan, Y. Zou, V. M. Le Corre, L. J. A. Koster, and D. Neher. Reliability of charge carrier recombination data determined with charge extraction methods. *J. Appl. Phys*. **2019**, 126, 205501.

8. M. Raoufi, U. Hörmann, G. Ligorio, J. Hildebrandt, M. Pätzel, T. Schultz, L. Perdigón-Toro, N. Koch, E. List-Kratochvil, S. Hecht, and D. Neher. Simultaneous Effect of Ultraviolet Radiation and Surface Modification on the Work Function and Hole Injection Properties of ZnO Thin Films. *Phys. Status Solidi Appl. Mater. Sci*. **2020**, 217, 1900876.

9. L. Perdigón-Toro, H. Zhang, A. Markina, J. Yuan, S. M. Hosseini, C. M. Wolff, G. Zuo, M. Stolterfoht, Y. Zou, F. Gao, D. Andrienko, S. Shoaee, and D. Neher. Barrierless Free Charge Generation in the High-Performance PM6:Y6 Bulk Heterojunction Non-Fullerene Solar Cell. *Adv. Mater*. **2020**, 32, 1906763.

10. S. Samson, J. Rech, L. Perdigón-Toro, Z. Peng, S. Shoaee, H. Ade, D. Neher, M. Stolterfoht, and W. You. Organic Solar Cells with Large Insensitivity to Donor Polymer Molar Mass across All Acceptor Classes. *ACS Appl. Polym. Mater*. **2020**, 2, 5300–5308.

11. L. Perdigón-Toro, L. Quang Phuong, S. Zeiske, K. Vandewal, A. Armin, S. Shoaee, and D. Neher. Excitons Dominate the Emission from PM6:Y6 Solar Cells, but This Does Not Help the Open-Circuit Voltage of the Device. *ACS Energy Lett*. **2021**, 6, 557–564.

12. N. Tokmoldin, J. Vollbrecht, S. M. Hosseini, B. Sun, L. Perdigón-Toro, H. Y. Woo, Y. Zou, D. Neher, and S. Shoaee. Explaining the Fill-Factor and Photocurrent Losses of Nonfullerene Acceptor-Based Solar Cells by Probing the Long-Range Charge Carrier Diffusion and Drift Lengths. *Adv. Energy Mater*. **2021**, 11, 2100804.

13. J. Diekmann, P. Caprioglio, M. H. Futscher, V. M. Le Corre, S. Reichert, F. Jaiser, M. Arvind, L. Perdigón-Toro, E. Gutierrez-Partida, F. Peña-Camargo, C. Deibel, B. Ehrler, T. Unold, T. Kirchartz, D. Neher, and M. Stolterfoht. Pathways toward 30% Efficient Single-Junction Perovskite Solar Cells and the Role of Mobile Ions. *Sol. RRL* **2021**, 5, 2100219.

14. P. Caprioglio, D. S. Cruz, S. Caicedo-Dávila, F. Zu, A. A. Sutanto, F. Peña-Camargo, L. Kegelmann, D. Meggiolaro, L. Gregori, C. M. Wolff, B. Stiller, L. Perdigón-Toro, H. Köbler, B. Li, E. Gutierrez-Partida, I. Lauermann, A. Abate, N. Koch, F. De Angelis, B. Rech, G. Grancini, D. Abou-Ras, M. K. Nazeeruddin, M. Stolterfoht, S. Albrecht, M. Antonietti, and D. Neher. Bi-functional interfaces by poly(ionic liquid) treatment in efficient pin and nip perovskite solar cells. *Energy Environ. Sci*. **2021**, 14, 4508–4522.

15. J. Thiesbrummel, V. M. Le Corre, F. Peña-Camargo, L. Perdigón-Toro, F. Lang, F. Yang, M. Grischek, E. Gutierrez-Partida, J. Warby, M. D. Farrar, S. Mahesh, P. Caprioglio, S. Albrecht, D. Neher, H. J. Snaith, and M. Stolterfoht. Universal Current Losses in Perovskite Solar Cells Due to Mobile Ions. *Adv. Energy Mater*. **2021**, 11, 2101447.

16. V. M. Le Corre, J. Diekmann, F. Peña-Camargo, J. Thiesbrummel, N. Tokmoldin, E. Gutierrez-Partida, K. P. Peters, L. Perdigón-Toro, M. H. Futscher, F. Lang, J. Warby, H. J. Snaith, D. Neher, and M. Stolterfoht. Quantification of Efficiency Losses Due to Mobile Ions in Perovskite Solar Cells via Fast Hysteresis Measurements. *Sol. RRL* **2022**, 2100772.

17. L. Perdigón-Toro, L. Q. Phuong, F. Eller, G. Freychet, E. Saglamkaya, J. I. Khan, Q. Wei, S. Zeiske, D. Kroh, S. Wedler, A. Köhler, A. Armin, F. Laquai, E. M. Herzig, Y. Zou, S. Shoaee, and D. Neher. Understanding the Role of Order in Y-Series Non-Fullerene Solar Cells to Realize High Open-Circuit Voltages. *Adv. Energy Mater*. **2022**, 2103422.

Acknowledgements

The successful completion of my thesis work would have been impossible without the contribution, support and encouragement of many people. It is with great pleasure that I attempt to put into words the immense gratitude I feel.

First and foremost, I would like to thank my supervisor Prof. Dieter Neher for giving me the opportunity to work in his group. I will be forever grateful for his constant guidance through the years, but also for giving me his trust and the freedom I needed to become the scientist I am today. I am thankful as well for all he has taught me and for always being enthusiastic to answer my questions and doubts.

I am also very grateful to my second supervisor Prof. Safa Shoaee. She has continuously shared her knowledge with me and guided me through the "scientific world" with her experiences. I thank her deeply for always having an open door. I shall always cherish her uncountable advices, both in my professional and personal life.

Thank you to Prof. Heinz Bässler for agreeing to review my thesis.

I owe my thanks to my brilliant collaborators, without whom this work would have not been possible. I thank Huotian Zhang for visiting our lab, for his enthusiasm and sharing his knowledge with me, but most importantly for helping me to make my first ever PM6:Y6 solar cell! This work would not have happened without the great chemists in the group of Prof. Yingping Zou, whom I thank for sharing her NFA molecules with us. I want to take the opportunity to thank: Dr. Stefan Zeiske, Dr. Anastasia Markina, Dr. Jun Yuan, Dr. Jeromy J. Rech, Fabian Eller, Dr. Jafar I. Khan, Daniel Kroh, Dr. Stefan Wedler.

I would like to express my gratitude to Prof. Dr. Koen Vandewal, Dr. Ardalan Armin, Prof. Dr. Eva Herzig, Prof. Dr. Anna Köhler Dr. Denis Andrienko, Prof. Dr. Feng Gao and Prof. Dr. Frédéric Laquai for inspiring discussions and countless advices on my research.

My work days in Potsdam would have not been so enjoyable without the companionship, help and support of the wonderful members of the "Soft Matter Physics and Optoelectronics", the "Optoelectronics of Disordered Semiconductors" and the "PotsdamPero" groups, past and present. Special thanks to Dr. Frank Jaiser, for always sharing his unlimited knowledge on every aspect of both our lab and Uni Potsdam in general, and for his patience. Thanks to Andreas Horka for having made and kept track of our orders up until the very end. I am grateful to Burkhard for his AFM training, and to Thomas and Florian for always being willing to help. I feel especial gratitude towards APu for his countlessly building, re-building and re-checking laser diodes and amplifiers on my behalf, and for always being up to have activities with the group! In the last couple of years of my PhD I have especially missed Malavika, Elisa, Christian and Pietro; I always enjoyed their company both in and out of work. During this time, though, I have gotten to meet my "PWM en español" crew - Pacho and Emilio, who can always cheer me up. For their help over the years, I have to thank Guangzheng, Vincent, Mehrdad, Ulli, Motiur, Joachim, Nurlan, Elifnaz, Bowen, Jona, Steffen, Meysam, Jarla, Felix, Jonny…! I have to specially thank Phuong because of his crucial role in my research; this work would have not been possible without his help and dedication. I also want to express my gratitude to the students I have supervised, Xue and Yueqi, for their hard work and for allowing me to grow as a scientist and mentor.

Last but not least, thanks to Martin for proof-reading this thesis, for his guidance and support, for believing in me, and for sharing with me his passion for science and many other precious things in life that make it all worth it.

My heartfelt thanks to all my friends in Germany and back home. To my *colgaos*, thanks for providing a safe and fun haven for me to always return to, you guys have taught me that some friendships are forever!

To my flat mates in Berlin, Aysu, Mara, Marta, Müge: I will always be grateful for your friendship and your kindness. Thank you for giving me much needed distraction from my PhD life but also for understanding when at times I could not let go of work and I'd be not on my “best mood”, your patience made it all better!

I want to thank my best friend Esra, for her encouragement and for always being there for me. Her friendship, care and countless advices have made my life greater in every aspect.

Finally, I want to say *gracias* to my family for their support over the years. They have shown me the importance of unity, even in the distance. Special thanks to my cousins and Anais for all the fun times, for visiting me, for being so special in such different ways, and for always making me feel like I would have still chosen them as friends even if we weren't family!

I owe my deepest gratitude to my parents. Without them, I would not be able to devote my life to doing what I love most: learning. Their encouragement, support and unconditional love have been the most important pillars of my life. They have taught me the true meanings of hard work and fairness, and for that I will always be indebted to them. I feel lucky to be their daughter.

Thesis Declaration

I declare that this thesis is composed of my original work and that I did not use source material or aids other than those mentioned. I have fully referenced all text directly or indirectly quoted from a source. This thesis was not submitted to another University.

Potsdam, März 2022

The author,

Lorena Perdigón Toro